The Chemical Evolution of Unresolved Stellar Populations: From Stellar Astrophysics to Cosmology

by

Jonas Johansson

THE THESIS IS SUBMITTED IN PARTIAL FULFILMENT OF THE REQUIREMENTS FOR THE AWARD OF THE DEGREE OF DOCTOR OF PHILOSOPHY OF THE UNIVERSITY OF PORTSMOUTH

December, 2011

Copyright

Till Mamma och Pappa

Abstract

Stars light up galaxies that are the major building blocks of the Universe. Throughout this thesis we cover the analysis of stars and stellar populations to gain knowledge on the formation of galaxies and the evolution of the Universe. Understanding massive early-type galaxies is key to understand mass assembly and the formation and evolution of galaxies in the Universe.

The spectra of stellar populations carry a wealth of information regarding galaxy formation and evolution. Absorption lines are particularly useful as they are tracers of galaxy formation epoch and time-scale. Models of stellar populations are important tools for the analysis of galaxies. The accuracy of such models are crucial for the accuracy of the derived results. The first step in my thesis is therefore to improve upon current single stellar population models of absorption line indices. Calibration of the models with galactic globular cluster is crucial, since these are known to be close to single stellar populations. The main aim of the thesis is to apply the models to the analysis of early-type galaxies and Type Ia supernovae (SN Ia) host galaxies.

The main novelty of the stellar population models are new empirical calibrations of absorption line indices. These are based on the most comprehensive stellar library available to date *MILES*. The stellar spectra of this library have been carefully flux-calibrated. The models are therefore applicable to data without Lick index calibrations. Based on the new stellar population models we have developed a method for deriving element abundance ratios, including [O/Fe], [C/Fe], [N/Fe], [Mg/Fe], [Ca/Fe] and [Ti/Fe]. The method is applied to galactic globular clusters and we find the models to be well calibrated. The pattern of derived element abundance ratios show strong evidence for self-enrichment within globular clusters.

The method for deriving element abundance ratios is then applied to $\sim$4000 SDSS early-type galaxies. The element abundance ratios [O/Fe], [Mg/Fe], [C/Fe] and [N/Fe] show strong correlations with stellar velocity dispersion. Using the derived trends of element abundance ratios we constrain the lower time-scale limit of star formation and star-burst components in massive early-type galaxies to $\sim$0.4 Gyr. Both in the globular cluster and early-type galaxy study we find that the heavy α-elements Ca and Ti scale

with Fe rather than with the lighter α-elements O and Mg. This implies that a significant contribution from SN Ia to the enrichment of heavy α-elements is universally found and puts strong constraints on supernova nucleosynthesis and models of galactic chemical evolution.

SN Ia as standard candles connect luminosity distance to redshift space to constrain cosmology. We derive stellar population parameters for a quality selected sample of 84 SN Ia host galaxies. We find that the stretch factor of SN Ia light-curves are mainly dependent on stellar population age, indicating that SN Ia progenitor mass is the main driver of the peak luminosities. We do not find any significant dependencies on host galaxy properties for the scatter in the luminosity-distance relationship after light-curve corrections. This implies that the derived cosmological parameters from SN Ia peak luminosities are robust.

Preface

The work of this Ph.D. thesis was carried out at the Institute of Cosmology and Gravitation, University of Portsmouth, United Kingdom, under the supervision of Dr. Daniel Thomas and Dr. Claudia Maraston.

Whilst registered as a candidate for the above degree, I have not been registered for any other research award. The results and conclusions embodied in this thesis are the work of the named candidate and have not been submitted for any other academic award.

This research has been supported by the Science and Technology Facilities Council (STFC) and by the Marie Curie Excellence Team Grant "UniMass" (MEXT-CT-2006-042754), P.I. Claudia Maraston.

The work of Chapter 2, 3, 4 and 5 was carried out in collaboration with Daniel Thomas and Claudia Maraston and are published in Johansson et al. (2010), Thomas et al. (2011a), Thomas et al. (2011b) and Johansson et al. (2012a), respectively.

The work of Chapter 6 was carried out in collaboration with Daniel Thomas, Claudia Maraston, Bob Nichol, Janine Pforr, Mathew Smith and Hubert Lampeitl and will be published in Johansson et al. (2012b).

Acknowledgements

First I would like to thank my supervisors, Dr. Daniel Thomas and Dr. Claudia Maraston, for all the ideas and dedication to my work. I would also like to thank the Institute of Cosmology and Gravitation, for giving me the opportunity to conduct a PhD, and all the members of the institute for the many useful discussions that helped improve the work embodied in this thesis.

A special thank goes to my parents Eva and Lars for always being a great support. Without pushing me I have always felt that you sincerely backed me up regardless of the choices I have made.

Finally, I would also like to thank my sister Maria and her family, Sabine and all my close friends, especially Jacob, Gustav and Jonatan, for always being there.

List of Abbreviations and Acronyms

AGB	Asymptotic Giant Branch
AGN	Active Galactic Nuclei
A/N	Amplitude-over-Noise
BOSS	Baryon Oscillation Spectroscopic Survey
BPT	Baldwin, Phillips & Terlevich (1981)
CALIFA	Calar Alto Legacy Integral Field spectroscopy Area survey
CMD	Colour-Magnitude Diagram
DD	Double-Degenerate
FMOS	Fibre Multi-Object Spectrograph
FWHM	Full Width at Half Maximum
GANDALF	Gas AND Absorption Line Fitting
GC	Globular Cluster
GGC	Galactic Globular Cluster
Gyr	Giga year
HB	Horizontal Branch
HR	Hubble Residual
IFU	Integral Field Unit
IMF	Initial Mass Function
ISM	Inter-Stellar Medium
JONES	Jones (1999)
KMOS	K-band Multi-Object Spectrometer
L10	Lampeitl et al. (2010)
Lick/IDS	Lick observatory/Intermediate Dispersion Spectrograph
LINER	Low-Ionization Nuclear Emission-line Region
LRG	Luminous Red Galaxy
M05	Maraston (2005)
MaNGA	Mapping Nearby Galaxies at the Apache point observatory

MILES	a Medium resolution Isaac Newton Telescope Library of Empirical Spectra
MOSES	MOrphologically Selected Early-types in SDSS
MPA/JHU	Max-Planck institut für Astrophysik/Johns Hopkins University
MS	Main-Sequence
P02	Puzia et al. (2002)
P10	Pipino et al. (2010)
PPXF	Penalised PiXel Fitting
rms	root mean square
S05	Schiavon et al. (2005)
SALT2	Spectral Adaptive Light-curve Template 2
SAURON	Spectroscopic Areal Unit for Research on Optical Nebulae
SD	Single-Degenerate
SDSS	Sloan Digital Sky Survey
SED	Spectral Energy Distribution
SF	Star-Forming
SFF	Schiavon (2007) Fitting Function
SFR	Star Formation Rate
SGB	Sub-Giant Branch
S/N	Signal-to-Noise
SN	Supernova
SN Ia	Type Ia supernovae
SN II	Type II supernovae
SNR	SuperNova Rate
SSFR	Specific Star Formation Rate
SSP	Single-Stellar Population
STELIB	a STEllar LIBrary for stellar population synthesis models
RGB	Red Giant Branch
T10	Thomas et al. (2010)
TMB/K	Thomas, Maraston & Bender (2003a)/ Thomas, Maraston & Korn (2004)
TP-AGB	Thermally Pulsing Asymptotic Giant Branch
VLT	Very Large Telescope
WD	White Dwarf
WFF	Worthey et al. (1994) Fitting Function
z	redshift

Table of Contents

List of Tables

List of Figures

Chapter 1

Introduction

Galaxies are systems containing up to hundreds of billions of stars. This makes them the main building blocks of the universe and are thus tracers of the cosmic evolution and mass assembly. Galaxies come in many flavours, first classified by Edwin Hubble in the Hubble sequence or "tuning fork" (Hubble, 1936). This classification scheme was later extended by de Vaucouleurs (1959) and Sandage (1961) to include more detailed structural features. The original Hubble sequence is shown in Fig. 1.1. On the left hand side are elliptical galaxies that are diffuse systems, dominated by random stellar motions (Illingworth, 1977; Schechter & Gunn, 1979; Davies, 1981; Davies & Illingworth, 1983). These are classified as En, where n is a measure of their degree of ellipticity on the sky as n=1-b/a, where a and b are the lengths of the semi-major and semi-minor axes of an ellipse, respectively. Hence E0's appear spherically symmetric with equally long semi-major and semi-minor axes. Moving towards the right of the Hubble sequence the elliptical galaxies become more elongated.

On the right hand side are spiral galaxies that have their mass (both stellar and gas) located in a central bulge, disk(s) and a faint halo. Bulges and halos are like elliptical galaxies dispersion dominated, while stellar motion in disks are rotation dominated (Rubin, Ford & Thonnard, 1980; Bosma, 1981; Persic, Salucci & Stel, 1996). Spiral galaxies show structural features with distinct spiral arms, hence the name, housing high concentrations of star formation. The size of the bulge and the tightness of the spiral arms determine the position in the Hubble sequence. A more open spiral feature and a smaller bulge place the object further to the right in the fork. Spiral galaxies can show the feature of a bar in the central part, dividing spiral galaxies into two categories, resulting in the two branches of the Hubble sequence. In the middle of the Hubble sequence are S0 galaxies, which consist of both a massive bulge and disk with no visible spiral structure.

Hubble used the naming convention early-type and late-type galaxies for ellipticals and spirals, respectively. He made clear that such a naming convention only refers to

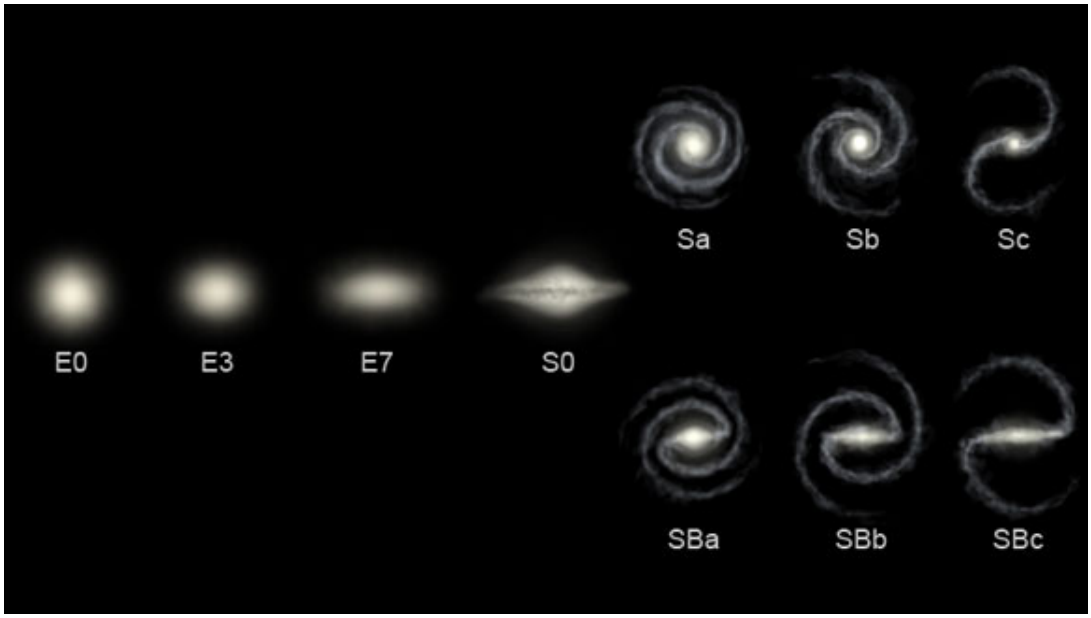

Figure 1.1: The Hubble sequence (or "tuning fork") of galaxy classification into different types, first published by Edwin Hubble in 1936 (image taken from http://eaae-astronomy.org/).

the position in the sequence, is purely empirical and without prejudice to theories of evolution. However, it has erroneously been interpreted as an evolutionary sequence where early-type galaxies transform into late-type galaxies. The ultimate goal of the theory of galaxy formation and evolution is to understand the origin of this sequence.

1.1 Galaxy evolution

Besides structural features early-type and late-type galaxies show several distinct differences both as populations and as individual systems. The densities of the two subpopulations are strongly dependent on the environmental density of the overall galaxy population. Groups and clusters of galaxies are dominated by early-types, while low density environments are instead dominated by late-types (Dressler et al., 1980; Postman & Geller, 1984; Giovanelli, Haynes & Chincarini, 1986; Dressler et al., 1997; Bamford et al., 2009). One of the most prominent distinctions between early-types and late-types is the colour bimodality. The former galaxies occupy a tight sequence in the colour-magnitude(mass) diagram known as the red sequence, while late-type galaxies form a less distinct sequence at bluer colours consequently named the blue cloud. This is illustrated in Fig. 1.2 (Fig. 10 from Faber et al., 2007). The colour-bimodality is well established for nearby galaxies (e.g. Strateva et al., 2001; Hogg et al., 2003; Kauffmann et al., 2003a; Balogh et al., 2004; Baldry et al., 2004), extends to z=1 (Lin et al., 1999;

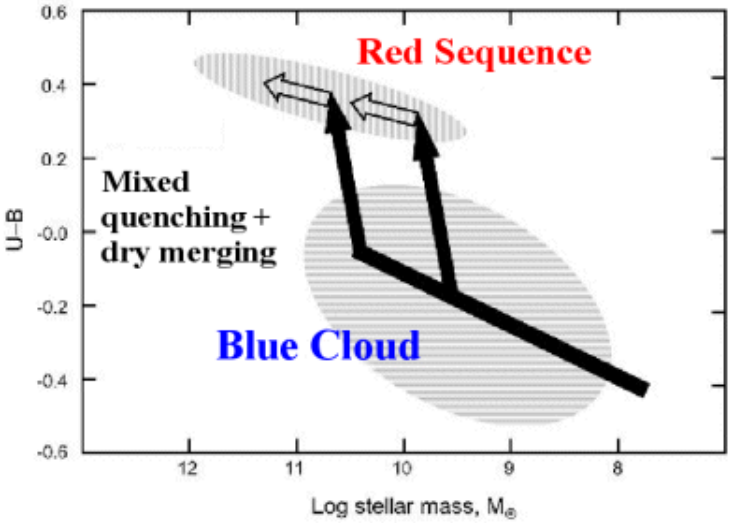

Figure 1.2: Illustration of the galaxy colour bimodality in the colour-mass(magnitude) diagram (Fig. 10 from Faber et al., 2007), with the division into a red sequence and blue cloud. Arrows show possible transformation scenarios where solid arrows/lines indicate wet merging and open arrows are dry merging. Galaxies move from the blue cloud to the red sequence through wet merging with sub-sequent quenching of star formation.

Bell et al., 2004; Weiner et al., 2005; Willmer et al., 2006) and possibly all the way up to z∼2-3 (Giallongo et al., 2005). It arises from the stellar populations inhibiting the different galaxy morphologies, since massive short lived stars have blue colours and stars in general become redder as they evolve. Early-type galaxies experience in general negligible or very low rates of star-formation, hence evolve passively, and thus have old, red stellar populations. Late-type galaxies instead show significantly higher rates of star formation and are therefore populated with a significant fraction of young, blue stars. Further, early-type and late-type galaxies contain in general low and high amounts of gas and dust, respectively. Although early-type galaxies in general fall on the red sequence a fraction of these galaxies in the nearby Universe exhibit blue colours, significant star-formation rates (e.g. Schawinski et al., 2007) and consequently young stellar population ages (e.g. Thomas et al., 2010). Likewise there is a fraction of the late-type galaxy population in the nearby Universe that show red colours (e.g. Masters et al., 2010).

Cold dark matter (CDM) models of hierarchical galaxy formation is the most accepted theory governing galaxy evolution (White & Rees, 1978). In such a scenario dark matter haloes form bottom-up, i.e less massive haloes merge into larger entities, and the baryonic matter is assumed to follow the dark matter (Kauffmann, White & Guiderdoni, 1993; Kauffmann, 1996). Thus small galaxies are formed in the early universe and as cosmic time progresses larger and larger galaxies are built-up. Hence larger galaxies are formed by the merging of smaller entities. This implies that more massive galaxies experienced longer formation time-scales. The hierarchical evolution of galaxies is well

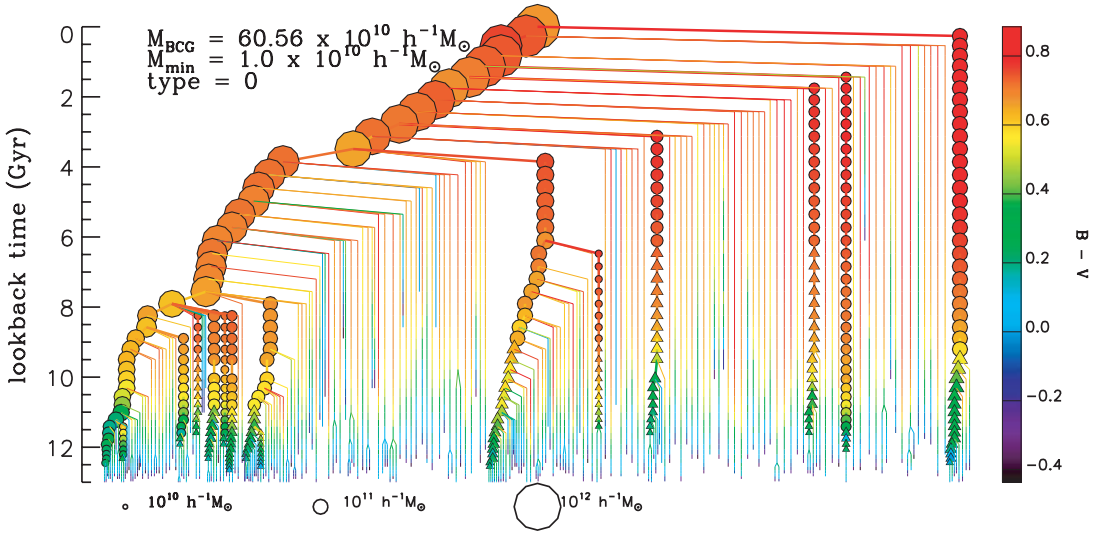

Figure 1.3: Fig. 1 of De Lucia & Blaizot (2007) showing the merger tree of hierarchical galaxy formation for brightest cluster galaxies (BCGs). Lookback time in Gyr (left hand y-axis) and colour of the stellar populations (right hand y-axis) are shown in relation to stellar mass of the systems. The size of the symbols scales with stellar mass and the colours represent B-V colour. Small systems merge into larger and larger systems as time evolves.

demonstrated in Fig. 1.3 where the build-up of brightest cluster galaxies is shown (credit De Lucia & Blaizot, 2007). CDM models are very successful in reproducing large scale clustering in the Universe (e.g. Springel et al., 2005a)

Hopkins et al. (2006) and Faber et al. (2007) explain the transformation of galaxies between the blue-cloud and red-sequence in the hierarchical frame-work of galaxy evolution, illustrated in Fig. 1.2. The merging of gas-rich late-type galaxies induces star-formation (wet merging). As a result the merged galaxies move towards higher masses in the blue cloud. The merging of late-type galaxies with the sub-sequent quenching of star-formation and removal of gas reservoirs instead move galaxies from the blue cloud to the red-sequence. Proposed mechanisms for the quenching of star-formation include heating through starbursts (Mihos & Hernquist, 1994; Sanders & Mirabel, 1996), winds of radiation acting on dust (Murray et al., 2005), injection of orbital energy during the merger (Cox et al., 2006), and active galactic nucleus (AGN) feedback (Granato et al., 1999; Springel et al., 2005b). Merging of galaxies has been shown to be able to disrupt spiral features and transform disk dominated galaxies into spheroids (e.g. Toomre & Toomre, 1972; Barnes & Hernquist, 1996). The most massive early-type galaxies are finally built up by the sub-sequent merging of gas-poor (dry merging) red-sequence galaxies. Hence it is rather believed that late-type galaxies evolve into early-type galaxies than the other way around as imposed by the naming convention.

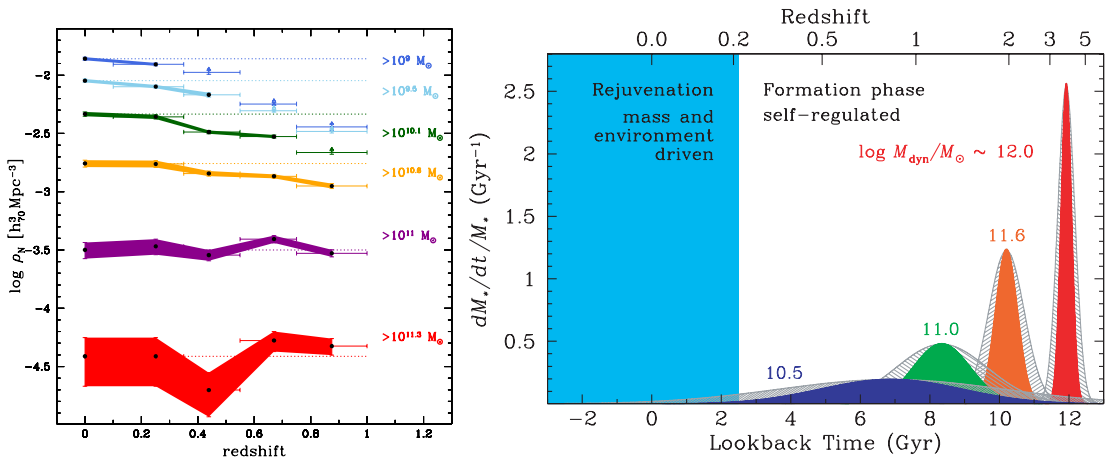

Figure 1.4: Two independent examples of downsizing. Left hand panel: Cosmological downsizing from Pozzetti et al. (2010) (Fig. 7), showing the number density of early-type galaxies of various masses between z∼1 and z=0. The number density of the most massive objects is constant, while the analogous for less massive systems increase towards lower redshifts. Right hand panel: Astro-archeological downsizing from Thomas et al. (2010) (Fig. 9), showing star-formation rates as a function of lookback time for various early-type galaxy masses and the gaussian widths represent formation time-scales. More massive galaxies clearly formed at earlier epochs, under shorter time-scales and experienced higher star-formation rates.

The scenario discussed above gets support from the observed density evolution of galaxies by Bell et al. (2004). They find that the stellar mass on the red sequence has increased by a factor ∼2 since a redshift of ∼1, while the number density of massive blue-sequence galaxies has dropped significantly over this period. On the other hand the study of Cimatti et al. (2006) shows that the number density of massive early-type galaxies is constant out to a redshift of ∼0.8, while the number density of less massive early-type galaxies increases over the same redshift range. Similarly, the left hand panel of Fig. 1.4 (taken from Pozzetti et al., 2010) shows that the evolution of the number density of early-type galaxies is strongly dependent on galaxy mass. Hence the number density of the most massive galaxies is constant out to z∼1. These results demonstrate cosmological downsizing of early-type galaxies, where more massive systems have assembled their stellar mass at earlier epochs. Cosmological downsizing can be explained in the Hierarchical formation paradigm through faster assembly of the baryonic matter that reside in deeper gravitational potential wells.

An alternative avenue to the cosmological approach is the astro-archeological approach, tracing the epoch when galaxies form their stars. The latter utilises the fact that stars are the fossil record of the parent gas clouds forming the stellar populations, thus creating links between different epochs of the Universe with the local galaxy population. The observables of stellar populations, however, are affected by stellar age and metallicity in similar fashions, known as the age-metallicity degeneracy (Worthey, 1994). This is

a long standing problem which is key to break in order to fully interpret observed stellar populations.

As mentioned above, with the astro-archeological approach we study the early universe and the formation histories of galaxies through the stellar populations at low redshifts. Early-type galaxies form tight relationships in the colour-magnitude 2D parameter space (Baum, 1959; Visvanathan & Sandage, 1977; Sandage & Visvanathan, 1978a,b; Bower, Lucey & Ellis, 1992) and in the 3D parameter space of the fundamental plane (effective radius, velocity dispersion and luminosity, Dressler et al., 1987; Djorgovski & Davis, 1987; Bender, Burstein & Faber, 1992; Renzini & Ciotti, 1993). These tight relations imply uniform star formation histories and a systematic trend of the stellar content with galaxy mass. The epoch of star formation of early-type galaxies has been constrained to occur at z>2, using the small scatter in the colour-magnitude relation (Bower et al., 1992) and the fundamental plane (Renzini & Ciotti, 1993).

Independent studies of absorption line strengths derived from galaxy spectra confirm old stellar population ages in early-type galaxies and most importantly find non-solar ratios of α- to Fe-elements (e.g. O'Connell, 1976; Peterson, 1976; Burstein et al., 1984; Worthey, Faber & Gonzalez, 1992; Davies, Sadler & Peletier, 1993). The α-elements are mainly ejected into the inter-stellar medium (ISM) through the explosion of collapsing massive stars as Type II supernovae (SN II) (e.g. Woosley & Weaver, 1995; Thielemann, Nomoto & Hashimoto, 1996). The short life-times of massive stars thus result in a prompt production of α-elements in respect to star formation. Fe-like elements are produced by SN II as well as by the delayed explosion of Type Ia supernovae (SN Ia, e.g. Nomoto, Thielemann & Yokoi, 1984). Hence, the α/Fe ratio is a good measure of the relative contribution from SN II and SN Ia to the chemical enrichment of the ISM (Greggio & Renzini, 1983; Matteucci & Greggio, 1986; Pagel & Tautvaisiene, 1995; Thomas, Greggio & Bender, 1998) and thus of the formation time-scales of stellar populations due to the prompt enrichment of α-elements and the delayed Fe enrichment in respect to star formation (Trager et al., 2000b; Thomas et al., 2005, 2010). Consequently, a higher α/Fe ratio implies shorter formation time-scales. Further investigations report that more massive early-type galaxies exhibit older stellar population ages and more importantly higher α/Fe ratios (Trager et al., 2000b; Nelan et al., 2005; Thomas et al., 2005; Bernardi et al., 2006; Clemens, Bressan, Nikolic, Alexander, Annibali & Rampazzo, 2006; Gallazzi et al., 2006; Graves et al., 2007; Jimenez et al., 2007; Allanson et al., 2009; Thomas et al., 2010). These results connote astro-archeological downsizing of early-type galaxies. This is quantified in the right hand panel of Fig. 1.4 showing older ages, higher star-formation rates and shorter formation time-scales for more massive early-type galaxies (credit Thomas et al., 2010). Hence more massive early-type galaxies both form stars and assemble their mass at earlier epochs. Since the most massive early-type galaxies are

also the most massive objects observed, understanding the formation of such systems is key to understand mass-assembly in the Universe.

Even though CDM models struggle in reproducing the observed α/Fe-mass trends (e.g. Thomas, 1999a), hierarchical galaxy formation is not necessarily contradicted by the astro-archeological downsizing scenario. This scenario mainly means that the stellar populations of more massive galaxies formed at higher redshifts. Hence the stellar populations may have formed in smaller entities that later merge without subsequent star formation.

Yet another definition of downsizing, apart from the astro-archeological and the stellar mass downsizing discussed above, has frequently been investigated, i.e. star formation rate (SFR) downsizing. Several authors report that the mass of star forming galaxies decrease with decreasing redshift (e.g. Cowie et al., 1996; Kodama et al., 2004). However, two recent studies Chen et al. (2009) and Karim et al. (2011) find that the specific star formation rate (SSFR), i.e. SFR per unit stellar mass, strongly declines with decreasing redshift (below z$\sim$1.5) at a rate that does not depend on mass. On the other hand Chen et al. (2009) and Karim et al. (2011) also find that out to z$\sim$1.0 and z$\sim$1.5, respectively, more massive galaxies consistently show lower SSFRs. This implies that the most massive galaxies are the first objects to fall below their past-average star formation activity (Karim et al., 2011). Hence the different downsizing scenarios discussed above agree in the sense that the main formation epoch of more massive galaxies took place at higher redshifts.

1.2 Stellar population modelling

The major tool for analysing the stellar populations in galaxies are stellar population models. Models of the full spectral energy distribution (SED, Maraston, 1998, 2005; Vazdekis et al., 1996, 2010; Bruzual & Charlot, 2003; Maraston & Strömbäck, 2011) are very useful for deriving specifically the stellar mass of galaxies, but also for studying stellar population ages and metallicities, star formation rates etc. (Pforr et al.). This can be done either through fitting of photometry which has the advantage of shorter observational integration times, because of the broad wavelength bands collecting light, or spectroscopic fitting that provides higher accuracy of the derived parameters. However, SED fitting is prone to the age-metallicity degeneracy. Including a very wide wavelength range seems promising for breaking such degeneracies.

A great advantage of instead using stellar population models of absorption line indices (Worthey, 1994; Trager et al., 2000a; Thomas et al., 2003a; Thomas et al., 2004;

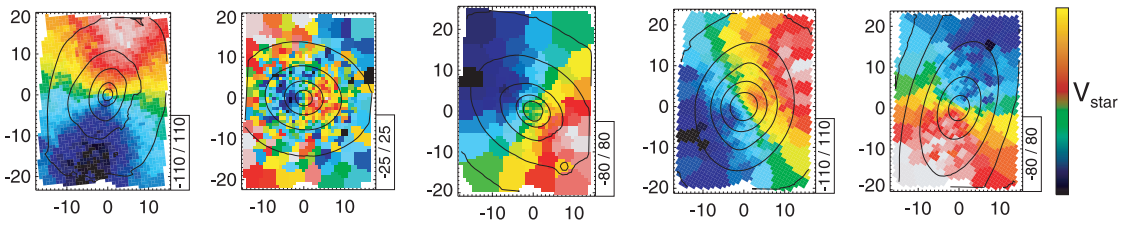

Figure 1.5: Part of Fig. 7 from Kuntschner et al. (2010) showing the spatial resolution of stellar velocities for five different galaxies. Four objects are clearly rotation dominated, while the fifth objects is dispersion dominated.

Schiavon, 2007; Annibali et al., 2007) is the possibility to study element abundance ratios besides stellar population ages and metallicities. This is not possible through current SED fitting techniques because reliable SED models with element abundance ratio variations do not exist. Such models are to date based on theoretical stellar spectra prone to incomplete line lists (Korn et al., 2005; Coelho et al., 2007; Rodríguez-Merino et al., 2005; Lee et al., 2009a; Walcher et al., 2009). Models of absorption line indices are also prone to the age-metallicity degeneracy, but the simultaneous consideration of metallicity sensitive and age sensitive absorption line indices have already proven to be useful for breaking (although not perfectly) this degeneracy (Faber et al., 1985; González, 1993; Worthey, 1994; Worthey & Ottaviani, 1997; Kuntschner & Davies, 1998; Thomas, Maraston & Bender, 2003a). Another advantage of the absorption line technique is the insensitivity to dust reddening, due to the short wavelength ranges used for measuring the absorption line strengths. On the other hand, absorption line indices require higher data quality compared to the study of the full SED.

Studying element abundance ratios have revealed the astro-archeological downsizing of early-type galaxies as discussed in the previous section. These are also degenerate with the stellar population parameters age and metallicity. Thus including the element abundance ratios are important for deriving stellar population parameters to a high precision.

1.3 Galaxy spectroscopy

One advantage of the astro-archeological approach compared to the cosmological approach is the shorter observational integration times needed to reach a desired signal-to-noise (S/N) compared to high redshift surveys. Hence surveys like the Sloan Digital Sky Survey (SDSS, York et al., 2000) have been able to observe millions of objects with decent data quality, introducing a statistical approach to study galaxy evolution.

Other options are smaller samples with high S/N. The use of integral-field-unit (IFU) spectroscopy and imaging is one great example pioneered by the SAURON team (Spectroscopic Areal Unit for Research on Optical Nebulae, e.g. Bacon et al., 2001; Davies et al., 2001; Kuntschner et al., 2010). IFU allows for high spatial resolution of extended objects for detailed studies of e.g. stellar and gas kinematics and absorption line strengths. Fig. 1.5 is taken from Kuntschner et al. (2010) showing the stellar velocities of five spatially resolved galaxies from the SAURON sample. Revealing gradients of stellar population parameters and kinematically decoupled populations are keys to understanding galaxy assembly histories.

Hence both the analysis of large samples such as the SDSS and IFU surveys providing high spatial resolution are important avenues to study galaxy formation.

1.4 Galaxies as cosmological probes

The detailed understanding of galaxies and their formation histories is important well beyond the field of galaxy evolution and has crucial impact on cosmology and our understanding of the expansion history of the Universe. Massive early-type galaxies can be used as cosmological probes thanks to their passive evolution out to z$\sim$1 (e.g. Bender et al., 1998; Carson & Nichol, 2010)

About a decade ago on of the most spectacular discoveries in observational cosmology was made. The expansion of the Universe was found to accelerate, inferred from the luminosity-redshift relation derived from SN Ia peak luminosities (Riess et al., 1998; Perlmutter et al., 1999). This is shown in Fig. 1.6 where the cosmological parameters are constrained using this relation. SN Ia are useful standard candles due to their very bright peak luminosities. These must be corrected for systematic variations to reliably constrain cosmology (Phillips, 1993; Jha et al., 2007; Guy et al., 2007; Conley et al., 2008; Kessler et al., 2009). However, even after corrections the peak luminosities and consequently the luminosity-redshift relationship show a non-negligible scatter (Hubble residuals). Secondary effects not accounted for are crucial to identify in order to further reduce the Hubble residuals and improve upon the derived cosmological parameters.

It is well established that the peak luminosity of SN Ia depend on host galaxy morphology (e.g. Oemler & Tinsley, 1979; van den Bergh, 1990; Mannucci et al., 2005; Sullivan et al., 2006), mass (Kelly et al., 2010; Lampeitl et al., 2010; Sullivan et al., 2010) and stellar population parameters (Hamuy et al., 2000; Gallagher et al., 2008; Howell et al., 2009; Neill et al., 2009). These studies indicate that stellar population age may be the main driver of SN Ia luminosity. However, either fairly small samples have been used or metallicity has been indirectly measured. The reason for such dependencies are

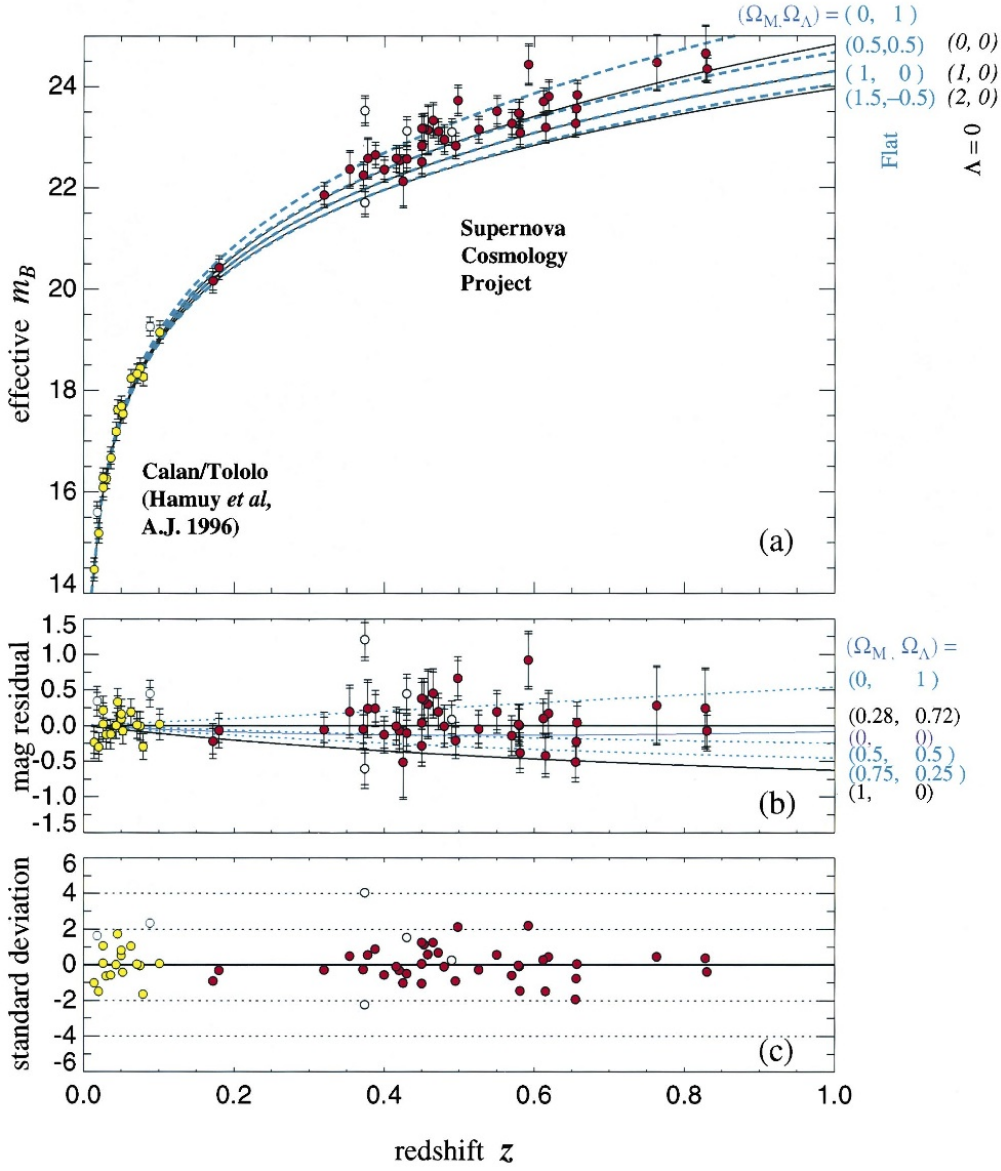

Figure 1.6: Fig. 2 from Perlmutter et al. (1999) showing the best-fit cosmology to the luminosity-redshift relation inferred from SNI Ia. The best-fit parameters indicate an accelerating expansion of the Universe.

obviously that the stellar progenitors of SN Ia are related to the stellar populations of the host galaxies.

Also for the Hubble residuals dependencies on host galaxy mass and stellar population parameters have been found (Gallagher et al., 2008; Howell et al., 2009; Neill et al., 2009; Kelly et al., 2010; Lampeitl et al., 2010; Sullivan et al., 2010). Even though metallicity is believed to be the main source of secondary effects, it is still debated which parameter that best can reduce the scatter in the luminosity-redshift relation. This is mainly because the dependencies are very weak, requiring high quality data and statistically significant samples to be detected.

The indications of systematic Hubble residual trends are alarming, since the derived cosmology may be biased towards the data samples used. Hence host galaxy studies are crucial for understanding systematics affecting the derived cosmological parameters.

1.5 Aim and outline of this thesis

The accuracy of stellar population models will ultimately determine the accuracy of the derived galaxy scaling relations. Starting from stars which are the major building blocks of galaxies we intend to improve upon current stellar population models of absorption line indices. The first step is thus to empirically calibrate absorption line indices with stellar parameters for the most comprehensive stellar library available (Chapter 2). The next step is consequently to incorporate these empirical calibrations to produce state of the art models of absorption line indices (Chapter 3)

Due to the importance of studying element abundance ratios the third step of this thesis is to develop a method for deriving individual element abundance ratios using the newly computed models of absorption line indices (Chapter 4). It is desired to calibrate the models and galactic globular clusters with independent measurements of stellar population parameters and element abundance ratios are used for this end. Galactic globular clusters are useful as they are known to be close to single stellar populations, i.e. single age and metallicity, which is also the nature of our models. The calibration is found to be very successful. Galactic globular clusters are interesting objects and thus we also aim at analysing the derived stellar population parameters in the light of globular cluster formation.

The main aim of this thesis is to study chemical enrichment of early-type galaxies. The wealth of information in SDSS spectra has not yet been fully exploited for the study element abundance ratios. The stellar population models and method developed is therefore applied to a large sample of SDSS galaxies (Chapter 5). We find that the analysis of the individual element abundance ratios sets strong constraints on various aspects of the formation and evolution of early-type galaxies.

Hence starting with the analysis of stars, we proceed through globular clusters and up to early-type galaxies. Finally we use this knowledge to contribute to cosmology and to our understanding of the evolution of the Universe. The final step of this thesis is therefore to study the stellar populations of SN Ia host galaxies (Chapter 6). The stellar population models and method developed are applied to host galaxies of the SDSS-II SN survey. We find, contrary to recent alarming claims, that Hubble residuals do not show any dependence on host galaxy properties. This implies that the cosmology derived from SN Ia is robust.

Chapter 2

Empirical fitting functions of the MILES stellar library

Stellar population models of absorption line indices are an important tool for the analysis of stellar population spectra. They are most accurately modelled through empirical calibrations of absorption line indices with the stellar parameters effective temperature, metallicity, and surface gravity, the so-called fitting functions. In this chapter we present new empirical fitting functions for the 25 optical Lick absorption line indices based on the new stellar library MILES (a Medium resolution Isaac Newton Telescope Library of Empirical Spectra). The major improvements with respect to the Lick/IDS library are the better sampling of stellar parameter space, a generally higher signal-to-noise, and a careful flux calibration. In fact we find that errors on individual index measurements in MILES are considerably smaller than in Lick/IDS. Instead we find the root mean square (rms) of the residuals between the final fitting functions and the data to be dominated by errors in the stellar parameters. We present fitting functions for both Lick/IDS and MILES spectral resolutions, and compare our results with other fitting functions in the literature. We further calculate the offsets in index measurements between the Lick/IDS system to a flux calibrated system. For this purpose we use the three libraries MILES, ELODIE, and STELIB. We find that offsets are negligible in some cases, most notably for the widely used indices Hβ, Mgb, Fe5270, and Fe5335. In a number of cases, however, the difference between flux calibrated library and Lick/IDS is significant with the offsets depending on index strengths. Interestingly, there is no general agreement between the three libraries for a large number of indices, which hampers the derivation of a universal offset between the Lick/IDS and flux calibrated systems.

2.1 Introduction

2.1.1 Background

Stellar population models of absorption line indices are a key tool for the analysis of star cluster and galaxy absorption spectra. They are used to derive the fundamental stellar population properties such as age, metallicity and element abundance ratios. In particular, optical absorption line diagnostics in the spectra of evolved stellar populations have successfully been adopted in the past in studies on galaxy evolution (e.g. Worthey et al., 1992; Davies et al., 1993; Vazdekis et al., 1997; Kuntschner & Davies, 1998; Worthey, 1998; Trager et al., 1998; Henry & Worthey, 1999; Kuntschner, 2000; Trager et al., 2000a; Thomas et al., 2005) and globular cluster formation (e.g. Kissler-Patig, 1998; Forbes et al., 2001; Kuntschner et al., 2002; Brodie et al., 2005; Puzia et al., 2005). The Lick/IDS system (Burstein et al., 1984; Faber et al., 1985; Gorgas et al., 1993; Worthey et al., 1994; Worthey & Ottaviani, 1997; Trager et al., 1998) is the standard set of absorption line indices (described in more detail in the next section) that has been used extensively during the last two decades for studying absorption features of stellar populations. This system consists of index definitions for 25 prominent absorption features between 4000 and 6500 Å present in the spectra of evolved stellar populations.

For studies of galaxy and star cluster evolution, absorption lines need to be modelled for stellar populations (e.g. Maraston, 1998, 2005; Bruzual & Charlot, 2003; Vazdekis, 1999; Leitherer et al., 1999; Worthey et al., 1994; Worthey & Ottaviani, 1997; Rose et al., 1994; Trager et al., 2000a; Thomas, Maraston & Bender, 2003a; Thomas, Maraston & Korn, 2004). A convenient way goes through the use of empirical calibrations. This is motivated by the fact that theoretical model atmospheres are known to suffer from incomplete line lists and continuum uncertainties. (e.g. Korn, Maraston & Thomas, 2005; Coelho et al., 2007; Rodríguez-Merino et al., 2005; Lee, Worthey & Dotter, 2009a; Walcher et al., 2009). Empirical calibrations on the other hand have the disadvantage to be hardwired to the chemical abundance pattern of the Milky Way, which can be overcome in a semi-empirical approach as in the models by Trager et al. (2000a), Thomas et al. (2003a); Thomas et al. (2004) and Schiavon (2007) (see further discussion in Chapter 3)

Empirical calibrations can be inserted in the models in two ways. In the first and most widely used approach, absorption line indices enter stellar population modelling through calibrations of the empirical relationship between the indices and the stellar atmospheric parameters $T_{\rm eff}$, $\log g$ and [Fe/H] as provided by stellar libraries. As these calibrations are usually obtained through polynomial fitting procedures they are commonly referred to as 'fitting functions'. The quality of the final stellar population model critically depends on

the accuracy with which these relationships can be inferred from stellar libraries, i.e. the coverage of stellar parameter space and the reliability of the index measurements. The computational procedure with which the fitting functions are determined is a further crucial step in producing accurate models. A number of studies in the literature are devoted to such empirical calibrations for various stellar libraries, either for the Lick indices, parts of the Lick indices or other prominent absorption features (Buzzoni, Gariboldi & Mantegazza, 1992; Buzzoni, Mantegazza & Gariboldi, 1994; Worthey et al., 1994; Borges et al., 1995; Gorgas et al., 1999; Cenarro et al., 2002; Schiavon, 2007; Maraston et al., 2009).

Alternatively to the use of fitting functions, absorption line indices can be measured directly on the SED from stellar population models that are based on empirical stellar libraries. The benefit of this method is that the full SED can be compared pixel-by-pixel to observations (e.g. Panter et al., 2007; Tojeiro et al., 2007).

The major strength of fitting functions, instead, lies in the fact that they allow for interpolation between well populated regions of stellar parameter space which increases the accuracy of the model in stellar parameter space that is only sparsely sampled by empirical stellar libraries. Moreover, each absorption index or spectral feature is represented by an individual fitting function, which is optimised to best reproduce its behaviour in stellar parameter space. Fitting functions are also easier to implement in a stellar population synthesis code, and models based on fitting functions are better comparable.

The widely used fitting functions of Worthey et al. (1994) and Worthey & Ottaviani (1997) are based on the Lick/IDS stellar library (Burstein et al., 1984; Faber et al., 1985). They are adopted in most stellar population models (Worthey, 1994; Vazdekis et al., 1996; Trager et al., 2000a; Thomas et al., 2003a; Thomas et al., 2004, 2005; Annibali et al., 2007) in the literature. Other fitting functions based on the same stellar library exist (Buzzoni et al., 1992, 1994; Borges et al., 1995) and lead to overall consistent results in the final stellar population model (Maraston et al., 2003). Major progress has been made with the advent of a new generation of stellar libraries (Jones, 1999; Prugniel & Soubiran, 2001; Le Borgne et al., 2003; Sánchez-Blázquez et al., 2006b) that have led to considerable improvements regarding coverage of stellar parameter space, spectral resolution, signal-to-noise ratio, and flux calibration.

In particular the latter is a critical step forward. As the Lick/IDS system is not flux calibrated, observations have to be re-calibrated onto the Lick/IDS system through comparison with Lick standard stars. This requirement hampers the analysis of data samples for which spectra of such calibration stars are either not available at sufficient quality or do not cover the appropriate rest-frame wavelength range. This problem is most imminent in high redshift observations and in galaxy redshift surveys such as SDSS (York et

al., 2000). The new flux calibrated libraries allow the analysis of flux calibrated spectra at any redshift without spectroscopic standard stars.

Flux-calibrated stellar libraries in the literature that are suitable for stellar population modelling include the *JONES* (Jones, 1999), *ELODIE* (Prugniel & Soubiran, 2001), *STELIB* (Le Borgne et al., 2003) and *MILES* (Sánchez-Blázquez et al., 2006b) libraries. The *MILES* library is particularly well suited for stellar population modelling of absorption line indices owing to its favourable combination of spectral resolution, wavelength range, stellar parameter coverage, and quality of flux calibration. In this chapter we present new Lick index fitting functions based on the *MILES* stellar library. To take advantage of the full spectral resolution of the *MILES* library we have produced fitting functions for both the lower Lick/IDS resolution ($8 - 11$ Å FWHM-Full Width at Half Maximum) and the higher resolution of the *MILES* library (2.54 Å FWHM). A new version of the Thomas et al. (2003a) (TMB) stellar population model of absorption line indices based on these new fitting functions are presented in Chapter 3.

This chapter is organized as follows. In Section 2.2 we present the Lick indices measured on the *MILES* library and a quality evaluation of the index measurements. We discuss offsets between the flux calibrated MILES and the Lick/IDS systems. The empirical fitting method is presented in Section 2.3 along with the resulting fitting functions. In Section 2.4 we compare the fitting functions of this work with fitting functions from the literature. We summarise in Section 2.5.

2.1.2 The Lick index system

Substantial progress in exploiting galaxy spectra has been made by the Lick group who defined the 25 Lick indices tracing the most prominent absorption features in the visual wavelength region. However, the absorption features of galaxy spectra are prone to stellar velocity dispersion broadening. This erases the continuum and the 25 the Lick indices (Burstein et al., 1984; Faber et al., 1985; Gorgas et al., 1993; Worthey et al., 1994; Worthey & Ottaviani, 1997; Trager et al., 1998) have thus been defined by the use of pseudo-continua. For each index the pass-band of the main feature is accompanied by two flanking pseudo-continuum pass-bands. The mean fluxes of these are connected at the central wavelengths defining the final pseudo-continuum. This is illustrated in Fig. 2.1 showing relative flux as a function of wavelength for a random SDSS early-type galaxy. Solid vertical lines are main feature pass-band definitions and dotted vertical lines are pseudo-continua pass-bands definitions. Solid horizontal lines are mean fluxes in the pseudo-continua pass-bands and the dashed line is the final pseudo-continuum.

The original index definitions were published in Worthey et al. (1994) for 21 indices and in Worthey & Ottaviani (1997) for the four higher order Balmer indices (Hδ_A, Hδ_F,

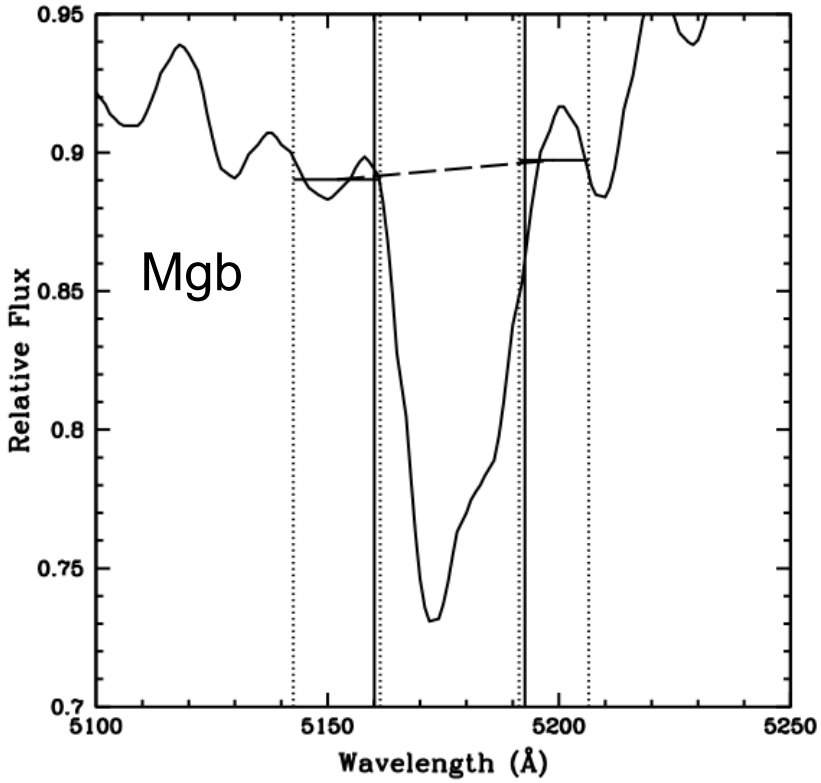

Figure 2.1: Lick definition of the Mgb index. Relative flux as a function of wavelength is shown for a random SDSS early-type galaxy. Solid vertical lines are definitions of the main feature pass-band, while dotted vertical lines are definitions of the pseudo-continua pass-bands. Solid horizontal lines are mean fluxes in the pseudo-continua pass-bands. The dashed line connects the central wavelengths of the pseudo-continua pass-bands defining the final pseudo-continuum.

Hγ_A and Hγ_F). The 21 index definitions of Worthey et al. (1994) were refined in Trager et al. (1998) through cross-correlation with more accurate, in terms of wavelength calibration, spectra. The index strengths are measured as the ratio between the flux in the feature pass-band and the pseudo-continuum as either equivalent widths (EW, narrow atomic features) or magnitudes (Mag, broad molecular features). The definitions for measuring the indices are

$$EW = \int_{\lambda_1}^{\lambda_2} \left(1 - \frac{F_{I\lambda}}{F_{C\lambda}}\right) d\lambda \tag{2.1}$$

$$Mag = -2.5log\left(\left(\frac{1}{\lambda_2 - \lambda_1}\right) \int_{\lambda_1}^{\lambda_2} \frac{F_{I\lambda}}{F_{C\lambda}} d\lambda\right) \tag{2.2}$$

where λ_1 and λ_2 are the wavelength limits of the feature pass-band and $F_{I\lambda}$ and $F_{C\lambda}$ are the fluxes per unit wavelength of the feature pass-band and pseudo-continuum, respectively.

2.2 The *MILES* stellar library

The *MILES* library (Sánchez-Blázquez et al., 2006b) consists of 985 stars with spectra in a wavelength range of 3525-7500 Å, well covering the Lick indices, and with a spectral resolution of 2.54 Å. Important for the aim of this work is the careful flux-calibration of the *MILES* spectra. Also, Sánchez-Blázquez et al. (2006b) selected the sample of stars to fill the gaps in stellar parameter space covered by previous stellar libraries. This makes the *MILES* library particularly suitable for modelling absorption line indices of stellar populations.

Stellar parameter estimates in the literature show a scatter due to varying methods applied, as discussed in Maraston et al. (2003) for [Fe/H]. The stellar parameters ($T_{\rm eff}$, $\log g$ or [Fe/H]) for the stars in the *MILES* library are presented in Cenarro et al. (2007), where estimates from the literature have been used and put on a homogeneous scale. 3 of 985 stars have no available estimates for any of the stellar parameters $T_{\rm eff}$, $\log g$ or [Fe/H]. 35 stars lack estimates for [Fe/H] only and are located in sparsely populated regions at the ends of the $T_{\rm eff}$ range. These stars have therefore been assigned a solar metallicity to increase the number of data points.

The resolution of the *MILES* library was originally published as 2.3 Å in Sánchez-Blázquez et al. (2006b). However, in Beifiori et al. (2011) we re-analyse the *MILES* stellar spectra using the GANDALF-PPXF CODE (Gas AND Absorption Line Fitting-Penalised PiXel Fitting, Cappellari & Emsellem, 2004; Sarzi et al., 2006) for high resolution theoretical and empirical stellar spectra and revise the resolution to 2.54 Å. This is a negligible change when it comes to absorption line indices and does not affect the derived Lick indices.

2.2.1 Empirical stellar Lick indices

Our aim was to produce fitting functions both for the resolution of the *MILES* library (2.54 Å) and for the resolution of the Lick/IDS library (8-11 Å). We have therefore measured the 25 Lick indices directly on the original stellar spectra and on the spectra downgraded to the Lick/IDS resolution described by the curve presented in Worthey & Ottaviani (1997). We have used the index definitions from Trager et al. (1998) and also from Worthey & Ottaviani (1997) for the higher order Balmer lines ($H\delta_A$, $H\delta_F$, $H\gamma_A$ and $H\gamma_F$). Observational errors and offsets to the Lick/IDS library are described in the following paragraphs.

Table 2.1: Typical Lick index errors and offsets to the Lick/IDS library. M-σ and L-σ corresponds to index errors at the resolution of the *MILES* and Lick/IDS libraries, respectively. T98-σ are the index errors presented in Trager et al. (1998) for the Lick/IDS library. I_{lib} are indices measured on the libraries (*MILES*, *ELODIE* and *STELIB*) for which offsets to the Lick/IDS library are presented. I_L are indices measured on the Lick/IDS library.

	Error			**Offset** $I_{lib} = a \cdot I_{Lick} + b$					
				MILES		ELODIE		STELIB	
Index	M-σ	L-σ	T98-σ	a	b	a	b	a	b
Hδ_A	0.164	0.125	0.64	0.960	-0.054	0.955	0.721	0.940	0.823
Hδ_F	0.093	0.075	0.40	0.965	0.049	0.936	0.397	0.956	0.242
CN$_1$	0.0042	0.0038	0.018	0.912	0.008	0.897	-0.012	0.986	-0.010
CN$_2$	0.0050	0.0042	0.019	0.907	0.006	0.900	-0.008	0.985	-0.013
Ca4227	0.063	0.047	0.25	0.904	0.074	0.771	0.163	0.918	-0.057
G4300	0.112	0.093	0.33	0.858	0.625	0.870	0.646	0.924	0.565
Hγ_A	0.142	0.107	0.48	0.976	-0.148	0.967	-0.057	1.022	-0.735
Hγ_F	0.069	0.059	0.33	0.963	-0.038	0.962	0.016	0.999	-0.238
Fe4383	0.155	0.127	0.46	0.932	-0.220	0.929	-0.184	0.915	0.796
Ca4455	0.073	0.056	0.22	0.747	-0.067	0.785	-0.105	0.891	-0.228
Fe4531	0.122	0.096	0.37	0.857	0.290	0.838	0.390	0.877	-0.002
C$_2$4668	0.179	0.156	0.57	0.903	0.484	0.913	0.295	0.992	0.512
Hβ	0.063	0.051	0.19	0.981	0.126	0.996	0.015	1.004	0.032
Fe5015	0.139	0.115	0.41	0.902	0.084	0.926	0.178	0.989	0.168
Mg$_1$	0.0017	0.0013	0.006	0.911	0.0004	0.923	0.005	0.903	-0.009
Mg$_2$	0.0023	0.0014	0.007	0.918	-0.003	0.940	0.0006	0.960	-0.013
Mgb	0.053	0.045	0.20	0.964	0.108	0.935	0.247	1.003	-0.026
Fe5270	0.058	0.047	0.24	0.923	0.101	0.919	0.180	0.932	0.173
Fe5335	0.063	0.044	0.22	0.960	0.135	0.963	0.032	0.946	0.110
Fe5406	0.044	0.031	0.18	0.874	0.269	0.913	0.165	0.853	0.264
Fe5709	0.060	0.050	0.16	0.979	-0.026	0.907	0.015	1.019	-0.046
Fe5782	0.057	0.043	0.19	0.920	0.037	0.879	-0.004	0.906	0.088
Na D	0.082	0.064	0.21	0.990	-0.162	0.979	-0.069	0.993	-0.071
TiO$_1$	0.0021	0.0017	0.006	0.918	-0.005	0.895	-0.006	0.918	0.0003
TiO$_2$	0.0022	0.0016	0.006	0.904	0.0007	0.912	0.005	0.940	0.009

2.2.2 Observational index errors

We have derived typical observational index errors in order to evaluate the quality of our index measurements. To this end we have used pixel 1-σ observational errors (P. Sánchez-Blázquez private communication) to perturb each stellar spectrum, both at *MILES* resolution and Lick/IDS resolution, through 600 Monte Carlo realizations. We have then measured the 25 Lick indices for each perturbed spectrum and determined 1-σ errors for each index by using the spread in index measurements from the realizations. The index errors of the individual stellar spectra are used for weighting the least square fits when deriving both the offsets to the Lick system (Section 2.2.3) and the fitting functions (Section 2.3).

Trends between the index errors and the atmospheric parameters or line-strength indices can in principle bias the fits, but we have found such trends not to affect the results. Only for the Balmer indices we find weak trends of increasing errors with decreasing

temperature and decreasing index strength. No trends with logg and Fe/H are found for the Balmer indices. These weak trends can probably be explained with higher S/N for bright hot stars where the Balmer indices increase significantly in strength. Since we compute the fitting functions in bins of temperature, these trends have no significant effects on the final fitting functions.

The final 1-σ typical index errors were determined by taking the median error of the whole stellar library for each index. The typical index errors are presented in Table 2.1 both for *MILES* and Lick/IDS resolution. Compared to the typical index errors for the Lick/IDS stellar library (Trager et al., 1998), also included in Table 2.1, we find the errors of the MILES library to have improved significantly. The stars of the Lick/IDS library were observed about thirty years before the *MILES* library. Considering the technical development in thirty years time, an improvement in the measured indices ought to be expected.

2.2.3 Lick Index offsets

Individual stellar library offsets

We have computed Lick index offsets between the *MILES* library and the Lick/IDS library using the stars in common between the two libraries. These offsets can be used for comparisons between models based on this work with models based on the Worthey et al. (1994) and Worthey & Ottaviani (1997) fitting functions. The offsets are also used in Section 2.4 to compare the fitting functions of this work with the fitting functions of Worthey et al. (1994) and Worthey & Ottaviani (1997).

Fig. 2.2 shows index by index comparisons for the residuals between the index measurements of the two libraries as function of index strength. Worthey & Ottaviani (1997), Kuntschner (2001) and Schiavon (2007) computed zero-point offsets to the Lick/IDS library, while Puzia et al. (2002) computed their offsets as 2nd order least-square fits. For most indices we find index strength dependent residuals between the two libraries (Fig. 2.2). We have therefore computed the offsets using a sigma-clipping linear least-square fitting routine, weighted with the individual index errors derived in Section 2.2.2. The slope and intercept of these fits are presented in Table 2.1 and also included in Fig. 2.2 (black solid lines). Sigma-clipped data points are indicated with red crosses in Fig. 2.2 and the error bars are the 1-σ index errors presented in Section 2.2.2. The error bars along the x-axes are represented by the index errors derived for the *MILES* library, while the error bars along the y-axes are represented by the combined errors of the *MILES* and Lick/IDS libraries in quadrature.

Extreme outliers, i.e. data points that clearly showed strong deviating values compared to the bulk of data points, were removed prior to running the fitting routine, in

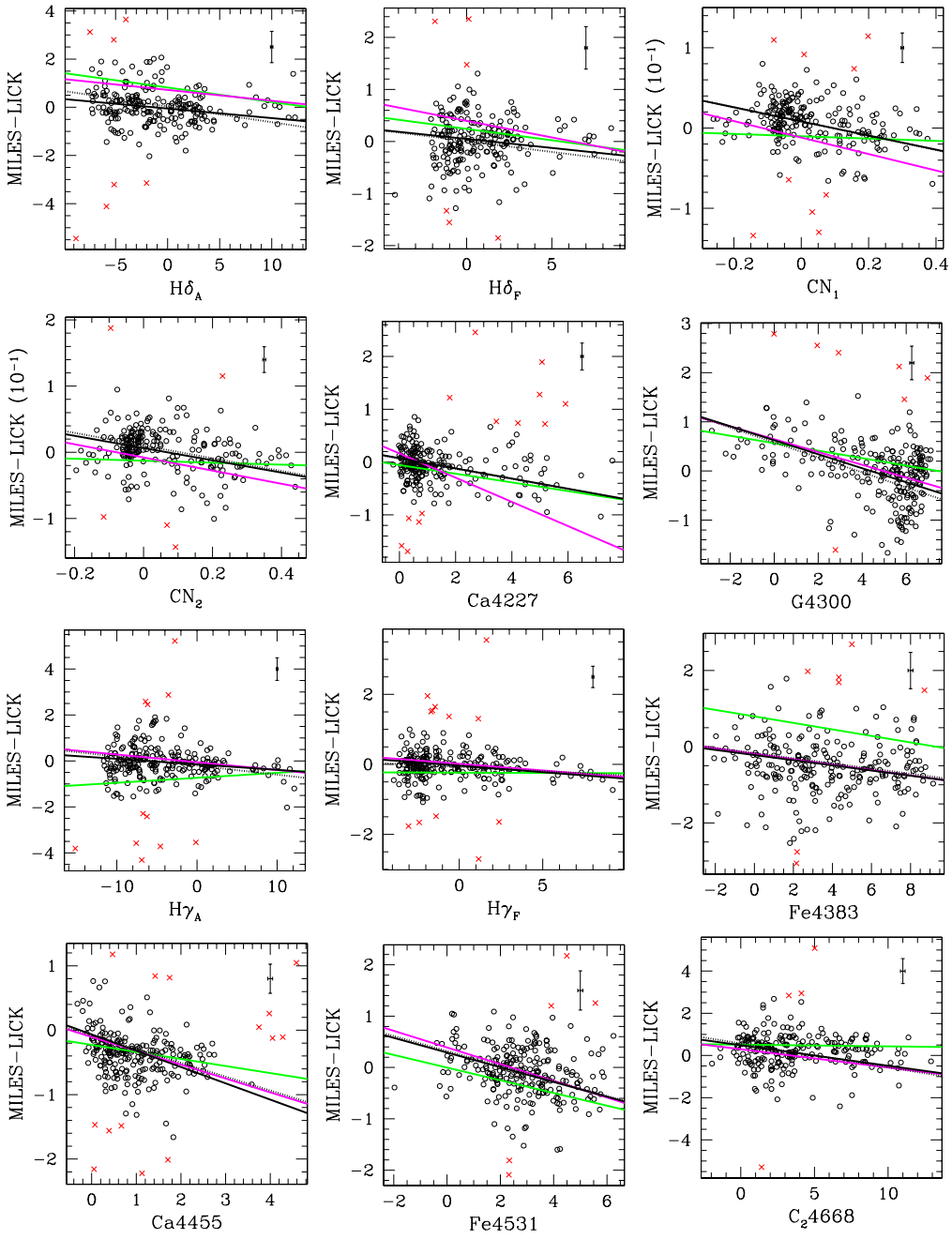

Figure 2.2: Index by index comparison between index strengths measured on the MILES library and the Lick/IDS library. Each panel shows the residual as a function of index strength. Included are also least-square fits of the residuals (black lines, coefficients presented in Table 2.1) that show clear index strength dependent offsets between the two libraries. Red crosses are sigma clipped data points in the least-square fitting routine. Typical index errors are indicated in the right top corners (see text for more details). Included are also offsets to the Lick/IDS library derived in this work for the *ELODIE* (magenta lines) and *STELIB* (green lines) libraries, as well as the offsets derived in Sánchez-Blázquez et al. (2009) for the *MILES* library (dotted lines).

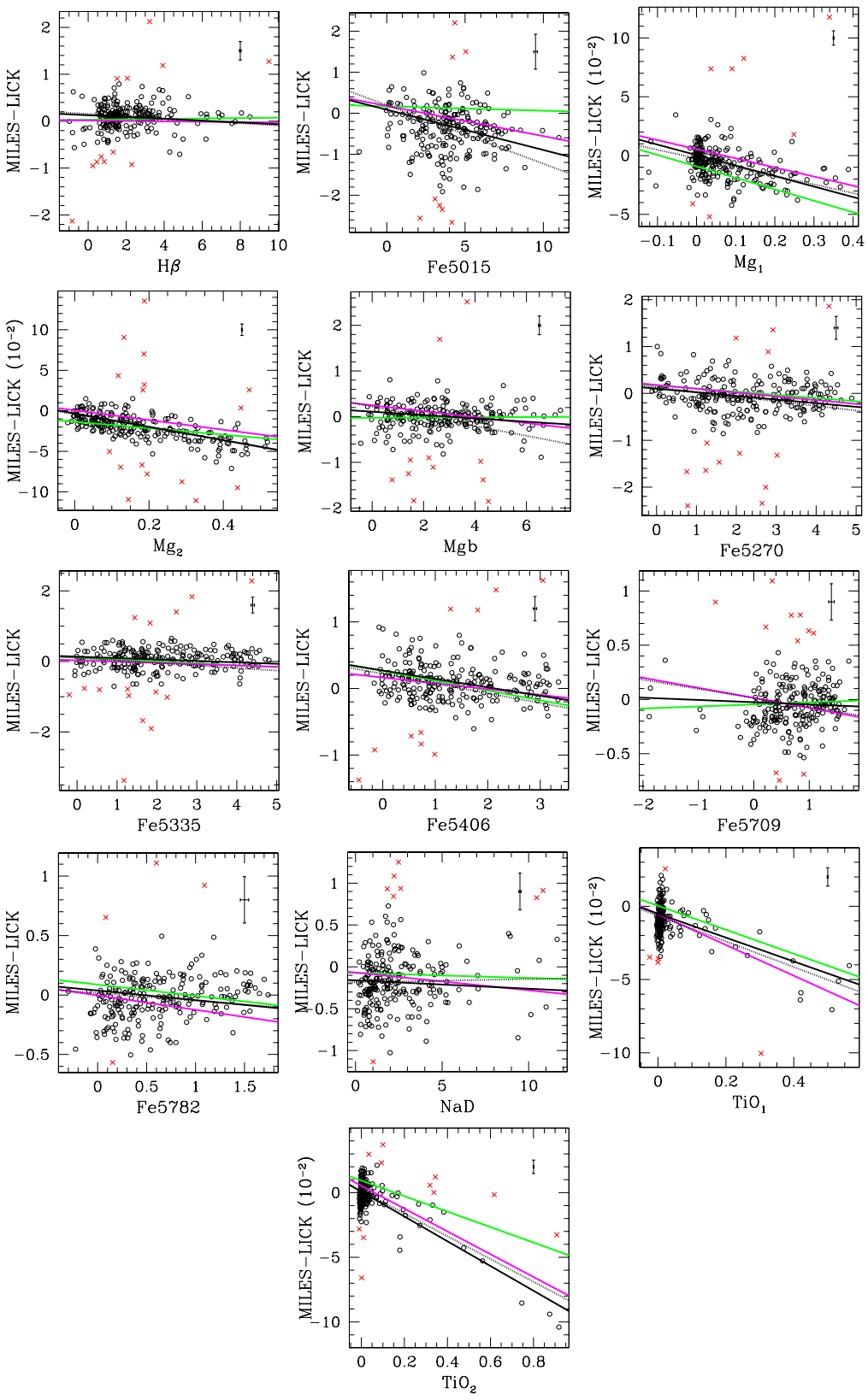

Figure 2.2: Continued.

order to avoid stars with anomalous index strengths to affect the final fits. For three indices ($C_2$4668, Fe5015 and Mgb) we found offsets at particularly high index strengths that deviated from the offset trends for the majority of data points. The low number of data points at these index strengths and the absence of data points at intermediate index strengths induced a bias in the derived offsets. The data points at particularly high index strengths were therefore discarded when determining the final offsets.

Offsets between the *MILES* and the Lick/IDS library derived in Sánchez-Blázquez et al. (2009) are also included in Fig. 2.2 (dotted lines). These offsets and the offsets derived in this work for the *MILES* library show in general very good agreement. Differences greater than the 1-σ index errors are mainly found for Mgb, one of the indices for which we excluded data points at high index strengths due to deviations in offset trends. Noticeable offset differences, but still within the 1-σ index errors, are also found for Fe5015, Fe5709, NaD, TiO_1 and TiO_2. Only small deviations are found between the offsets derived in Sánchez-Blázquez et al. (2009) and in this work for the rest of the indices.

For comparison, and for the derivation of a possible universal offset between flux-calibrated system and the Lick/IDS system, we have also determined offsets to the Lick/IDS library for two other flux-calibrated stellar libraries, namely *ELODIE* (Prugniel & Soubiran, 2001) and *STELIB* (Le Borgne et al., 2003). These offsets were determined using the same procedure as described above for the *MILES* library, except that no individual index errors were used as weights in the least-square fitting. For *STELIB* the lack of information did not allow for a computation of index errors, while the derived index errors for *ELODIE* were found to be unreliable as they showed unrealisticly small values. Since we only found small deviations in the offsets derived for the *MILES* library when not weighting as compared to weighting the least-square fits, we compare the offsets derived for all three libraries.

In accordance with the *MILES* library we found index strength dependent offsets also for the *ELODIE* and *STELIB* libraries. We found deviating offsets trends at high index values for the same indices as for the *MILES* library ($C_2$4668, Fe5015 and Mgb).

The offsets derived for the *ELODIE* and *STELIB* libraries are also presented in Table 2.1 and Fig. 2.2 (magenta and green lines, respectively). Clearly, deviations in the offsets are found between the libraries, especially for the *STELIB* library compared to the other two libraries. However, the *STELIB* library is also the library having the least number of stars in common with the Lick/IDS library, giving a higher statistical uncertainty in the derived offsets. The *STELIB* library only has 44 stars in common with the Lick/IDS library, while *ELODIE* has 112 stars and the *MILES* library has 237 stars in common with the Lick/IDS library. Ca4227 showed particularly strange behaviour with index strength and the accuracy of the final offsets for this index could be questionable.

In Fig. 2.2 we find agreements within the 1-σ index errors between the offsets derived for all three libraries for Hβ, Mgb, Fe5270, Fe5335, Fe5406, Fe5709, Fe5782 and NaD. This implies a better agreement between all libraries at wavelengths redder than $\sim$4800 Å, with the exception for the broader molecular indices Mg_1, Mg_2, TiO_1 and TiO_2 that show differences greater than the 1-σ index errors, which is also found for Fe5015. Agreements between offsets derived for *MILES* and *ELODIE* only, well within the 1-σ index errors, are found for G4300, Hγ_A, Hγ_F, Fe4383, Ca4455, Fe4531 and $C_2$4668. This instead implies a worse agreement between *MILES* and *ELODIE* at wavelengths bluer than $\sim$4250 Å (Hδ_A, Hδ_F, CN_1, CN_2 and Ca4227), where we in general find inconsistencies between all three libraries. The significant deviation in offset between the libraries for several indices hamper the derivation of a universal offset between the Lick/IDS and flux-calibrated systems as described by these libraries.

This conclusion gets further support from the study of Sánchez-Blázquez et al. (2006b) who show that offsets exist between the three flux-calibrated libraries *MILES*, *STELIB* and *ELODIE*. These offsets are generally in good agreement with the individual Lick offsets found in this work.

Universal offsets

As discussed above the differences between the three libraries considered in this work hamper the derivation of a universal Lick offset. Despite this we have made and attempt in deriving such an offset by choosing the libraries that show the best agreement for each index. The chosen libraries are then used for computing the universal offsets.

The number of stars in common with the Lick/IDS library varies significantly between the three libraries as discussed above. Thus straightforwardly combining the different libraries will bias the derived universal offsets towards the library with the highest number of stars in common with the Lick/IDS library. We have instead used the number of stars in common with the Lick/IDS library for *STELIB* (44) for all three libraries and for 100 random selections, i.e. the same *STELIB* sample is used for each selection while the sample varies for *MILES* and *ELODIE*. For each selection the offsets are derived, using the least-square fitting method described above, for all possible library combinations, i.e. *MILES*+*ELODIE* (M+E), *MILES*+*STELIB* (M+S) and *ELODIE*+*STELIB* (E+S). For each selection we also derive the individual library offsets. We use this to quantify which two libraries that best agree with each other for each index, using a Meta-χ^2 value computed for each selection

$$Meta-\chi^2 = \sum_{i=1}^{2}\left(\frac{s_i - s_c}{\Delta s_i - \Delta s_c}\right)^2 + \sum_{i=1}^{2}\left(\frac{i_i - i_c}{\Delta i_i - \Delta i_c}\right)^2 \quad (2.3)$$

Table 2.2: Choice of library combinations for universal Lick offsets for each index. Column 2-4 gives the percentage each library combination ME, MS and ES was preferred in the 100 selections (see text). Column 5 are the preferred library combinations used to compute universal offsets. Column 6 and 7 are the slope and intercept of the final universal offsets, respectively.

Index	**M+E**	**M+S**	**E+S**	**Comb.**	**a**	**b**
Hδ_A	1	0	99	ES	0.949	0.789
Hδ_F	1	14	85	ES	0.953	0.317
CN_1	15	2	83	ES	0.943	-0.011
CN_2	53	4	43	MES	0.936	-0.004
Ca4227	26	73	0	MS	0.937	-0.011
G4300	61	18	21	MES	0.892	0.586
Hγ_A	100	0	0	ME	0.969	-0.133
Hγ_F	82	18	0	ME	0.964	-0.020
Fe4383	98	1	1	ME	0.925	-0.169
Ca4455	27	23	50	MES	0.771	-0.098
Fe4531	80	12	8	ME	0.848	0.364
$C_2$4668	30	58	12	MES	0.947	0.422
Hβ	33	10	57	MES	1.006	0.041
Fe5015	55	14	31	MES	0.940	0.137
Mg_1	42	58	0	MES	0.918	-0.002
Mg_2	81	13	6	ME	0.932	-0.002
Mgb	41	57	2	MES	0.967	0.102
Fe5270	24	37	39	MES	0.932	0.150
Fe5335	7	32	61	MES	0.956	0.087
Fe5406	23	40	37	MES	0.905	0.191
Fe5709	50	32	18	MES	0.928	0.009
Fe5782	41	42	17	MES	0.911	0.030
Na D	10	33	57	MES	1.002	-0.123
TiO_1	61	17	22	MES	0.916	-0.004
TiO_2	40	3	57	MES	0.940	0.005

where s(i)$_i$ and s(i)$_c$ are the slope(intercept) of the fit for the individual library offsets and the combined offset, respectively. The Meta-χ^2 is a measure of the spread in offset for the different combinations. If a specific library combination have the lowest Meta-χ^2 in more than 70% of the 100 selections that combination is used for computing the universal offset. If instead non of the combinations are preferred we use a combination of all libraries, i.e. *MILES+ELODIE+STELIB* (M+E+S). The final universal offset is then computed by taking the average slope and intercept of the individual offsets from Table 2.1 for the libraries of the preferred combination. Table 2.2 gives the percentage each combination was chosen for each index (column 2-4), the preferred combination (column 5) and the slope and intercept of the final universal offset (column 6 and 7, respectively).

We find that the preferred combination of libraries for each index agrees with the expected combination just by studying the differences of the individual offsets in Fig. 2.2. Indices where a specific combination is preferred are also indices where two libraries clearly agree better. However, due to the inconsistencies found between the three libraries

for several indices the reliability of the universal offsets derived here are is severely questioned. For this reason we have instead chosen to put preference to the *MILES* stellar library since it is the best suited library for stellar population modelling, owing to its favourable combination of spectral resolution, wavelength range, stellar parameter coverage,and quality of flux calibration. In the next section we derive new empirical fitting functions based on this library.

2.3 Fitting functions

In order to produce empirical fitting functions for the MILES library, we combine our measured Lick indices with the corresponding stellar atmospheric parameters (see Section 2.2). It is a complex task to find the best relationship between indices and stellar atmospheric parameters, with several methods available in the literature. The method adopted in this work is presented in this section along with the derived fitting functions.

2.3.1 Fitting method

The relationship between Lick index strengths and stellar parameters shows a complex behaviour, making it difficult to find one reliable empirical fitting function for the whole parameter space. To solve this problem the parameter space must be divided into subregions where local fitting functions can be computed. However, it is desirable to find the simplest set of fitting functions and achieve a final representation of the data that is as accurate as possible. Hence the limits of the subregions have to be carefully chosen. It has also to be assured that adjacent subregions overlap, making smooth transitions possible. For these transitions we have adopted cosine-weighted interpolations following Cenarro et al. (2002). The choice of subregions are discussed in Section 2.3.2.

Following the extensive number of published fitting functions in the literature (Worthey et al., 1994; Gorgas et al., 1999; Cenarro et al., 2002; Schiavon, 2007; Maraston et al., 2009), we use a linear least square fitting routine to determine the local relationships as polynomials in the following way

$$I(\theta, [Fe/H], \log g) = \sum_i \beta_i \cdot \theta^j \cdot [Fe/H]^k \cdot \log g^l \tag{2.4}$$

where $j, k, l \geq 0$ and the atmospheric effective temperature is represented by $\theta = 5040/T_{\rm eff}$. The representation of $T_{\rm eff}$ using θ is chosen due to the wide range of spectral types in the stellar library. The number of terms in Eq. 2.4 can be made arbitrarily high. However, the goal is to find the best compromise between simplicity and accuracy by discarding terms with higher order polynomials that are negligible or induce unphysical

behaviours. To this end several methods have been developed in the literature. Worthey et al. (1994) presented a method to find the converging rms scatter by successively including terms and test if the rms scatter was significantly reduced by means of a F-test. Gorgas et al. (1999) and Cenarro et al. (2002) instead test if each term significantly differed from zero through a T-test. Schiavon (2007) point out that both methods mentioned above are sensitive to the coverage of parameter space. Therefore Schiavon (2007) combine the two methods by first successively removing statistically insignificant terms and then interactively testing the remaining terms for unphysical behaviours and their effect on the rms scatter.

In this work we adopt a mix of the above mentioned methods. We choose successive inclusion over successive removal of terms. The main reason for this choice is that the normal equations of the linear least square routine run a high risk of becoming degenerate when terms that respond similarly to the data are combined. By including terms we can better control the degeneracy of the normal equations. If degenerate normal equations were reached after the inclusion of a new term, this new term was discarded since a possible lower order term already responded to the data in a similar fashion.

Finally, we determined the local fitting functions through an error weighted linear least square routine (for individual index errors see Section 2.2.2). Terms were successively included following the procedure described in Gorgas et al. (1999), by starting with the constant ($j, k, l = 0$ in Eq. 2.4) and then increasing the sum of powers $j + k + l$ up to a maximum of $j + k + l = 3$, including all possible cross terms. However, since the effective temperature is the parameter showing the most complex behaviour we included polynomials of θ up to $j = 5$. If the variance was not reduced at the inclusion of a new term the term was discarded. When a reduced variance was found the new term and all the previously included terms were tested by means of a T-test to determine if the coefficients β_i were statistically different from zero (by using the coefficient errors following Gorgas et al. 1999 and Cenarro et al. 2002). Terms with coefficients having a significance level $\alpha \leq 0.1$ was kept. We then interactively studied the fitting functions and removed terms inducing unphysical behaviours or not affecting the rms scatter significantly. At the end of each run the sample was σ-clipped, by removing data points deviating more than 3 σ, and the fitting redone on the new sample.

Extreme outliers that clearly deviated from the bulk of data points were discarded prior to running the fitting routine. Hence to avoid stars with anomalous index strengths affecting the fitting functions.

2.3.2 Definition of subregions in parameter space

Thanks to the good coverage of stellar parameters the *MILES* library show a complex behaviour of the relationship between the Lick indices and the stellar parameters. We have therefore divided parameter space into several subregions.

The relationship between the Lick indices and the stellar parameters show a bimodality between high and low gravity stars (i.e. *Giants* and *Dwarfs*). The first major subregions that we have chosen are therefore in high and low values of $\log g$ space (from now on referred to as the *Dwarf* and *Giant* subregion, respectively), in accordance with Gorgas et al. (1999), Cenarro et al. (2002) and Schiavon (2007). The same $\log g$ subregion limits have been used for all indices. The lower limit for the *Dwarf* subregion was set to $\log g = 3.6$, while the upper limit for the *Giant* subregion was set to $\log g = 4.0$, giving an overlap region of $\Delta \log g = 0.4$. In Fig 2.3 the subregions are shown together with the analogous in the stellar population models of Maraston (2005), for $\log g$ as a function of θ. The different evolutionary phases for the models are indicated in Fig 2.3. This shows that the choice of limits for the *Dwarf* and *Giant* subregions coincides very well with the division into the main-sequence and the post-main-sequence, as the $\log g$ overlap region mainly covers the sub-giant branch (SGB).

To fully recover the detailed behaviour within the $\log g$ subregions we divided the full θ/T$_{\rm eff}$ range into four subregions. The choice of the limits for θ/T$_{\rm eff}$ subregions follow the behaviour of the models and the distribution of stars as a function θ/T$_{\rm eff}$. This can be seen in Fig 2.3 where the limits of the θ/T$_{\rm eff}$ subregions are represented by the midpoints in the overlap regions, averaged over all indices. The θ/T$_{\rm eff}$ subregions are discussed in the following bullet points, by referring to the θ/T$_{\rm eff}$ subregions using the names (D1-4 and G1-4) in Fig 2.3, first for the *Giant* subregion

- Only the tip of the the red-giant branch (RGB) for high metallicities fall within G1 (Fig 2.3). The lower limit (in θ) for this subregion coincides with the strong drop-off in the distribution of data points (Fig 2.3). With the weak dependency on metallicity for this subregion and the low number of data points we fit this subregion independently of metallicity.

- G2 and G3 clearly separates out RGB to be fitted mainly in G2 (Fig 2.3).

- Most indices show a distinct change in the behaviour of the index strengths as a function of the stellar parameters for hot A-type stars, around $\theta = 0.5 - 0.6$, see Fig. 2.4 (and Fig. A1-A24 of Appendix A in Johansson et al., 2010). The overlap regions between G3 and G4 are therefore located around this range in θ.

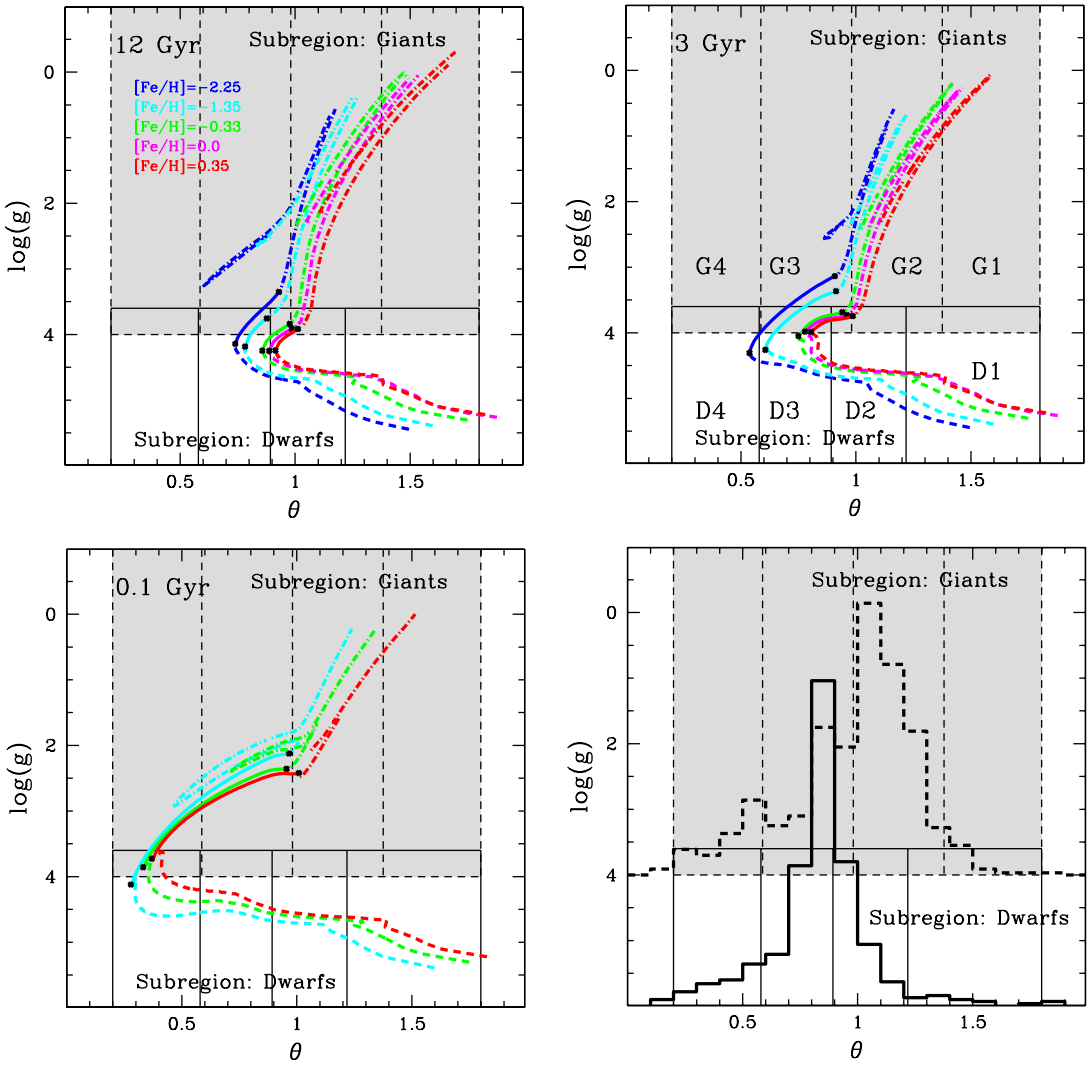

Figure 2.3: The top panels and the lower left panel show the relationship between the chosen subregions and the analogous in the stellar population models of Maraston (2005). The three panels show models for different ages (as indicated) and for each age the models are presented for varying metallicities as indicated by the corresponding colors. Each single model is divided into the main-sequence (dashed lines), sub-giant branch (solid line) and the rest of the post-main-sequence phases (dash-dotted lines). The lower right panel shows the relationship between the chosen subregions and the distribution of data points as a function of $\theta/T_{\rm eff}$ for *Dwarfs* ($\log g > 3.6$, solid lined histogram) and *Giants* ($\log g > 4.0$, dashed line histogram) separately. In all panels the $\theta/T_{\rm eff}$ subregions for the *Dwarf* subregion (solid lines) are indicated with D1-4 and for the *Giant* subregion (shaded area and dashed lines) with G1-4.

and then for the *Dwarf* subregion

- The lowest part of the main-sequence fall within D1 (Fig. 2.3). As for the *Giant* subregion, the lower limit (in θ) for this subregion coincides with the strong drop-off in the distribution of data points.

- The division of θ/T$_{\rm eff}$ space into D2 and D3 were found to improve the fits in terms of a significantly reduced rms scatter.

- As for the *Giant* subregion, most indices show a distinct change in the behaviour of the index strengths as a function of the stellar parameters for hot A-type stars, around $\theta = 0.5 - 0.6$, see Fig. 2.4 (and Fig. A1-A24 of Appendix A in Johansson et al., 2010). The overlap regions between D3 and D4 are therefore located around this range in θ.

The number of the θ/T$_{\rm eff}$ subregions is the same for all indices. With the exceptions for TiO$_1$ and TiO$_2$ that show a much simpler behaviour and we have therefore used less $\theta/T_{\rm eff}$ subregions (see Fig. A23-A24, Table A23-A24 and Table B24-B25 in Appendix A and B of Johansson et al., 2010). Since the different indices show a varying dependence on the stellar parameters, the limits for the subregions have been adjusted for each index individually to reduce the rms scatter.

The choice of subregions in $\log g$ and θ/T$_{\rm eff}$ space make up the base for our fitting functions. On top of these, metallicity space had to be divided into two subregions for 10 indices (CN$_1$, CN$_2$, Ca4227, G4300, Fe4383, Fe5015, Mg$_1$, Mg$_2$, Mgb and NaD) in order to fully reproduce the metal-poor end, but only in the low gravity subregion and in the specific temperature range around $1.0 < \theta < 1.4$ ($5040 < T_{\rm eff} < 3600$). We have therefore independently fitted metal-rich and metal-poor stars, divided at [Fe/H]~ -1.0 for the affected temperatures in the low gravity subregion for the 12 indices.

Even though the *MILES* library covers an extensive range of stellar parameter space, the very ends are obviously still sparsely populated. Therefore, the fitting functions are not valid beyond $\theta > 1.8$ ($T_{\rm eff} < 2800$) and $\theta < 0.2$ ($T_{\rm eff} > 25200$). The dwarf main-sequence that extends to very low temperatures is well covered within these limits (Fig. 2.3). Very hot young stars with temperatures greater than 25200 K do not have strong indices in the visual parts of their spectra.

2.3.3 [α/Fe] trends

Globular cluster stars are significantly [α/Fe]-enhanced with respect to solar values (~ 0.3, Carney, 1996). The [α/Fe]-trend of field stars in the solar neighborhood instead show increasing [α/Fe]-enhancements with decreasing metallicity down to [Fe/H]~ -1.0

(Edvardsson et al., 1993; Fuhrmann, 1998; Milone, Sansom & Sánchez-Blázquez, 2009). It is first at this metallicity that the field stars reach globular cluster [α/Fe]-values. Having globular cluster stars for [Fe/H]> -1.0 can therefore induce [α/Fe] trends biased towards globular cluster values in stellar libraries dominated by field stars. The globular cluster M71 has a metallicity of [Fe/H]$= -0.84$ and is represented by a significant number of 28 stars in the *MILES* library, which could possibly induce such a bias. The stars from this globular cluster were therefore discarded when computing the final fitting functions, since the *MILES* library is reasonably well populated with field stars around the metallicity of M71.

The [α/Fe]-bias of the solar neighborhood must be taken into account when deriving stellar population models based on empirical stellar libraries, as discussed in Maraston et al. (2003). Model adjustments are therefore needed when adopting the fitting functions of this work. Such adjustments are described in Tripicco & Bell (1995); Thomas et al. (2003a); Thomas et al. (2004); Korn et al. (2005); Thomas et al. (2005) and further discussed in Sections 3.3.4-3.3.5.

2.3.4 Spectral resolution

We have computed fitting functions for both the *MILES* and Lick/IDS resolutions (see Section 2.2.1). The same final set of terms were used for both resolutions. Coefficients and coefficient errors for the fitting functions are presented in Appendix A for Lick resolution and Appendix B for *MILES* resolution in Johansson et al. (2010). The sigma clipped number of data points (N) for the local fitting functions are also included in the coefficient Tables, along with the rms of the residuals between the data and the final fitting functions, both local and overall. The visual behaviours, residuals and distribution of residuals of the fitting functions are shown for Lick resolution in Appendix A of Johansson et al. (2010). An example is presented for Fe5335 and Lick resolution in Table 2.3 and Table 2.4 for coefficients and coefficient errors, respectively. The visual behaviours of the fitting functions for Fe5335 are shown in Fig. 2.4, where they are presented for the *Dwarf* and *Giant* subregions separately and for varying metallicity. In Appendix A of Johansson et al. (2010) the visual behaviour of fitting functions for several $\log g$ values at fixed θ are also presented for indices showing strong $\log g$ dependencies within the $\log g$ subregions.

2.3.5 Errors

In this section we briefly discuss possible error sources affecting the final fitting functions. Such error sources include the index measurements of the *MILES* spectra, but

Table 2.3: Fe5335 fitting function coefficients for Lick/IDS resolution

	overall rms=0.2586							
	$\log g \leq 4.0$ and θ limits:				$\log g \geq 3.6$ and θ limits:			
Term	≤ 0.58	$0.50-1.1$	$0.95-1.5$	≥ 1.2	≤ 0.58	$0.50-1.0$	$0.85-1.4$	≥ 1.2
Const.	-0.05682	-1.257	125.1	-279.0	-0.8217	-43.41	56.65	10.18
θ	0.4726	1.861	-343.3	591.9	9.547	217.8	-190.9	-4.614
[Fe/H]	x	-0.6719	x	x	x	1.336	-14.42	0.6270
$\log g$	x	x	x	x	x	x	0.3445	x
θ^2	x	1.797	314.1	-406.0	-30.62	-397.3	205.6	x
[Fe/H]^2	x	x	x	x	x	x	0.9821	x
θ[Fe/H]	x	1.808	1.048	x	x	-4.202	31.08	x
θ^3	x	x	-93.45	90.94	30.84	313.2	-69.81	x
[Fe/H]^3	x	-0.05781	-0.1268	x	x	x	x	x
θ^2[Fe/H]	x	x	x	x	x	4.535	-15.09	x
θ[Fe/H]^2	x	x	-0.2159	x	x	0.2707	-0.7390	x
θ^4	x	x	x	x	x	-87.19	x	x
rms	0.1111	0.2352	0.3446	0.7921	0.08168	0.1348	0.1879	0.7221
N	81	358	365	113	51	349	207	17

Table 2.4: Fe5335 fitting function coefficient errors for Lick/IDS resolution

	$\log g \leq 4.0$ and θ limits:				$\log g \geq 3.6$ and θ limits:			
Term	≤ 0.58	$0.50-1.1$	$0.95-1.5$	≥ 1.2	≤ 0.58	$0.50-1.0$	$0.85-1.4$	≥ 1.2
Const.	0.01305	0.04702	1.237	2.860	0.1784	2.914	2.000	0.06966
θ	0.03082	0.1169	3.120	5.928	1.544	15.82	5.800	0.04788
[Fe/H]	x	0.01732	x	x	x	0.1617	0.3727	0.01636
$\log g$	x	x	x	x	x	x	0.01056	x
θ^2	x	0.07110	2.603	4.059	4.200	31.77	5.571	x
[Fe/H]^2	x	x	x	x	x	x	0.08236	x
θ[Fe/H]	x	0.01959	0.008170	x	x	0.4293	0.7186	x
θ^3	x	x	0.7181	x	3.624	27.99	1.772	x
[Fe/H]^3	x	0.001251	0.003640	x	x	x	x	x
θ^2[Fe/H]	x	x	x	x	x	0.2782	0.3495	x
θ[Fe/H]^2	x	x	0.01012	x	x	0.005307	0.08761	x
θ^4	x	x	x	x	x	9.138	x	x

these show very high quality, in terms of typical observational index errors, as discussed in Section 2.2.2. However, the overall rms of the final fitting functions (see Section 2.3.4) are considerably larger than the typical observational index errors (see Section 2.2.2). Possible error sources for this scatter are instead uncertainties in the stellar parameter estimates and intrinsic scatter in the index strengths.

The residuals between the final fitting functions and the data, presented in the lower left panels of Fig. 2.4 (and Fig. A1-A24 of Appendix A in Johansson et al., 2010) as a function of θ, show typically larger scatter for cooler temperatures where index values exhibit strong sensitivities to $T_{\rm eff}$. The source of this correlation is probably, at least

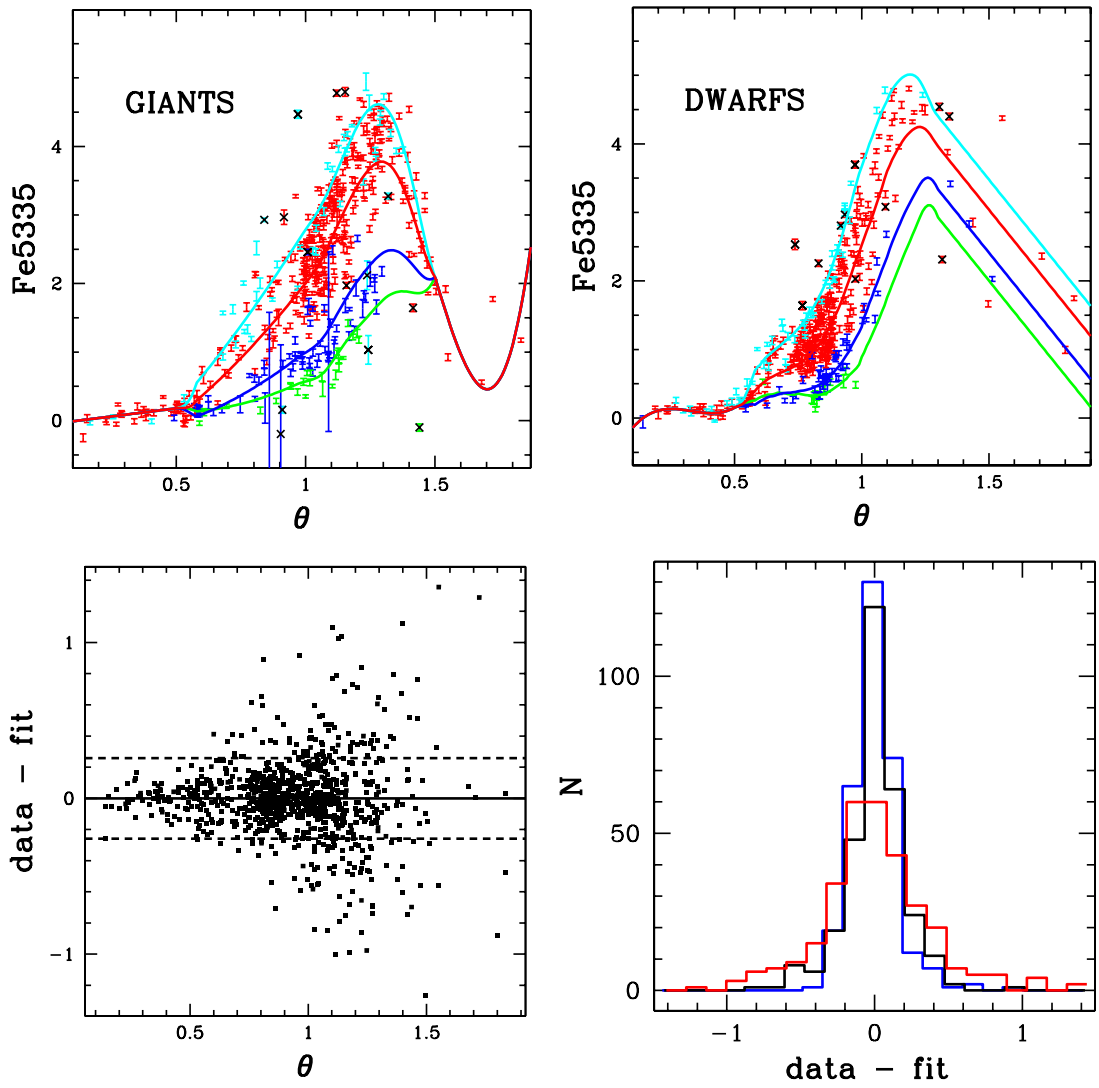

Figure 2.4: The fitting functions for Fe5335 (Lick resolution) are shown in the upper panels for various metallicities and over-plotted on data in corresponding metallicity bins. The error bars on the data are observational index errors (see Section 2.2.2). The colors correspond to [Fe/H]$= -2.0$ (green) , [Fe/H]$= -1.35$ (blue), [Fe/H]$= -0.35$ (red) and [Fe/H]$= 0.35$ (cyan) for the fitting functions and [Fe/H]< -1.8 (green) , $-1.8 <$[Fe/H]< -1.0 (blue), $-1.0 <$[Fe/H]< 0.2 (red) and [Fe/H]> 0.2 (cyan) for the data. The left and right upper panels show Giants ($\log g < 3.6$) and Dwarfs ($\log g > 3.6$) , respectively, for the average $\log g$ of the data in bins of $\Delta\theta = 0.1$ at steps of $\theta = 0.01$. Fixed $\log g$ values are used at the ends of the θ/$T_{\rm eff}$ range, with $\log g = 1.0, 2.0$ (cold,warm end) and $\log g = 4.6, 4.0$ (cold,warm end) for Giants and Dwarfs, respectively. Data points with black crosses have been sigma clipped by the least-square fitting routine. The lower left panel shows the residuals between the data and the fitting functions as a function of θ and the dashed lines represents the overall rms value for the fitting functions. The lower right panel shows the distribution of the residuals for three θ/$T_{\rm eff}$ bins, indicated by different colors where blue have $\theta < 0.841$ black $0.841 \geq \theta < 1.045$ and red $\theta \geq 1.045$.

Table 2.5: Limits for the different bins of $\theta/T_{\rm eff}$ space used in the fitting function comparisons. SFF-G and SFF-D correspond to the fitting functions of Schiavon (2007) for *Giants* and *Dwarfs*, respectively.

FF	*COLD* ($T_{\rm eff}$)	*INTER.* ($T_{\rm eff}$)	*WARM* ($T_{\rm eff}$)
WFF	2800-4582	4582-7200	7200-12263
SFF-G	2800-4582	4582-(∼)6300	-
SFF-D	3220-4582	4582-7200	7200-18000

partly, uncertainties in the stellar parameters, since these will have a larger effect when the index strengths show strong dependencies on the stellar parameters, i.e. $\theta/T_{\rm eff}$ uncertainties will have less effect when the index strengths show weaker dependencies on $\theta/T_{\rm eff}$.

2.4 Comparisons with the literature

In this section we compare the fitting functions derived in this work with fitting functions in the literature derived for stellar libraries other than *MILES*. We search for differences in various parameter regimes. Comparisons are made with the classical and extensively adopted fitting functions of Worthey et al. (1994) and Worthey & Ottaviani (1997) (from now on WFF), shifted with the offsets derived in Section 2.2.3, and with the more recent fitting functions of Schiavon (2007) (from now on SFF) which were based on the *JONES* library (Jones, 1999).

We have performed the comparisons in different regions of parameter space to find the regimes where major differences roam. The comparisons have been divided into three $\theta/T_{\rm eff}$ bins, referred to as *Cold*, *Intermediate* and *Warm* temperatures, with $\theta/T_{\rm eff}$ limits presented in Table 2.5. Each of these bins have been further divided into two $\log g$ bins with $\log g = 2.0$ (referred to as *Giants*) and $\log g = 4.5$ (referred to as *Dwarfs*) to make up a total of six bins. The average residuals between the fitting functions were computed in each bin at [Fe/H] steps of 0.5 in the range $-2 \leq$[Fe/H]≤ 0.5 and presented in Fig. 2.5 and Fig. 2.6 as a function of metallicity for the comparisons with WFF and SFF, respectively.

The comparisons have only been made within the parameter limits for which the fitting functions are applicable, described in Worthey et al. (1994) (WFF), Schiavon (2007) (SFF) and Section 2.3.2 (this work), resulting in the limits of the $\theta/T_{\rm eff}$ bins presented in Table 2.5. Due to the limitations of the SFF we can not make comparisons for the *Warm* $Giant$ regime, while the *Intermediate* $Giant$ regime have a varying lower θ limit (see Schiavon 2007 for individual index limits).

The overall rms of the final fitting functions (see Section 2.3.4) are shown in Fig. 2.5 - 2.6 as grey shaded areas (1rms dark grey and 2rms light grey). This gives a reference to the differences found between the libraries.

Overall there is good agreement between fitting functions within the rms. We find the biggest residuals to occur at the ends of parameter space, i.e. at the metallicity and temperature ends (see Fig. 2.5 - 2.6). This was expected since the number of data points decrease towards the ends of parameter space, resulting in larger uncertainties of the fitting functions. In the rest of this Section we discuss the comparisons for individual indices in terms of stellar parameter regions that show differences beyond the 1rms and 2rms levels.

H$\delta_{\mathbf{A}}$

WFF comparison (Fig. 2.5): The Balmer indices are very sensitive to surface gravity at T_{eff} $\gtrsim$7200 K (θ $\lesssim$0.7), such that they decrease for lower $\log g$. The coverage of hot supergiants in the *MILES* library allows us to model this behaviour, while the WFF predict too strong Balmer indices for hot stars with low surface gravities. For this reason the *Warm Giants* extend well beyond the 2rms level where this work show much weaker indices. We find both *Warm* and *Cold Dwarfs* to show stronger indices for this work, even extending beyond the 2rms level for the metal-poor and metal-rich ends, respectively. Otherwise, this work show slightly weaker indices extending to the 1rms level.
SFF comparison (Fig. 2.6): Cold Dwarfs show weaker indices for this work, beyond the 1rms level. *Warm* and *Intermediate* temperature *Dwarfs* show stronger indices for this work out to the 2rms level in the metal-poor regime. *Intermediate* temperature *Giants* show stronger indices out to the 2rms level at the ends of the metallicity scale. Otherwise are mainly differences within the 1rms level found.

H$\delta_{\mathbf{F}}$

WFF comparison (Fig. 2.5): For the same reason as for Hδ_A, the most obvious difference is found for *Warm Giants* where this work show much weaker indices, extending well beyond the 2rms level. Otherwise are differences mainly within the 1rms level, except for the metal-rich end of *Cold* and *Warm Dwarfs* that show stronger indices for this work beyond the 2rms level.
SFF comparison (Fig. 2.6): This work shows in general stronger indices in the metal-poor regime, beyond the 1 rms level for *Intermediate* temperature and *Warm Dwarfs* and beyond the 2rms level for *Intermediate* temperature *Giants*. In the metal-rich regime we

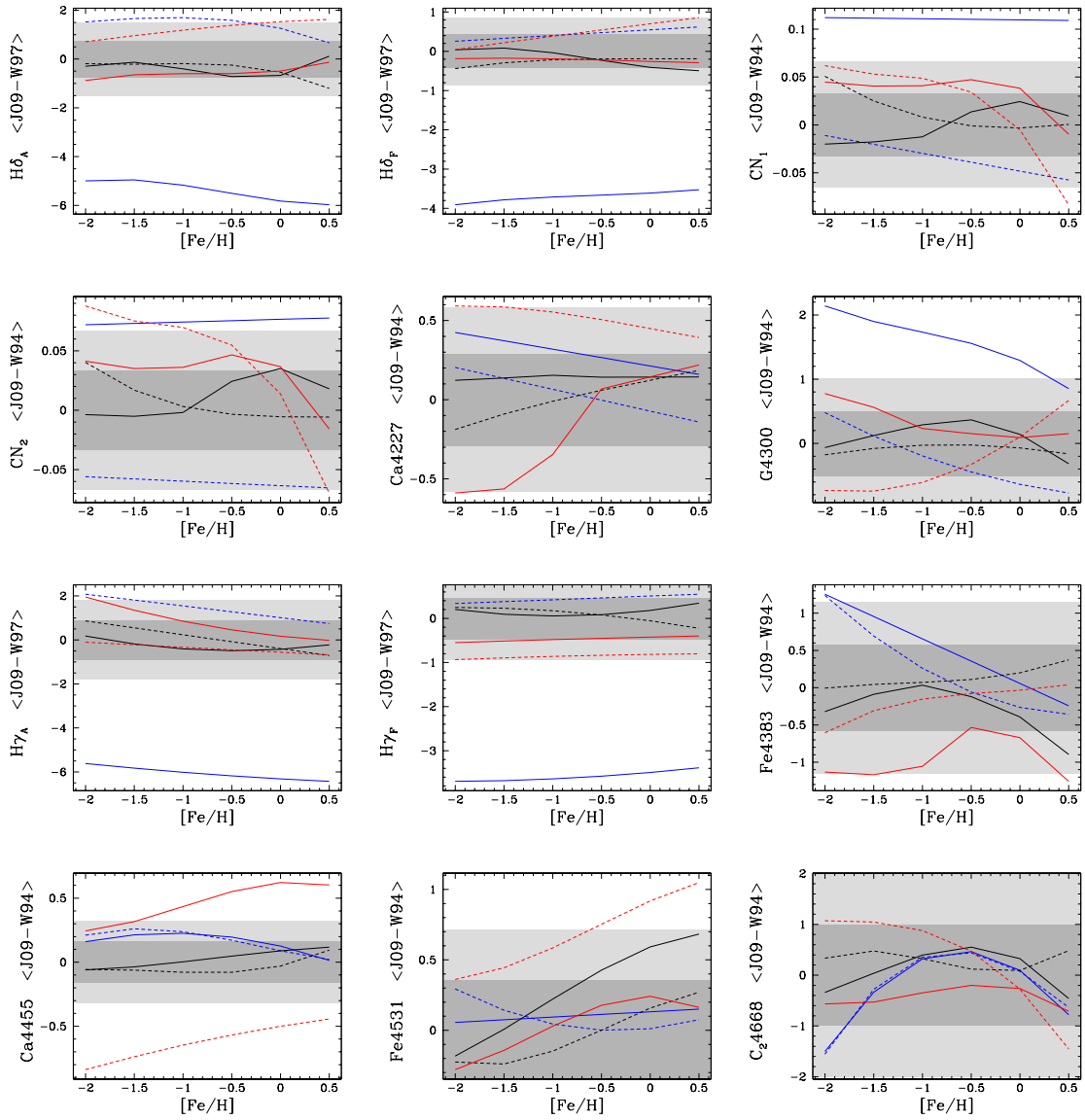

Figure 2.5: Comparisons between the fitting functions of this work (referred to as J09) and Worthey et al. (1994) (W94), and with Worthey & Ottaviani (1997) (W97) for Hδ_A, Hδ_F, Hγ_A and Hγ_F. The panels show the difference J09-W94/W97 as a function of metallicity for each Lick index. The comparisons are made for *Giants* ($\log g = 2.0$, solid lines) and *Dwarfs* ($\log g = 4.5$, dashed lines). The different colors correspond to the different bins of $\theta/T_{\rm eff}$ space, with limits stated in Table 2.5, where the average difference has been computed, blue for the *Warm*, black for the *Intermediate* and red for the *Cold* temperature bin. Fitting function residuals in terms of 1rms (dark grey shaded areas) and 2rms levels (light grey shaded areas) are indicated. The errors are represented by the combined errors of the *MILES* and Lick/IDS libraries in quadrature (for more on the errors see Section 2.2.2).

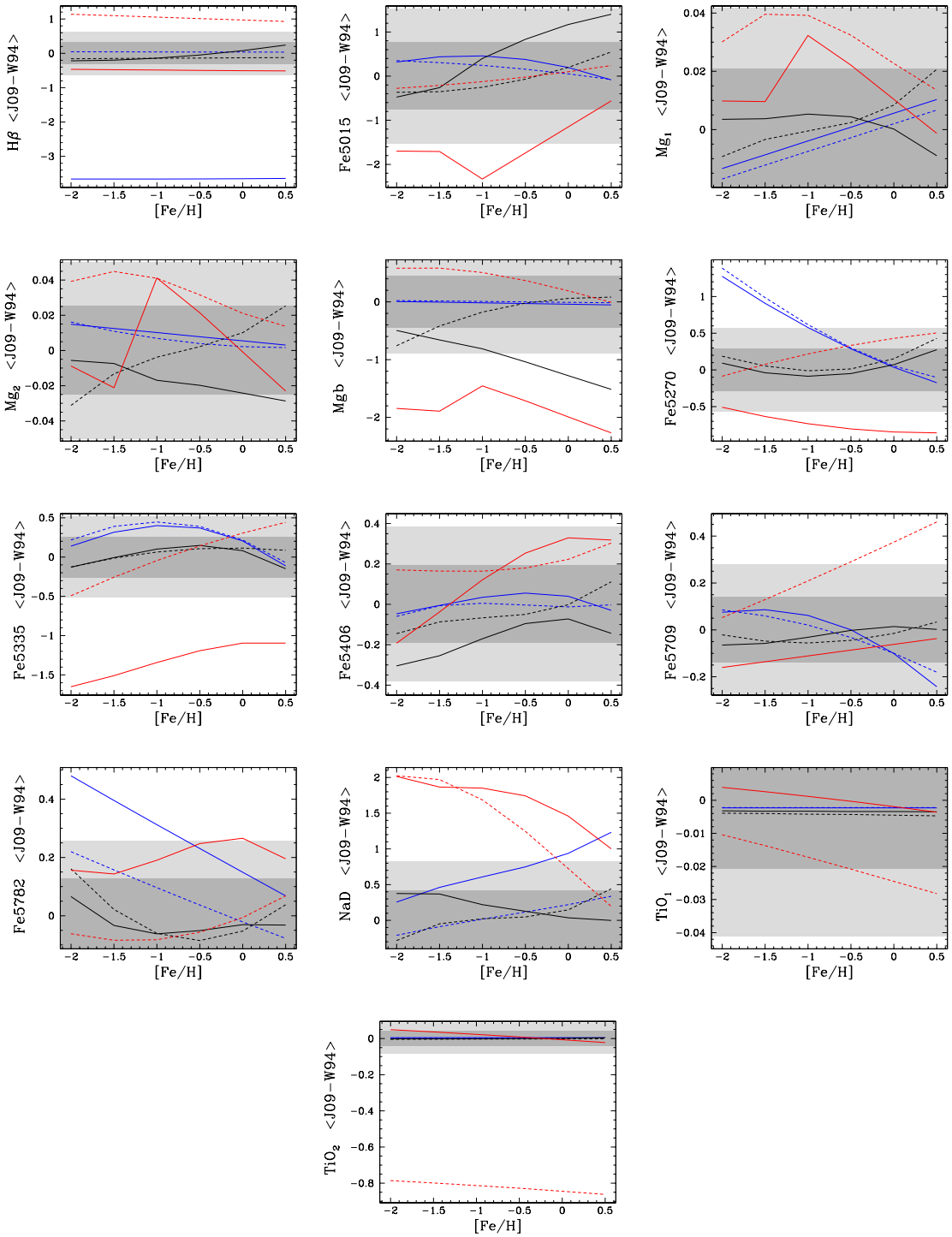

Figure 2.5: Continued.

instead find weaker for this work, out to the 2rms level for *Intermediate* temperature and *Cold Giants*.

CN_1

WFF comparison (Fig. 2.5): Like the Balmer indices the CN indices are sensitive to surface gravity at $T_{eff} \gtrsim 7200$ K ($\theta \lesssim 0.7$), but they instead increase for lower $\log g$. Hence due the better sampling of hot supergiants by the *MILES* library compared to the Lick/IDS library we find the *Warm* end for *Giants* to show significantly stronger indices for this work, extending well beyond the 2rms level. Otherwise, this work show in general stronger indices at the metal-poor end and weaker indices at the metal-rich end, out to the 2rms level in both cases.
SFF comparison (Fig. 2.6): Intermediate temperature *Giants* and *Dwarfs* show weaker and stronger indices for this work, respectively, at the metal-rich end. Otherwise are agreements within the 1rms level mainly found.

CN_2

WFF comparison (Fig. 2.5): Similar to the previous index, but *Warm Dwarfs* show weaker indices for the entire metallicity scale for this work, out to the 2rms level. The *Warm Giant* offset is beyond the 2rms level, but less pronounced compared to CN_1.
SFF comparison (Fig. 2.6): Due to problems with implementing the SFFs we can not make a reliable comparison.

Ca4227

WFF comparison (Fig. 2.5): Cold Dwarfs show stronger indices for this work, extending out to the 2rms level in the metal-poor regime, while *Cold Giants* instead show weaker indices for this work out to the 2rms level at the metal-poor end. *Warm Giants* show stronger indices for this work beyond the 1rms level at the metal-poor end. *Cold Dwarfs* show stronger indices for this work, even extending beyond the 2rms level at the metal-poor end.
SFF comparison (Fig. 2.6): The most prominent difference is found for *Cold Giants* in the metal-poor regime, extending well beyond the 2rms level. *Cold Dwarfs* show stronger indices for this work at the metal-rich end, beyond the 1rms level. Otherwise are differences within the 1rms level found.

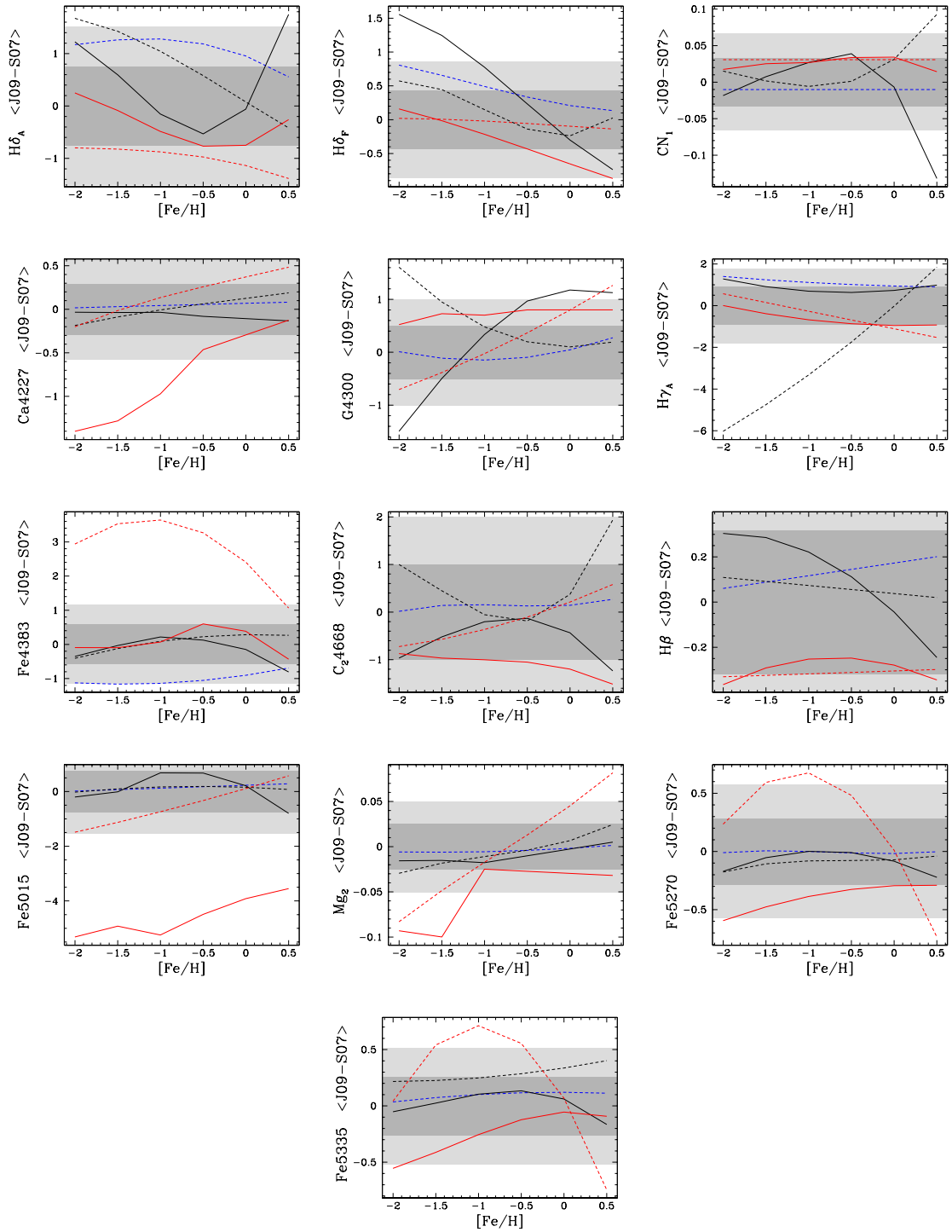

Figure 2.6: Same as Fig. 2.5, but for the comparison between this work (J09) and Schiavon (2007) (S07). The errors are represented by index errors of the *MILES* library (see Section 2.2.2).

G4300

WFF comparison (Fig. 2.5): *Warm Giants* extend well beyond the 2rms level with stronger indices found for this work. Like for the CN indices this is due to better sampling of hot supergiants for the *MILES* library and the sensitivity to surface gravity at $T_{eff} \gtrsim$7200 K ($\theta \lesssim$0.7), such that the G4300 strength increase for lower $\log g$. Metal-poor *Cold Giants* show stronger indices for this work, extending to the 2rms level. *Cold* metal-poor *Dwarfs* extend beyond the 1rms level, showing weaker indices for this work. *Cold* and *Warm* metal-rich *Dwarfs* show stronger and weaker indices for this work, respectively, beyond the 1rms level.
SFF comparison (Fig. 2.6): Differences beyond the 1rms and 2rms levels are found in several regimes, strongest at the ends of the metallicity scale.

Hγ_A

WFF comparison (Fig. 2.5): For the same reason as for Hδ_A, *Warm Giants* show significantly weaker indices for this work, well beyond the 2rms level. *Warm Dwarfs* and *Cold Giants* show stronger indices for this work out to the 2rms level. Otherwise are mainly differences within the 1rms level found.
SFF comparison (Fig. 2.6): The most significant difference is found for *Intermediate* temperature *Dwarfs*, showing weaker indices for this work in the metal-poor regime well beyond the 2rms level. Otherwise are differences mainly found around the 1rms level.

Hγ_F

WFF comparison (Fig. 2.5): Weaker indices are found for this work for *Warm Giants* (for the same reason as for Hδ_A) and *Cold Dwarfs* beyond the 2rms and 1rms level, respectively. Otherwise are mainly differences within the 1rms level found.
SFF comparison (Fig. 2.6): Due to problems with implementing the SFFs we can not make a reliable comparison.

Fe4383

WFF comparison (Fig. 2.5): *Warm Giants* and *Warm Dwarfs* show stronger indices out to the 2rms level at the metal-poor end. *Cold Giants* show weaker indices, out to the 2rms level at the metal-poor and metal-rich ends. Otherwise are mainly differences within the 1rms level found.

SFF comparison (Fig. 2.6): *Cold Dwarfs* show significantly stronger indices for this work, well beyond the 2rms level in the metal-poor region. *Warm Dwarfs* instead show weaker indices, out to the 2rms level. Otherwise are mainly differences within the 1rms found.

Ca4455

WFF comparison (Fig. 2.5): The better parameter coverage of the *MILES* library allow us to model a metallicity dependency in the *Cold Dwarfs* regime in more detail compared to WFF. This results in an offset that increases with decreasing metallicity, such *Cold Dwarfs* show weaker indices for this work extending well beyond the 2rms level in the low metallicity regime. *Cold Giants* instead show stronger indices for this work, extending well beyond the 2rms level in the metal-rich regime. Finally, the *Warm* regime show stronger indices for this work, extending beyond the 1rms level in the metal-poor regime.

Fe4531

WFF comparison (Fig. 2.5): *Cold Dwarfs* show stronger indices for this work at the 1rms level for the metal-poor end and increasing well beyond the 2rms level at the metal-rich end. *Intermediate* temperature *Giants* show stronger indices for this work, out to the 2rms level at the metal-rich end.

$C_2$4668

WFF comparison (Fig. 2.5): The metal-rich end show weaker indices for this work, mainly down to the 1rms level. The metal-poor end show weaker and stronger indices for this work extending beyond the 1rms level for the *Warm* bins and *Cold Dwarfs*, respectively.
SFF comparison (Fig. 2.6): *Cold Giants* show weaker indices for this work beyond the 1rms level in the metal-rich regime. *Intermediate* temperature *Dwarfs* show stronger indices for this work at the metal-rich end out to the 2rms level.

Hβ

WFF comparison (Fig. 2.5): For the same reason as for Hδ_A, we find this work to show weaker indices for *Warm Giants* well beyond the 2rms level. *Cold Dwarfs* show stronger indices for this work beyond the 2rms level. *Cold Giants* show weaker indices for this work beyond the 1rms level.
SFF comparison (Fig. 2.6): Cold Dwarfs show the biggest differences right beyond the 1 rms level. Otherwise are differences within the 1rms level are found.

Fe5015

WFF comparison (Fig. 2.5): Cold Giants show weaker indices for this work, beyond the 2rms level in the metal-poor regime. *Intermediate* temperature *Giants* show stronger indices for this work beyond the 2rms level in the metal-rich regime.
SFF comparison (Fig. 2.6): Cold Giants show significantly weaker indices for this work, well beyond the 2rms level. This work shows weaker indices for *Cold Dwarfs* beyond the 1rms level in the metal-poor regime. Otherwise are differences within the 1rms mainly found.

Mg$_1$

WFF comparison (Fig. 2.5): The *Cold Dwarfs* show stronger indices for this work, out to the 2rms level in the metal-poor regime. The *Cold Giants* show stronger indices for this work at intermediate metallicities. No differences found beyond the 2rms level.

Mg$_2$

WFF comparison (Fig. 2.5): Cold Dwarfs show stronger indices for this work beyond the 1rms level in the metal-poor regime. *Cold Giants* show stronger indices for this work beyond the 1rms level for intermediate metallicities. Otherwise are mainly differences within the 1rms level found.
SFF comparison (Fig. 2.6): The *Cold* end show weaker indices for this work in the metal-poor regime, beyond the 2rms level. *Cold Dwarfs* instead show stronger indices for this work beyond the 2rms level at the metal-rich end.

Mgb

WFF comparison (Fig. 2.5): *Cold Giants* show weaker indices for this work, extending beyond the 2rms level. This is due to Lick offset effects (see Section 2.2.3). As discussed in Section 2.2.3 we found objects with high Mgb index strengths that showed particularly high Lick offsets, such that index strengths measured on the *MILES* stars were significantly weaker. These objects turns out to be *Cold Giants*. *Intermediate* temperature *Giants* also show weaker indices for this work, extinding beyond the 2rms level in the high metallicity regime. *Intermediate* temperature and *Cold Dwarfs* show weaker and stronger indices, respectively, for this work in the Metal-poor regime, beyond the 1rms level.
SFF comparison (Fig. 2.6): Due to problems implementing the SFFs we can not make a reliable comparison.

Fe5270

WFF comparison (Fig. 2.5): The *Warm* end show stronger indices beyond the 2rms level in the metal-poor regime. *Cold Giants* show weaker indices for this work beyond the 2rms level. The metal-rich end show stronger indices for this work beyond the 1rms level for *intermediate* temperature *cold Dwarfs*.
SFF comparison (Fig. 2.6): We find weaker indices for this work beyond the 1rms level for *Cold Giants*. Stronger indices for this work beyond the 2rms level are found for *Cold Dwarfs* in the intermediate metallicity regime. Otherwise are differences well within the 1rms level found.

Fe5335

WFF comparison (Fig. 2.5): *Cold Giants* show weaker indices for this work well beyond the 2rms level. This is due to stars in the Lick/IDS library with high Fe5335 index strengths that are not present in the *MILES* library for the T_{eff}-range in question. The *Warm* end shows stronger indices out to the 1rms level at intermediate metallicities. *Cold Dwarfs* show weaker and stronger indices out to the 1rms level a the metal-poor and metal-rich ends, respectively.
SFF comparison (Fig. 2.6): *Cold Dwarfs* show stronger indices beyond the 2rms level at intermediate metallicities and weaker indices beyond the 2rms level at the metal-rich end. *Cold Giants* show weaker indices for this work beyond the 1rms level. *Intermediate* temperature *Dwarfs* instead show stronger indices for this work, beyond the 1rms level in the metal-rich regime.

Fe5406

WFF comparison (Fig. 2.5): The *Cold* end show stronger indices for this work beyond the 1rms level in the metal-rich regime. *Intermediate* temperature *Giants* show weaker indices for this work beyond the 1rms level. No differences found beyond the 2rms level.

Fe5709

WFF comparison (Fig. 2.5): Cold Dwarfs show stronger indices for this work, extending beyond the 2rms level at the metal-rich end. Otherwise, no significant differences beyond the 1rms level.

Fe5782

WFF comparison (Fig. 2.5): Warm Giants show stronger indices for this work in the metal-poor regime, extending beyond the 2rms level at the metal-poor end. *Cold Giants* show stronger indices for this work regime, beyond the 1rms level. *Warm Dwarfs* show stronger indices for this work beyond the 1rms level at the metal-poor end.

NaD

WFF comparison (Fig. 2.5): The *Cold* end show stronger indices for this work extending well beyond the 2rms level, especially in the metal-poor regime. *Intermediate* temperature *Giants* show stronger indices for this work, extending beyond the 2rms level in the metal-rich regime.

TiO_1

WFF comparison (Fig. 2.5): Cold Dwarfs show weaker indices for this work, extending well beyond the 1rms level at the metal-rich end. Otherwise, no differences found beyond the 1rms level.

TiO_2

WFF comparison (Fig. 2.5): We find significantly weaker indices for this work for *Cold Dwarfs*, extending very far beyond the 2rms level. Similarly to the Mgb case, this is due Lick offset effects. In the last panel Fig. 2.2 we can see objects with high TiO_2 index strengths with a large offset, such that index strengths measured on the *MILES* library are significantly weaker. These objects turn out to be *Cold Dwarfs*. Otherwise, no significant differences found beyond the 1rms level.

2.5 Summary

We have derived new empirical fitting functions for the relationship between Lick absorption indices and stellar atmospheric parameters ($T_{\rm eff}$, [Fe/H] and $\log g$) described by the *MILES* library of stellar spectra, both for the resolution of the *MILES* library and for the resolution of the Lick/IDS library. The *MILES* library consists of 985 stars selected to produce a sample with extensive stellar parameter coverage. The *MILES* library was also chosen because it has been carefully flux-calibrated, making standard star derived offsets unnecessary. This becomes important when comparing stellar population models to high redshift data where no resolved individual stars are available.

We find the index measurements of the *MILES* spectra to have very high quality in terms of observational index errors. These errors are also found to be significantly smaller than for the Lick/IDS library. This was expected since the *MILES* library was observed nearly thirty years after the Lick/IDS library. Given the high quality of the index measurements, index errors should not be the major error sources for the final fitting functions. We instead find indications that the stellar parameter estimates are significant error sources.

Lick Index offsets between the *MILES* library and the classic Lick/IDS library are derived in order to be able to compare stellar population models based on this work with models in the literature. We find these offsets to be dependent on index strength and have therefore derived least-square fits for the residual between the two libraries. Offset to the Lick/IDS library are also derived for the flux-calibrated *ELODIE* and *STELIB* libraries. We find clear offset deviations between the libraries. The largest deviations are found for the *STELIB* library compared to the other two libraries, which is also the library having least stars in common with the Lick/IDS library. The deviations in offsets found between the three libraries undermine the derivation of universal offsets between the Lick/IDS and these flux-calibrated systems.

We compare the fitting functions of this work to fitting functions in the literature, namely the fitting functions of Worthey et al. (1994), Worthey & Ottaviani (1997) and Schiavon (2007). Generally we find good agreement within the rms of the residuals between the data and the fitting functions of this work. The differences found in the comparisons vary significantly from index to index and especially from one stellar parameter region to another for individual indices. However, the major differences are found in the outskirts of stellar parameter space, i.e. at the temperature and metallicity ends. This is probably due to a low number of data points in these regimes for the stellar libraries, inducing uncertainties which result in the major differences found.

In the next chapter the fitting functions presented here are implemented in stellar population models following the techniques of Maraston (2005) and Thomas et al. (2003a).

Chapter 3

Flux-calibrated stellar population models of Lick absorption-line indices with variable element abundance ratios

In this chapter we present stellar population models of Lick absorption-line indices with variable element abundance ratios. The models are based on the new calibrations of absorption-line indices with stellar parameters derived from the MILES stellar library and presented in Chapter 2. The key novelty compared to the previous Thomas et al. (2003a) models is that they are now available at the higher spectral resolution of MILES (2.5 full width at half-maximum) and flux calibrated, hence not tied anymore to the Lick/IDS system. This is essential for the interpretation of galaxy spectra where calibration stars are not available, such as large galaxy redshift surveys or other high-redshift observations. Another novelty is random errors for the model predictions based on the uncertainties in the calibration functions and the underlying stellar parameter estimates. We show that random errors are small except at the edges of the parameter space (high/low metallicities and young ages $\lesssim$1 Gyr) where the stellar library is undersampled. We calibrate the base model for the parameters age, metallicity and α/Fe ratio with galactic globular cluster and galaxy gradient data. We discuss two model flavours with different input stellar evolutionary tracks from the Frascati and Padova groups. The model includes abundance variations of the elements C, N, Mg, Na, Si, Ca, Ti, Cr and Fe. The individual elements that are best accessible with these models and the standard set of Lick absorption features are C, N, Mg, Ca, Ti and Fe.

3.1 Introduction

3.1.1 Background

The spectra of galaxies and globular clusters carry a wealth of information about gas and stellar population properties. Emission lines are used to derive gas kinematics, star formation activity and black hole accretion (e.g. Kauffmann et al., 2003a; Tremonti et al., 2004; Sarzi et al., 2006; Schawinski et al., 2007). The absorption line and stellar continuum component of the spectrum, instead, discloses stellar population properties that act as fossil record and can be used to derive ages, formation epochs, star formation histories, and element abundances (e.g. Trager et al., 2000b; Kuntschner, 2000; Thomas et al., 2005; Nelan et al., 2005; Bernardi et al., 2006; Thomas et al., 2010). The absorption features in a spectrum are particularly useful for several reasons. They can easily be measured and calibrated to a common system (Burstein et al., 1984; Faber et al., 1985), they are largely insensitive to dust attenuation (MacArthur, 2005), and they allow to dissect 'metallicity' into individual element abundances (Greggio, 1997; Tantalo et al., 1998; Trager et al., 2000a; Thomas et al., 2003a) that in turn set valuable constraints on the chemical enrichment history (Thomas et al., 1999b).

The Lick indices (see Section 2.1.2) are an agglomeration of a large number of absorption lines from various chemical elements, so that their use for the derivation of individual element abundances is nontrivial. Tripicco & Bell (1995) made a critical step forward and determined the sensitivity of Lick absorption-line indices to individual element abundance variations through model atmosphere calculations. Trager et al. (2000a) developed a method to incorporate these results in the analysis of stellar populations, which formed the bases for the first stellar population models of Lick absorption-line indices with variable element abundance ratios (Thomas et al., 2003a). These models have subsequently been updated with new model atmosphere calculations by Korn et al. (2005, see also Houdashelt et al 2005) for non-solar metallicities and the higher-order Balmer line indices (Thomas et al., 2004, hereafter TMB/K models). A number of other element abundance sensitive models have been published since either for absorption-line indices following this semi-empirical method (Annibali et al., 2007; Schiavon, 2007; Lee et al., 2009b) or full spectral energy distributions using a purely theoretical approach (Coelho et al., 2007; Walcher et al., 2009).

Most of the models quoted above, including TMB/K, use the empirical calibrations of the Lick absorption-line indices with stellar parameters based on the Lick/IDS stellar library (Worthey et al., 1994). As comprehensively describe in the previous chapter this library has now been superseded by modern samples, most notably MILES (see Section 2.2). An update of the Maraston (2005, hereafter M05) stellar population model of

full spectral energy distributions including the MILES library is published in Maraston & Strömbäck (2011). In this chapter we include the MILES library in the TMB/K model using the new empirical fitting functions presented in Chapter 2.

This new model is the flux-calibrated version of the TMB/K model. It has been extended further by considering both MILES and Lick spectral resolution, the inclusion of additional computations based on the Padova stellar evolutionary tracks and a large range of individual element abundance variations considering the complete set of ten elements provided in Korn et al. (2005). We test this model on galactic globular cluster data. In Chapter 4 it is used to derive the element abundance ratios [C/Fe], [N/Fe], [O/Fe], [Mg/Fe], [Ca/Fe], and [Ti/Fe]. For the first time we provide statistical errors for each model prediction. The flux calibration in particular eases the application of these models to observational data where calibrating stars are not available, ie galaxy redshift surveys such as SDSS (York et al., 2000) or other high-redshift observations (Zielger et al., 2005; Bernardi et al., 2006; Kelson et al., 2006; Sánchez-Blázquez et al., 2009; Thomas et al., 2010; Carson & Nichol, 2010).

The chapter is organised as follows. In Sections 3.2 and 3.3 we present the model. The calibration of the models with galactic globular clusters and galaxy data is shown in Section 3.4 as well as the comparison with other models in the literature. The chapter concludes with Section 3.5.

3.1.2 Stellar evolution and nucleosynthesis

As stars evolve their luminosity and surface temperature change. This is demonstrated in Fig. 3.1 showing the colour-magnitude diagram (CMD) of a globular cluster, indicating the different stellar evolutionary phases. After the ignition of H-burning in the core for protostars with masses greater than $\sim$0.08M$_\odot$ (the core temperature never reaches high enough values to ignite H-burning below this mass limit) the newly formed stars start their life on the main-sequence (MS). The MS forms a more or less diagonal line in the CMD and the initial mass of the star determines the position along this sequence. More massive stars burn H more efficiently in the core, due to higher pressure and temperature. These stars are thus more luminous and have higher surface temperatures, i.e. they show bluer colours.

H-burning occur in two different processes the *pp*-chain and the CNO-cycle. The former takes in place in stars of all masses by the fusion of two H-nuclei into deuterium and the subsequent fusion of deuterium and a H-nuclei into a He-nuclei. The CNO-cycle requires higher temperatures and only occurs in stars with masses greater than 1.4 M$_\odot$ where it becomes the dominant process. In the CNO-cycle H is converted to He in a

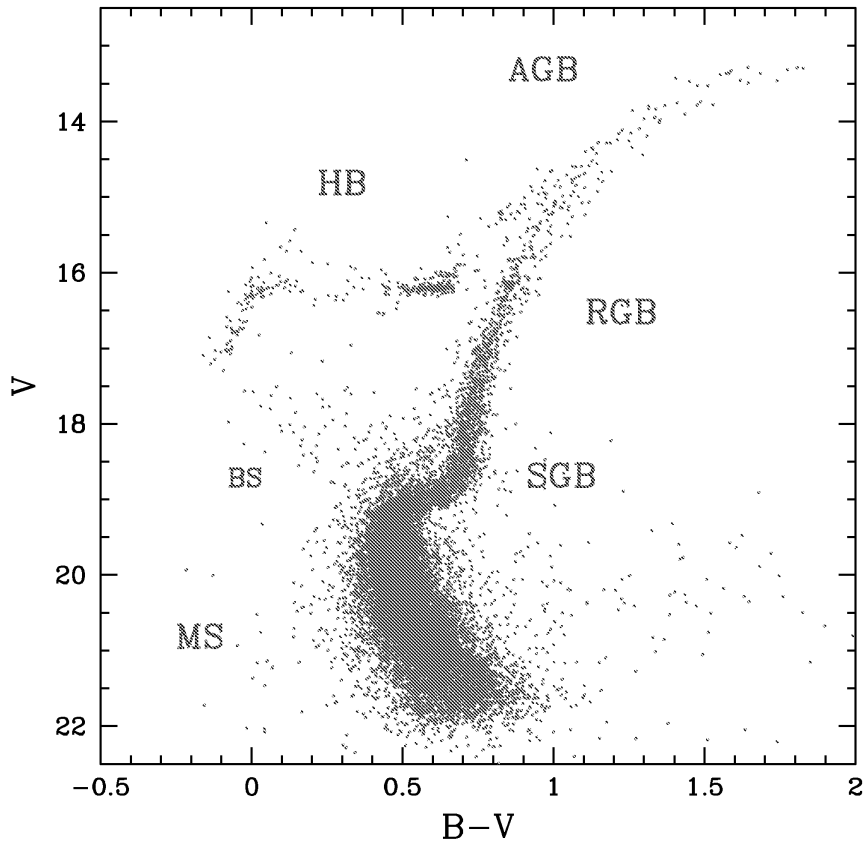

Figure 3.1: Fig. 3 in Maraston (2005). The CMD of the MIlky Way globular NGC 1851, indicating the different stellar evolutionary phases. These are indicated by the labels, i.e. the MS, the SGB, the RGB, the HB, the AGB and also blue stragglers (BS).

number of steps involving the elements C, N and O. The net result of the CNO-cycle besides He is ^{14}N due to the slow reaction of ^{14}N(p, γ)^{15}O.

When the star has used up all the core H it starts to move away from the MS in the CMD. More massive stars consume the H in the core faster, due to the more efficient H-burning, and will consequently spend less time on the MS. When the core H is exhausted the core starts to contract which increases the temperature and triggers an accelerating rate of shell H-burning. Before the outer regions have become fully convective the surface cools down. This moves the star horizontally towards redder colours in the CMD along the sub-giant branch (SGB). When the envelope becomes fully convective the outer regions begin to expand increasing the luminosity. The star is now moving along the RGB and a significant amount of mass is lost through stellar winds. The convective envelope can reach into the H-burning shell and bring He and CNO processed elements to the surface, known as the first dredge-up (Iben & Truran, 1978; Renzini & Voli, 1981; van den Hoek & Groenewegen, 1997).

As the star moves along the RGB the He-core continues to contract due to the increase in mass of He from the H-burning shell. When the temperature is high enough He-burning is ignited in the core for stars with masses greater than $\sim$0.26$M_{\odot}$. The energy released by He-fusion causes the core to expand which slows down the shell H-burning. This results in a decrease of the total energy generated and the outer layers will therefore contract. The star becomes less luminous and bluer moving along the Horizontal branch (HB). He-burning produce ^{12}C through the triple-alpha process and ^{16}O through fusion of a ^{12}C- and He-nuclei. Hence a C and O rich core (CO-core) will be the result of He fusion. Shell H-burning takes place during core He-fusion.

Shell He-burning will take place after He is exhausted in the core. Similarly to the course following the MS the outer layers will expand and the star becomes more luminous and redder climbing the CMD parallel to the RGB. This stellar evolutionary phase is called the Asymptotic giant branch (AGB). On the early-AGB the convective envelope brings H-fusion products from the H-burning shell to the surface, known as the second dredge-up (Iben & Truran, 1978; Renzini & Voli, 1981; van den Hoek & Groenewegen, 1997). This occurs in stars with masses greater than 3$M_{\odot}$. During the AGB phase the star is prone to further mass-loss. As the shell He-burning ceases the surrounding H-shell contracts and H-fusion is ignited. This provide the He-shell with more fuel making it contract and again triggering He-fusion. This course of events is repeated in what is called the thermally pulsating AGB (TP-AGB). At this point the convective envelope can reach down into the He-burning shell and bring C up to the surface, known as the third dredge-up (Iben & Truran, 1978; Renzini & Voli, 1981; van den Hoek & Groenewegen, 1997). This can produce a carbon star. However, the emergence of a carbon star can be prevented by the processing of newly dredged-up material in the CNO-cycle at the bottom of the convective envelope, know as hot bottom burning (HBB). HBB can occur if the initial mass of the star is greater than 3-4 $M_{\odot}$ (Renzini & Voli, 1981; van den Hoek & Groenewegen, 1997).

Depending on the initial mass of the star electron-degeneracy in the CO-core will stop the core from further contraction and the star will end up as a slowly fading white dwarf (WD). If the mass is high enough, M>8-10$M_{\odot}$, the pressure will be too high for electron-degeneracy to prevent contraction. This will ignite the fusion of C and in all but the most massive stars (M>50 $M_{\odot}$, Tsujimoto et al., 1995) sub-sequent nuclear burning of produced elements proceeds until an Fe-core is reached. The result is an onion shape structure with each layer being composed of different elements. The core then collapses and the star explodes as a core-collapse supernovae, SN II, expelling the elements in the outer layers. Explosive nucleosynthesis also takes place and produce elements beyond Fe through neutron capture known as the r-process. Hence SN II enrich the ISM with

a wide range of elements, peaking in abundance around the light α-elements O and Mg (Thielemann et al., 1996).

As the core contracts prior to the explosion event, the pressure is high enough to overcome electron degeneracy. However, depending on the initial mass of the star the core either becomes a neutron star, where further gravitational collapse is prevented by neutron degeneracy, or the core-mass is high enough to collapse completely to form a black hole.

3.2 The base model

The stellar population model of absorption-line indices presented here is an extension of the TMB/K model. The underlying model of single-stellar populations (SSPs, i.e. single age and single metallicity stellar populations) are based on the evolutionary population synthesis code of Maraston (2005, M05) assuming a Salpeter initial stellar mass function (IMF). We refer the reader to these papers for details. In the following we briefly summarise the major ingredients to the base model.

For the chosen IMF the M05 code computes the SSP models by integrating the flux contributions of different mass bins along isochrones of varying age and metallicity. For each mass bin the stellar parameters $T_{\rm eff}$ and $\log g$ are given besides metallicity. These parameters are input to the empirical fitting functions presented in Chapter 2 to compute the Lick indices for each mass bin. The Lick indices are then scaled with the flux contributions along the isochrones to compute the integrated indices of the SSP models.

3.2.1 Stellar evolutionary tracks

Following M05 and to ensure continuity with the TMB/K model, the isochrones are based on the stellar evolutionary tracks from Cassisi et al. (1997, hereafter Cassisi), except for the highest metallicity model where Padova tracks (Girardi et al., 2000, hereafter Padova) are used. In the present work we complement the model set with further calculations based on Padova tracks at high metallicities with $[Z/{\rm H}] \geq -0.33$ where differences are significant between the two model sets. Hence two separate flavours of the model based on two different sets of stellar tracks (Cassisi and Padova) are provided.

Padova tracks have been chosen as comparison set, because these tracks are the most widely used in most other stellar population synthesis models in the literature (M05, and references therein), in particular in other models of Lick absorption line indices (Schiavon, 2007; Vazdekis et al., 2010). Cassisi and Padova tracks have also been chosen because they are different in some key aspects such as the treatment of overshooting or the mixing-length parameter as summarised below. In this way, the two model flavours

presented here encompass some of the uncertainties in stellar evolution theory. A major difference that impacts on the present model is the fact that at high metallicities, the Padova Red Giant Branches are cooler than those of the Cassisi tracks (Fig. 9 in M05). This generally leads to stronger metal absorption indices and weaker Balmer line absorption indices (see Section 3.4.2). In the following we discuss some of the key ingredients in stellar evolutionary tracks.

3.2.2 Mass loss

Stellar mass loss cannot be predicted by stellar tracks. This comes from the fact that a theory relating mass-loss rates to the basic stellar parameters does not exist. Therefore, mass loss has to be parametrised and its efficiency calibrated with data. In M05 the amount of mass loss is usually parametrised by means of the Reimers (1975) empirical formula that includes a mass loss efficiency parameter η. In order to trace the Horizontal Branch evolution properly, M05 uses the evolutionary track for the He-burning phase of the mass that is obtained after mass loss is applied to the Red Giant Branch track. Here we follow the approach by Maraston & Thomas (2000) that was to modify the mass loss parameter η as a function of metallicity such that the Balmer absorption indices of globular clusters can be reproduced (see Section 3.4.1).

3.2.3 Convective overshooting

Another large uncertainty in the theory of stellar evolution is convective core overshoot. Unlike the Padova tracks, the Cassisi tracks are canonical stellar evolutionary tracks, i.e. the efficiency of the overshooting parameter is assumed to be zero (M05). The inclusion of this effect in stellar evolutionary tracks is still controversially discussed in the literature, and a detailed assessment of this issue goes beyond the scope of the present work. Briefly, if overshooting is included the boundary limit for the stellar core becomes larger and convective motions bring unprocessed material from the outer layers to the center. Hence stellar models with overshooting have more massive convective cores, therefore they run to higher luminosities and live longer than classical models.

The main-sequence life-time is thus longer for stellar tracks with convective overshooting compared to canonical tracks. Also, the Red Giant Branch phase transition occurs at 0.5 Gyr in classical models and at 1 Gyr in models with overshooting (M05). The Padova tracks have a turnoff mass at given age that is larger than that of canonical tracks as a consequence of the different treatment of convective overshooting (M05).

3.2.4 Mixing length

The efficiency of convective energy transfer is parametrized by the mixing length parameter. The calibration of this parameter for the Cassisi tracks is described in Salaris & Cassisi (1996). The tracks with solar metallicity are computed for $\alpha = 2.25$, a value that matches the Sun. This same value is kept in the tracks with supersolar metallicities (Bono et al., 1997). At subsolar metallicities, however, the mixing-length parameter is not assumed to be the same, but to vary with Z, such that the temperatures of the Red Giant Branch tips of Milky Way globular clusters are reproduced (M05). The values range from 2 to 1.75, with a trend of decreasing mixing length with metallicity. In the Padova tracks, instead, the same value of the mixing-length parameter that is calibrated with the Sun is assumed at all metallicities. This results in a cooler RGB at higher metallicities and a warmer RGB at lower metallicities compared to the Cassisi tracks (see Fig. 9 in M05).

3.2.5 Non-solar α/Fe ratios

Note that in TMB/K solar-scaled tracks were adopted, as α/Fe-enhanced stellar tracks at the time appeared too blue and led to unrealistically old ages for galaxies (Thomas & Maraston, 2003). It turned out that indeed the effect of α/Fe enhancement on the stellar evolutionary tracks was overestimated previously (Weiss et al., 2006), and the recent work by Dotter et al. (2007) confirms that α/Fe enhanced stellar evolutionary tracks are not significantly different from their solar-scaled counterparts. We therefore continue to use the solar-scaled stellar tracks employed in TMB/K.

3.2.6 Stellar atmosphere

It should be emphasised that stellar atmosphere calculations enter the present model only marginally. Continuum fluxes are adopted from the model atmospheres in order to calculate the final absorption index. The spectral features themselves, however, that are produced in the stars atmospheres (measured as Lick indices) are included in the model through the empirical fitting functions (see Chapter 2).

3.3 Models of Lick absorption line indices with varying element abundance ratios

The TMB/K model was developed to compute Lick absorption-line index strengths for various chemical element abundance ratios. In the following we provide a brief overview

of the TMB/K approach with particular emphasis on the novelties of the present model calculations. For more details on the model the reader is referred to Thomas et al. (2003a); Thomas et al. (2004).

3.3.1 Calculation of statistical errors

The construction of the model through fitting functions allows us to make a straightforward assessment of the statistical errors on each individual index prediction that is caused by the uncertainties in the index calibrations. We calculate errors in the model predictions through Monte Carlo simulations. In 600 realisations per simulation we perturb both index measurements and stellar parameters for each star using the errors given in Sánchez-Blázquez et al. (2006b). For each realisation we re-derive the fitting functions and insert those in the stellar population code. This yields 600 index predictions per index and stellar population parameter age, metallicity, and α/Fe ratio. We then fit a Gaussian to the distribution of index strengths and derive the 1-σ error. Note that these errors do not include systematic effects such as a change of stellar evolutionary track, for instance.

3.3.2 Spectral resolution

In Chapter 2 we compute fitting functions for both the resolution of the MILES library and the resolution of the Lick/IDS library. In this work we therefore compute index predictions for both spectral resolutions. Note that the stellar population spectral resolution of MILES turns out to be somewhat worse than stated in Sánchez-Blázquez et al. (2006b) and Vazdekis et al. (2010) (see Section 2.2).

3.3.3 Index response functions

The models include different chemical mixtures and element abundance ratios. To compute optical Lick indices for these chemical mixtures, the impact from element ratio changes has to be assessed. This is done with the help of the so-called index response functions of Korn et al. (2005). Extending the work of Tripicco & Bell (1995), Korn et al. (2005) calculate model atmospheres with solar-scaled element ratios for various combinations of temperature, gravity, and total metallicity. In subsequent models the abundances of the elements C, N, O, Na, Mg, Si, Ca, Ti, Fe, and Cr are doubled in turn, in order to determine the sensitivity of the Lick absorption indices to element abundance variations. For the absolute index I_0 and a logarithmic abundance increment of the *i*th element $\Delta[X_i] = \log X_i^1/X_i^0 = \log 2 = 0.3$ dex Korn et al. (2005) compute the index change ΔI(i) at fixed temperature, gravity and metallicity. These response functions are

included in the model following an extension of the method developed in Trager et al. (2000a).

More specifically, Korn et al. (2005) compute the model index by splitting the base SSP model in the three evolutionary phases, dwarfs, turnoff stars and giants. Lick index strengths I of the base model for each phase are computed separately, and modified using the fractional responses of the index strengths $\delta I/I_0$. As discussed in Korn et al. (2005), these are applied to the flux in the absorption line rather than to the absorption index, as the former is always a positive quantity, while indices can be technically negative. In this way numerical robustness is ensured. Following Maraston et al. (2003) the SSP index strength is related to the line flux F_l and continuum flux F_c through

$$I = \Delta\left(1 - \frac{F_l}{F_c}\right) \tag{3.1}$$

where Δ is the width of the feature pass-band (see Section 2.1.2). If the SSP index strength is integrated over a specific number of sub-phases Eq. 3.1 can be re-written as

$$I_{SSP} = \Delta\left(1 - \frac{\sum_j F_l^j}{\sum_j F_c^j}\right) \tag{3.2}$$

where F_l^j is the line flux and F_c^j is the continuum flux of the jth subphase. Derived from Eq. 3.1 and the fractional index response Korn et al. (2005) compute the fractional response of the flux with

$$\frac{\delta F_l}{F_l^0} = \frac{\delta I}{I_0 - \Delta} \tag{3.3}$$

Following TMB/K and Korn et al. (2005) the new flux is then calculated from the flux variations with

$$F_l^{new} = F_l \prod_{i=1}^{n} exp\left\{\frac{1}{F_l^0}\frac{\delta F_l}{\delta[X_i]}0.3\right\}^{\Delta[X_i]/0.3} \tag{3.4}$$

The new SSP indices are calculated with Eq. 3.1 and F_l^{new} and the integrated SSP index is finally computed as

$$I_{new}^{ssp} = \frac{I_{new}^D \times F_c^D + I_{new}^T \times F_c^T + I_{new}^G \times F_c^G}{F_c^D + F_c^T + F_c^G} \tag{3.5}$$

where I_{new}^D, I_{new}^T and I_{new}^G are the new model indices in the dwarf, turn-off and giant phase, respectively, and F_c^D, F_c^T and F_c^G are the corresponding continuum fluxes. Eq. 3.5 and 3.2 are mathematically equivalent.

3.3.4 Inclusion of element abundance variations in TMB/K

The so-called α-elements (i.e. O, Mg, Si, Ca, Ti) and other light elements (i.e. C, N, Na) are combined to the 'enhanced group', while the iron peak elements (Fe, Cr) form the 'depressed group'. The ratio between those two groups is varied at fixed total metallicity, and is called α/Fe. Hence the abundances of all elements in one group are modified in lockstep. Model predictions of Lick absorption index strengths for the following element ratios are provided in the TMB/K model: $[\alpha/\mathrm{Fe}] = -0.3, 0.0, 0.3, 0.5$ dex. On top of this, the abundances of the individual elements carbon, nitrogen, and calcium are modified in separate model predictions providing the element ratios $[\alpha/\mathrm{N}] = -0.5$, $[\alpha/\mathrm{C}] = -0.1$, and $[\alpha/\mathrm{Ca}] = -0.1, 0.2, 0.5$ dex. A technical description of the inclusion of element abundance ratios in the models is included in Section 4.3.3.

The solar abundances from Grevesse et al. (1996) are adopted. It should be emphasised that differences between these values and more recent determinations can be considered small (Asplund et al., 2009). Most importantly, however, variations of the solar abundances do not affect the models presented here. The solar abundances only serve as reference frame to which the element abundance ratios of our models are normalised. A change in solar abundance can be easily accounted for a posteriori by simple re-scaling.

As introduce in Section 2.3.3 the models take into account the fact that the empirical stellar libraries used to compute model indices follow the chemical enrichment history of the MilkyWay, and are therefore biased towards super-solar α/Fe ratios at sub-solar metallicities. We correct for this bias, so that the models have well-defined α/Fe ratios at all metallicities. Particular care has been taken at calibrating the TMB/K models with galactic globular clusters, for which ages, metallicities and element abundance ratios are known from independent sources.

3.3.5 New element abundance variations

For the new model presented here we complement and extend the list of element ratios provided by the TMB/K model. The new model is computed for the standard element ratios $[\alpha/\mathrm{Fe}] = -0.3, 0.0, 0.3, 0.5$ dex and additional model calculations. In each of these, only one of the elements C, N, Na, Mg, Si, Ca, and Ti is increased by 0.3 dex relative to the α-element abundance. Hence, this yields seven different additional model tables with the element ratios $[\mathrm{X}/\alpha] = 0.3$ dex for X =C, N, Na, Mg, Si, Ca, Ti. These can be used to assess the effect of abundance variations of these elements. In Chapter 4 we introduce a method for deriving the simultaneous enhancement of several element ratios. We do not include O, because this element dominates total metallicity, and Fe, because this element is already considered with varying α/Fe ratio.

Table 3.1: Element ratio bias for the various metallicities.

Element ratio	-2.25	-1.35	-0.33	0.0	0.35	0.67
[C/Fe]	0.30	0.30	0.10	0.00	0.00	0.00
[N/Fe]	0.30	0.30	0.10	0.00	0.00	0.00
[O/Fe]	0.30	0.30	0.10	0.00	0.00	0.00
[Na/Fe]	0.30	0.30	0.10	0.00	0.00	0.00
[Mg/Fe]	0.30	0.30	0.10	0.00	0.00	0.00
[Si/Fe]	0.30	0.30	0.10	0.00	0.00	0.00
[Ca/Fe]	0.20	0.20	0.07	0.00	0.00	0.00
[Ti/Fe]	0.15	0.15	0.05	0.00	0.00	0.00
[Cr/Fe]	0.00	0.00	0.00	0.00	0.00	0.00

We emphasise again that metallicity is kept fixed in these calculations. Note, however, that these elements do not contribute significantly to the overall mass budget when treated individually. Therefore, one can safely consider those enhancements as minor perturbations. Since this does not apply to O, we do not calculate individual enhancements for this element. As discussed in Chapter 4 and 5, there is strong evidence now that the heavier of the α elements like Ca and Ti are less enhanced than O or Mg in metal-poor Milky Way stars (Feltzing et al., 2009; Bensby et al., 2010). Unlike the TMB/K model we consider these elements separately in the new model, therefore this differential bias in the library stars has to be taken into account (see Section 3.3.4). We assume a bias of 0.3 dex for the light elements, which we reduce to $0.2 - 0.15$ dex for those elements with higher atomic number. The detailed bias adopted is summarised in Table 3.1. Note that the element ratio [O/Fe] is included in the bias table, even though we do not consider individual O/Fe ratios. The reason is that O abundance is included in the 'enhanced group' . Like in TMB/K we do not assume any bias at super-solar metallicity as suggested by Proctor et al. (2004), as the various elements still exhibit conflicting trends (see discussion in Thomas et al., 2005).

A detailed description of how the modelling of individual element abundance ratios is performed is given in Chapter 4 (more precisely in Section 4.3.2) where the method for deriving these element ratios is presented.

3.3.6 Summary of new features

The new features of this model are. 1) Based on a flux-calibrated version of the Lick/IDS index system. This is achieved through the new flux calibrated fitting functions of Chapter 2 based on the MILES stellar library. 2) Error estimates for each index as function of stellar population parameters. 3) Model predictions provided for MILES and Lick spectral resolutions. 4) Two different stellar evolutionary tracks (Cassisi and Padova). 5) Additional sets of models. In each of these, only one of the elements C, N, Na, Mg, Si,

Ca, and Ti is increased by 0.3 dex relative to the α-element abundance. A differential element ratio bias in the stellar libraries at low metallicities is considered to account of the fact that heavier α elements tend to be less enhanced in metal-poor halo stars.

3.4 Model testing

Following the strategy of the TMB/K models, we compare the model predictions with observational data of galactic globular clusters, as the latter are the closest analogues of simple stellar populations in the real universe (Maraston et al., 2003). Key is that independent estimates of ages, metallicities, and element abundance ratios are available for the globular clusters of the Milky Way from deep photometry and stellar high-resolution spectroscopy. As discussed in Thomas et al. (2003a, see references therein) galactic globular clusters are known to be old and α/Fe enhanced similar to halo field stars (for more recent compilations see de Angeli et al., 2005; Pritzl et al., 2005; Mendel et al., 2007).

The globular cluster samples considered here are from Puzia et al. (2002) and Schiavon et al. (2005). We do not use the indices tabulated in Puzia et al. (2002) directly, because these measurements have been calibrated onto the Lick/IDS system by correcting for Lick offsets. Schiavon et al. (2005) do not provide line index measurements. Hence we measure line strengths for all 25 Lick absorption-line indices directly on the globular cluster spectra using the definitions by Trager et al. (1998) and Worthey & Ottaviani (1997). Both globular cluster sample have been flux calibrated, so that no further offsets need to be applied for the comparison with the models presented here. We have smoothed the spectra to Lick spectral resolution before the index measurement in order to allow for a straight comparison with the TMB/K model. Note that the Schiavon et al. (2005) spectra are corrupt around 4546 and 5050 Å, so that the indices Fe4531 and Fe5015 cannot be measured (S05). A detailed description of the globular cluster data and index measurements is given in Section 4.2. The aim of this section is to test the new models with globular cluster data.

3.4.1 Comparison with globular cluster data

Figs. 3.2, 3.3, 3.4, 3.5 are a re-make of Fig. 2 from Thomas et al. (2003a). Following Thomas et al. (2004) we plot predictions for the 25 absorption-line indices as functions of the index $[\mathrm{MgFe}]'$ in order to visualise better the α/Fe sensitivity of each individual index. This index has been defined in Thomas et al. (2003a) as

$$[\mathrm{MgFe}]' \equiv \sqrt{\mathrm{Mg}\,b\,(0.72 \cdot \mathrm{Fe5270} + 0.28 \cdot \mathrm{Fe5335})} \tag{3.6}$$

in order to eliminate the residual α/Fe dependence of the index [MgFe] introduced by González (1993). The plots show three models at Lick spectral resolution with an age of 13 Gyr, the metallicities $[Z/\mathrm{H}] = -2.25,\ -1.35,\ -0.33,\ 0.0,\ 0.35,\ 0.67$ dex, and $[\alpha/\mathrm{Fe}] = 0.0, 0.3, 0.5$ dex as solid magenta, yellow, and cyan lines, respectively. Hence each line is a model at fixed age and α/Fe ratio with total metallicity increasing from left to right. The grey shaded area along the model with $[\alpha/\mathrm{Fe}] = 0.3$ dex (yellow line) indicates the 1-σ error of the model prediction.

Dotted lines are the original TMB/K model for comparison. Note that this model is inherent to the Lick/IDS system. Discrepancies between the TMB/K and the new model will be caused mostly by differences in the fitting functions adopted, and the flux-Lick/IDS calibration.

Data of galactic globular clusters from Puzia et al. (2002) and Schiavon et al. (2005) are filled squares and open squares, respectively. The typical errors in the globular cluster index measurements (see Chapter 4) are given by the error symbol at the bottom of each panel. Finally, the small black dots are early-type galaxies from the MOSES catalogue (see Section 5.2). Only measurements on high signal-to-noise spectra with $S/N > 40$ are shown, primarily in order to provide an indication for the locus of massive galaxies in this diagram.

We split the presentation in four different figures: the five Balmer line indices in Fig. 3.2 ($\mathrm{H}\delta_\mathrm{A}$, $\mathrm{H}\delta_\mathrm{F}$, $\mathrm{H}\gamma_\mathrm{A}$, $\mathrm{H}\gamma_\mathrm{F}$, $\mathrm{H}\beta$), the indices with a positive response to α/Fe enhancement in Fig. 3.3 (CN_1, CN_2, Ca4227, G4300, Mg_1, Mg_2, $\mathrm{Mg}\,b$), the indices with negative responses to α/Fe enhancement in Fig. 3.4 (Fe4383, Fe4531, Fe5015, Fe5270, Fe5335, Fe5406, Fe5709, Fe5782) , and the remaining indices that are insensitive to α/Fe in Fig. 3.5 (Ca4455, $\mathrm{C}_2$4668, NaD, TiO_1, TiO_2). Following Thomas et al. (2003a); Thomas et al. (2004) we consider a model well calibrated if the model track with $[\alpha/\mathrm{Fe}] = 0.3$ matches the globular cluster data.

To quantify this comparison, we calculate the median reduced χ^2 values for this comparison. We perform two tests, one including all globular clusters, and one focusing on high metallicity clusters with $[Z/\mathrm{H}] > -0.8$ dex. The results are listed in Table 3.2. Note that these numbers should be interpreted with care. Their aim is to aid the identification of well calibrated and badly calibrated indices in the following discussion. Low χ^2 can be produced by large errors, and may not necessarily indicate a good match. Furthermore, this exercise does not include the variation of other element ratios, that we know are crucial for some indices, in particular those that are sensitive to individual elements whose abundances may show anomalies in galactic globular clusters. For instance, the indices CN_1 and CN_2 are very sensitive to N abundance, and it is known that nitrogen

Table 3.2: Reduced χ^2 values for model-data comparison in Figs. 3.2−3.5 and median relative errors in the globular cluster sample.

Index	all $[Z/\mathrm{H}]$	$[Z/\mathrm{H}] > -0.8$ dex	$\delta I/I$	calibrated
(1)	(2)	(3)	(4)	(5)
$\mathrm{H}\delta_\mathrm{A}$	0.9	0.9	0.12	yes
$\mathrm{H}\delta_\mathrm{F}$	0.8	1.5	0.18	no
CN_1	0.8	5.5	0.11	yes[a]
CN_2	0.8	4.8	0.09	yes[a]
Ca4227	1.8	2.9	0.13	yes[a]
G4300	0.7	1.3	0.07	yes
$\mathrm{H}\gamma_\mathrm{A}$	0.7	1.1	0.08	yes
$\mathrm{H}\gamma_\mathrm{F}$	0.7	1.1	0.11	yes
Fe4383	0.6	0.9	0.11	yes
Ca4455	0.5	0.9	0.28	no
Fe4531	0.5	1.2	0.06	yes
$\mathrm{C}_2$4668	0.8	2.1	0.12	yes[a]
$\mathrm{H}\beta$	0.8	1.5	0.09	no
Fe5015	2.9	2.9	0.05	no
Mg_1	0.6	0.8	0.14	yes
Mg_2	0.5	0.5	0.06	yes
$\mathrm{Mg}\,b$	0.6	0.6	0.06	yes
Fe5270	0.6	0.6	0.09	yes
Fe5335	0.6	0.6	0.09	yes
Fe5406	0.6	0.6	0.11	yes
Fe5709	0.8	0.8	0.15	no
Fe5782	1.2	2.2	0.14	no
NaD	4.1	6.5	0.05	no
TiO_1	0.9	0.9	0.59	no
TiO_2	0.7	0.9	0.63	no

[a]Sensitive to other element ratios beyond $[\alpha/\mathrm{Fe}]$, see text for details.

abundance is additionally enhanced in galactic globular clusters (comprehensive discussion given in Chapter 4). A proper fit to the data including the variation of various other element abundance ratios is presented in Chapter 4.

Therefore, we deem an index badly calibrated if the model prediction for $[\alpha/\mathrm{Fe}] = 0.3$ dex deviates significantly from the globular cluster data ($chi^2 \geq 1.5$ in either Columns 2 or 3 in Table 3.2), if the median observational relative error in the globular cluster sample exceeds 0.15 (Column 4 in Table 3.2), and if the index is not sensitive to other element ratios beyond the α/Fe ratio (see Fig. 4.1). The result of this selection process is summarised in Column 5 of Table 3.2.

Finally, it is interesting to note that model errors are generally very small and well below the observational errors around solar metallicity. Errors rise considerably and become comparable to the typical observational error toward the highest and lowest metal-

licities. This behaviour ought to be expected and is a direct consequence of the empirical stellar library, in which the stellar parameter space is inevitably sampled worse at the ends of the distribution. This is well consistent with a recent conclusion of Vazdekis et al. (2010) who show that the stellar population model quality decreases toward the edges of parameter space.

Balmer line indices

Fig. 3.2 confirms previous results that the Balmer line indices are generally quite sensitive to α/Fe ratio variations. Absorption-line strengths of the higher-order Balmer lines H$\delta_{\rm A}$, H$\delta_{\rm F}$, and H$\gamma_{\rm A}$ increase considerably with increasing α/Fe at super-solar metallicities. This is critical for the derivation of galaxy ages (Thomas et al., 2004; Thomas & Davies, 2006). As discussed in Thomas et al. (2004) and Korn et al. (2005) this is caused by prominent Fe absorption in the pseudo-continuum windows of the index definition. The indices H$\gamma_{\rm F}$ and Hβ, instead, are only very little sensitive to α/Fe.

The globular cluster data seems generally well reproduced by the model for all Balmer line indices. In particular the trend of increasing Balmer line strength with decreasing metallicity is well matched. In more detail, however, it can be seen that globular clusters at higher metallicities are below the models for the indices H$\delta_{\rm F}$ and, most prominently, Hβ. The χ^2 values quoted in Table 3.2 confirm this conclusion. Other recent models in the literature show the same pattern (Schiavon, 2007; Lee et al., 2009b; Cervantes & Vazdekis, 2009; Vazdekis et al., 2010; Poole et al., 2010), which has therefore been called 'Hβ anomaly' by Poole et al. (2010). Fig. 3.2 shows that this anomaly may extend to the other Balmer lines, at least H$\delta_{\rm F}$, while the other higher-order Balmer line indices seem not to be affected. The location of the index measurements for SDSS galaxies is well covered by the models. Younger ages would need to be considered, of course, to match objects with stronger Balmer line indices.

The TMB/K model is shown by the dotted lines. Offsets between Lick and flux-calibrated systems are clearly small, as the predictions from the new model are almost identical to TMB/K. The significantly lower Balmer line strengths at low metallicities come partly from lower index values in the fitting functions for hot giant stars (see Section 2.4) and partly from a re-adjustment of the mass loss parameter η such that the globular cluster data are matched. The efficiency of mass loss along the Red Giant Branch evolution is expected to decrease with deceasing metallicity (e.g. Renzini & Voli, 1981). To minimise the problem of the Balmer anomaly, we had to set $\eta = 0$ at the lowest two metallicities. Note that the Horizontal Branch morphology is still not completely red, because the metallicity is so low that the Horizontal Branch track has naturally a high

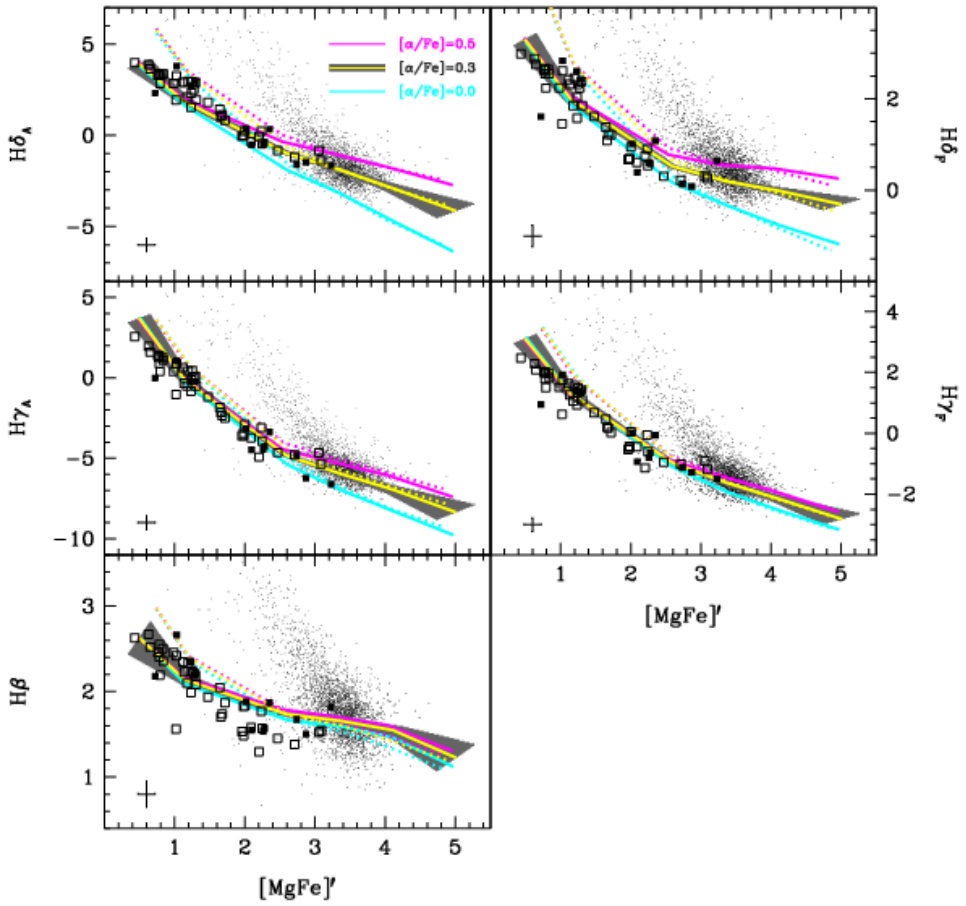

Figure 3.2: Calibration of the Balmer line indices. Three models at Lick spectral resolution with an age of 13 Gyr, the metallicities $[Z/\mathrm{H}] = -2.25, -1.35, -0.33, 0.0, 0.35, 0.67$ dex, and $[\alpha/\mathrm{Fe}] = 0.0, 0.3, 0.5$ dex are shown as solid magenta, yellow, and cyan lines, respectively. Each line is a model at fixed age and α/Fe ratio with total metallicity increasing from left to right. The grey shaded area along the model with $[\alpha/\mathrm{Fe}] = 0.3$ dex (yellow line) indicates the 1-σ error of the model prediction. Dotted lines are the original TMB/K model that is inherent to the Lick/IDS system. Galactic globular clusters from Puzia et al. (2002) and Schiavon et al. (2005) are filled and open squares, respectively. The typical errors in the globular cluster index measurements are given the error symbol at the bottom of each panel. The small black dots are early-type galaxies from the MOSES catalogue (see Section 5.2) including only high signal-to-noise spectra with $S/N > 40$.

enough effective temperature such that a non-negligible amount of fuel is spent blue-wards of the RR Lyrae strip even without mass loss (Fig. 11 in M05).

Indices that correlate with α/Fe

Fig. 3.3 presents the calibration of the indices whose strengths increase with an increase of the α/Fe ratio, i.e. CN_1, CN_2, Ca4227, G4300, Mg_1, Mg_2, and $\mathrm{Mg}\,b$. Note that most of this correlation with α/Fe is actually caused by an anti-correlation with Fe abundance

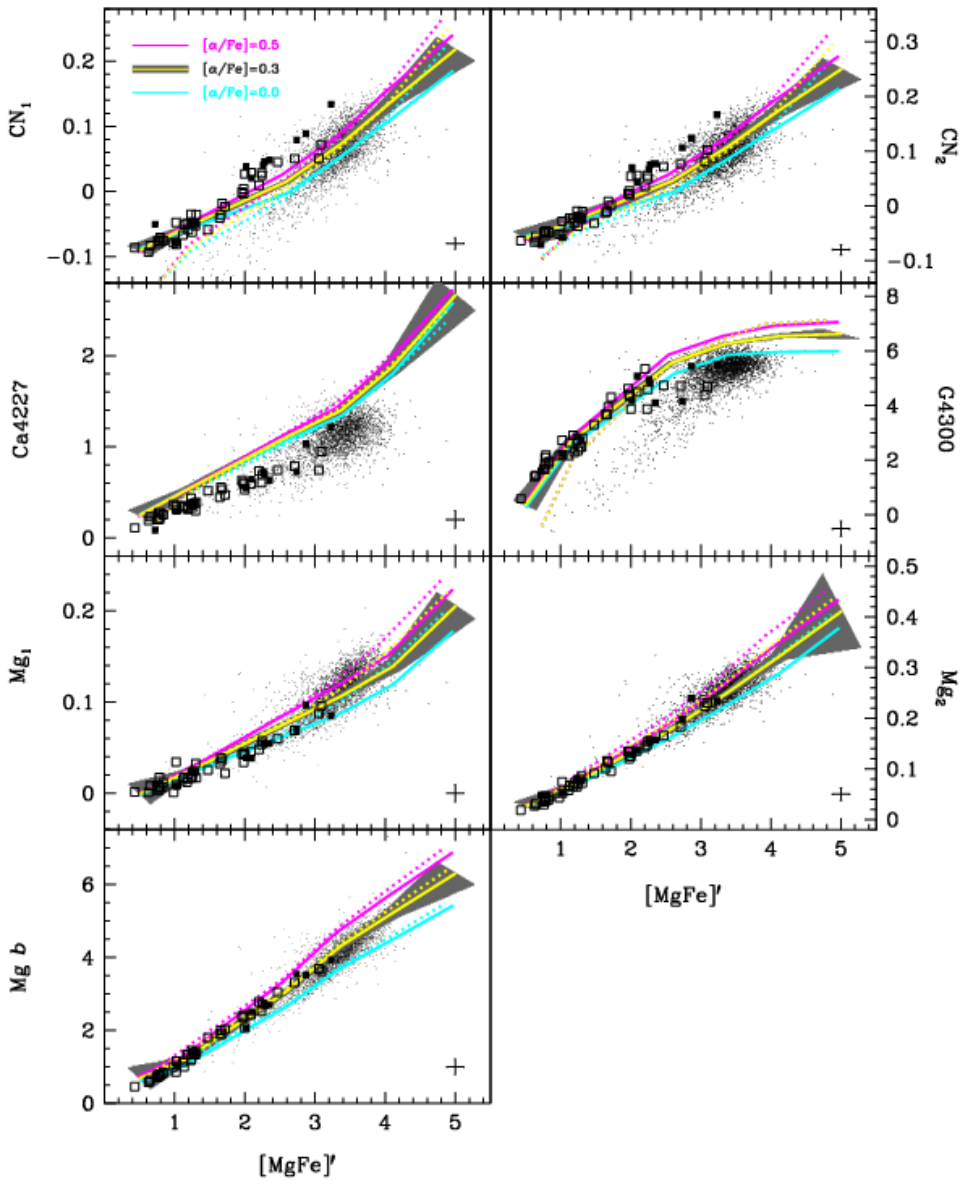

Figure 3.3: Calibration of the indices that correlate with α/Fe. Symbols, model-grids and colour-coding are the same as in Fig. 3.2.

(Thomas et al., 2003a). The index that is most sensitive to the α/Fe ratio is Mg b. Globular cluster data are very well matched for G4300, Mg_2, and Mg b. The models are well off, instead, for the indices CN_1, CN_2, Ca4227 as confirmed by the high χ^2 values in Table 3.2. Mg_1 appears to be slightly below the model, but the observational error is large enough to keep the χ^2 low. This is caused by the variation of further chemical elements these indices are sensitive to. As already discussed in Thomas et al. (2003a), the stronger CN indices in the globular cluster data indicate an enhancement of nitrogen, while the weaker indices Ca4227 and Mg_1 can be explained by a depression of calcium and carbon.

In Chapter 4 we present the full analysis of these element abundance variations and show that the globular cluster data can be recovered very well.

It can further be seen that SDSS galaxies are on line with with globular clusters as far as the enhancement of the α/Fe ratio is concerned, but may well have different chemical mixtures regarding other elements like carbon, nitrogen, or calcium. A full chemical analysis of SDSS galaxies is the subject of Chapter 5.

Finally, the TMB/K model (dotted lines) is quite consistent with our new, flux-calibrated model for the indices Ca4227, G4300, and $\mathrm{Mg}\,b$. Deviations are significant, instead, for CN_1, CN_2, Mg_1, and Mg_2, even though the fitting functions used in TMB/K and in this work are consistent for these indices and do not explain this offset (see Section 2.4). The most likely cause for deviations is the fact that these indices have their pseudo-continuum windows placed relatively far from the actual index bandpass, so that variations of the shape of the stellar continuum play a larger role.

Indices that anti-correlate with α/Fe

Fig. 3.4 presents the calibration of the indices whose strengths decrease with an increase of the α/Fe ratio, i.e. all Fe indices Fe4383, Fe4531, Fe5015, Fe5270, Fe5335, Fe5406, Fe5709, and Fe5782. Clearly, the anti-correlation with α/Fe comes from the response to the depression of Fe abundance. The indices most sensitive to α/Fe are Fe4383, Fe5335, and Fe5406. The globular cluster data are reproduced well for indices Fe4383, Fe4531, Fe 5270, Fe5335, and Fe5406 as also indicated by the low χ^2 in Table 3.2. The models are clearly off the data for Fe5015 and Fe5782, which is further supported by the high χ^2 values. Fe5709 has a low χ^2 in spite of a bad match, which is caused by the relatively large measurement errors on this index (see Table 3.2). For the badly calibrated indices, is not clear at this point whether the problem lies in the model or the globular cluster data, but it is certainly advisable not to use these two indices in an analysis of absorption line spectra.

Most model predictions are consistent with the TMB/K model. The new model predicts lower index strengths at high metallicities for the indices Fe4383, Fe4531, and Fe5015, which is almost entirely caused by the offset between the Lick and the flux-calibrated systems.

Indices insensitive to α/Fe

Finally, the indices that are not sensitive to α/Fe ratio variations are shown in Fig. 3.5 . These are Ca4455, $\mathrm{C}_2$4668, NaD, TiO_1, and TiO_2. The three reddest indices are clearly not well calibrated as has already been concluded in Thomas et al. (2003a), and we cannot recommend these features for the analysis of absorption line spectra. Again, the

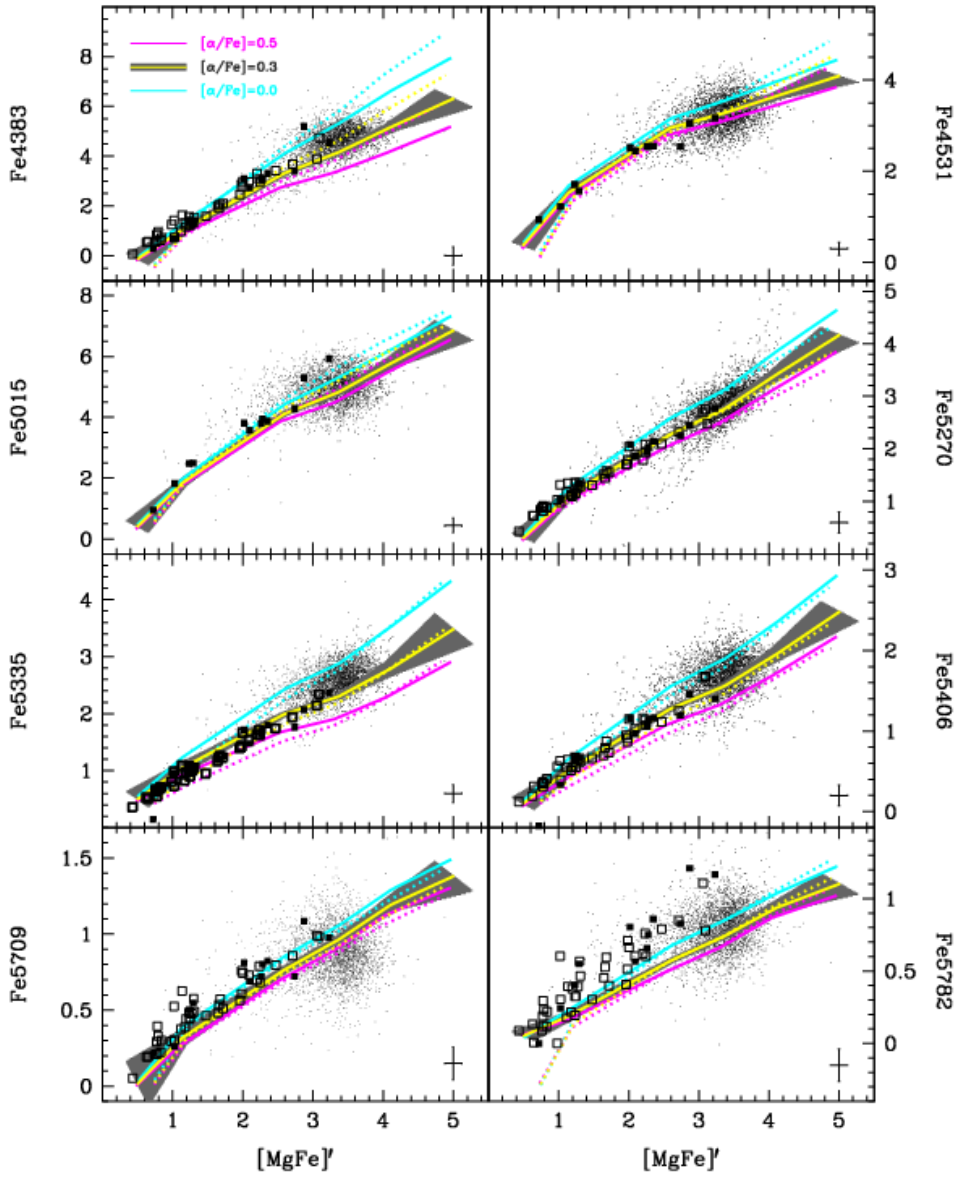

Figure 3.4: Calibration of the indices that anti-correlate with α/Fe. Symbols, model-grids and colour-coding are the same as in Fig. 3.2.

relatively large observational errors in the TiO index measurements lead to low χ^2 values despite the clear offset between models and observations (see Table 3.2). NaD is notoriously difficult because it is affected by interstellar absorption, so that the observational measurement becomes meaningless. The same difficulty seems to apply to TiO_1, in which case the interstellar Na absorption affects the blue pseudo-continuum window and leads to weaker index measurements. Note also that the scatter in the Schiavon (2007) cluster measurements is unusually large for all three indices, which further hampers a meaningful model calibration. It is less clear, though, why the model fails for TiO_2.

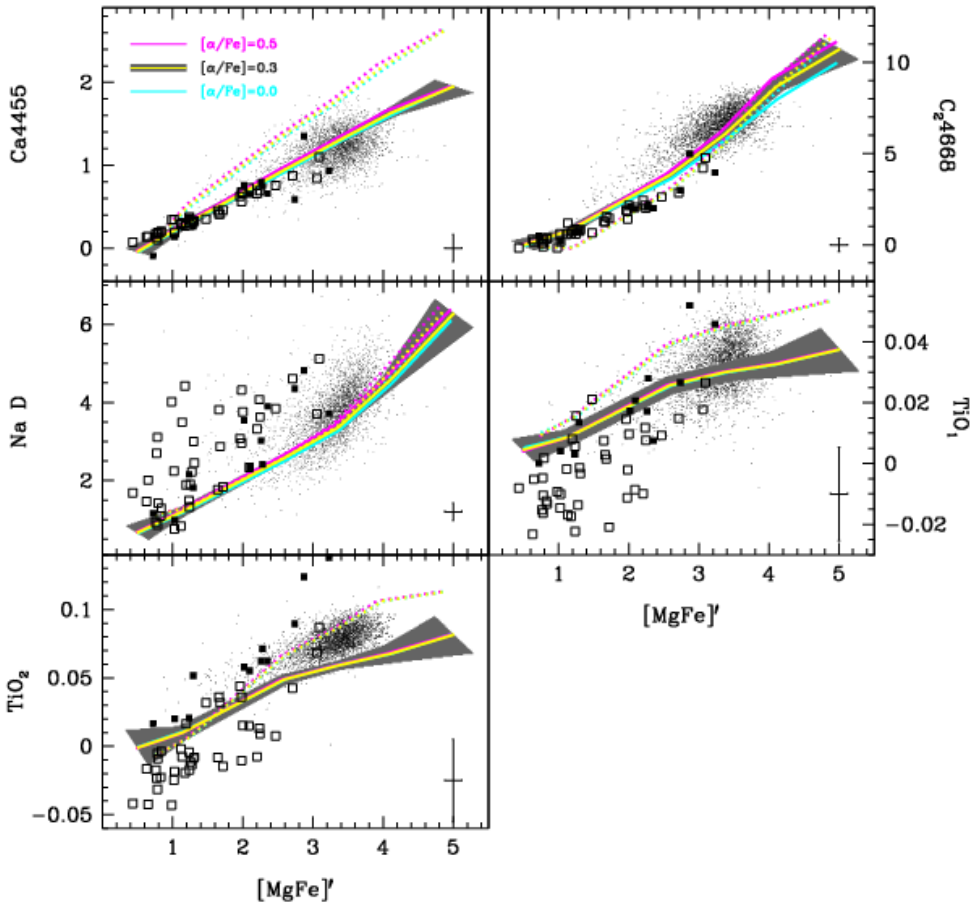

Figure 3.5: Calibration of the indices that are insensitive to α/Fe. Symbols, model-grids and colour-coding are the same as in Fig. 3.2.

Ca4455 is reasonably well calibrated. Most notably, the calibration has improved significantly. The TMB/K model seemed to fail in reproducing observations, most likely because of a wrong Lick calibration of the Puzia et al. (2002) data as discussed already in Maraston et al. (2003) and Thomas et al. (2003a). This problem has been solved now with our new flux-calibrated models. Still, we exclude Ca4455 from the recommended set of indices because of its relatively large measurement error (see Table 3.2). $C_2$4668 is offset as supported by the enhanced χ^2 in Table 3.2. This particular index is sensitive to C abundance, though, so the mismatch might well be an abundance ratio effect.

3.4.2 Models with Padova tracks and literature comparison

In this section we compare the models based on the Cassisi tracks with our second set of models based on the Padova stellar evolutionary tracks at high metallicities ($[Z/\mathrm{H}] \geq -0.33$ dex) and with the models of Schiavon (2007). As far as we are aware, the latter is the only other model in the current literature that includes variable element ratios and

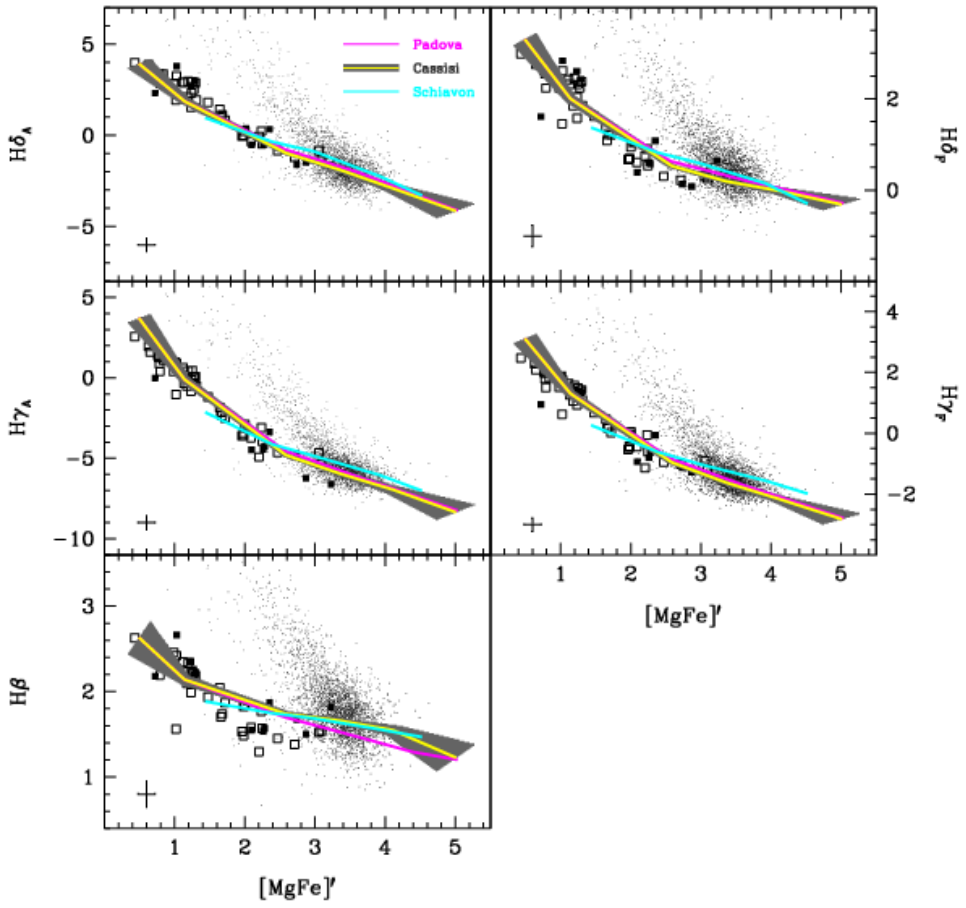

Figure 3.6: Calibration of Balmer line indices, equivalent to Fig. 3.2. Three models at Lick spectral resolution with an age of 13 , the metallicities $[Z/\mathrm{H}] = -2.25,\ -1.35,\ -0.33,\ 0.0,\ 0.35,\ 0.67$ dex, and $[\alpha/\mathrm{Fe}] = 0.3$ dex are shown. The yellow lines are the same model as in Fig. 3.2 based on the Cassisi stellar evolutionary tracks.The grey shaded area along the model indicates the 1-σ error of the model prediction. The magenta lines are the model based on Padova tracks at $[Z/\mathrm{H}] \geq -0.33$ dex. The cyan lines are the model by Schiavon (2007). Each line is a model at fixed age and α/Fe ratio with total metallicity increasing from left to right. Galactic globular clusters from Puzia et al. (2002) and Schiavon et al. (2005) are filled and open squares, respectively. The typical errors in the globular cluster index measurements are shown as the error symbol at the bottom of each panel. The small black dots are early-type galaxies from the MOSES catalogue (see Section 5.2) including only high signal-to-noise spectra with $S/N > 40$.

is flux-calibrated hence not tied to the Lick/IDS system. The figures showing this comparison equivalent to Figs. 3.2, 3.3, 3.4, and 3.5 are Figs. 3.6, 3.7, 3.8, and 3.9. The plots show again three models at Lick spectral resolution with an age of 13 Gyr, all six metallicities, and $\alpha/\mathrm{Fe} = 0.3$ dex. The yellow lines are the same model as in Fig. 3.2 based on the Cassisi stellar evolutionary tracks. The magenta lines are the model based on Padova tracks at high metallicities, and the cyan lines are the model of Schiavon (2007).

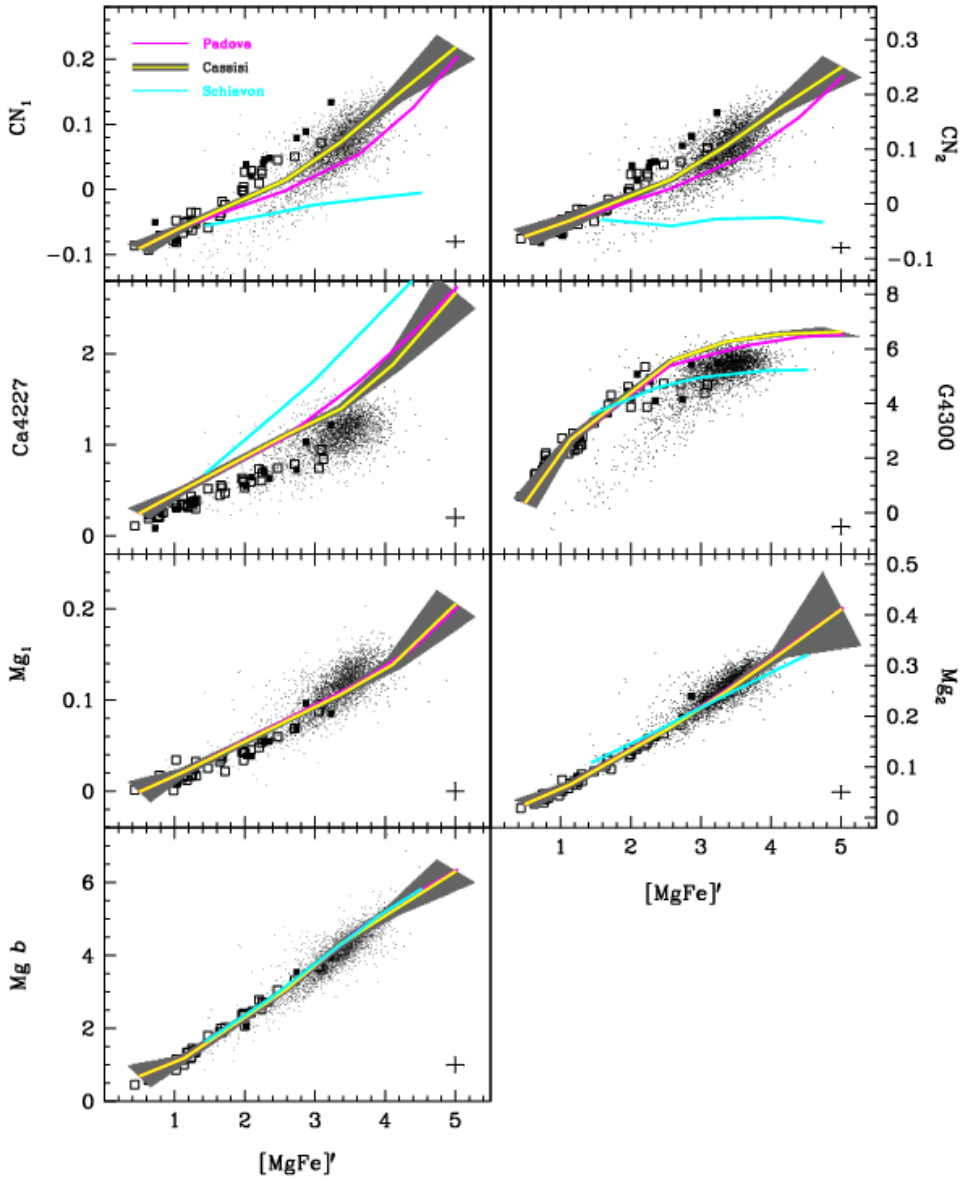

Figure 3.7: Comparison of the indices that correlate with α/Fe, equivalent to Fig. 3.3. Symbols, model-grids and colour-coding are the same as in Fig. 3.6.

There is good agreement between our model and the model by Schiavon (2007) for the indices Mg_2, $\mathrm{Mg}\,b$, Fe5015, Fe5270, and Fe5335. The higher-order Balmer line strengths tend to be somewhat higher in the Schiavon (2007) model at solar and super-solar metallicities. The largest discrepancies are found for CN_1, CN_2, Ca4227, G4300, Fe4383, and $\mathrm{C}_2$4668. Note that in all these cases the discrepancies are far larger than the differences between our models with different evolutionary tracks (yellow and magenta lines).

Our model produces significantly stronger CN_1 and CN_2 at all metallicities, which is better in line with the globular cluster data. Likewise, the slightly higher Fe4383 index

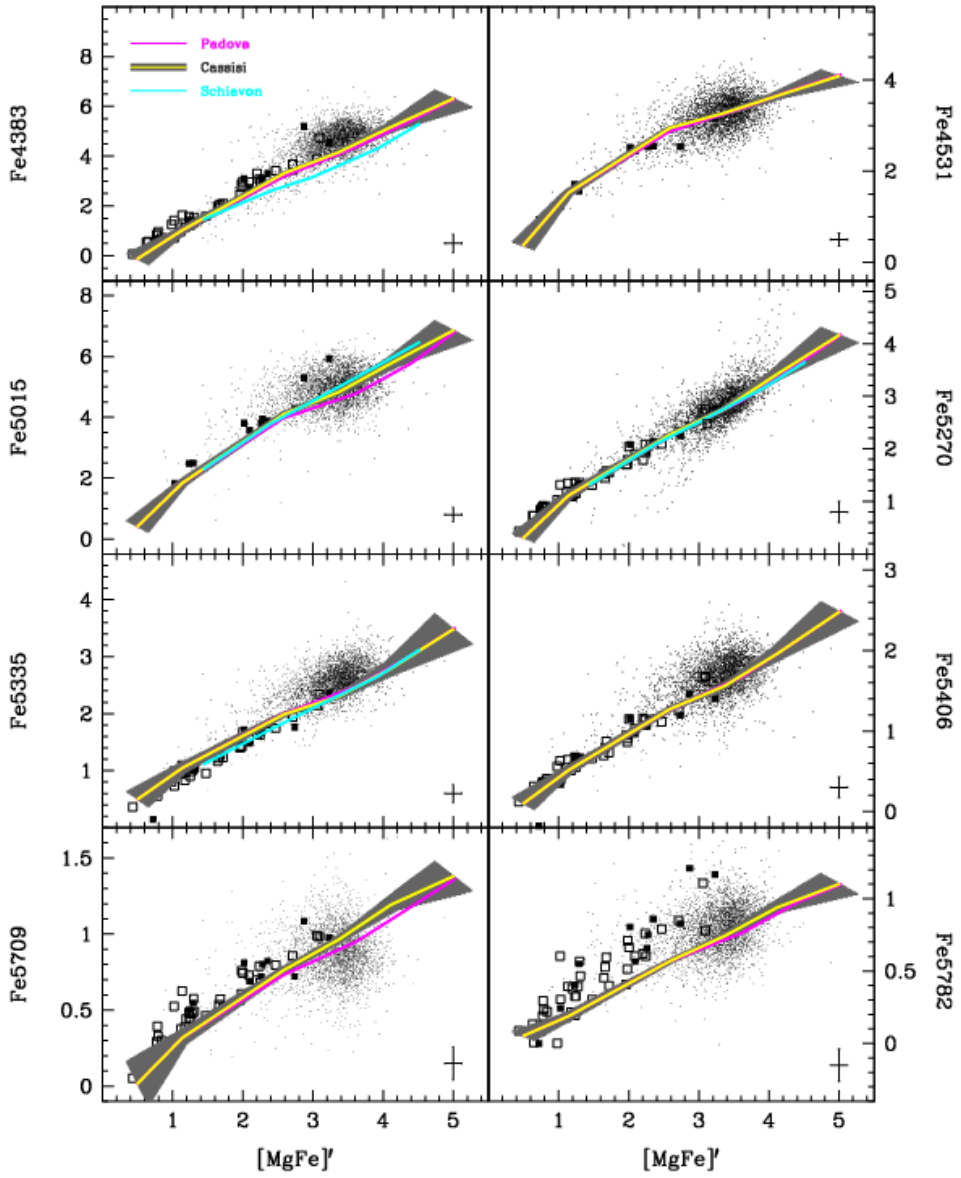

Figure 3.8: Comparison of the indices that anti-correlate with α/Fe, equivalent to Fig. 3.4. Symbols, model-grids and colour-coding are the same as in Fig. 3.6.

prediction in our model gets support from the observations. The G4300 index also is lower in the Schiavon (2007) models, but fits the data better than our model. Ca4227 is significantly stronger in Schiavon (2007). The comparison with the globular cluster data is less decisive in this case, however, as both model deviations can be corrected through a modification of Ca abundance. The Schiavon (2007) models will lead to considerably lower Ca abundances. Finally, $C_2$4668 is stronger in our models only at high metallicities, which inhibits the direct comparison with globular cluster data. The Schiavon (2007) are expected to yield larger carbon abundances for galaxies.

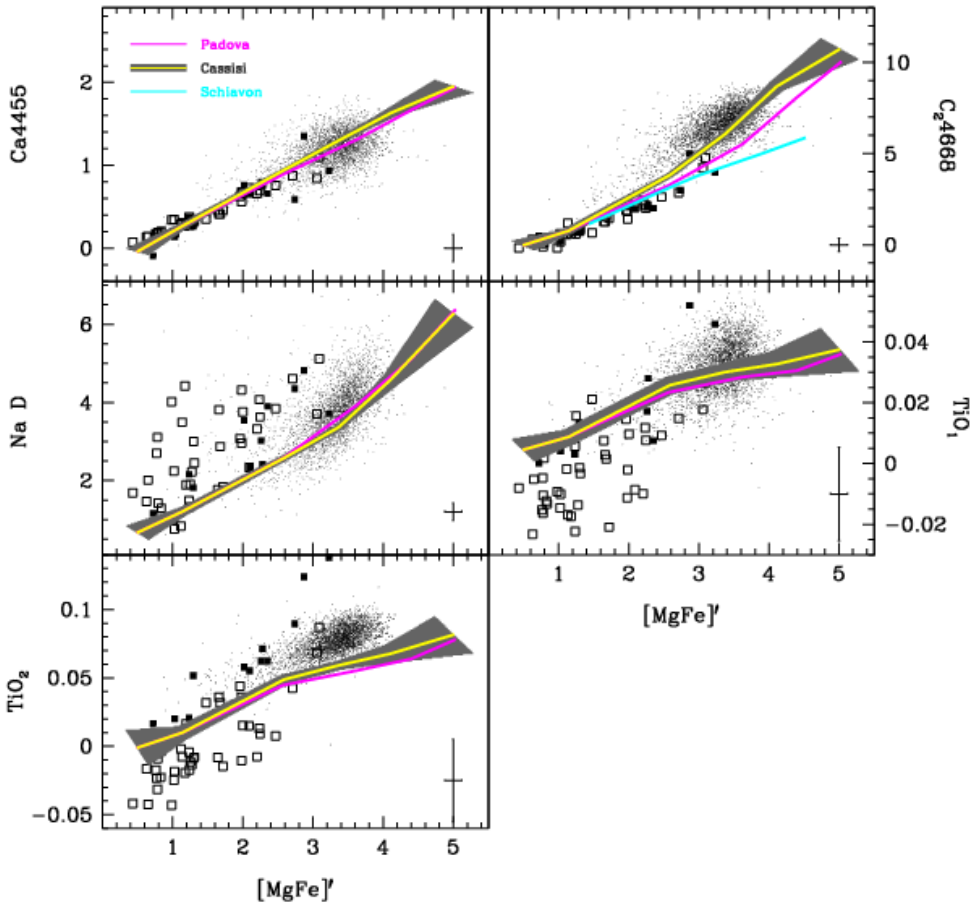

Figure 3.9: Comparison of the indices that are insensitive to α/Fe, equivalent to Fig. 3.5. Symbols, model-grids and colour-coding are the same as in Fig. 3.6.

Our model based on Padova tracks (magenta lines) is consistent with the base model for the majority of the indices. The cases for which the discrepancy significantly exceeds the model error (grey shaded area) are Hβ, CN_1, CN_2, and $C_2$4668. Small deviations are found for Ca4227, G4300, Ca4455, Fe5015, Fe5709. In all cases, equally for the Balmer and the metal lines, the Padova based models produce lower index strengths. This effects kicks in at super-solar metallicities, however, where no globular cluster data is available for calibration.

3.4.3 Comparison with galaxy data

We therefore turn to consider galaxy data for a more detailed comparison between our models sets with Cassisi and Padova tracks. We use the recently published index gradient data from SAURON (Kuntschner et al., 2006, 2010). This data provides high signal-to-noise measurements of the absorption-line indices Hβ, Fe5015, and Mg b. Most critically for the comparison with our new models is that this data has been carefully flux

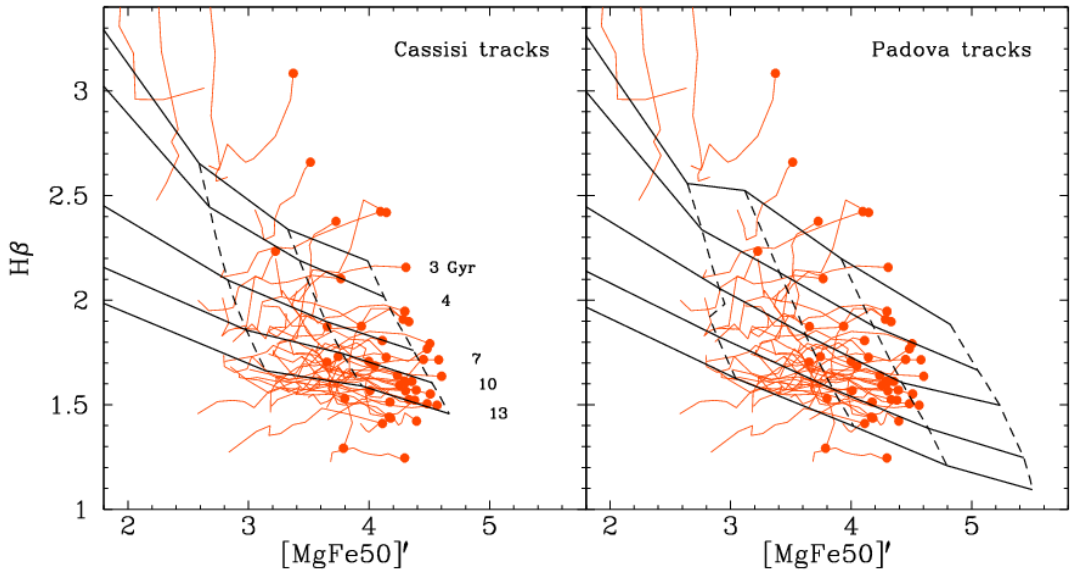

Figure 3.10: Remake of Fig. 3 in Kuntschner et al. (2010). Hβ is plotted as a function of [MgFe50]′ (Kuntschner et al., 2010). The SAURON central galaxy data are the circles with the tails indicating the index gradients to larger radii. Stellar population models are over-plotted for various ages and metallicities at fixed solar α/Fe. Models based on Cassisi and Padova tracks are shown in the left-hand and right-hand panels, respectively. The age of the oldest model track is 13 Gyr. Different from Fig. 3 in Kuntschner et al. (2010) this plot compares observational and model data in flux-calibrated space independently of Lick offsets. Note that the Padova tracks reach higher metallicities (vertical lines) than the Cassisi tracks, i.e. up to [Z/H]=0.67 dex compared to [Z/H]=0.35 dex for the Cassisi tracks.

calibrated. Fig. 3.10 is a remake of Fig. 3 in Kuntschner et al. (2010) plotting Hβ as a function of [MgFe50]′. This latter index has been defined in Kuntschner et al. (2010) in the style of $[\mathrm{MgFe}]'$ combining $\mathrm{Mg}\,b$ with Fe5015 rather than Fe5270 and Fe5335 because of the restricted wavelength range sampled in SAURON observations.

$$[\mathrm{MgFe50}]' \equiv \frac{0.69 \times \mathrm{Mg}\,b + \mathrm{Fe5015}}{2} \tag{3.7}$$

The stellar population model grid is shown for various ages and metallicities (at solar α/Fe) on top of the galaxy data. Models based on Cassisi and Padova tracks are shown in the left-hand and right-hand panels, respectively. The age of the oldest model track is 13 Gyr. Unlike Fig. 3 in Kuntschner et al. (2010) this plot compares observational and model data in flux-calibrated space independently of Lick offsets. We confirm the conclusion by Kuntschner et al. (2010) that observations at all galaxy radii are reasonably well covered by the models. While globular cluster data do not allow for the calibration at these high metallicities, the galaxy data clearly suggests that the model based on Padova tracks performs better. This applies to Hβ mainly and further investigations are hampered

by the narrow wavelength coverage of the SAURON spectra. Note that the oldest model track plotted is 13 Gyr, hence well within the age of the universe (Komatsu et al., 2011).

We conclude that galaxy data do not confirm the existence of an Hβ anomaly indicated by globular cluster data (Poole et al., 2010). This indicates that the cause for the Balmer anomaly in globular clusters is more likely to be found in the observational measurement. The origin of the problem could be a failure of the observations to sample all evolutionary phases properly (Maraston et al., 2003). Fig. 3.10 suggests that here is no problem with galaxy age-dating through the Hβ index, instead.

3.5 Conclusions

We present new stellar population models of absorption-line indices with variable element abundance ratios. The model is an extension of the TMB/K model, which is based on the evolutionary stellar population synthesis code of Maraston (1998, 2005). The new models are based on our new calibrations of absorption-line indices with stellar parameters derived from the MILES stellar library presented in Chapter 2. The MILES library consists of 985 stars selected to produce a sample with extensive stellar parameter coverage. The MILES library was also chosen because it has been carefully flux-calibrated, making standard star-derived offsets unnecessary.

The key novelty compared to the previous models is that they are flux-calibrated, hence not tied anymore to the Lick/IDS system. This is essential for the interpretation of galaxy spectra where calibration stars are not available, such as large galaxy redshift surveys like SDSS or other high-redshift observations (Zielger et al., 2005; Bernardi et al., 2006; Kelson et al., 2006; Sánchez-Blázquez et al., 2009; Thomas et al., 2010; Carson & Nichol, 2010). A further new feature is that model predictions are provided for both the original Lick and the higher MILES spectral resolutions. Note that the latter turns out to be comparable to the SDSS resolution, so that our new high-resolution models can be applied to SDSS data without any corrections for instrumental spectral resolution.

The construction of the model through fitting functions allows us to make a straightforward assessment of the statistical errors on each individual index prediction. Hence as a further novelty we calculate errors in the model predictions through Monte Carlo simulations, which are provided in a separate table in the model data release. It turns out that the model errors are generally very small and well below the observational errors around solar metallicity. Errors rise considerably and become comparable to or may exceed the typical observational error toward the highest and lowest metallicities. This behaviour ought to be expected and is a direct consequence of the empirical stellar library, in which stellar parameter space is inevitably sampled worse at the ends of the distribution.

The data release now provides models with two different stellar evolutionary tracks by Cassisi (used in TMB/K) and Padova at high metallicities. The model based on Padova tracks is consistent with the base model for the majority of indices. The cases of indices for which the discrepancy exceeds the model error significantly are $\mathrm{H}\beta$, CN_1, CN_2, and $\mathrm{C}_2$4668. Small deviations are found for Ca4227, G4300, Ca4455, Fe5015, and Fe5709. In all cases, equally for the Balmer and the metal lines, the Padova based models produce lower index strengths.

Finally, as the last novelty of this model, we compute additional models with enhancement of each of the elements C, N, Na, Mg, Si, Ca, Ti, and Cr separately by 0.3 dex.

We calibrate the base model for the parameters age, total metallicity and α/Fe ratio with galactic globular cluster and galaxy gradient data. Key is that independent estimates of ages, metallicities, and element abundance ratios are available for the globular clusters of the Milky Way from deep photometry and stellar high-resolution spectroscopy. The globular cluster samples considered here are from Puzia et al. (2002) and Schiavon et al. (2005). For both samples we measure line strengths of all 25 Lick absorption-line indices directly on the globular cluster spectra (see Chapter 4). Both globular cluster samples have been flux calibrated, so that no further offsets need to be applied for the comparison with the models presented here.

The globular cluster data is well reproduced by the model for all Balmer line indices. In particular the trend of increasing Balmer line strength with decreasing metallicity is well matched. We confirm previous findings of a mild $\mathrm{H}\beta$ anomaly with models generally predicting too strong $\mathrm{H}\beta$ indices at intermediate metallicities. We show that a similar problem, even though slightly less severe, exists for $\mathrm{H}\delta_\mathrm{F}$. The problem is not replicated, however, in the comparison with galaxy data at similar metallicities from Kuntschner et al. (2010). A good match with globular cluster data is seen for the α/Fe sensitive, metallic indices G4300, Mg_2, and $\mathrm{Mg}\,b$. The models are well off, instead, for the indices CN_1, CN_2, Ca4227, $\mathrm{C}_2$4668, and Mg_1, which is caused by the variation of further chemical elements these indices are sensitive to. We present the full analysis of these element abundance variations in Chapter 4 and show that also these indices can be recovered very well. The Fe indices Fe4383, Fe4531, Fe5270, Fe5406 are well reproduced by the new model, while Fe5015/Fe5335 are slightly too weak/strong in the model. Offsets are largest for the two reddest Fe indices Fe5709 and Fe5782 that clearly cannot be regarded well calibrated (see also TMB/K). Finally, the indices Ca4455, NaD, TiO_1, and TiO_2 are not sensitive to α/Fe ratio variations and are not well calibrated (see also Thomas et al., 2003a).

To summarise, the set of indices that turns out to be most useful for element abundance ratio studies includes the Balmer line indices $\mathrm{H}\delta_\mathrm{A}$, $\mathrm{H}\gamma_\mathrm{A}$, and $\mathrm{H}\gamma_\mathrm{F}$, the metallic indices CN_1, CN_2, Ca4227, G4300, $\mathrm{C}_2$4668, Mg_1, Mg_2, $\mathrm{Mg}\,b$, and the Fe indices Fe4383,

Fe4531, Fe5270, Fe5335, and Fe5406. We will use these indices to derive element abundance ratios for the globular cluster data in Chapter 4.

Chapter 4

Chemical abundance ratios of galactic globular clusters from modelling integrated light spectroscopy

In Chapter 3 we present new, flux-calibrated stellar population models of Lick absorption-line indices with variable element abundance ratios. The model includes a large variety of individual element variations, which allows the derivation of the abundances for the elements C, N, O, Mg, Ca, Ti, and Fe besides total metallicity and age. We use this model to develop a method for deriving the element abundance ratios [O/Fe] (inferred from [α/Fe]), [C/Fe], [N/Fe], [Mg/Fe], [Ca/Fe] and for the first time (for unresolved stellar populations) [Ti/Fe], and apply it to the integrated light spectroscopy of galactic globular clusters. We show that the model fits to a number of indices improve considerably when various variable element ratios are considered. The ages we derive agree well with the literature and are all consistent with the age of the universe within the measurement errors. There is a considerable scatter in the ages, though, and we overestimate the ages preferentially for the metal-rich globular clusters. Our derived total metallicities agree generally very well with literature values on the Zinn & West (1984) scale once corrected for α-enhancement, in particular for those cluster where the ages agree with the CMD ages. We tend to slightly underestimate the metallicity for those clusters where we overestimate the age, in line with the age-metallicity degeneracy. It turns out that the derivation of individual element abundance ratios is not reliable at an iron abundance $[\mathrm{Fe/H}] < -1$ dex where line strengths become weaker, while the [α/Fe] ratio is robust at all metallicities. The discussion of individual element ratios focuses therefore on globular clusters with $[\mathrm{Fe/H}] > -1$ dex. We find general enhancement of light and α elements, as expected, with significant variations for some elements. The elements O and Mg follow the same general enhancement with almost identical distributions of

[O/Fe] and [Mg/Fe]. We obtain slightly lower [C/Fe] and very high [N/Fe] ratios, instead. This chemical anomaly, commonly attributed to self-enrichment, is well known in globular clusters from individual stellar spectroscopy. It is the first time that this pattern is obtained also from the integrated light. The α elements follow a pattern such that the heavier elements Ca and Ti are less enhanced. More specifically, the [Ca/Fe] and [Ti/Fe] ratios are lower than [O/Fe] and [Mg/Fe] by about 0.2 dex. Most interestingly this trend of element abundance with atomic number is also seen in recent determinations of element abundances in globular cluster and field stars of the Milky Way. This suggests that SN Ia contribute significantly to the enrichment of the heavier α elements as predicted by nucleosynthesis calculations and galactic chemical evolution models.

4.1 Background

The abundances of a large variety of chemical elements can be derived from high-resolution spectroscopy of individual stars in the field and globular clusters of the Milky Way as well as nearby dwarf galaxies in the Local Group (e.g., McWilliam, 1997; Carretta et al., 2005; Pritzl et al., 2005; Tolstoy et al., 2009; Bensby et al., 2010). This level of detail cannot be achieved for most galaxies and extra-galactic globular clusters, because the individual stars are not resolved. Observations have to resort to integrated light spectroscopy, which is applicable to unresolved stellar populations. It allows us to study element abundances in distant galaxies and globular clusters, but is naturally more limited. Nearby globular clusters are the interface between these two extremes. They allow detailed chemical analyses from resolved stellar spectroscopy as well as the study of their integrated light. They are therefore vital for the calibration of stellar population models and integrated light analyses.

In Chapter 3 we have updated the TMB/K models that are now flux calibrated thanks to the use of the newly computed index calibrations from Chapter 2 based on the flux-calibrated stellar library MILES. The Korn et al. (2005) model atmosphere calculations provide index response functions for the variation of the ten elements C, N, O, Mg, Na, Si, Ca, Ti, Fe, and Cr. Through additional features in the same part of the spectrum and modifications of the index definitions even more elements may be accessible (Serven et al., 2005; Lee et al., 2009b). Here we focus on those elements that can be best derived from the 25 Lick indices considered in our models. These are C, N, Mg, Ca, Ti, and Fe besides total metallicity Z/H, age, and α/Fe ratio.

Thomas et al. (2003a) derived abundances of nitrogen and calcium for globular clusters and galaxies. Through a simple approach they could show that galactic globular clusters must be significantly enhanced in nitrogen at fixed carbon abundance in order

to reproduce the observed CN indices. Thomas et al. (2003b) instead derive calcium abundances of galaxies. Subsequent work has developed this further. Clemens et al. (2006) add C abundances in their study of SDSS galaxies, and Kelson et al. (2006) derive N abundances of distant galaxies. Graves & Schiavon (2008) and Smith et al. (2009) present the first full analyses of the abundances of C, N, Mg, Ca, and Fe in galaxies. In this chapter we conduct the next step by adding the element titanium and derive the element abundance ratios [C/Fe], [N/Fe], [O/Fe], [Mg/Fe], [Ca/Fe], and [Ti/Fe] for galactic globular clusters.

This chapter is organised as follows. In Section 4.2 we describe the globular cluster data used. In Section 4.3 we introduce our method to derive element ratios. The main analysis is presented in Section 4.4. The results are discussed in Section 4.5, and the chapter concludes with Section 4.6.

4.2 Globular cluster data

In Chapter 3 we compare the model predictions with observational data of galactic globular clusters, as the latter are the closest analogues of simple stellar populations in the real universe (Maraston et al., 2003). Key is that independent estimates of ages, metallicities, and element abundance ratios are available for the globular clusters of the Milky Way from deep photometry and high-resolution stellar spectroscopy.

The globular cluster samples are from Puzia et al. (2002, hereafter P02) and Schiavon et al. (2005, hereafter S05). Critical for the integrated light spectroscopy is a representative sampling of the underlying stellar population (Renzini, 1998; Maraston, 1998). To ensure this P02 obtained several spectra with slightly offset pointings. In general three long-slit spectra were taken for each of the target clusters, and the observing pattern was optimized to obtain one spectrum of the nuclear region and spectra of adjacent fields. Exposure times were adjusted according to the surface brightness of each globular cluster to reach a statistically secure luminosity sampling of the underlying stellar population. S05, instead, obtained each observation by drifting the spectrograph slit across the core diameter of the cluster. The telescope was positioned so as to offset the slit from the cluster center by one core radius. A suitable trail rate was chosen to allow the slit to drift across the cluster core diameter during the typically 15 minute long exposure.

We do not use the indices tabulated in P02 directly, because these measurements have been calibrated onto the Lick/IDS system by correcting for Lick offsets. S05 do not provide line index measurements. Hence we measure line strengths of all 25 Lick absorption-line indices for both samples directly on the globular cluster spectra using the

definitions by Trager et al. (1998). Both globular cluster samples have been flux calibrated, so that no further offsets need to be applied for the comparison with our models. We have smoothed the spectra to Lick spectral resolution before the index measurement. Note that the spectral resolutions of both samples are below the resolution of the MILES library, so that we work with our models at Lick resolution.

For the P02 sample we adopt the errors quoted in their paper using the quadratic sum of the statistical (Poisson) error, the statistical error derived from slit to slit variations, and the systematic error introduced through uncertainties in the radial velocity. This information is not directly available from S05. We therefore evaluate the measurement errors in two steps. First we compute the Poisson errors from the error spectra provided through Monte Carlo simulations. Then we scale these errors with the complete errors from P02 from the overlapping globular clusters.

We add the slit-to-slit error evaluated in P02 in order to account for possible stellar population fluctuations that are not included in the statistical error. The observing strategies in both P02 and S05 have been designed to minimise such an error. Still, this effect may not negligible. The slit-to-slit variations overestimate this effect, as P02 have typically observed three slits per cluster. We regard the errors used in this study therefore as conservative estimate, and true errors are likely to be smaller.

Finally, it should be noted that the S05 spectra are corrupt around 4546 and 5050 Å, so that the indices Fe4531 and Fe5015 cannot be measured (S05). In case of multiple observations in S05 we use the spectra with the highest signal-to-noise ratio.

4.3 Method

This section describes the method developed to derive individual element ratios, which is based on the our models of absorption line indices described in Chapter 3.

4.3.1 Index responses

Fig. 4.1 shows the response of the 25 Lick indices to individual element abundance changes for a 12 Gyr, solar metallicity stellar population. The fractional index change is calculated for an enhancement of the respective element by a factor two normalised to the typical observational measurement error for MILES stars from Section 2.2.2. The scale on the x-axis in the left hand panel of Fig. 4.1 is different for each element. Hence the left-hand panel should be read vertically demonstrating the most sensitive indices for the individual elements. The scale on the x-axis is instead kept fixed for all elements in the right hand panel. This panel should then instead be read horizontally to identify easily

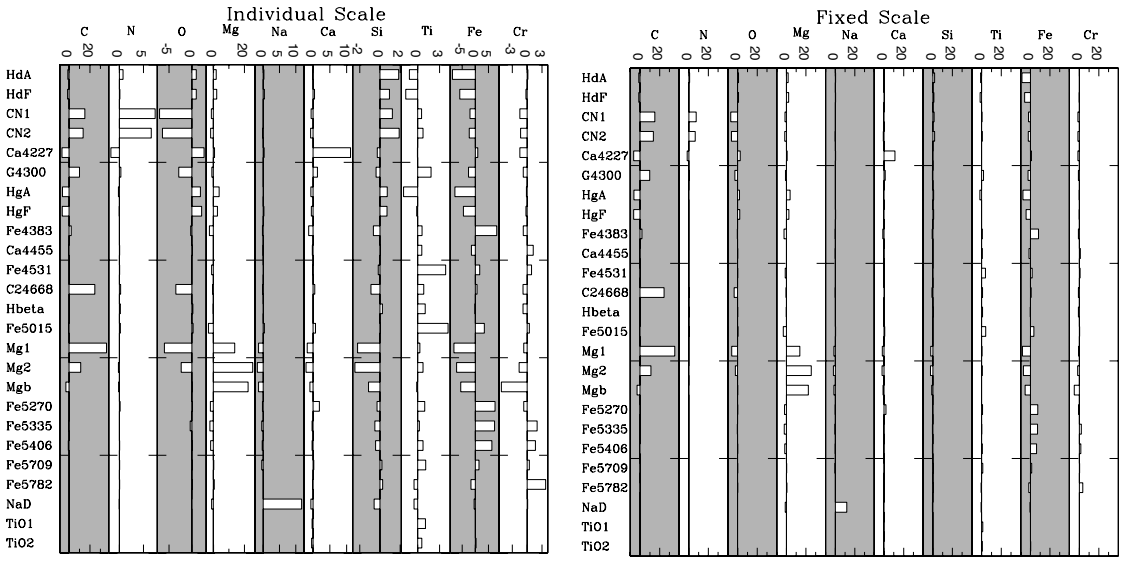

Figure 4.1: The response of the 25 Lick indices to changes in individual element abundances for a 12 Gyr solar metallicity modelled stellar population. The response is defined as the fractional index changes for enhancements of a specific element abundance by a factor two and normalised to the typical observational index errors presented in Section 2.2.2. For each element we display the index responses on an individual scale (left-hand panel) as well as those referred to a fixed scale (right-hand panel, see text for details).

those elements that are best traced by a specific index for the current set of models. It can be seen that the elements C, N, Na, Mg, Ca, Ti, and Fe are best accessible.

The abundance of nitrogen is obtained from the CN indices that are also highly sensitive to C abundance. However, this degeneracy can be easily broken through other C sensitive indices such as $C_2$4668 and Mg_1. The Mg indices Mg_1, Mg_2, and $\mathrm{Mg}\,b$ are very sensitive to Mg abundance. Note, however, that all three additionally anti-correlate with Fe abundance (Trager et al., 2000a; Thomas et al., 2003a). Ca can be measured well from Ca4227, except that this particular index is quite weak and requires good data quality. Na abundance can be derived quite easily from NaD in principle. However, in practise this is problematic as the stellar component of this absorption feature is highly contaminated by interstellar absorption, which makes this index useless and hence Na inaccessible at least for globular clusters (Thomas et al., 2003a). Iron is well sampled through the Fe indices.

There are two among the Fe indices, however, that are also sensitive to Ti abundance besides Fe. These are Fe4531 and Fe5015. They offer the opportunity to estimate also Ti abundance. We will only use Fe4531, as Fe5015 is contaminated by a non-negligible Mg sensitivity besides Fe, which weakens its usefulness for Ti abundance determinations.

The remaining three elements O, Si and Cr cannot easily be measured through the available indices. As discussed extensively in Thomas et al. (2003a), however, oxygen has a special role. O is by far the most abundant metal and clearly dominates the mass

budget of 'total metallicity'. Moreover, the α/Fe ratio is actually characterised by a depression in Fe abundance relative to all light elements (not only the α elements), hence α/Fe reflects the ratio between total metallicity to iron ratio rather than α element abundance to iron. As total metallicity is driven by oxygen abundance, the α/Fe derived can be most adequately interpreted as O/Fe ratio. We therefore re-name the parameter α/Fe to O/Fe under the assumption that this ratio provides an indirect measurement of oxygen abundance

$$[\mathrm{O/Fe}] \equiv [\alpha/\mathrm{Fe}] \; . \tag{4.1}$$

4.3.2 Element abundance ratios

As introduced in Section 3.3.4 in the TMB/K models, hence also in our new models (see Chapter 3), the total metallicity is kept fixed while varying the element abundance ratio [α/Fe]. Briefly, Fe-peak elements (Fe and Cr) are locked together (depressed group) and the rest of the elements are locked to the α-elements (enhanced group). Solar values of element ratios are known from measurements of the individual abundances (Grevesse, Noels & Sauval, 1996). A non-solar [α/Fe] ratio is computed by simultaneously changing the abundances of elements in the enhanced and depressed group to counter-balance a change of total metallicity. A non-solar [α/Fe] ratio mainly means a change in the abundances for the Fe-peak elements, since α-elements and in particular Oxygen dominate total metallicity in the Sun, as discussed in Trager et al. (2000a) and Thomas et al. (2003a).

We keep the total metallicity fixed also when we produce models with enhancements of the individual elements C, N, Mg, Ca and Ti. Starting from an [α/Fe] ratio the models are perturbed by enhancing/depressing the individual element E. Hence we actually consider elements ratios of given element over α, e.g. a N-enhanced model have varying [N/α] ratios. The [E/Fe] ratio is then calculated with [E/Fe]=[E/α]+[α/Fe], where [α/Fe] is the starting element ratio. The element E is detached from the rest of the elements in the enhanced group, while the ratio between elements in the enhanced and depressed group is locked. Thus when enhancing/depressing the individual element E the total metallicity is conserved and the abundance ratios between the rest of the elements remain unchanged. Varying [E/Fe] mainly means a change in the abundance of the element E, since the rest of the elements, locked together, dominate total metallicity.

4.3.3 Re-calculation of [Fe/H]

In addition to the parameters discussed above we derive [Fe/H]. Following Tantalo, Chiosi & Bressan (1998), Trager et al. (2000a) and Thomas et al. (2003a) we have the relationship between iron abundance [Fe/H] and total metallicity [Z/H] when only considering the element ratio [α/Fe]

$$[Fe/H] = [Z/H] + A[\alpha/Fe] = [Z/H] + A[O/Fe] \tag{4.2}$$

if we assume that α/Fe reflect O/Fe (see Section 4.3.1). Hence Eq. 4.2 remains valid if the analysis is restricted to [α/Fe] ([O/Fe]). Eq. 4.2 instead needs to be revised when considering more element ratios besides [α/Fe] ([O/Fe]). Modifying the individual element ratios with [O/Fe] as a starting point as in this work (see Section 4.3.2), perturbations to Eq. 4.2 arise in the form [E/O] for element E. We rewrite the general relationship of Eq. 4.2 to

$$[Fe/H] = [Z/H] + A[O/Fe] + \sum_x B_x[E_x/O] \tag{4.3}$$

for x number of individual elements E_x with corresponding coefficients B_x. Changing an individual element abundance while keeping total metallicity and the ratio between the rest of the elements fixed, Eq. 4.3 becomes

$$\Delta[Fe/H] = B_x\Delta[E_x/O] = B_x(\Delta[E_x/H] - \Delta[O/H]) \tag{4.4}$$

leading to

$$B_x = \frac{\Delta[Fe/H]}{\Delta[E_x/H] - \Delta[O/H]} \tag{4.5}$$

Following Thomas et al. (2003a), when varying the [α/Fe] ratio only, total metallicity is kept fixed while enhancing the α-elements through

$$f_\alpha X^+ + f_{Fe}X^- = X^+ + X^- \tag{4.6}$$

where X^+ and X^- are the mass fractions of the enhanced and depressed groups (see Section 4.3.2), respectively, changed by the factors f_α and f_{Fe}. Hence for an increase in the [α/Fe]-ratio a higher abundance of the α-elements is counter-balanced by a decrease in the abundance of Fe-like elements to keep total metallicity fixed. Further, changing an individual element abundance keeping total metallicity and the ratio between the rest of the elements fixed, Eq. 4.6 is extended to

$$f_E(f_\alpha X^E) + f_O(f_{Fe}X^- + f_\alpha(X^+ - X^E)) = f_\alpha X^+ + f_{Fe}X^- = X^+ + X^- \quad (4.7)$$

where the individual element abundance is now multiplied by the factor f_E and the rest of the elements by f_O. Hence if the abundance of element E is changed by the factor f_E, the abundances of the rest of the elements are changed by the factor f_O to counter-balance a change in total metallicity. Also, since all other elements besides E are changed by the same factor the ratios between these elements remain constant. This implies secondary abundance changes due to f_E and f_O besides that of f_α and f_{Fe}. The logarithmically solar scaled iron abundance is defined as

$$[Fe/H]_{old} = \log\left(\frac{X^{Fe}}{X^H}\right) - \log\left(\frac{X^{Fe}_\odot}{X^H_\odot}\right) \quad (4.8)$$

where X^{Fe} and X^H are the mass fractions of Fe and H, while $X^{Fe}_\odot$ and $X^H_\odot$ are the corresponding solar values. If the mass fraction is changed by the factor f_O the iron abundance becomes

$$[Fe/H]_{new} = \log\left(\frac{f_O}{1}\right) + \log\left(\frac{X^{Fe}}{X^H}\right) - \log\left(\frac{X^{Fe}_\odot}{X^H_\odot}\right) \quad (4.9)$$

Eq. 4.8-4.9 give Δ[Fe/H]=[Fe/H]$_{new}$-[Fe/H]$_{old}$=$\log(f_O)$. In the same way we get Δ[O/H]=$\log(f_O)$ and Δ[E$_x$/H]=$\log(f_E)$ such that Eq. 4.5 becomes

$$B_x = \frac{\log(f_O)}{\log(f_E) - \log(f_O)} \quad (4.10)$$

Similarly to Eq. 4.8-4.9 we can enhance the element ratio [E/O] from

$$[E/O]_{old} = \log\left(\frac{f_\alpha}{f_\alpha}\right) + \log\left(\frac{X^E}{X^O}\right) - \log\left(\frac{X^E_\odot}{X^O_\odot}\right) \quad (4.11)$$

to

$$[E/O]_{new} = \log\left(\frac{f_E}{f_O}\right) + \log\left(\frac{f_\alpha}{f_\alpha}\right) + \log\left(\frac{X^E}{X^O}\right) - \log\left(\frac{X^E_\odot}{X^O_\odot}\right) \quad (4.12)$$

For a new abundance ratio [E/O]$_{new}$=0.3 starting from solar values [E/O]$_{old}$=0.0 Eq. 4.11 and Eq. 4.12 give

$$\log\left(\frac{f_E}{f_O}\right) = 0.3 \quad (4.13)$$

Following Thomas et al. (2003a) with the difference of having C locked to the enhanced group we re-derive f_{Fe} and f_α. Adopting the solar abundance fractions X^+=0.91 and X^-=0.079 derived from Grevesse et al. (1996) we find f_{Fe}=0.521 and f_α=1.042, resulting in A=0.94. Individual abundance fractions derived from Grevesse et al. (1996) are

Table 4.1: Element abundance fractions derived from Grevesse et al. (1996) (column 2). Fractional abundance changes for the enhancement [E/O]=0.3 for the enhanced element E (f_E) and the rest of the considered elements (f_O) are given in column 3 and 4, respectively. The final coefficients B_x are given in column 5.

E_x	$X_\odot^E$	f_E	f_O	B_x
C	0.172	1.693	0.847	-0.24
N	0.053	1.894	0.947	-0.079
Mg	0.038	1.923	0.962	-0.056
Ca	0.003	1.994	0.997	-0.0043
Ti	0.0002	1.9996	0.9998	-0.00029

presented in Table 4.1 along with the corresponding values for f_E and f_O derived using Eq. 4.7 and Eq. 4.13. Eq. 4.10 then gives the final coefficients B_x, also presented in Table 4.1. The final relationship becomes

$$[Fe/H] = [Z/H] - 0.94[O/Fe] - 0.24[C/O] - 0.079[N/O] - 0.056[Mg/O] - 0.0043[Ca/O] - 0.00029[Ti/O] \quad (4.14)$$

4.3.4 Choice of indices

We discard badly calibrated indices from the start. In Chapter 3 we find that the set of indices that appears to be best calibrated and most suited for the present aims are the Balmer line indices $H\delta_A$, $H\gamma_A$, and $H\gamma_F$, the metallic indices CN_1, CN_2, Ca4227, G4300, $C_2$4668, Mg_1, Mg_2, Mg b, and the Fe indices Fe4383, Fe4531, Fe5270, Fe5335, and Fe5406. As discussed in the next section we use different sets of indices for different elements.

The indices Hβ and Hγ_A are not included due to the Balmer anomaly discussed in Section 3.4.1. Since this phenomenon only applies to Globular clusters we consider these indices for studies of other types of objects (e.g. galaxies in Chapter 5-6). In Section 4.3.6 where the general features of the developed method are presented the indices Hβ and Hγ_A are included, but for the Globular cluster results (Section 4.4) these indices have not been used.

4.3.5 The χ^2 technique

The derivation of the set of element ratios is done in various iterative steps by means of the χ^2 code of Thomas et al. (2010). Galactic globular cluster data generally are very close to the 15 Gyr model (see Chapter 3), which is the highest age for which we have stellar evolutionary track calculations available. Therefore, we extrapolate the models logarithmically to a maximum age of 20 Gyr for the initial set of templates, in order

not to impose an upper age limit. Note that the index strengths evolve very little as a function of age at these old ages, therefore we do not expect this extrapolation to affect the derivation of individual element abundances significantly. As a sanity check we have verified that the globular clusters with ages above 15 Gyr are not biased to particular element abundance ratios.

The code computes the χ^2 between model prediction and observed index value for all model templates summing over the n indices considered:

$$\chi^2 = \sum_{i=1}^{n} \left(\frac{I_i^{\rm obs} - I_i^{\rm model}}{\sigma} \right)^2 \tag{4.15}$$

The resulting χ^2 distribution is then transformed into a probability distribution. By means of the incomplete Γ function adopting the degrees of freedom as $\nu = n_{\rm indices} - n_{\rm para}$ we compute the probability Q that the chi-square should exceed a particular value χ^2 by chance. This computed probability gives a quantitative measure for the goodness-of-fit of the model. If Q is a very small probability, then the apparent discrepancies are unlikely to be chance fluctuations. The solution with the highest Q (i.e. lowest χ^2) is chosen. If $Q < 0.0001$ the fit is considered to be unacceptable and the index with the largest χ^2 is discarded. This procedure is repeated until $Q \geq 0.0001$.

Since we determine which indices that are well calibrated for the globular cluster sample in Chapter 3, indices are not discarded when deriving the results presented in Section 4.4. However, when used there is a risk of introducing a bias in the results to certain combinations of modelled indices by discarding the index with the largest χ^2. In Chapter 5 the method is applied to a sample of $\sim$4000 galaxies. We find that only for 5.2% of the objects one index is discarded and that the index (G4300) with the highest discard percentage only reaches 3.8%. Hence the results are robust, but the risk of having biased results should be kept in mind for future data sets by keeping an eye on the discard percentage.

4.3.6 Derivation of individual element abundances

Deriving all parameters (age, [Z/H], [O/Fe], [C/Fe], [N/Fe], [Mg/Fe], [Ca/Fe] and [Ti/Fe]) at the same time requires a $\sim 10^8$ parameter grid of models. The method developed is instead of iterative nature. At each step a smaller number of parameters (1-3) are derived while keeping the rest fixed, thus requiring a significantly smaller parameter grid of models. First we determine the traditional light-averaged stellar population parameters age, total metallicity and [O/Fe] (representing [α/Fe], see Section 4.3.2) from a base set of indices, using the χ^2 minimization routine described in Section 4.3.5. This

base set of indices includes Mg b, the Balmer indices $H_{\delta A}$, $H_{\delta F}$ and $H\beta$ and the iron indices Fe4383, Fe5270, Fe5335, Fe5406, chosen as they are well calibrated with galactic globular clusters without individual element abundance variations (see Section 4.3.4 and Chapter 3). The models used at this point have step sizes of 0.024 dex for log(age) and 0.05 dex for both [Z/H] and [O/Fe], over the ranges 0<age<20 Gyr, -2.25<[Z/H]<0.7 and -0.3<[O/Fe]<0.5. Only indices that are sensitive to these three parameters are included in the base set. Mgb is included in the base set of indices since it is useful in combination with Iron indices to constrain [O/Fe] (e.g. Thomas et al., 2003a).

In the subsequent steps we add in turn particular sets of indices that are sensitive to the element the abundance of which we want to determine (see step 2-6, Fig. 4.2). In each step we re-run the χ^2 fitting code with a new set of models to derive the abundance of this element. This new set of models is a perturbation to the solution found for the base set of indices. It is constructed by keeping the stellar population parameters age, metallicity, and O/Fe fixed and by modifying the element abundance of the element under consideration by ± 1 dex in steps of 0.05 dex around the base value.

A new best fit model is obtained from the resulting χ^2 distribution. Then we move on to the next element. Due to the fact that several indices respond to the same elements (see Fig. 4.1) an iterative method allows for the simultaneous derivation of the individual element abundance ratios, illustrated in Fig. 4.2. We start with the element abundance affecting the largest number of indices (C) and proceed with elements affecting less and less indices. This prevents over/under predictions of specific abundances. For C the risk of over/under predicting the [C/Fe] ratio due to e.g. the strong sensitivity to Mg for Mg_1 is prevented by the other indices used. On the other hand only Ca4227 is sensitive to Ca such that the [Ca/Fe] ratio could be over/under predicted due to the sensitivity to C besides Ca for Ca4227, if the iteration started with this element ratio. The derivation of individual abundance ratios (Step 2-6) is iterated until the abundance ratios remain unchanged within the model grid step of 0.05 dex. A fast convergence of 3-4 iterations is generally found for this inner loop and a maximum of 5 iterations is set as an upper limit.

At the end of the sequence we re-determine the overall χ^2 and re-derive the base parameters age, metallicity, and O/Fe for the new set of element ratios. At this final step we use models with the base parameters age, total metallicity, and O/Fe ratio perturbed around the previously derived values by $\Delta log(age)/\Delta[Z/H]/\Delta[O/Fe] = \pm 0.1$ dex and with step sizes of 0.02 dex for log(age) and [Z/H] and 0.05 dex for [O/Fe]. A bigger step size for [O/Fe] improves upon speed for the routine and it was found that it did not affect the final results. All indices considered in the inner loop (step 2-6) are used at the final step together with the base set of indices. Then we go back to the second step and use the new base parameters to derive individual element abundances. This outer loop is iterated until the final χ^2 stops improving by more than 1 per cent. The method converges

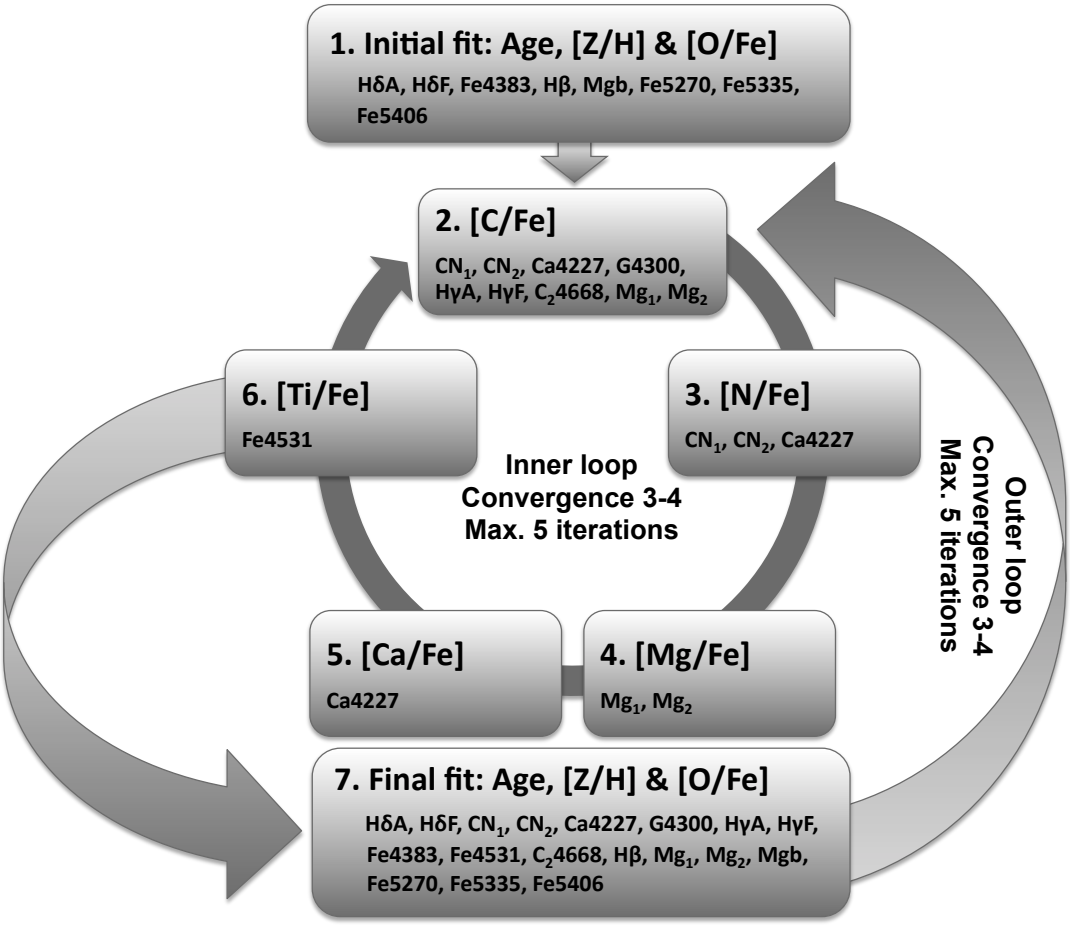

Figure 4.2: Method to derive element abundance ratios. A χ^2-minimisation routine is used at all steps to find the best fit model. Step 1 computes an initial fit for the base parameters age, [Z/H] and [O/Fe] using a base set of indices sensitive to these parameters only. The base parameters are fixed when deriving the individual element abundance ratios (inner loop, step 2-6) by adding indices sensitive to the element considered in each step to the base set of indices. At convergence, i.e. the element abundance ratios remain unchanged, the routine exit the inner loop and the base parameters are re-derived for the computed set of abundance ratios using all indices. This outer loop is iterated until the χ^2 at step 7 stops improving by less than 1%. Models with varying abundance ratios of the element considered are produced in step 2-6, while models perturbed around the previously derived base parameters are produced in step 7. The indices used at each step are presented in each box and the typical number of iterations are indicated as convergence along with the maximum number iterations allowed for both the inner and outer loop.

relatively fast, again generally requiring 3-4 iterations and 5 iterations is set as an upper limit. At step 1 and 7 we allow the procedure to discard indices with a bad χ^2.

In more detail, the sequence of elements is as follows. The first element in the loop is carbon, for which we use the indices CN_1, CN_2, Ca4227, $\mathrm{H}\gamma_\mathrm{A}$, $\mathrm{H}\gamma_\mathrm{F}$, G4300, $\mathrm{C}_2$4668, Mg_1, and Mg_2 on top of the base set. Next we drop these C-sensitive indices and proceed deriving N abundance, for which we use the N-sensitive indices CN_1, CN_2, and Ca4227.

Then we move on to Mg_1 and Mg_2 for Mg abundance, Ca4227 for Ca, and finally Fe4531 for the element Ti.

4.3.7 Parameter errors

Errors on the parameters are estimated by taking the FWHM of the probability distributions around the χ^2-minimum of the model fits (see Section 4.3.5 for details) and converting to 1σ errors using σ=FWHM/2.355. $\Delta\log(age)$, $\Delta[Z/H]$ and $\Delta[O/Fe]$ are derived at step 1 since the the models grids are too narrow at step 7 to reliably estimate the errors. Since the individual abundance ratios are derived as perturbations to the [O/Fe] ratio, errors on these parameters are estimated by in quadrature adding the errors on the derived perturbations $\Delta[E/Fe]_p$ to $\Delta[O/Fe]$

$$\Delta[E/Fe]^2 = \Delta[O/Fe]^2 + \Delta[E/Fe]_p^2 \tag{4.16}$$

For the globular cluster sample the typical errors are 0.165 dex for log Age, 0.21 dex for $[Z/\mathrm{H}]$, 0.08 dex for $[\mathrm{O}/\mathrm{Fe}]$, and about 0.15 dex for the other element ratios. It should be emphasised again that these are very conservative error estimates.

4.3.8 Comparison with methods in the literature

Trager et al. (2000a) introduced models with varying element abundance ratios by using the SSP models of Worthey (1994) together with the Lick index response functions of Tripicco & Bell (1995). They investigate the nature of the elements O and C by using different model treatments of these elements, i.e. locked to the enhanced group (see Section 4.3.2), locked the depressed group or kept fixed at solar values. Sánchez-Blázquez et al. (2006a) follow the technique of Trager et al. (2000a), but use the SSPs of Vazdekis et al. (2010) and modelled indices with different treatments for C, N and Mg to find the description that in general best resembles the overall behaviour of the data considered.

Sánchez-Blázquez et al. (2003) indirectly predict differences in the element abundances of C and N. They use absorption line indices known to be sensitive to variations of the abundances of these elements. If these indices show differences, while indices insensitive to abundance variations of the elements considered show no difference the stellar populations are believed to have different element abundance ratios. They also consider the SSPs of Vazdekis et al. (1996), but without element abundance ratios.

Clemens et al. (2006) treat [C/H] as a separate variable and consequently fit modelled indices (SSPs from Annibali et al., 2007) with the free parameters age, [Z/H], [α/Fe] and [C/H] to data. Kelson et al. (2006) consider modelled indices (TMB/K) with the

free parameters age, [Z/H], [α/Fe] and [α/C], [α/N] and [α/Ca], but not all parameters simultaneously.

The first authors to develop a method that simultaneously consider a full grid of element abundance ratios were Graves & Schiavon (2008), based on the models of Schiavon (2007). They start by deriving a fiducial Age and [Fe/H] using the index Hβ in combination with <Fe>. Hβ is then exchanged with an index sensitive to a specific element. This element is then either enhanced or depressed until the fiducial Age and [Fe/H] is matched. The method developed in this work is based on a different philosophy. In our method a χ^2 routine finds the model with an enhancement of a specific element that best fits the data keeping a set of base (fiducial) parameters (Age, [Z/H] and [O/Fe]) fixed. Initially deriving [O/Fe] together with age and [Z/H] gives more freedom to the choice of age-sensitive indices. Thus we can use the Fe-sensitive higher order balmer indices (Hδ_A, Hδ_F, Hγ_A and Hγ_F) besides Hβ for initially constraining age. A major difference is that we allow for iteration between the base model and the solution with varying element ratios. In chapter 5 we apply the method to $\sim$4000 early-type galaxies (see Section 5.2) and we find that the average differences between the initially derived base parameters and the final values are 0.11 dex for log(age), 0.09 dex for [Z/H] and 0.04 dex for [O/Fe].

For each element we use all indices that are sensitive to its abundance (see Fig. 4.1, Section 4.3.1), while Graves & Schiavon (2008) use the most sensitive index only for each element. Using all indices extracts all information available and protects against anomalies in individual indices, i.e. noise and emission line fill affecting the absorption features. Still, more sensitive indices will have a greater weight than less sensitive indices. Graves & Schiavon (2008) set a fixed value of [O/Fe] and simultaneously derive [C/Fe], [N/Fe], [Mg/Fe] and [Ca/Fe]. We extend this and further include [Ti/Fe], while we also trace [O/Fe] inferred from [α/Fe] (see Section 4.3.1).

4.4 Results

From the method described in the previous section we obtain age, total metallicity [Z/H], iron abundance [Fe/H] and the individual element abundance ratios [O/Fe], [C/Fe], [N/Fe], [O/Fe], [Mg/Fe], [Ca/Fe], and [Ti/Fe] for a total of 52 globular clusters. We exclude the 47 Tucanae from our analysis, as age dating of this cluster from Balmer line indices is known to be problematic (Schiavon et al., 2002; Vazdekis et al., 2001). In this section we present the results and compare with literature data obtained from CMD fitting (age) and high-resolution spectroscopy of individual stars (metallicity and element abundance ratios).

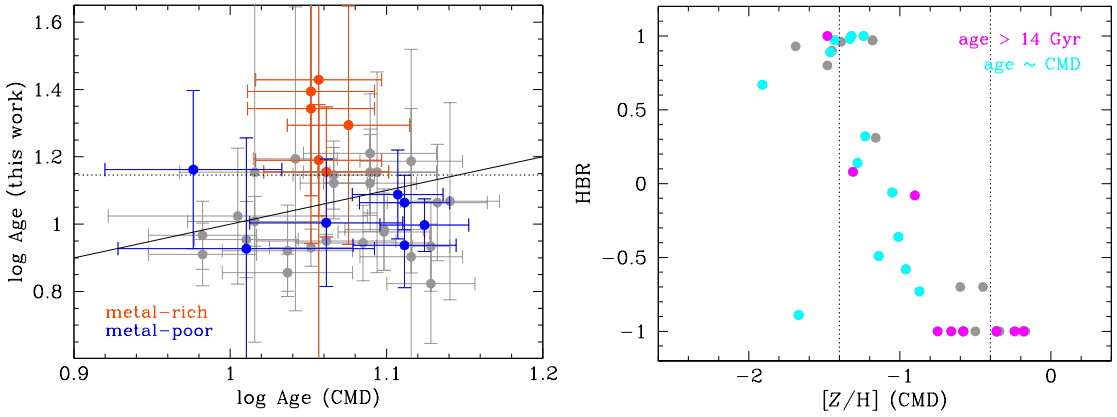

Figure 4.3: Ages of galactic globular clusters derived from integrated light spectroscopy in comparison with literature data. Globular cluster spectra are taken from Puzia et al. (2002) and Schiavon et al. (2005). Literature ages from colour-magnitude isochrone fitting are adopted from Marín-Franch et al. (2009). *Left-hand panel:* Grey symbols are the full sample, orange and blue symbols are metal-rich ($[Z/\mathrm{H}] > -0.8$ dex) and metal-poor ($[Z/\mathrm{H}] < -1.55$ dex) sub-samples, respectively. The dotted line marks the age of the universe as derived in Komatsu et al. (2011). *Right-hand panel*: Metallicity versus horizontal branch morphology (horizontal branch ratio HBR adopted from Harris (1996)). The literature metallicities on the Zinn & West (1984) scale are taken from the compilation by Harris (1996). The magenta symbols are those clusters for which we obtain ages larger than 14 Gyr, while the cyan symbols are clusters for which our ages agree with the CMD ages within 0.1 dex. The dotted lines are the metallicity limits from the left-hand panel. Literature ages are generally well reproduced. We tend to over-estimate ages for the most metal-rich globular clusters. Horizontal branch morphology only plays a minor role.

4.4.1 Ages

First we discuss the comparison of the derived ages with literature data. CMD ages are taken from Marín-Franch et al. (2009) and de Angeli et al. (2005) where not available in Marín-Franch et al. (2009). The overlap of the two samples contains 39 clusters.

The age comparison is shown in the left-hand panel of Fig. 4.3, where we plot our derived ages as a function of the CMD ages. The grey symbols are the full sample, orange and blue are metal-rich and metal-poor sub-samples, respectively. The age derivation through the Lick indices works reasonably well. Almost half of the sample our globular cluster ages agree with Marín-Franch et al. (2009) within 0.1 dex (18 out of 39), and three quarters (29) of the clusters agree within the (conservative) measurement errors. Most importantly, 35 clusters out of 52 (two thirds) are younger than the universe as derived by Komatsu et al. (2011, dotted line) from a combination of cosmic microwave background, supernova, and large-scale structure data, and the vast majority (45 out of 52) are consistent with age of the universe within 0.1 dex. All but one cluster ages are consistent with the age of the universe within our (conservative) measurement errors.

Generally, the ages from Lick indices agree well with the CMD ages, albeit with quite a large scatter. Note that Mendel et al. (2007) derived systematically larger ages

with the TMB/K model[1]. The turnoff brightness, being the major indicator for the age of a stellar population, is highly sensitive to the distance of the object. As a consequence, only relative ages can be reliably measured (Ortolani et al., 1995; de Angeli et al., 2005; Marín-Franch et al., 2009).

Still, it is interesting to investigate the reason for the exceedingly large ages of some clusters. Fig. 4.3 shows that the clusters for which we overestimate the ages with respect to the age of the universe tend to be metal-rich with $[Z/\mathrm{H}] > -0.4$ dex (orange symbols). Most of the clusters whose ages agree well with the CMD ages, instead, are metal-poor with $[Z/\mathrm{H}] < -1.4$ dex (blue symbols). To investigate this further, in the right-hand panel of Fig. 4.3 we plot metallicity (on Zinn & West (1984) scale adopted from Marín-Franch et al. (2009)) versus horizontal branch morphology expressed as horizontal branch ratio HBR adopted from Harris (1996). The magenta symbols are those clusters for which we obtain ages larger than 14 Gyr, while the cyan symbols are clusters for which our ages agree with the CMD ages within the measurement errors. It can be seen clearly that horizontal branch morphology only plays a minor role at a given metallicity. Metallicity is the main driver for the age discrepancy. To summarise, globular cluster ages derived from absorption-line indices tend to be overestimated for the most metal-rich clusters around slightly sub-solar metallicity. This is a more general manifestation of the $\mathrm{H}\beta$ anomaly of globular cluster data noted by Poole et al. (2010), which may well be a 'Balmer anomaly' rather than being restricted to $\mathrm{H}\beta$. Note, however, that this pattern is more likely to be caused by problems in the globular cluster data than the models, as galaxy data appear to be well matched instead (Kuntschner et al., 2010, see Chapter 3). An example of such a problem may be the sample selection. Clusters close to the galactic Bulge will be more prone to uncertainties in the derived stellar population parameters due to higher dust reddening affecting the derived CMD ages. The sample of Puzia et al. (2002) was chosen to study the metal-rich stellar populations of the galactic Bulge, hence 9 out 12 Puzia et al. (2002) clusters are found close to the Bulge. The Schiavon et al. (2005) sample was chosen to cover a broad range of stellar parameters and therefore also include a significant fraction of Bulge clusters.

4.4.2 Metallicity

For the comparison of metallicity we adopt literature values from Marín-Franch et al. (2009) on the Zinn & West (1984) scale. These represent total metallicity $[Z/\mathrm{H}]$ as

[1]Note that Thomas et al. (2003a) have not explicitly derived globular cluster ages with respect to CMD. The major difference is that Mendel et al. (2007) adopted CMD ages from de Angeli et al. (2005) who derived systematically younger absolute ages than Marín-Franch et al. (2009). It should be kept in mind, however, that the derivation of *absolute* globular cluster ages through CMDs carries its own problems as pointed out in both de Angeli et al. (2005) and Marín-Franch et al. (2009)

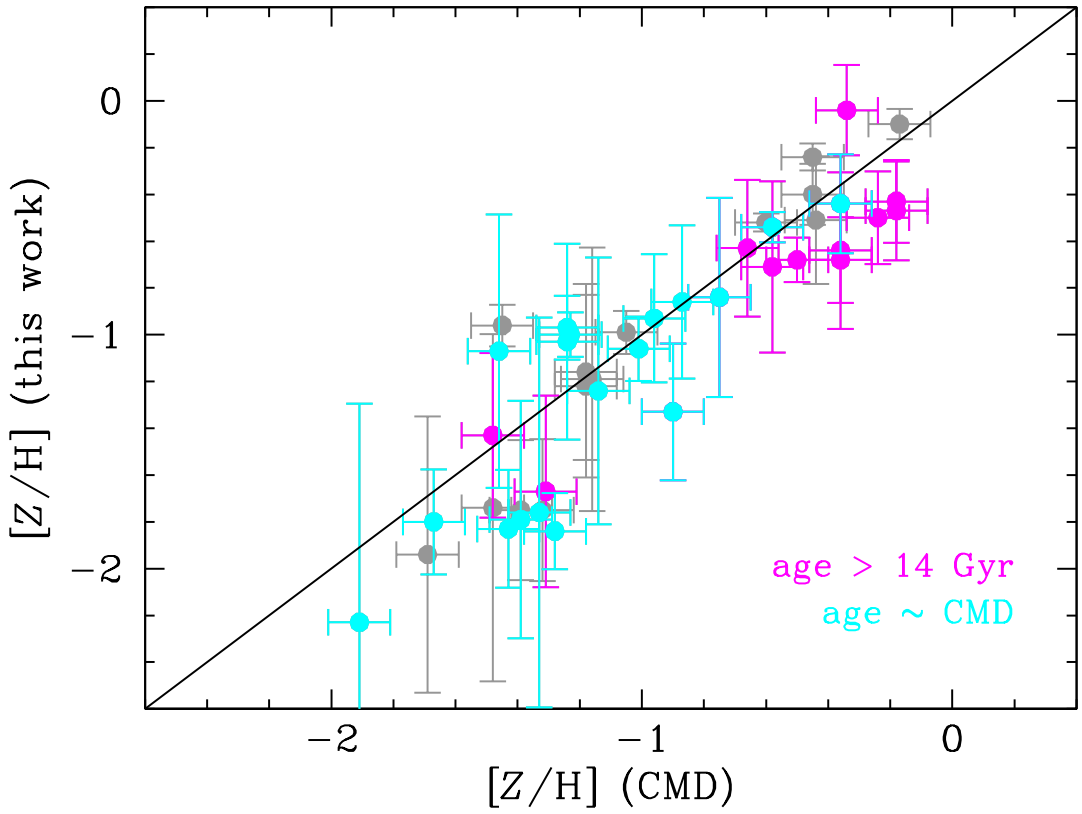

Figure 4.4: Total metallicities $[Z/\mathrm{H}]$ of galactic globular clusters derived from integrated light spectroscopy in comparison with literature data. Globular cluster spectra are taken from Puzia et al. (2002) and Schiavon et al. (2005). The literature metallicities on the Zinn & West (1984) scale and corrected for α-enhancement are taken from Marín-Franch et al. (2009). The magenta symbols are those clusters for which we obtain ages larger than 14 Gyr, while the cyan symbols are clusters for which our ages agree with the CMD ages within 0.1 dex. Literature metallicities are well reproduced. Metallicities are slightly underestimated for those clusters for which we overestimate the age.

Marín-Franch et al. (2009) have corrected the iron measurement using the prescription of Salaris et al. (1993). We therefore confront these literature values with our measurements of total metallicity $[Z/\mathrm{H}]$ in Fig. 4.4. The magenta symbols are those clusters for which we obtain ages larger than 14 Gyr, while the cyan symbols are clusters for which our ages agree with the CMD ages within 0.1 dex.

Metallicities agree very well, with a tendency of slightly lower metallicity estimates from the present work at low metallicities. It can further be seen from Fig. 4.4 that this match is particularly good for those clusters whose Lick index ages agree best with the CMD ages (cyan symbols). For the clusters with the oldest Lick index ages (magenta symbols), instead, we tend to underestimate metallicity by ~ 0.2 dex This might in fact

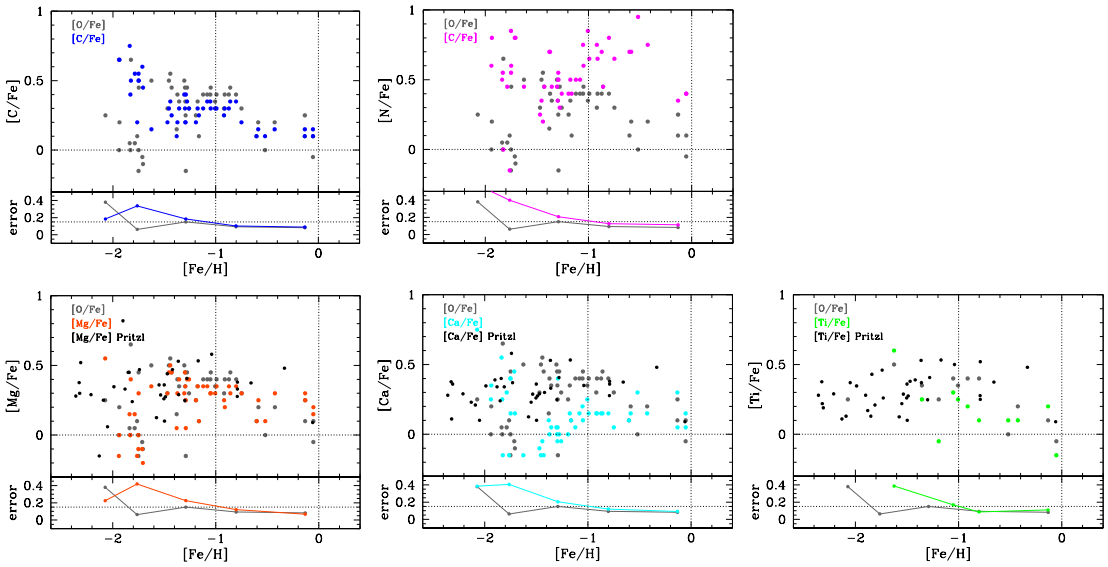

Figure 4.5: Abundance ratios [C/Fe], [N/Fe], [Mg/Fe], [Ca/Fe], and [Ti/Fe] (coloured symbols) in comparison to the the [O/Fe] ratio (grey symbols) as functions of iron abundance [Fe/H] for galactic globular clusters. The globular cluster spectra are taken from Puzia et al. (2002) and Schiavon et al. (2005). The black dots are the element ratios of globular cluster stars from Pritzl et al. (2005). The bottoms panels show the 1-σ error on the element ratios with the dotted horizontal lines indicating an error of 0.15 dex. The typical abundance pattern of Milky Way field and globular cluster stars is well reproduced for [O/Fe]. The other element ratios have too large errors at low metallicities below [Fe/H] ~ -1 dex, hence meaningful conclusions can only be drawn at [Fe/H] $\gtrsim -1$ dex.

be an artefact produced by the age-metallicity degeneracy, i.e. we tend to underestimate the metallicity of those globular clusters for which we overestimate the age.

4.4.3 Element abundance ratio pattern

We now turn to discuss the individual abundances of the elements C, N, O, Mg, Ca, and Ti relative to the abundance of Fe. Fig. 4.5 presents the abundance ratios [C/Fe], [N/Fe], [Mg/Fe], [Ca/Fe], and [Ti/Fe] (coloured symbols) as functions of iron abundance [Fe/H] in comparison to [O/Fe] (grey symbols). The bottom panels indicate the typical measurement error as a function of iron abundance.

The element ratio [O/Fe], being equivalent to [α/Fe] (see equation 4.1), carries the smallest measurement error. This element ratio is well determined at all metallicities. The expected pattern of super-solar [α/Fe] with a slight decrease toward solar metallicity is reproduced. The individual element abundance ratios, instead, have significantly larger errors. In all cases the typical errors increase with decreasing metallicity, and exceed $\sim$ 0.1 dex at [Fe/H] < -1 dex. In fact, the abundance pattern loses structure at such low iron abundance. This ought to be expected as the sensitivity of the models to

element ratio variations decreases dramatically with decreasing metallicity (e.g., Thomas et al., 2003a). Moreover, model errors become comparable to model variations for only moderate abundance ratio changes (see Chapter 3), which further hampers the analysis. Hence abundance ratios cannot be reliably determined. At $[\mathrm{Fe/H}] > -1$ dex, instead, our results reveal interesting abundance trends.

4.4.4 Comparison with stellar spectroscopy

Before discussing these abundance patterns in detail, we present the direct comparison of our results with the measurements of Pritzl et al. (2005), who have derived element abundance ratios of a large sample of galactic globular clusters form individual stellar spectroscopy. Pritzl et al. (2005) have observed between one and ten stars per cluster and derived the element ratios $[\mathrm{Mg/Fe}]$, $[\mathrm{Ca/Fe}]$, and $[\mathrm{Ti/Fe}]$. The ratio $[\alpha/\mathrm{Fe}]$ is computed from the geometrical mean of these three measurements. We have computed the straight average when more than one star has been observed. In total, the Pritzl et al. (2005) sample has 18 clusters in common with the present work.

In Fig. 4.6 we plot the abundance ratios [Mg/Fe], [Ca/Fe], and [Ti/Fe] (coloured symbols) as derived in the present work from integrated light spectroscopy as functions of the measurements from Pritzl et al. (2005). Black symbols show $[\alpha/\mathrm{Fe}]$ ratios. The error symbols indicate typical errors in both $[\alpha/\mathrm{Fe}]$ and $[\mathrm{Mg/Fe}]$. The small coloured symbols are globular clusters with $[\mathrm{Fe/H}] < -1$ dex, for which individual element ratios from integrated light spectroscopy are less reliable (see Fig. 4.5). There is a satisfactory agreement for $[\alpha/\mathrm{Fe}]$ at all metallicities, in agreement with the results of Mendel et al. (2007) obtained with the TMB/K models. This is confirmed with a t-test that shows that the slope of a regression line fitted to the data is equal to 1 (i.e. 1-to-1 relation) at a 71% significance level. $[\mathrm{Mg/Fe}]$ ratios are still in reasonable agreement at $[\mathrm{Fe/H}] > -1$ dex. The t-test shows that the significance level of the regression slope being equal to 1 is higher when only data points with $[\mathrm{Fe/H}] > -1$ dex are considered, however, it is still below a 10% significance level. There is a hint for systematically lower $[\mathrm{Ca/Fe}]$ and $[\mathrm{Ti/Fe}]$ ratios in our work, instead. Similarly to the $[\mathrm{Mg/Fe}]$ case, the significance level is below 10% for the regression slope being equal to 1 for $[\mathrm{Ca/Fe}]$ when only data points with $[\mathrm{Fe/H}] > -1$ dex are considered. The low significance levels for $[\mathrm{Mg/Fe}]$ and $[\mathrm{Ca/Fe}]$ are obviously hampered by the low number of data points in common with the Pritzl et al. (2005) sample for $[\mathrm{Fe/H}] > -1$ dex, i.e. five data points. For $[\mathrm{Ti/Fe}]$ the number of data points is only two such that a significance test is pointless. In the next section we instead compare the the full element ratio distributions for [Mg/Fe], [Ca/Fe] and [Ti/Fe] to the full distributions of corresponding element ratios from Pritzl et al. (2005).

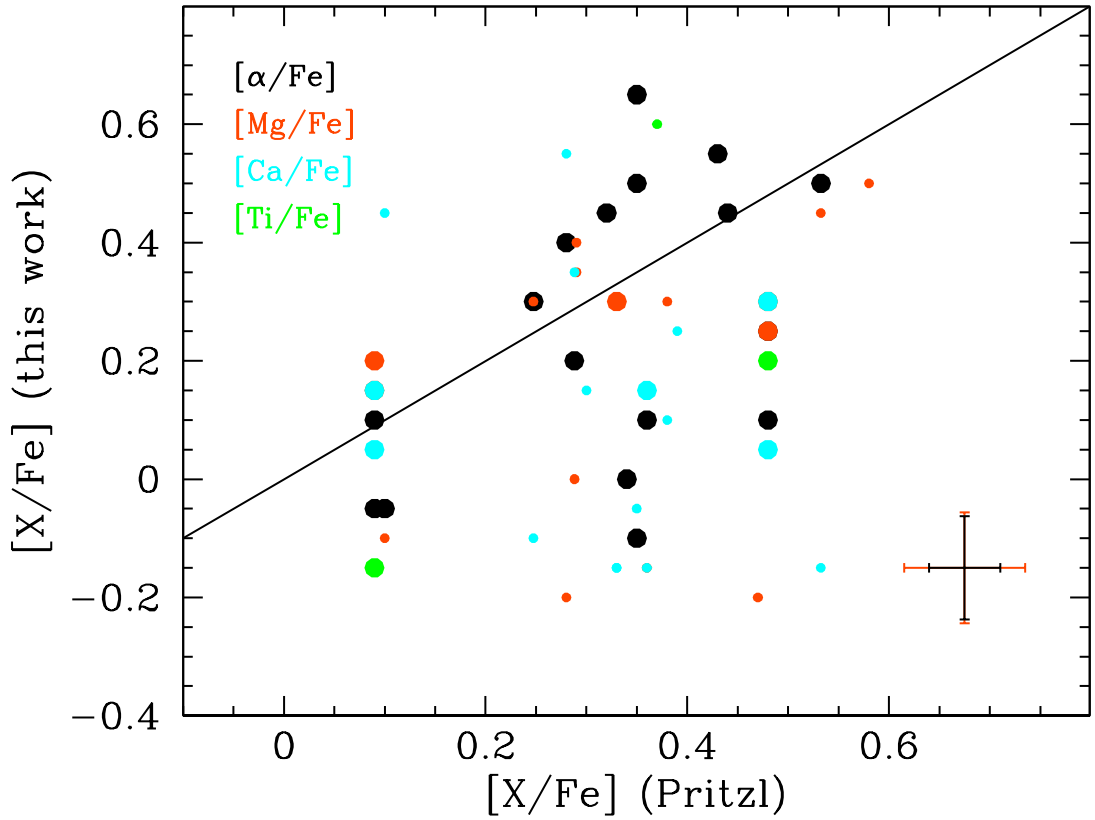

Figure 4.6: Abundance ratios [Mg/Fe], [Ca/Fe], and [Ti/Fe] (coloured symbols) of galactic globular clusters measured in this work from integrated light spectroscopy in comparison with literature values from individual stellar spectroscopy by Pritzl et al. (2005). Black symbols show $[\alpha/\mathrm{Fe}]$ ratios. The error symbols indicate typical errors in both $[\alpha/\mathrm{Fe}]$ and $[\mathrm{Mg/Fe}]$. The small symbols are globular clusters with $[\mathrm{Fe/H}] < -1$ dex, for which element ratios from integrated light spectroscopy are unreliable (see Fig. 4.5).

4.4.5 Element abundance distributions

In the following we compare the distributions of element ratios from the integrated and stellar spectroscopy. We only consider clusters with $[\mathrm{Fe/H}] > -1$ dex in our analysis leaving us with a sample of 16 objects (out of 52). The reason is that element ratios cannot be reliably determined at lower metallicities, because the relative sensitivity of the model predictions to element ratio changes is too small (see Fig. 4.5). Note also that we only can consider the P02 sample for Ti (6 out of 12) as the Ti sensitive index Fe4531 cannot be measured for the S05 clusters.

Fig. 4.7 shows the distributions of [C/Fe], [N/Fe], [Mg/Fe], [Ca/Fe], and [Ti/Fe] ratios (coloured histograms) in comparison with the distribution of the [O/Fe] ratio (grey histograms). The median values of these distributions are given in Table 4.2. The distribution of $[\mathrm{O/Fe}]$ is reasonably tight with a median value of 0.24 dex as expected for Milky Way globular clusters. The other of the light α elements considered, [Mg/Fe],

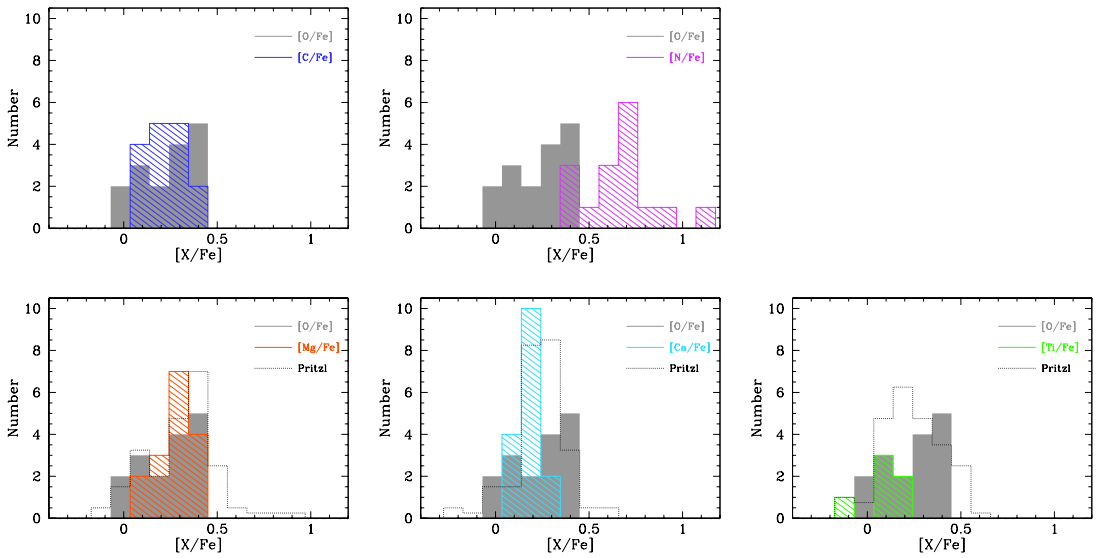

Figure 4.7: Distributions of [C/Fe], [N/Fe], [Mg/Fe], [Ca/Fe], and [Ti/Fe] ratios (coloured histograms) in comparison to the distribution of the $[\mathrm{O/Fe}]$ ratio (grey histogram) for galactic globular clusters. The globular cluster spectra are taken from Puzia et al. (2002) and Schiavon et al. (2005). Only clusters with $[\mathrm{Fe/H}] > -1$ dex are considered (16 objects out of 52) as element ratios cannot be reliably determined at lower metallicities (see text). The dotted black lines (for [Mg/Fe], [Ca/Fe], [Ti/Fe] only) are the fractional distributions of the element ratios of globular cluster stars from Pritzl et al. (2005), scaled to fit the y-axis since this sample is significantly larger than the sample studied in this work. We find a general trend such that the heavier of the light elements (Ca and Ti) are less enhanced than O and Mg. N is strongly enhanced in a sub-population of clusters accompanied by a slight depression of [C/Fe] with respect to O and Mg.

follows this distribution very closely with a very similar median of 0.25 dex. The other light elements, instead, deviate from this pattern. [C/Fe] and [Ca/Fe] ratios show similarly peaked distributions, but with different median values. The element ratio [C/Fe] has a median slightly lower by ~ 0.04 dex, while [Ca/Fe] peaks at significantly lower values with a median of 0.15 dex. A Kolmogorov-Smirnov test confirms that the distributions in $[\mathrm{O/Fe}]$ and [Ca/Fe] come from different underlying distributions at the $> 6\sigma$ level. The distribution of [N/Fe] has a pronounced peak at a significantly larger value of 0.71 dex. The distribution of [Ti/Fe] is somewhat scattered. Still, the data show a clear trend toward lower [Ti/Fe] ratios with a median of 0.09 dex in line with the neighbouring α element Ca.

The significant enhancement of nitrogen together with the slight depression of carbon relative to the other light elements is a well known abundance pattern in globular clusters observed in high-resolution spectroscopy studies of individual stars (e.g., Norris et al., 1984; Carretta et al., 2005). This chemical anomaly is commonly attributed to self-enrichment during the formation of the star cluster (Ventura et al., 2009). Such N enhancement has been quantified in Thomas et al. (2003a) for the first time for integrated

Table 4.2: Median values of element ratio distributions (in dex).

[O/Fe]	[C/Fe]	[N/Fe]	[Mg/Fe]	[Ca/Fe]	[Ti/Fe]
0.24	0.20	0.71	0.25	0.15	0.09

light observations of globular clusters, while the accompanying depression of C found in the present work is new. The [C/Fe] and [N/Fe] ratios derived here appear to be well consistent with the measurements from Carretta et al. (2005).

The next heavier of the light elements, Mg, follows the distribution of [O/Fe] closely. This ought to be expected as these elements are close in atomic number and created in very similar processes during supernova nucleosynthesis (Woosley & Weaver, 1995; Thielemann et al., 1996). However, the heavier α-elements Ca and Ti deviate from this pattern. The typical [Ca/Fe] ratio is significantly lower than the typical [O/Fe] and [Mg/Fe] ratios. The $[\mathrm{Ti/Fe}]$ ratio is less well determined, but the results suggest that this element continues this trend with even lower $[\mathrm{Ti/Fe}]$ ratios.

The element ratio distributions from Pritzl et al. (2005) are also plotted in Fig. 4.7 (dotted black histograms) for [Mg/Fe], [Ca/Fe] and [Ti/Fe]. These distributions clearly follow the pattern derived in this work, i.e. the [Ca/Fe] distribution peaks at lower values compared to [Mg/Fe] and [Ti/Fe] peaks at even lower values. This, together with the reproduced pattern of enhanced nitrogen and depressed carbon, is a very reassuring signal that we can predict the element ratios for galactic globular clusters.

4.4.6 New model fits

The adjustment of individual element abundances helps to improve the fits to a number of indices. In Figs. 4.8 and 4.9 we revisit the calibration figure from Chapter 3 for the model after the full chemical analysis. We only show those indices that have been used in the analysis, plotting index strengths as functions of $[\mathrm{MgFe}]'$. Three models at Lick spectral resolution with an age of 13 Gyr are shown for the metallicities $[Z/\mathrm{H}] = -2.25,\ -1.35,\ -0.33,\ 0.0,\ 0.35,\ 0.67$ dex. Metallicity increases from left to right. The solid lines are the final model for the average of the individual element abundance ratios derived through the χ^2 fit. The dotted and dashed lines are the base models with $\alpha/\mathrm{Fe} = 0.0$ dex and $\alpha/\mathrm{Fe} = 0.3$ dex for comparison. The grey shaded area along the model indicates the 1-σ error of the model prediction. Galactic globular clusters from P02 and S05 are filled and open squares, respectively. The typical errors in the globular cluster index measurements are given the error symbol at the bottom of each panel. The small black dots are early-type galaxies from the MOSES catalogue (see Section 5.2) including only high signal-to-noise spectra with $S/N > 40$.

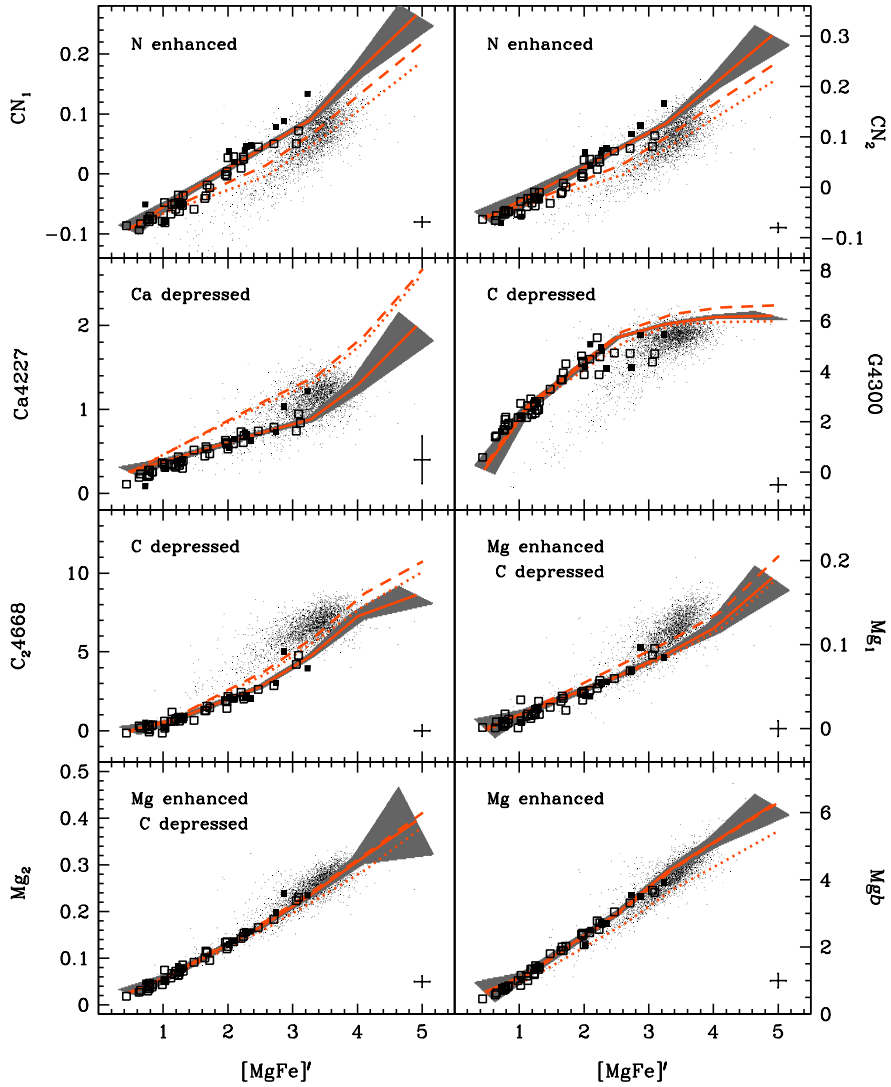

Figure 4.8: Calibration of the line indices that are sensitive to light elements. Three models at Lick spectral resolution with an age of 13 Gyr and the metallicities $[Z/\mathrm{H}] = -2.25, -1.35, -0.33, 0.0, 0.35, 0.67$ dex are shown. The solid lines are the final model for the average of the individual element abundance ratios derived through the χ^2 fit. The dotted and dashed lines are the base models with $[\alpha/\mathrm{Fe}] = 0.0$ dex and $[\alpha/\mathrm{Fe}] = 0.3$ dex. The grey shaded area along the model indicates the 1-σ error of the model prediction. Galactic globular clusters from Puzia et al. (2002) and Schiavon et al. (2005) are filled and open squares, respectively. The typical errors in the globular cluster index measurements are given the error symbol at the bottom of each panel. The small black dots are early-type galaxies from the MOSES catalogue (MOrphologically Selected Early-type galaxies in SDSS Schawinski et al., 2007; Thomas et al., 2010) drawn from the SDSS data base (York et al., 2000) including only high signal-to-noise spectra with $S/N > 40$.

Light element indices

Fig. 4.8 shows the indices that are sensitive to light element abundances, namely CN_1, CN_2, Ca4227, G4300, $\mathrm{C}_2$4668, Mg_1, Mg_2, and $\mathrm{Mg}\,b$. It can be seen from the top pan-

els that the strengths of the CN indices are clearly underestimated in both solar-scaled and α/Fe enhanced base models (dotted and dashed lines). As already discussed in Thomas et al. (2003a) a significant enhancement in N is required to explain the high index strengths. At the same time, the indices G4300, and $C_2$4668, and Mg_1 are slightly too strong in the base models, which leads to a slight reduction of C abundance in the final best-fitting model.

Another striking element abundance pattern that can be inferred from Fig. 4.8 directly is the abundance of Ca. The strength of the index Ca4227 is significantly over-predicted by the solar-scaled and α/Fe enhanced base models. The model matches the globular cluster data very well, instead, when a depression of Ca abundance is included. Finally, the indices Mg_2 and $Mg\,b$ (bottom panels) are well reproduced by the α/Fe enhanced model (dashed line), and only a negligible adjustment of Mg abundance is required to optimise the fit.

Iron and Balmer line indices

Fig. 4.9 presents the Fe and Balmer line indices used in the fitting procedure. The solar-scaled model (dotted lines) generally over-predicts the index strengths of the Fe indices, which is remedied through a depression of Fe abundance in the α/Fe enhanced model (dashed lines). The index strength of Fe4531 is slightly re-adjusted through a depression of Ti abundance. The signal is very weak, though, and the determination of Ti abundance in this work must in fact be considered tentative, in particular since only a handful of clusters from P02 are available for the Ti abundance measurement. In general, the full chemical model only leads to minor corrections of the Fe indices. The same is true for the Balmer line indices. Here the solar-scaled model under-predicts line strengths, which is remedied by the enhancement of the α/Fe ratio. Again, other elements only have negligible impact on these indices.

4.5 Discussion

We have derived, for the first time, detailed chemical element abundance patterns of galactic globular clusters from integrated light spectroscopy. The light elements O and Mg show the well-known enhancement with respect to Fe, hence [O/Fe] $\sim$ [Mg/Fe] $\sim$ 0.3 dex. For C, N, and the heavier α elements Ca and Ti, however, we detected interesting abundance anomalies. N is further enhanced to very high [N/Fe] ratios, while C is slightly depressed. Ca exhibits significantly lower [Ca/Fe] ratios than O or Mg, a pattern that appears to be present also in [Ti/Fe]. These anomalies have interesting

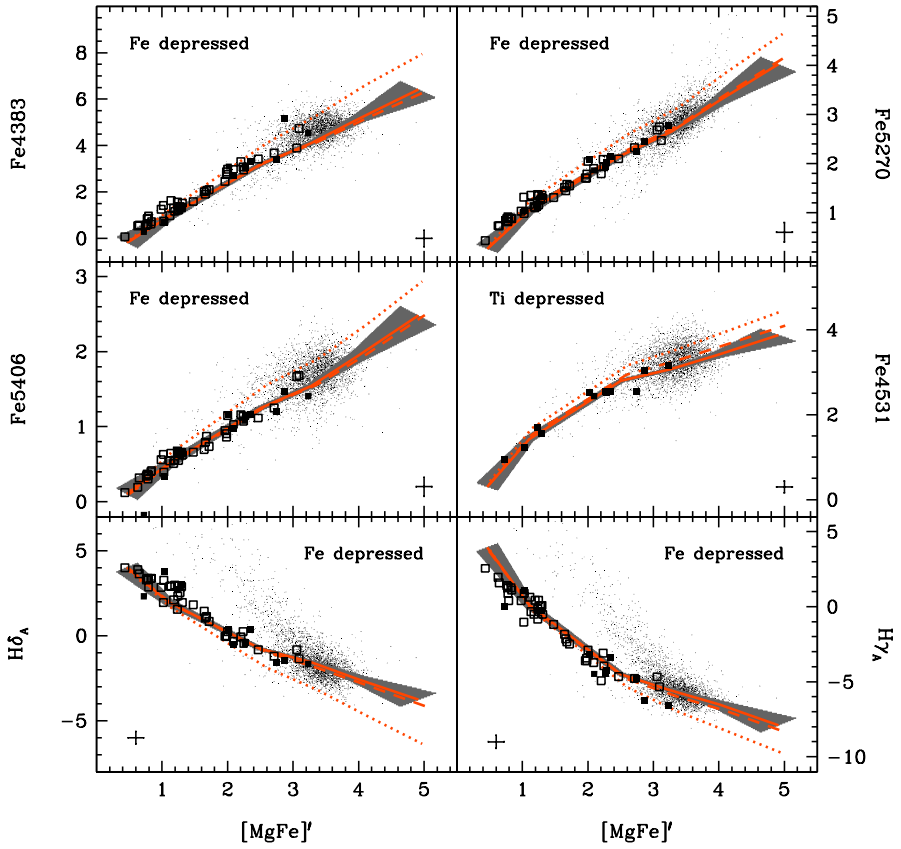

Figure 4.9: Calibration of the Fe and Balmer line indices. Three models at Lick spectral resolution with an age of 13 Gyr and the metallicities $[Z/\mathrm{H}] = -2.25, -1.35, -0.33, 0.0, 0.35, 0.67$ dex are shown. The solid lines are the final model for the average of the individual element abundance ratios derived through the χ^2 fit. The dotted and dashed lines are the base models with $[\alpha/\mathrm{Fe}] = 0.0$ dex and $[\alpha/\mathrm{Fe}] = 0.3$ dex. The grey shaded area along the model indicates the 1-σ error of the model prediction. Galactic globular clusters from Puzia et al. (2002) and Schiavon et al. (2005) are filled and open squares, respectively. Note that the indices Fe4531 and Fe5015 cannot be measured for the Schiavon et al. (2005) sample. The typical errors in the globular cluster index measurements are given the error symbol at the bottom of each panel. The small black dots are early-type galaxies from the MOSES catalogue (MOrphologically Selected Early-type galaxies in SDSS Schawinski et al., 2007; Thomas et al., 2010) drawn from the SDSS data base (York et al., 2000) including only high signal-to-noise spectra with $S/N > 40$.

consequences for supernova nucleosynthesis and the chemical enrichment in the Milky Way.

First we confront these results with the element ratios of individual stars in globular clusters as measured by Pritzl et al. (2005). These are shown by the dotted lines in Fig. 4.7 for [Mg/Fe], [Ca/Fe], and [Ti/Fe]. The distributions of the [Mg/Fe] ratios agree very well. [Ca/Fe] and [Ti/Fe] ratios, instead, are somewhat higher in Pritzl et al. (2005). The latter do suggest slightly lower enhancement of these elements, but not as pronounced as found here. But our finding gets support from the study by Feltzing et al. (2009) who analyse

six horizontal branch stars in the metal-rich galactic globular cluster NGC 6352. As expected the cluster is enhanced in the α-elements. But like in the present work Feltzing et al. (2009, see their Fig. 7) find a sequence of decreasing element ratios relative to iron for increasing atomic numbers from Mg through Ca to Ti.

It should be expected that field stars show the same behaviour since globular cluster element abundances generally follow the ones of the field stars in the galactic halo and discs (Pritzl et al., 2005). In fact the trend reported here starts to crystallise out now from recent high quality stellar spectroscopy of galactic field stars in bulge and disc. Bensby et al. (2010) analyse bulge and thick/thin disc stars and find [Ca/Fe] and [Ti/Fe] ratios to be lower than [O/Fe] and [Mg/Fe] ratios for all three populations.

The implication is that some fraction of the abundance in the heavier α elements must come from SN Ia explosions, while the lighter elements O and Mg remain to be enriched exclusively by SN II. The yields of standard models for SN Ia explosions do indeed predict the production of traces of the heaviest α elements. As a consequence, galactic chemical evolution models predict lower [Ca/Fe] ratios for halo stars (Chiappini et al., 1997), which had not been confirmed from observational data so far. The results discussed here provide a new observational support for this pattern.

This is critical for the chemical enrichment histories of galaxies. It leads to the most natural explanation for the shallow slope of the $[\mathrm{Ca/Fe}]$-galaxy mass relation of early-type galaxies (Saglia et al., 2002; Thomas et al., 2003b; Cenarro et al., 2003; Michielsen et al., 2003). In this scenario, Ca is underabundant relative to the lighter α elements in massive galaxies for the same reason as Fe is underabundant (see discussion in Thomas et al., 2003b). The short formation time-scales inhibit SN Ia to play a role in the chemical enrichment history of the stellar populations in these galaxies, such that elements that are produced in SN Ia are depleted in the stars. In fact chemical evolution models of bulges and spheroids predict lower element abundances for the heavier α elements, Ca in particular (Matteucci et al., 1999). This implies that also Ti would have to be underabundant in massive galaxies. Indeed we find that this is the case in Chapter 5.

4.6 Conclusions

Modelling integrated light spectroscopy of unresolved stellar populations allows us to study the detailed element abundances in distant galaxies and globular clusters. In Chapter 3 we present new, flux-calibrated stellar population models of Lick absorption-line indices with variable element abundance ratios. The new model includes a large variety of individual element variations, which allows the derivation of the abundances for the elements C, N, O, Mg, Ca, Ti, and Fe besides total metallicity and age. In this chapter

we use this model to obtain estimates of these parameters and element abundance ratios from integrated light spectroscopy of galactic globular clusters.

The globular cluster data is taken from Puzia et al. (2002) and Schiavon et al. (2005). We measure line strengths of all 25 Lick absorption-line indices for both samples directly on the globular cluster spectra. Both globular cluster samples are flux calibrated, so that no further offsets need to be applied for the comparison with our models.

We derive the element abundance ratios [C/Fe], [N/Fe], [O/Fe], [Mg/Fe], [Ca/Fe], [Ti/Fe] through an iterative χ^2 fitting technique. First we determine the traditional light-averaged stellar population parameters age, total metallicity, and α/Fe ratio from the indices Mg b, the Balmer index H$\delta_{\rm A}$, and the iron indices Fe4383, Fe5270, Fe5335, and Fe5406. In the subsequent steps we *add in turn* particular sets of indices that are sensitive to the element the abundance of which we want to determine. The indices used are $\rm CN_1$, $\rm CN_2$, Ca4227, H$\gamma_{\rm A}$, H$\gamma_{\rm F}$, G4300, $\rm C_2$4668, $\rm Mg_1$, and $\rm Mg_2$ for carbon, $\rm CN_1$, $\rm CN_2$, and Ca4227 for nitrogen, $\rm Mg_1$ and $\rm Mg_2$ for magnesium, Ca4227 for calcium, and Fe4531 for titanium. The Ti sensitivity of Fe4531 is relatively weak, hence the abundance derivations for this element are only tentative. The [O/Fe] ratio is indirectly inferred by assuming that [O/Fe] $\equiv$ [α/Fe]. We show that the model fits to these indices in globular clusters improve considerably through this full chemical analysis.

The ages we derive agree well with the literature. In particular the ages derived here are all consistent with the age of the universe within the measurement errors. There is a considerable scatter in the ages, though, and we overestimate the ages preferentially for the metal-rich globular clusters, which appears to extend the previously reported Hβ anomaly of globular clusters to the other Balmer indices. Our derived total metallicities agree generally very well with literature values on the Zinn & West (1984) scale once corrected for α-enhancement, in particular for those cluster where the ages agree with the CMD ages. We tend to slightly underestimate the metallicity for those clusters where we overestimate the age, in line with the age-metallicity degeneracy.

It turns out that the derivation of individual element abundance ratios is highly unreliable at [Fe/H] < -1 dex, while the [α/Fe] ratio is robust at all metallicities. The discussion of individual element ratios focuses therefore on globular clusters with iron abundances [Fe/H] > -1 dex. We find general enhancement of light and α elements as expected with significant variations for some elements. The elements O and Mg follow the same general enhancement with almost identical distributions of [O/Fe] and [Mg/Fe]. We find slightly lower [C/Fe] and very high [N/Fe] ratios, instead. Hence N is significantly enhanced and C slightly depressed in globular clusters with respect to the other light elements. This chemical anomaly commonly attributed to self-enrichment is well known in globular clusters from individual stellar spectroscopy, and it is the first time that this pattern is derived also from the integrated light.

The α elements follow a pattern such that the elements with higher atomic number, namely Ca and Ti, are less enhanced. More specifically, [Ca/Fe] ratios are lower than [O/Fe] and [Mg/Fe] by about 0.2 dex. Ti continues this trend. We compare this result with recent determinations of element abundances in globular cluster and field stars of the Milky Way. We come to the conclusion that this pattern is now universally found. It suggests that SN Ia contribute significantly to the enrichment of the heavier α elements as predicted in supernova explosion calculations and galactic chemical evolution models. This explains the presence of a Ca under-abundance (close to solar [Ca/Fe] ratios) in massive early-type galaxies and predicts similarly low [Ti/Fe] ratios in populations with short formation time-scales, which we confirm the next chapter.

Chapter 5

Chemical element ratios of SDSS early-type galaxies

In this chapter we discuss chemical enrichments for ∼4000 SDSS early-type galaxies using as tracers a large variety of element abundance ratios, namely [C/Fe], [N/Fe], [O/Fe], [Mg/Fe], [Ca/Fe] and [Ti/Fe]. We utilise the stellar population models of absorption line indices and method presented in Chapter 3 and 4, respectively. We confirm previous results of increasing age, [Z/H] and [O/Fe] ratios (most often represented by [α/Fe] in the literature) with stellar velocity dispersion. We derive identical correlations with velocity dispersion for the abundance ratios [O/Fe], [Mg/Fe] and [C/Fe], implying that C/Mg and C/O are close to solar values. This sets a lower limit on the formation time-scales and star-burst components of early-type galaxies to ∼0.4 Gyr, which is the lifetime of a 3M$\odot$ star, since the full C enrichment must be reached. [N/Fe] correlates with velocity dispersion, but offset to lower values and with a steeper slope compared to the other element ratios. We do not find any environmental dependencies for the abundances of C and N, contrary to previous reports in the literature. [Fe/H] does not correlate with velocity dispersion over the entire parameter range covered, but for fixed age we find a steep trend for the [Fe/H]-σ relation. This trend is weaker than the analogous for total metallicity (which also shows steeper trends at fixed age) owing to the lower Fe contribution from SN Ia for more massive early-type galaxies. We find [Ca/Fe] ratios that are close to solar values over the entire velocity dispersion range covered. Tentative, due to large scatter, the results for [Ti/Fe] indicate that Ti follows the trends of Ca. This implies a significant contribution from SN Ia to the enrichment of heavy α-elements and puts strong constraints on supernova nucleosynthesis and models of galactic chemical evolution.

5.1 Introduction

5.1.1 Background

The chemical compositions of stellar atmospheres are tracers of the element abundances of the parent gas clouds forming the stars throughout the formation history of a galaxy. Some elements are also affected by dredge-up during stellar evolution (e.g. Sweigart, Greggio & Renzini, 1989). Stellar populations are therefore a powerful tool to extract information on chemical evolution in the Universe. Element abundances can be directly determined for individual stars of resolved stellar populations in the Milky Way or in nearby dwarf galaxies, using absorption lines measured in high resolution stellar spectra (e.g. Edvardsson et al., 1993; Fuhrmann, 1998; Bensby, Feltzing & Lundström, 2004; Feltzing, Primas & Johnson, 2009; Bensby et al., 2010). Light averaged spectra must instead be used for determining element abundances of distant unresolved stellar populations.

Elements are produced in stellar nucleosynthesis besides the primordial nucleosynthesis of H and He (see Section 3.1.2). The chemical enrichment of stellar populations depends on the star formation history, initial mass function, fraction of exploding supernovae etc. The chemical pattern of the parent gas clouds will be carried on to new stellar generations. Thus the chemical enrichment of stellar populations is also affected by mechanisms affecting the ISM such as the efficiency of stellar winds to mix newly synthesised elements with the ISM, efficiency of outflow from galactic winds to remove enriched gas, inflow of less enriched gas from gas reservoirs etc. (e.g. Matteucci & Francois, 1989; Matteucci, 1994). Chemical enrichment sets stringent constraints on galaxy formation and evolution.

Studies beginning in the late 1970's have revealed non-solar abundance ratios for the stellar populations of early-type galaxies (e.g. O'Connell, 1976; Peterson, 1976; Burstein et al., 1984; Worthey, Faber & Gonzalez, 1992; Davies, Sadler & Peletier, 1993; Surma & Bender, 1995), indicating different chemical enrichment histories. This triggered more detailed investigations showing that the ratio between α-elements and Fe-peak elements increases with increasing galaxy mass for early-type galaxies (e.g. Trager et al., 2000b; Thomas et al., 2005; Bernardi et al., 2006; Clemens et al., 2006; Thomas et al., 2010). Most interestingly, the [α/Fe] ratio participates in the E-E dichotomy, i.e. elliptical galaxies with low [α/Fe] ratios have core-less central profiles, while [α/Fe]-enhanced galaxies with short formation time-scales have cores (Graham et al., 2003; Trujillo et al., 2004; Kormendy et al., 2009).

As we have seen in the previous chapter individual element abundance ratios, in addition to α/Fe, can further disentangle the formation of different stellar populations. Edvardsson et al. (1993) and Bensby et al. (2010) derive as many as 12 different element abundance ratios to distinguish between the different formation histories of the stellar populations in the Milky Way. A number of studies have derived individual element abundance ratios for early-type galaxies (Sánchez-Blázquez et al., 2003, 2006a; Clemens et al., 2006; Kelson et al., 2006; Graves et al., 2007; Graves & Schiavon, 2008; Smith et al., 2009; Price et al., 2011), in several cases for fairly small samples. Different methods are applied in these studies, but they are all based on absorption line indices. The results are dependent on the method applied and the sample used.

To fully interpret observed element abundance ratio trends, stellar nucleosynthesis needs to be understood. Pipino et al. (2010) find up-to-date models of chemical evolution to struggle in simultaneously reproducing observed abundance ratios for Carbon and Nitrogen from the unresolved stellar populations of early-type galaxies.

We adopt the method presented in Chapter 4 for deriving the element abundance ratios [O/Fe] (representing [α/Fe]), [C/Fe], [N/Fe], [Mg/Fe], [Ca/Fe] and [Ti/Fe], which is based on the new flux-calibrated stellar population models of absorption line indices presented in Chapter 3. We analyse a sample of 3802 SDSS early-type galaxies for which we investigate element ratio scaling relations with velocity dispersion.

The chapter is organised as follows. The SDSS early-type galaxy sample used is presented in Section 5.2. The results of derived element abundance ratios are presented in Section 5.3 and further discussed and compared with the literature in Section 5.4. Conclusions are given in Section 5.5.

5.1.2 Formation time-scales from element abundance ratios

Different elements are produced in stars of varying masses and consequently different stellar life-times (see Section 3.1.2). Hence the time-scales for the enrichment of the ISM varies from element to element. As star formation progresses the element abundances will increase in each new generation of stars, but with varying rate for the different elements. The ratio of different element abundances found in the stars will therefore be strongly dependent on the duration of star-formation.

The α/Fe ratio is a particularly strong indicator of star formation time-scales. Short-lived massive stars (M$>$8M$_{\odot}$) expel heavy elements all the way up to Fe through SN II explosions (see Section 3.1.2), with an abundance peak found around the light α-elements O and Mg (Thielemann et al., 1996). SN Ia yields are instead strongly peaked at the atomic numbers of Fe-like elements (Nomoto et al., 1984). In addition, SN Ia span a wide range of delay times (see Chapter 6 for more details), resulting in an extended

chemical enrichment of Fe-like elements compared to the prompt enrichment of light α-elements from SN II. Hence the α/Fe ratio and the individual element ratios Mg/Fe and O/Fe reflect the duration of star formation, where lower element ratios are expected for more extended star formation histories. Modelled yields and delay times for the explosions of SN II and SN Ia can be used to establish a relation between the element ratios mentioned above and star formation time-scales (e.g. Thomas et al., 2005, 2010).

The sources of C and N production are still debated (see Section 5.4.3-5.4.4 for further discussions), but stars in the mass range $3M_{\odot}<M<8M_{\odot}$ are believed to be major contributors to the production of these elements (Renzini & Voli, 1981; van den Hoek & Groenewegen, 1997). Hence the N/Mg, N/O, C/Mg and C/O ratios are also sensitive to star formation time-scales. The life-time of a $3M_{\odot}$ star is $\sim$0.4 Gyr (Castellani et al., 1992; Bertelli et al., 2009), while the delay times of SN Ia can reach above 10 Gyr (see Chapter 6). Hence the N/Mg, N/O, C/Mg and C/O ratios are only sensitive to very short star formation time-scales, while the α/Fe (Mg/Fe, O/Fe) ratio(s) are sensitive to extended time-scales.

5.2 The data sample

The selected sample is part of the MOSES catalogue (MOrphologically Selected Early-types in SDSS). This is described in detail in Schawinski et al. (2007) and Thomas et al. (2010) (T10) and only a brief description is given here. The MOSES sample consists of 48 023 galaxies from the SDSS Data Release 4, selected to have a magnitude $r < 16.8$ in the redshift range $0.05 < z < 0.10$. The selection criteria ensured a reliable visual inspection of galaxy morphology and the full sample was divided into late-types (31 521) and early-types (16 502) through a purely visual classification scheme.

As comprehensively described in T10 the 25 standard Lick absorption line indices were measured on the galaxy spectra downgraded from the SDSS spectral resolution to the Lick/IDS resolution and corrected for emission line fill in using GANDALF/PPXF (Cappellari & Emsellem, 2004; Sarzi et al., 2006). The stellar kinematics and best-fit stellar templates from PPXF were used in T10 for correcting the measured indices for stellar velocity dispersion broadening effects. The velocity dispersion measurements derived and published in T10 are used in Section 5.3 as proxies for galaxy mass.

The visual classification does not bias against star forming galaxies and the sub-sample of early-type galaxies will therefore include galaxies with blue colours, having possible on-going star formation or recent star formation. These galaxies can have possible emission line contamination in the absorption features, but the use of GANDALF gives reliable Lick index measurements for the full sample.

Table 5.1: Discard percentage for all Lick indices

Index	Discard %
$H_{\delta A}$	< 1.0
$H_{\delta F}$	< 1.0
CN_1	< 1.0
CN_2	< 1.0
Ca4277	< 1.0
G4300	3.8
$H_{\gamma A}$	< 1.0
$H_{\gamma F}$	< 1.0
Fe4383	< 1.0
Ca4455	not used
Fe4531	< 1.0
$C_2$4668	< 1.0
$H\beta$	< 1.0
Fe5015	not used
Mg_1	< 1.0
Mg_2	< 1.0
Mgb	< 1.0
Fe5270	1.1
Fe5335	< 1.0
Fe5406	< 1.0
Fe5709	not used
Fe5782	not used
NaD	not used
TiO_1	not used
TiO_2	not used

The final sample (3802 objects) used in this work was selected according to T10. This is a sub-sample of early-type classified galaxies in the narrow redshift range $0.05 < z < 0.06$, chosen to minimise evolutionary effects present when using the full range of redshifts, affecting the derivation of stellar population parameters.

5.3 Results

In the following we present stellar population parameters and element abundance ratios as functions of the stellar velocity dispersion measurements derived in T10 (see Section 5.2). Since this is a continuation of the work of T10 we compare the results of the base parameters (age, Z/H and O/Fe) with their results. Further comparisons with the literature are discussed in Section 5.4.

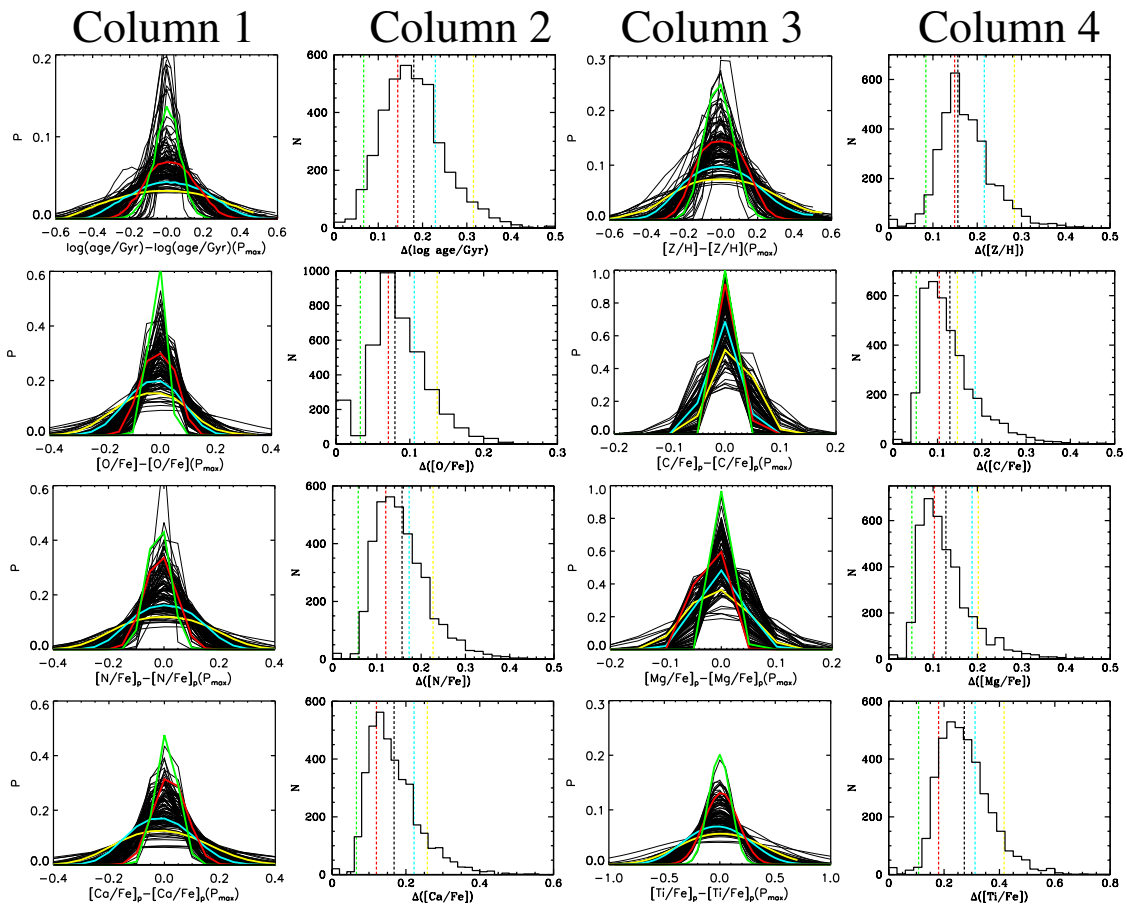

Figure 5.1: Column 1 and 3: Probability distributions for 100 randomly selected objects (black gaussians) and 4 highlighted objects with varying parameter errors (coloured gaussians). Column 2 and 4: Distributions of parameter errors, which are estimated from the probability distributions (see text for more details), for the the full sample. Black dashed line shows the average errors, while colour dashed lines shows the errors for the highlighted probability distributions in column 1 and 3 with corresponding colours.

5.3.1 Discarded indices

The procedure developed and presented in Section 4.3 allow the removal of badly fitted indices. In 5.2% of the cases one index was discarded, while more than one index was discarded for 1.6% of the 3802 objects. Compared to T10 the percentage where at least one index is discarded has been reduced from >30% to 5.8%. This is partly due to the fact that some indices used in T10 have not been considered here (see Section 4.3.4), e.g. Ca4455 and NaD that were the most frequently discarded indices in T10. The inclusion of individual element abundance ratios improve the fit for several indices and is thus also responsible for the lower number of discarded indices. Table 5.1 gives the discard percentage for all Lick indices. G4300 is the index most frequently removed, as it was discarded in 3.8% of the cases, while Fe5270 reached 1.1% and the rest of the indices had a discard percentage less than 1.0%.

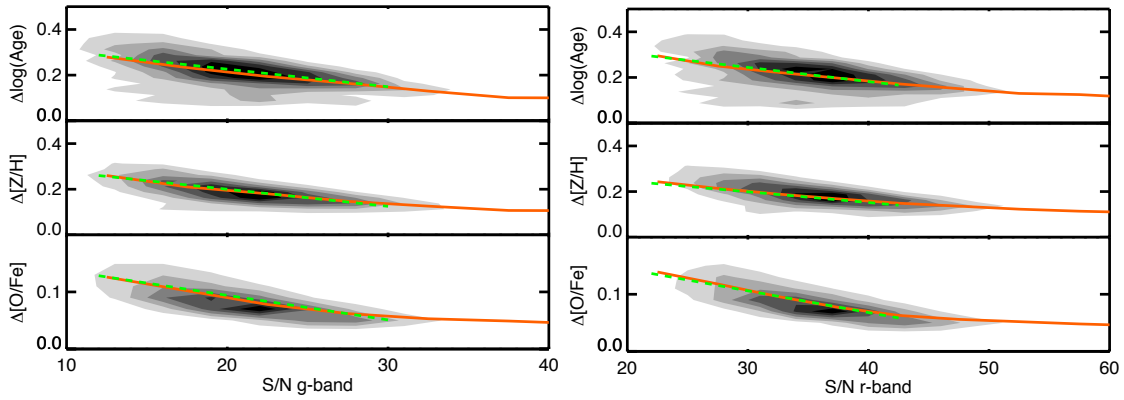

Figure 5.2: Relationship between the estimated errors of the base parameters age, [Z/H] and [O/Fe] with S/N ratio in the g-band (left hand panel) and r-band (right hand panel) for the 3802 early-type galaxies studied (contours). Orange solid lines are mean errors in bins of S/N with a width of 5 dex and green dashed lines show linear relationships below a S/N of ∼30 and ∼45 for the g-band and r-band, respectively, on the form error=a×S/N+b. The fit parameters a and b are given in Table 5.2.

5.3.2 Parameter errors

Fig. 5.1 shows the normalised probability distributions around the χ^2-minimum of the model fits (see Section 4.3.5 for details) for 100 randomly selected objects (Eiffel tower plots in 1st and 3rd column, black gaussians) of our sample (see Section 5.2) together with the distributions of the estimated errors (2nd and 4th column). Four objects are highlighted demonstrating the relationship between the sizes of the errors and the widths of the probability functions. The dashed vertical lines in column 2 and 4 show the error estimates of these objects and are coloured according to the highlighted probability distributions in column 1 and 2. Black dashed vertical lines in column 2 and 4 are average errors. The probability distributions are moved to a common position by shifting them with the parameter value at peak probability (P_{max}). In general we find very well defined one-peaked gaussians. For increasing errors the probability distributions clearly increase in width.

Fig 5.2 shows the relationship between the estimated errors for the base parameters (age, [Z/H] and [O/Fe]) and the signal-to-noise (S/N) ratio of the galaxy spectra for the 3802 early-type galaxies studied in this work (contours). The left hand and right hand panels show the relationship for S/N in the g-band and r-band, respectively. The S/N ratios are the median values of S/N per pixel in each band as given by the SDSS spectroscopic fits-headers. Orange solid lines are mean errors in bins of S/N with a width of 5 dex. Below a S/N of ∼30 and ∼45 for the g-band and r-band, respectively, the error-S/N relationships are close to linear. Thus the green dashed lines show linear relationships in

Table 5.2: Linear error-S/N relationships below S/N∼30 and S/N∼45 for the g-band and r-band, respectively, on the form error=a×S/N+b.

Band	Parameter	a	b
g	Δ log(age)	-0.0077	0.38
g	Δ[Z/H]	-0.0075	0.35
g	Δ[O/Fe]	-0.0043	0.18
r	Δ log(age)	-0.0062	0.43
r	Δ[Z/H]	-0.0047	0.34
r	Δ[O/Fe]	-0.0038	0.22

these regimes on the form error=a×S/N+b with the values of the fit parameters a and b given in Table 5.2.

5.3.3 A direct comparison with T10

In Fig. 5.3 we compare the ages, [O/Fe] ratios and total metallicities derived using the method presented in Section 4.3 (J11 setup) to the corresponding parameters from T10 (where [α/Fe] corresponds to [O/Fe] of this work, see Section 4.3.1). Contours show the density of data points and dashed lines are 1-to-1 relationships. Solid lines are least-square fits with fit parameters given by the labels. We find a very good agreement for the derived ages and generally good agreements for total metallicity and [O/Fe]. For the latter two this work shows overall higher values and the differences increase towards lower parameter values. Still, the average differences are small within the parameter range containing the majority of data points ($<$0.2 dex for [Z/H] and $<$0.1 dex for [O/Fe]) .

Using our new models (see Chapter 3) we have also derived the stellar population parameters age, [α/Fe] and total metallicity using the same setup as used in T10 (TMJ25 setup), i.e. using all 25 Lick indices and not considering element ratios beyond [α/Fe]. With these results we can disentangle the effect on the derived parameters from using both new models and accounting for individual element ratios. A direct comparison between the TMJ25 and T10 is also included in Fig. 5.3 (least-square fit dash-dotted lines). Again we find a good agreement between the derived ages. In the old age regime the TMJ25 ages are somewhat higher (∼0.1 dex). Hence in this regime our new models seem to result in slightly older ages compared to the TMB/K models, while accounting for element ratios results in younger ages. The TMJ25 and T10 metallicities are very similar within the parameter range containing the majority of data points (contours). Hence, the metallicities do not change considerably when using the new models. Instead, the metallicities are slightly lower if individual element ratios are not taken into account.

For [α/Fe] TMJ25 produces overall higher element ratios by ∼0.1 dex compared to T10. In this case the choice of models matters as well as accounting for individual

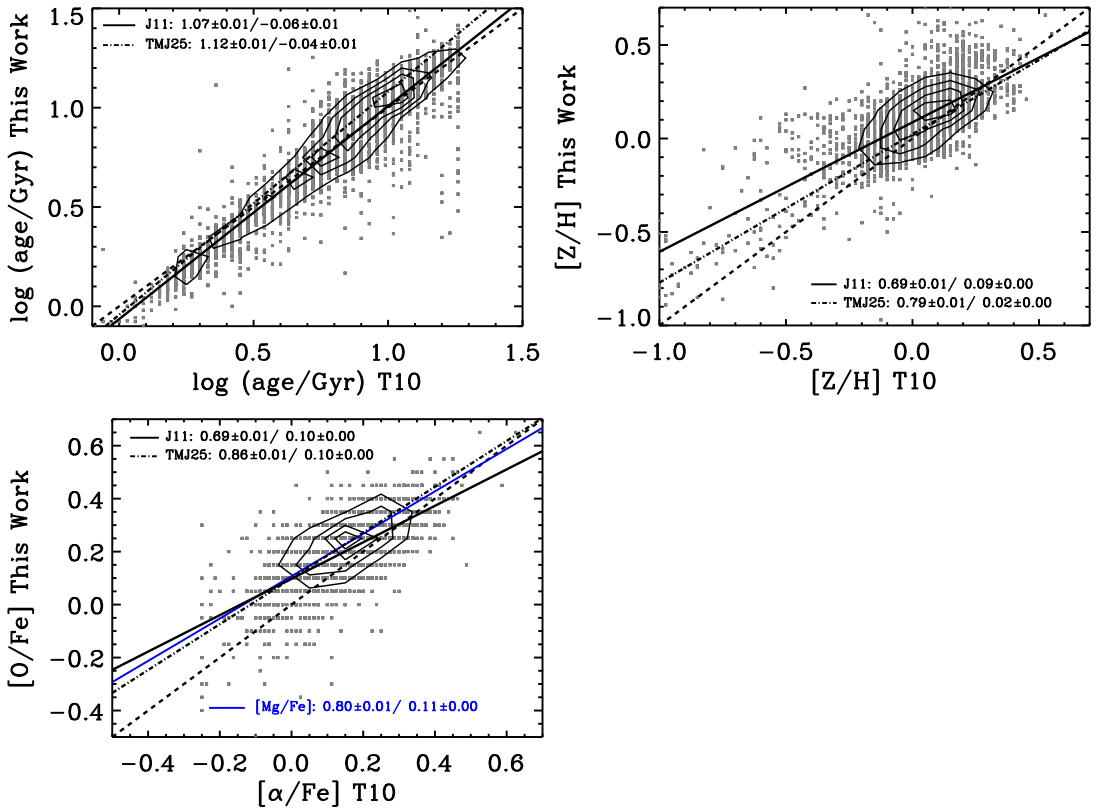

Figure 5.3: Comparison between the derived parameters of this work (y-axes) and T10 (x-axes) for age (upper left hand panel), total metallicity (upper right hand panel) and [O/Fe] (lower panel). For the latter we compare to the [α/Fe] ratios from T10 as it corresponds to [O/Fe] of this work (see Section 4.3.1). Contours show the density of data points and solid lines are least-square fits. These results are derived using the method presented in Section 4.3 (J11 setup). For our new models (see Chapter 3) we have also derived the stellar population parameters with the same setup as used in T10 (TMJ25 setup). Least-square fit representing the relationship between these results and T10 are shown as dot-dashed lines. Fit parameters are given by the labels and dashed lines are 1-to-1 relationships

element ratios. In the lower panel we have also included a comparison between the J11 [Mg/Fe] ratios and the [α/Fe] ratios from T10 (least-square fit blue line). In fact the [Mg/Fe] ratios agree very well with the TMJ25 [α/Fe] ratios as the blue and dash-dotted are very similar. Hence the [α/Fe] ratios derived without taking individual element ratios into account reflect [Mg/Fe] rather than [O/Fe]. This is probably due to the fact that the Lick indices are more sensitive to variations in the abundance of Mg than O (see Section 4.3.1).

The TMJ25 setup consider all Lick indices and the J11 setup a selection of 18 indices best calibrated with galactic globular clusters (see Section 4.3). The difference seen between these two setups may therefore arise from the choice of indices instead of accounting for element ratios. To evaluate this we also derived ages, [α/Fe] ratios and total metallicities using our new models without element ratios, but for the 18 indices

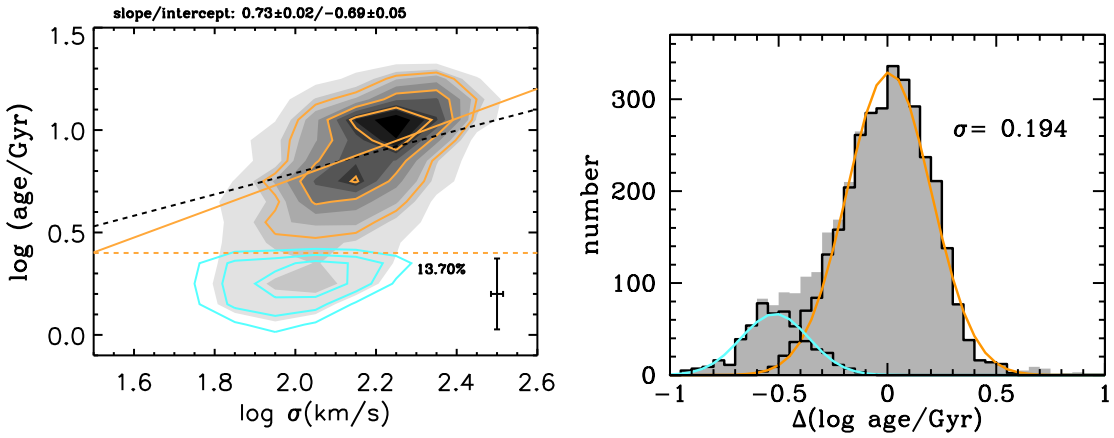

Figure 5.4: Left hand panel: shows the relationship between the derived light-average ages and velocity dispersion. The dashed orange line indicate the separation of an old red sequence population (orange contours) from a rejuvenated population (cyan contours) with light-average ages smaller than 2.5 Gyr (Thomas et al., 2010). The fraction of rejuvenated galaxies is indicated below the separation line. The whole sample is shown as grey-scaled filled contours. The orange solid line is a least-square fit to the red sequence population and the parameters of the fit are given at the top of the panel. The dashed black line is the analogous fit from T10 for comparison. Median 1σ-errors are shown in the lower right corner. Right hand panel: shows the distribution of deviation in age from the least-square fit to the red sequence population with the same colour coding as in the left hand panel. The standard deviation of the gaussian fitted to the distribution of the red sequence population (orange line) is indicated in the upper right corner.

considered in this work. These result are very similar to that of TMJ25, such that the different choices of indices do not matter significantly.

5.3.4 Ages

The relationship between luminosity-weighted age and velocity dispersion is presented in the left hand panel of Fig 5.4. The full sample is shown with grey-scaled, filled contours. We reproduce the result from T10 of having a bimodal distribution of ages in analogy to a red sequence population (log(age)>0.4, orange contours) and a rejuvenated blue cloud population (log(age)<0.4, cyan contours) of low mass early-type galaxies, identified thanks to the purely visual classification of the MOSES sample (see Section 5.2). The fraction of rejuvenated galaxies is 13.70%, close the corresponding fraction of 10.15% found in T10. The rejuvenated population is further discussed in the following sections and in more detail in Section 5.4.1. Fig. 5.4 also shows a σ-clipped (3σ limit) linear least-square fit to the red sequence population (orange solid line), along with the analogous from T10 for comparison (dashed black line). We find very similar trends, but with a slightly steeper slope, as in T10, i.e. increasing ages with increasing velocity dispersion.

The distribution around the fit to the red sequence population is shown in the right hand panel of Fig. 5.4, for the whole sample (grey histogram), red sequence population

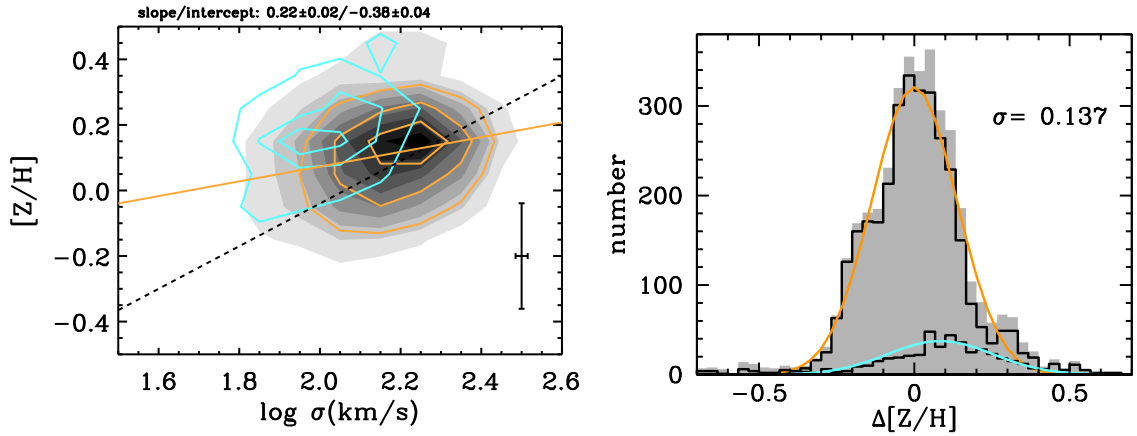

Figure 5.5: Left hand panel: shows the relationship between the derived total metallicities and velocity dispersion. Rejuvenated objects with light-averaged ages smaller than 2.5 Gyr (see Fig. 5.4) are presented with cyan contours and the orange contours show the old red sequence population. The whole sample is shown as grey-scaled filled contours. The orange solid line is a least-square fit to the red sequence population and the parameters of the fit are given at the top of the panel. The dashed black line is the analogous fit from T10 for comparison. Median 1σ-errors are shown in the lower right corner. Right hand panel: shows the distribution of deviation in age from the least-square fit to the red sequence population with the same colour coding as in the left hand panel. The standard deviation of the gaussian fitted to the distribution of the red sequence population (orange line) is indicated in the upper right corner.

and rejuvenated population (black open histograms). Gaussians fitted to the rejuvenated and red sequence distributions are shown with the same colour coding as in the left hand panel, with the standard deviation of the latter given by the label. The rejuvenated population shows a distinct peak, offset from the red sequence population to younger ages by $\sim$0.55 dex.

5.3.5 [Z/H]

The left hand panel of Fig. 5.5 shows the relationship between total metallicity and velocity dispersion, with the same colour coding as in Fig. 5.4. The least-square fit to the red sequence population (orange line) indicate a strong correlation between total metallicity and velocity dispersion. This is in agreement with T10, but the slope of the fit derived here is smaller than the corresponding fit derived in T10 (black dashed line). In Section 5.3.3 we find that not accounting for element ratios produce lower metallicities in T10 compared to this work. This difference increases towards lower metallicities and produce the flatter slope of the [Z/H]-σ relation.

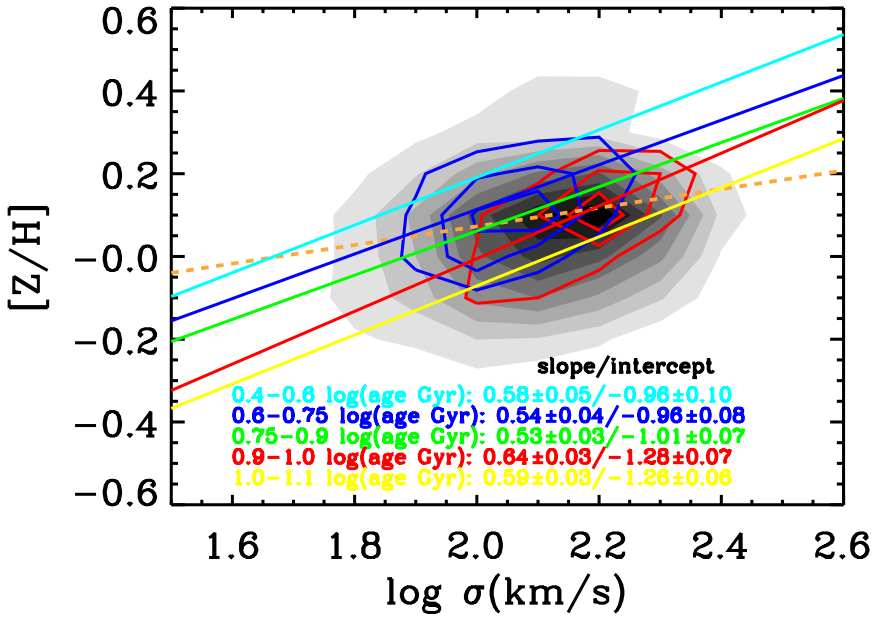

Figure 5.6: Contour plots for the relationship between total metallicity and velocity dispersion in bins of narrow log(age) intervals. Blue contours are for 0.6<log(age)<0.75 Gyr and red contours for 0.9<log(age)<1.0. Grey filled contours show the whole sample. Coloured lines are least-square fits to bins of varying age intervals, indicated by the correspondingly coloured labels that also give the parameters of the fits. The orange dashed line is the least-square fit to the whole sample (see Fig. 5.5)

The distribution around the fit to the red sequence population is shown in the right hand panel of Fig. 5.5. The rejuvenated population (cyan gaussian) shows an offset towards higher metallicities by ∼0.1 dex compared to the red sequence population (orange gaussian), a behaviour also found by T10.

In Fig. 5.6 we show least-square fits to the [Z/H]-σ relationship in five narrow age-bins. These fits are indicated by the different colours with correspondingly coloured labels. The size of the bins were chosen to include a similar number of objects in each bin. Contours for two of the age bins are also shown, representing the fits with corresponding colours, and the grey-scaled filled contours represent the full sample. The fits to the age bins clearly show steeper slopes than for the entire red sequence population (dashed orange line). The fits to the age bins also show a parallel behaviour differing mainly in zero point offsets. This indicates a planar dependence on age and velocity dispersion for total metallicity, i.e. total metallicity correlate with velocity dispersion at fixed age and anti-correlate with age at fixed velocity dispersion. Such a behaviour has previously been found by Trager et al. (2000b). The large scatter in [Z/H] found for the entire sample is partly an effect of this planar dependence. The shallower slope for the entire red sequence sample is due to the generally older ages found for galaxies with a higher velocity dispersion and vice versa (see Fig. 5.4).

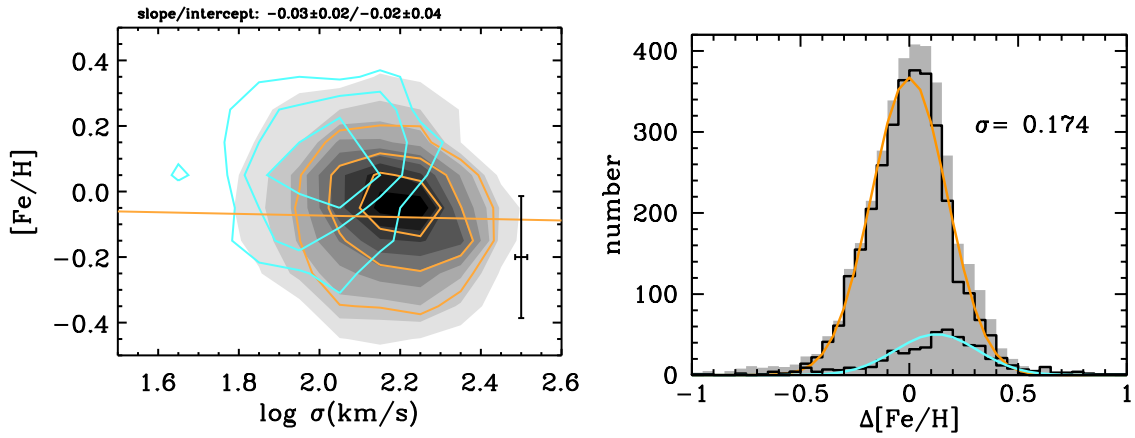

Figure 5.7: Left hand panel: shows the relationship between iron abundance and velocity dispersion. Rejuvenated objects with light-averaged ages smaller than 2.5 Gyr (see Fig. 5.4) are presented with cyan contours and the orange contours show the old red sequence population. The whole sample is shown as grey-scaled filled contours. The orange solid line is a least-square fit to the red sequence population and the parameters of the fit are given at the top of the panel. Median 1σ-errors are shown in the lower right corner. Right hand panel: shows the distribution of deviation in age from the least-square fit to the red sequence population with the same colour coding as in the left hand panel. The standard deviation of the gaussian fitted to the distribution of the red sequence population (orange line) is indicated in the upper right corner.

5.3.6 [Fe/H]

Iron abundances derived using Eq. 4.14 in Section 4.3.3 are presented in the left hand panel of Fig. 5.7 as a function of velocity dispersion, with the same colour coding as in Fig. 5.4 for the results of this work. The least-square fit (orange line) shows no correlation between iron abundance and velocity dispersion for the full red sequence population. Hence the [Fe/H]-σ relation is significantly flatter than the [Z/H]-σ relationship presented in the previous section. Similar patterns have also been found by Trager et al. (2000b) and Graves et al. (2007), but the slopes of their [Fe/H]-σ relations are different from zero. Similar to this work Price et al. (2011) find a relatively flat [Fe/H]-$\log \sigma$ slope for a sample of 222 passive galaxies.

The distribution around the fit to the red sequence population is shown in the right hand panel of Fig. 5.7. The rejuvenated population (cyan gaussian) shows an offset ($\sim$0.15 dex) towards higher [Fe/H] compared to the red sequence population (orange gaussian). This offset is more pronounced than for [Z/H] (compare with the right hand panel of Fig. 5.5).

In Fig. 5.8 we show least-square fits to the [Fe/H]-σ relationship in five narrow age-bins, with the same colour coding and bin sizes as in Fig. 5.6. Similar to the total metallicity case, we find a planar dependence on velocity dispersion and age, i.e. iron abundance correlate with velocity dispersion at fixed age and anti-correlate with age at fixed velocity

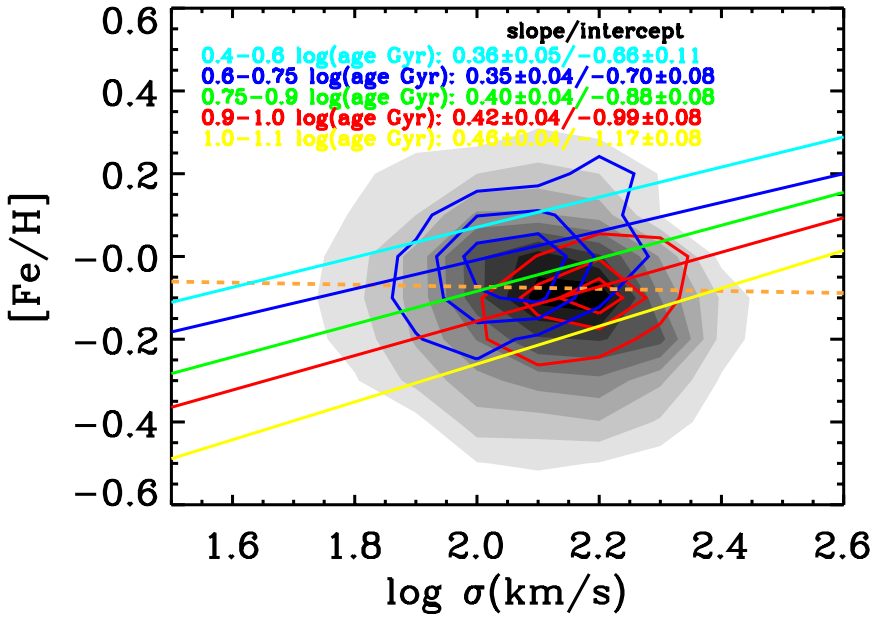

Figure 5.8: Contour plots for the relationship between iron abundance and velocity dispersion in bins of narrow log(age) intervals. Blue contours are for 0.6<log(age)<0.75 Gyr and red contours for 0.9<log(age)<1.0. Grey filled contours show the whole sample. Coloured lines are least-square fits to bins of varying age intervals, indicated by the correspondingly coloured labels that also give the parameters of the fits. The orange dashed line is the least-square fit to the whole sample (see Fig. 5.7)

dispersion. Such a behaviour have again been found by Trager et al. (2000b) and also by Smith et al. (2009). The planar dependence is partly responsible for the large scatter in iron abundance found for the full sample. Compared to total metallicity we find flatter slopes for the [Fe/H]-σ relationships in the age-bins as well as for the full sample. The fits to the age bins in Fig. 5.8 clearly show steeper slopes than for the full red sequence population sample (dashed orange line), since older ages are in general found for galaxies with a higher velocity dispersion and vice versa (see Fig. 5.4 and Section 5.3.5). Hence, at fixed age the effective Fe yields are higher in more massive systems. However, Fe enrichment is suppressed in older galaxies, because of time-scale dependent contribution from SN Ia (see Section 5.1.2). Therefore the relation becomes flat for the overall population and the [Fe/H]-age anti-correlation is steeper than the [Z/H]-age anti-correlation.

5.3.7 [O/Fe]

The relationship between [O/Fe] ratio and velocity dispersion is presented in the upper left panel of Fig 5.9, with the same colour coding as in Fig. 5.4. For the red sequence population we find a somewhat shallower slope for the [O/Fe]-σ relation (orange line) compared to the [α/Fe]-σ relation from T10 (dashed black line), but the general agreement is

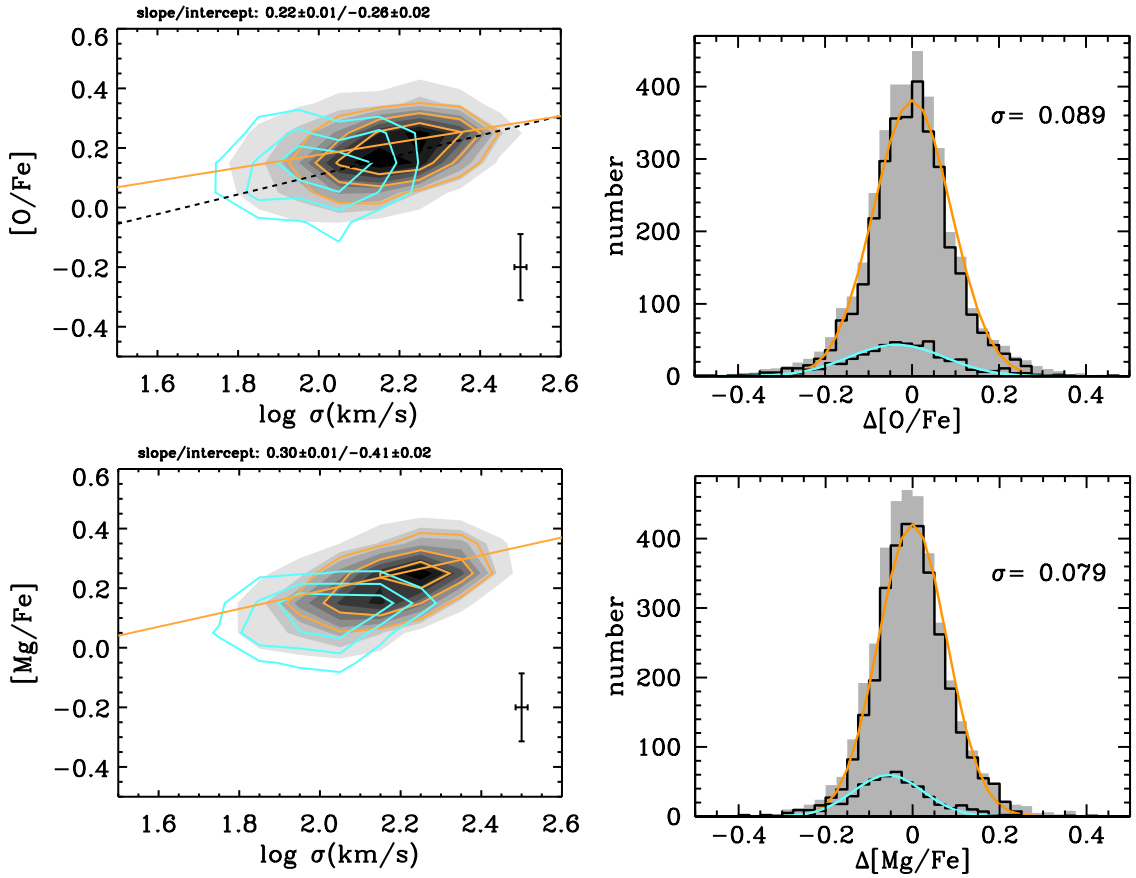

Figure 5.9: Left hand panels: show the relationships for the derived O/Fe (upper) and Mg/Fe ratios (lower) with velocity dispersion. Rejuvenated objects with light-averaged ages smaller than 2.5 Gyr (see Fig. 5.4) are presented with cyan contours and the orange contours show the old red sequence population. The whole sample is shown as grey-scaled filled contours. The orange solid lines are least-square fits to the red sequence population and the parameters of the fits are given at the top of the panels. Median 1σ-errors are shown in the lower right corners. The dashed line in the upper left panel is the [α/Fe]-$\log\sigma$ relation from T10. Right hand panels: show the distribution of deviation in age from the least-square fits to the red sequence population for O/Fe (upper) and Mg/Fe (lower), with the same colour coding as in the left hand panels. The standard deviation of the gaussians fitted to the distributions of the red sequence population (orange lines) are indicated in the upper right corners.

very good, i.e. a tight correlation between [O/Fe] and velocity dispersion. The shallower slope can be explained by metallicity dependent C yields that depress the amount of O in more metal-rich systems (see discussion in Section 5.4.3).

Delayed enrichment of Fe-like elements from SNIa explosion compared to the prompt enrichment of α-elements from SNII explosion, results in lower α/Fe ratios for objects with more extended star formation histories. Hence T10 interpreted the higher [α/Fe] ratios found in more massive galaxies as shorter formation time-scales for such objects, and evidence for down-sizing of early-type galaxies. This interpretation gets support from the [O/Fe]-σ found in this work, since O belongs to the α-elements.

The upper right panel of Fig. 5.9 shows the distribution around the fit to the red sequence population. The rejuvenated population (cyan gaussian) shows an offset towards lower [O/Fe] ratios compared to the red sequence population (orange gaussian). This offset is less pronounced compared to what T10 found for [α/Fe].

5.3.8 [Mg/Fe]

The [Mg/Fe]-σ relationship is presented in the lower left panel of Fig. 5.9, with the same colour coding as in Fig. 5.4 for the contours and least-square fit. For the red sequence population [Mg/Fe] clearly increases with velocity dispersion, a pattern also found by Sánchez-Blázquez et al. (2006a), Graves et al. (2007), Smith et al. (2009) and Price et al. (2011). This result gives further support to the down-sizing scenario discussed in T10 (see Section 5.3.7), since Mg also belongs to the α-elements. The [Mg/Fe]-σ relationship shows a similar trend as [O/Fe]-σ (compare with the upper left panel of Fig. 5.9). A steeper slope is found for the former relationship, which is in better agreement with the slope of [α/Fe]-σ relation from T10. Thus the T10 [α/Fe] ratios trace [Mg/Fe] rather than [O/Fe] as discussed in Section 5.3.3.

The distribution around the fit to the red sequence population is shown in the lower right panel of Fig. 5.9, with the same colour coding as in Fig. 5.4. The rejuvenated population (cyan gaussian) is offset towards lower [Mg/Fe] ratios compared to the red sequence population (orange gaussian). This offset is more pronounced than for [O/Fe] (see upper right panel of Fig. 5.9, Section 5.3.7). This is again in better agreement with the results for [α/Fe] in T10, which suggests that the [α/Fe] ratio derived in T10 is closest to the true [Mg/Fe] ratio.

5.3.9 [C/Fe]

The [C/Fe]-σ relationship is shown in the upper left panel of Fig. 5.10, with the same colour coding as in Fig. 5.4 for the contours and the least-square fit to the red sequence population. The [Mg/Fe]-σ relationship is included for comparison (dashed orange line). Considering the red sequence population we find a very similar trend for the [C/Fe]-σ relationship (solid orange line) as for [Mg/Fe]-σ (dashed orange line), but the latter trend is slightly steeper. The stronger trend for [C/Fe] can be explained by metallicity dependent C yields (see discussion in Section 5.4.3).

Increasing [C/Fe] ratios with velocity dispersion has also been found by Sánchez-Blázquez et al. (2006a), Graves et al. (2007) and Smith et al. (2009). Sánchez-Blázquez et al. (2006a) report a stronger increase in [Mg/Fe] than [C/Fe] for a sample of 98 early-type galaxies. Graves et al. (2007) and Smith et al. (2009) study $\sim$6000 red sequence SDSS

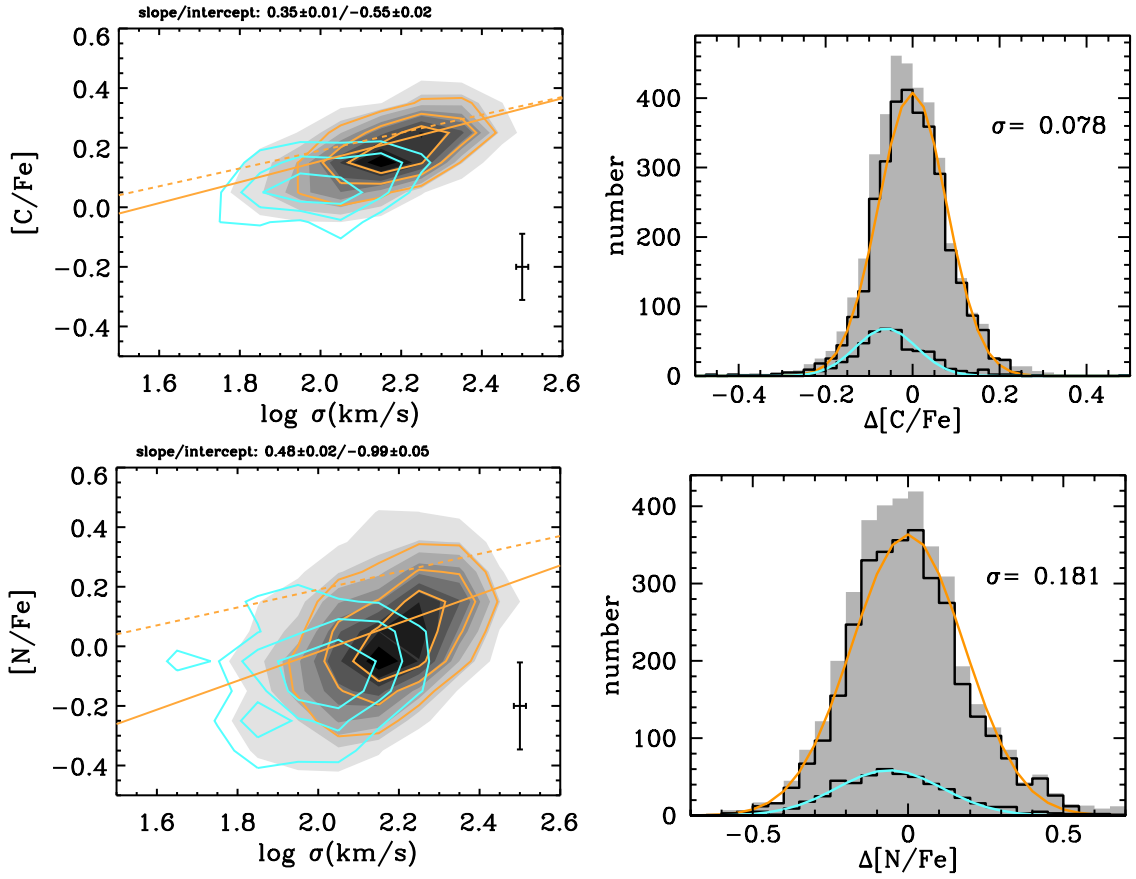

Figure 5.10: Left hand panels: show the relationships for the derived C/Fe (upper) and N/Fe ratios (lower) with velocity dispersion. Rejuvenated objects with light-averaged ages smaller than 2.5 Gyr (see Fig. 5.4) are presented with cyan contours and the orange contours show the old red sequence population. The whole sample is shown as grey-scaled filled contours. The orange solid lines are least-square fits to the red sequence population and the parameters of the fits are given at the top of the panels. Median 1σ-errors are shown in the lower right corners. The dashed orange lines are the [Mg/Fe]-$\log\sigma$ fit. Right hand panels: show the distribution of deviation in age from the least-square fits to the red sequence population for C/Fe (upper) and N/Fe (lower), with the same colour coding as in the left hand panels. The standard deviation of the gaussians fitted to the distributions of the red sequence population (orange lines) are indicated in the upper right corners.

early-type galaxies and 147 red sequence galaxies, respectively, and find, in agreement with this work, a shallower trend for [Mg/Fe] than for [C/Fe]. A similar pattern was also found by Price et al. (2011).

The distribution around the fit to the red sequence population is shown in the upper right panel of Fig. 5.10. The rejuvenated population (cyan gaussian) shows an offset of lower [C/Fe] ratios compared to the red sequence population (orange gaussian). Again very similar to [Mg/Fe] we find a clear offset towards lower [C/Fe] ratios for the rejuvenated population compared to the red sequence population. Hence we find that the [α/Fe] ratio derived in T10 resembles both [Mg/Fe] and [C/Fe]. In fact the slope of the [α/Fe]-σ

relationship from T10 (0.33) falls right in between the slope for [Mg/Fe]-σ (0.30) and [C/Fe]-σ (0.35). Following the discussion in Section 5.3.3 this is probably due to the fact that T10 use absorption line indices sensitive to various element abundance variations to derive [α/Fe] without considering individual abundance ratios. These indices show the strongest signals to Mg and C, such that their derived [α/Fe] ratios reflect [Mg/Fe] and [C/Fe] rather than [O/Fe].

In Section 5.4.3 we discuss the controversy of the origin of C and that the similarity between the derived [Mg/Fe] and [C/Fe] ratios reflect a significant contribution of C from massive stars.

5.3.10 [N/Fe]

The [N/Fe]-σ relationship is shown in the lower left panel of Fig. 5.10, with the same colour coding as in Fig. 5.4 for the contours and least-square fit to the red sequence population. The [Mg/Fe]-σ relationship is shown for comparison (dashed orange line). Despite a fairly large scatter we find a clear correlation between [N/Fe] and velocity dispersion for the red sequence population, i.e. [N/Fe] strongly increases with velocity dispersion. This correlation shows a significantly steeper trend than the analogous found for [Mg/Fe] and [C/Fe]. The [N/Fe] ratios are also offset towards lower abundance ratios by $\sim$0.2 dex compared to [Mg/Fe] and [C/Fe]. An increase in [N/Fe] with velocity dispersion has also been found by Sánchez-Blázquez et al. (2006a), Graves et al. (2007) and Smith et al. (2009). The result of Sánchez-Blázquez et al. (2006a) show steeper trends with velocity dispersion for [Mg/Fe] than for [N/Fe], while Smith et al. (2009) report similar trends, steeper than [Mg/Fe], for [N/Fe] and [C/Fe]. Graves et al. (2007) and Price et al. (2011) find, again in agreement with this work, the steepest trends with velocity dispersion for [N/Fe]. Also in agreement with this work they find [N/Fe] to be offset towards lower abundance ratios compared to [Mg/Fe] and [C/Fe]. However, this offset is dependent on their adopted, fixed value for [O/Fe] (see Section 4.3.8).

The distributions around the fit to the red sequence population are shown in the lower right panel of Fig. 5.10. The rejuvenated population (cyan gaussian) shows no clear offset compared to the red sequence population (orange gaussian), considering the fairly large scatter in the data.

The differences in the derived [C/Fe] and [N/Fe] ratios are interesting as both elements are expected to be enriched through the same processes. A thorough discussion on the origins of C and N are given in Section 5.4.3 and 5.4.4, respectively, and related to the derived element ratios.

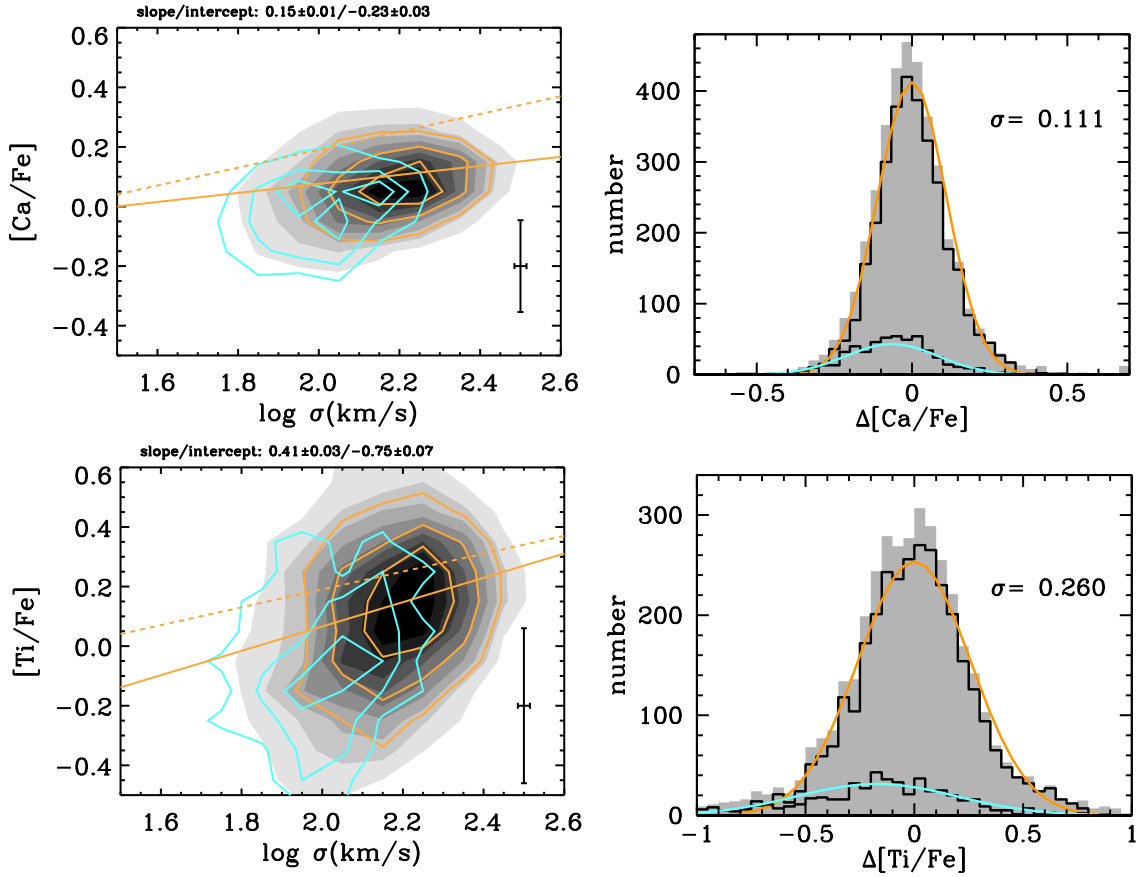

Figure 5.11: Left hand panels: show the relationships for the derived Ca/Fe (upper) and Ti/Fe ratios (lower) with velocity dispersion. Rejuvenated objects with light-averaged ages smaller than 2.5 Gyr (see Fig. 5.4) are presented with cyan contours and the orange contours show the old red sequence population. The whole sample is shown as grey-scaled filled contours. The orange solid lines are least-square fits to the red sequence population and the parameters of the fits are given at the top of the panels. Median 1σ-errors are shown in the lower right corners. The dashed orange lines are the [Mg/Fe]-log σ fit. Right hand panels: show the distribution of deviation in age from the least-square fits to the red sequence population for Ca/Fe (upper) and Ti/Fe (lower), with the same colour coding as in the left hand panels. The standard deviation of the gaussians fitted to the distributions of the red sequence population (orange lines) are indicated in the upper right corners.

5.3.11 [Ca/Fe] and [Ti/Fe]

Trends with velocity for [Ca/Fe] and [Ti/Fe] are shown in the upper left hand and lower left hand panels of Fig. 5.11, respectively, with the same colour codings as in Fig. 5.4. The derived [Ca/Fe] ratios show very weak trends with velocity dispersion and a fairly small scatter. The trend is significantly flatter than compared to the [Mg/Fe]-σ relationship (dashed orange line) and [Ca/Fe] is generally lower than [Mg/Fe] by $\sim$0.1-0.2 dex. This implies an underabundance of Ca compared to Mg, such that Ca scales more closely with Fe rather than Mg. The [Ti/Fe] ratios show a very large scatter, which is due to just a weak response to Ti found for the Lick indices (see Fig. 4.1), requiring very high

S/N observations to constrain [Ti/Fe]. Thus, we can't draw any strong conclusions on the [Ti/Fe]-σ derived trends. Still, when compared to the [Mg/Fe]-σ relationship (dashed orange line) the data suggest an overall under-abundance of Ti compared to Mg with an offset similar to Ca. Milone, Barbuy & Schiavon (2000) instead find that [Ti/Fe]≈[Mg/Fe] using the TiO bands for a sample of 12 galaxies.

The under-abundance of Ca compared to Mg, C and O is in good agreement with previous findings (Thomas et al., 2003b; Graves et al., 2007; Smith et al., 2009; Price et al., 2011). This has been interpreted as a contribution of Ca from SNIa besides SNII. Since Ti is a heavier element than Ca the under-abundance of both of these elements imply that SN Ia also contributes to Ti. These results hint that the contribution from SN Ia is dependent on atomic number for the α-elements. This pattern of lower Ca and Ti abundances compared to Mg, O, and C has also been found for the stellar populations of the Milky Way (Thomas et al., 2011a, and references therein). Hence heavy α-elements are universally produced in SNIa.

The right hand panels of Fig. 5.11 show the distributions around the red sequence populations for Ca (upper panel) and Ti (lower panel), with the same colour coding as in Fig. 5.4. The rejuvenated population (cyan gaussian) show weaker abundance ratios compared to the red sequence population. This is however less pronounced than for Mg and Ca because of a significant contribution from both SN II and SN Ia to Ca. Clearly the standard deviation of the rejuvenated population is fairly large indicating that the exact position of the rejuvenated [Ca/Fe] peak is not very well defined. For Ti the peak of the rejuvenated population is even less well defined and no conclusions regarding the this population can be drawn from Ti.

5.4 Discussion

We present a method for simultaneously deriving the element abundance ratios [C/Fe], [N/Fe], [Mg/Fe], [Ca/Fe] and [Ti/Fe] for unresolved stellar populations, together with the classical stellar population parameters age, [Z/H] and [O/Fe] (representing [α/Fe], see Section 4.3.1). The method is based on the new flux-calibrated stellar population models of absorption line indices presented in Chapter 3. It has been calibrated on galactic globular clusters in Chapter 4, showing a good agreement for the derived parameters with the corresponding of high resolution spectra of individual cluster stars. We apply the method to a sample of 3802 SDSS early-type galaxies. A very similar, but slightly smaller, sample of galaxies was used in T10 who derived the stellar populations parameters age, [Z/H] and [α/Fe], based on the TMB/K models. Hence the analysis presented here can be regarded as an extension to the work of T10. The results derived here are

in good agreement with the results of T10, i.e. age, total metallicity and [α/Fe] increase with increasing velocity dispersion. This is remarkable given that we use new models and a new method for measuring the stellar population parameters that includes individual element abundance ratios.

5.4.1 Rejuvenated population

T10 find the sample of visually identified early-type galaxies to have, in addition to a dominant red sequence galaxy population, a sub-population of rejuvenated galaxies, i.e. galaxies with mainly old stellar populations that have experienced minor recent star formation producing stars that overshine the dominant old stellar populations and thus mimicking overall young stellar populations. The rejuvenated galaxy population was identified by a secondary peak in the derived age distribution showing younger ages than the primary peak and consists mainly of low mass early-type galaxies. This was supported by higher total metallicities and most importantly by lower [α/Fe] ratios and detection of residual star formation through presence of emission lines. Schawinski et al. (2007) and T10 present the emission line diagnostics and show that most of the galaxies in the the young subpopulation have emission lines caused by star formation activity.

The higher total metallicities imply that residual star formation in the rejuvenated galaxies occurred in an ISM containing a fraction of gas that have been chemically enriched compared to pristine metal-poor gas (Thomas et al., 2010). In this work we further show that the rejuvenated population shows a stronger excess in iron abundance compared to total metallicity. This is due to the delayed Fe enrichment from SN Ia, which consequently produces lower [α/Fe] ratios. Hence the extended star formation histories of the rejuvenated galaxies allow enough time for the ISM to be highly enriched in Fe. Table 5.3 summarises the offsets between the distributions of the rejuvenated and red sequence populations derived in Section 5.3.4 - 5.3.11. The standard deviations (σ) divided by $N^{1/2}$, where N is the number of data points, for the two distributions are also included. The result of T10 is reproduced in this work, as we find younger ages together with higher [Z/H], higher [Fe/H] and lower [E/Fe] ratios for the rejuvenated population. In more detail we find [O/Fe], [Mg/Fe], [C/Fe], [N/Fe] and [Ca/Fe] to be offset towards lower abundance ratios by 0.03-0.06 dex. However, the precision of the offsets varies significantly and shows the highest accuracy for [Mg/Fe] and [C/Fe], while the offset for [N/Fe] is less well determined. [Ti/Fe] shows the largest offset, but also with the lowest precision. The accuracy of the offsets is due to the sensitivity of the indices to the variation of the different element abundances (see Section 4.3.1). [Z/H] and [Fe/H] show positive offsets for the rejuvenated population, with [Fe/H] being more offset by $\sim$0.04 dex, i.e. reflecting the offset found for [E/Fe].

Table 5.3: Average offsets in abundance ratios, metallicity and iron abundance for the rejuvenated population compared to the red sequence population. The first column states the parameters, the second and third columns the average offsets for the rejuvenated and red sequence populations, respectively, together with the standard deviations divided by $N^{1/2}$ where N is the number of data points.

Parameter	$<$[E/X]$_{rej}$ $>\pm\sigma_{rej}/N^{1/2}$	$<$[E/X]$_{red}$ $>\pm\sigma_{red}/N^{1/2}$
[O/Fe]	-0.0265±0.0058	0.0±0.0016
[C/Fe]	-0.0577±0.0042	0.0±0.0014
[N/Fe]	-0.0526±0.0082	0.0±0.0032
[Mg/Fe]	-0.0539±0.0044	0.0±0.0014
[Ca/Fe]	-0.0600±0.0058	0.0±0.0020
[Ti/Fe]	-0.143±0.016	0.0±0.0046
[Z/H]	0.106±0.011	0.0±0.0024
[Fe/H]	0.147±0.012	0.0±0.0031

5.4.2 Environment

T10 find environmental dependencies for the fraction of rejuvenated galaxies, while the red sequence galaxy population is unaffected by the environment for the classic parameters age, total metallicity and α/Fe. In brief the fraction of rejuvenated galaxies increases with decreasing velocity dispersion and environmental density. We reproduce these results and do not further discuss environmental dependencies for the classic parameters, the reader is instead referred to T10 for more details. We have also looked at environmental dependencies for the various element abundance ratios and no such can be seen (see Appendix B).

Hence we do not confirm earlier findings of Sánchez-Blázquez et al. (2003) and Sánchez-Blázquez et al. (2006a), who report over-abundances of carbon and nitrogen in environments of lower density for 98 early-type galaxies. The work of Clemens et al. (2006) studies a large sample of SDSS (York et al., 2000) early-type galaxies and find, in agreement with the results derived here, that the environment does not influence the enhancement of carbon.

5.4.3 Lower limit on formation time-scales from [C/Mg]

Fig. 5.12 shows contours and least-square fits for [C/O] (black contours and lines) and [C/Mg] (orange contours and lines) as functions of velocity dispersion for the red sequence population. Both of these abundance ratios are close to solar values. However, differences are noticeable. [C/Mg] is ∼0.0 for the most massive systems and ∼-0.05 for the less massive galaxies. [C/O] is instead ∼0.05 for the most massive systems and ∼-0.05 for the less massive galaxies. The sources of C production have been the subject of a long standing debate. Henry et al. (2000) compared abundances of galactic

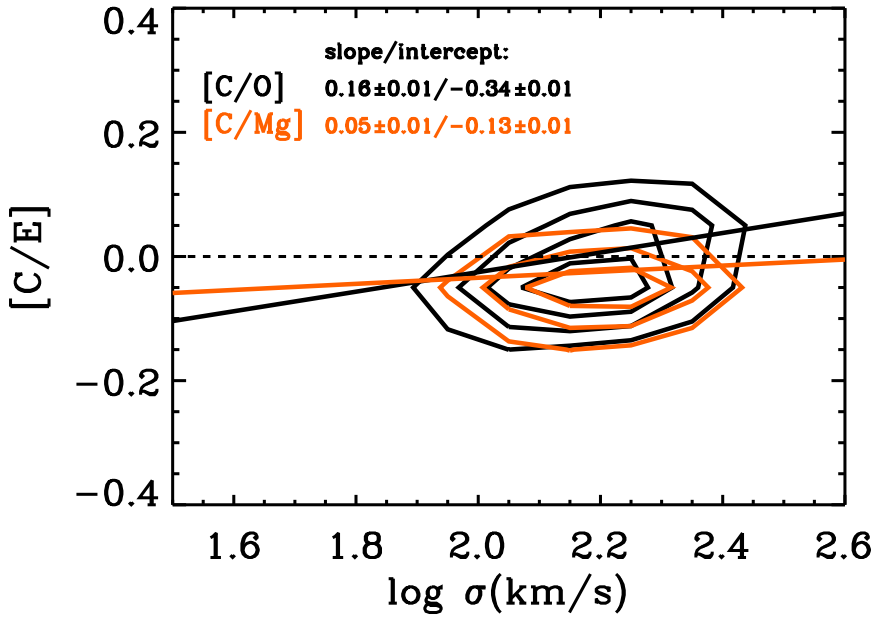

Figure 5.12: [C/O] (black contours) and [C/Mg] (orange contours) as functions of velocity dispersion for the red sequence population. The solid lines are least-square fits to the relationships with corresponding colours and the dashed black line indicate solar abundance ratios. The slope and intercept of the least-square fits are given by the labels.

and extra-galactic HII regions to models of chemical evolution. To match the data they needed stellar yields where massive stars dominate the production of C. Cescutti et al. (2009) found that stellar yields with metallicity dependent C produced in massive stars are needed to match models of chemical evolution with element abundance ratios derived from individual stellar spectra of the galactic stellar populations. Stellar yields take mass-loss and rotation into account. The latter cause newly synthesised C to be brought to the surface layers and ejected into the ISM (Meynet & Maeder, 2002) by mass-loss. The mass-loss rate is dependent on metallicity such that more metal-rich massive stars experience higher mass-loss rates and consequently contribute higher abundances of C.

Hence recent results indicate that massive metal-rich stars are a major C source. Still, intermediate mass stars do also contribute significant amounts of C (Renzini & Voli, 1981; van den Hoek & Groenewegen, 1997). As introduced in Section 3.1.2 dredge-up on the AGB phase of stellar evolution bring C up to the surface layers. This occurs following He-shell flashes when the convective envelope reach down to the inner layers where He-burning has taken place. The dredged-up C is then ejected into the ISM by mass-loss. van den Hoek & Groenewegen (1997) show that C yields from $3M_{\odot}$ stars are significant. To reach solar C/Mg values star formation must continue over long enough time-scales to allow for the contribution of C from both massive and intermediate mass stars (see Section 5.1.2). This sets a lower limit for the star formation time-scales of $\sim$0.4 Gyr, which is the lifetime of a $3M_{\odot}$ stars (Castellani et al., 1992; Bertelli et al., 2009).

This is thus the lower limit for the formation of the most massive early-type galaxies of our sample, since these have [C/Mg]$\sim$0 (see Fig. 5.12). In a scenario where self-enriched bursts of star-formation build up the stellar populations of early-type galaxies, the bursts must last for at least $\sim$0.4 Gyr. However, the formation time-scales must be long enough to allow the enrichment of the ISM to produce the high metallicities observed in massive early-type galaxies. Indeed, a similar time-scale ($\sim$0.4 Gyr) for the onset of galactic winds in models of chemical evolution can produce massive early-type galaxies with metallicities in agreement with observed values (Pipino et al., 2010).

Although weak, the trend of increasing [C/Mg] with velocity dispersion (see Fig. 5.12) could be caused by a metallicity dependent production of C in massive stars. The more massive galaxies are also more metal-rich (see Section 5.3.5). Maeder (1992) predict metallicity dependent C yields from increasing mass-loss in more metal-rich, massive stars. The net result is an ejection of large amount of Carbon before this element is turned into heavier elements. The side effect is that less Carbon is available for producing Oxygen. Thus Maeder (1992) also predicts a depression of Oxygen along with the enhancement of Carbon at higher metallicities, while at low metallicities the opposite situation is apparent. This behaviour was confirmed by e.g. Cescutti et al. (2009) for the Milky Way. In Fig. 5.12 we have also seen that [C/O] increases with velocity dispersion such that super-solar and sub-solar [C/O] ratios are found for the most massive and least massive galaxies, respectively. Hence the flatter slope found for the [O/Fe]-σ relationship compared to [Mg/Fe]-σ can be explained by the metallicity dependent balance between C and O yields from massive stars, since higher velocity dispersion galaxies are more metal-rich. The effects discussed above are expected to be weak considering the short metallicity range covered.

5.4.4 The Nitrogen puzzle

The origin of N is probably even more debated than the origin of C. It remains controversial whether N is a secondary and/or a primary element. N is produced in the CNO-cycle from C and O (see Section 3.1.2). Primary N then comes from the CNO processing in stars, while secondary N is produced from C and O already present in the collapsing gas-clouds forming the stars (e.g. Matteucci, 1986). The amount of primary N produced is proportional to the abundances of other primary elements (e.g. C and O). The N abundance from secondary production is instead proportional to the initial C and O abundances. Primary and secondary production in intermediate mass stars, with masses in the range $4M_{\odot}<M<8M_{\odot}$, are believed to be the dominant sources of N, where dredge-up, hot bottom burning and mass-loss eject N into the ISM (Renzini & Voli, 1981; van den Hoek & Groenewegen, 1997). Meynet & Maeder (2002) show that N can also

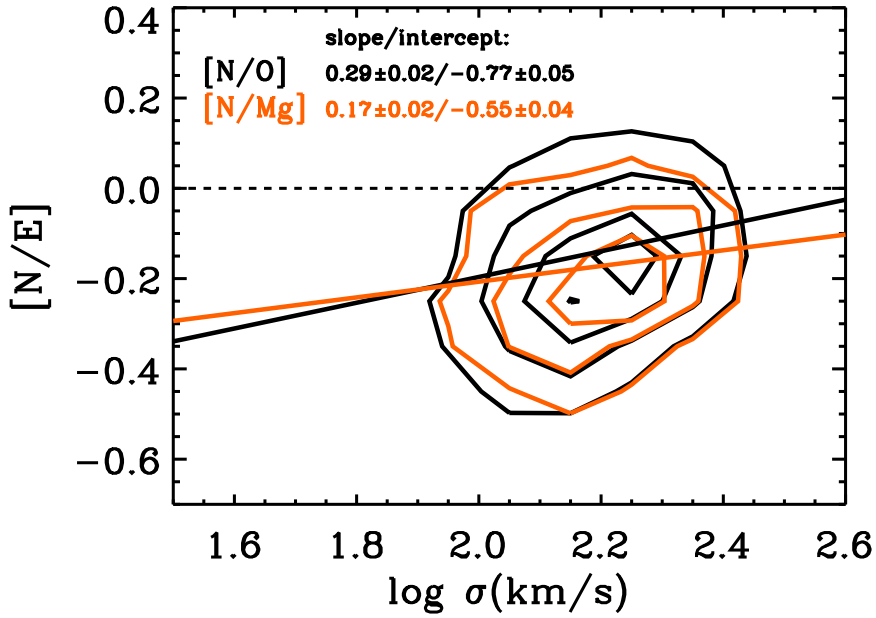

Figure 5.13: [N/O] (black contours) and [N/Mg] (orange contours) as functions of velocity dispersion for the red sequence population. The solid lines are least-square fits to the relationships with corresponding colours and the dashed black line indicate solar abundance ratios. The slope and intercept of the least-square fits are given by the labels.

be ejected by massive stars through the inclusion of stellar rotation. Observations indicate that primary N in low metallicity massive stars is required to explain observed trends of abundance ratios. Izotov & Thuan (1999) found HII regions in low metallicity blue compact galaxies to show a flat log(N/O) trend with 12+log(O/H) for their lowest metallicity galaxies, while the log(N/O) ratio starts to increase at a certain metallicity ($7.6<12+\log(O/H)<8.2$). The interpretation is that the primary N is produced by massive stars at low metallicities and the contribution from intermediate mass stars is delayed in time and kicks in at higher metallicities.

Fig. 5.13 shows the [N/O]-σ (black contours) and [N/Mg]-σ relationships (orange contours) together with least-square fits (solid lines) with corresponding colours. Fit parameters are given by the labels. An under-abundance of N of $\sim$0.2 dex compared to O and Mg is accompanied by a significant slope that is more prominent for the [N/O]-σ relation. The different origins of N compared to Mg and O make the N/Mg and N/O ratios useful formation time-scale indicators (see Section 5.1.2). Following our discussion on the C/Mg ratio as a lower limit time-scale indicator (see Section 5.3.9), the low N/Mg ratios suggest that the formation time-scales of the red sequence sample are too short for the full N production to reach solar N/Mg ratios. As discussed in Section 5.1.2 stars of lower mass and longer life-times contribute significantly to the production of N compared to the enrichment of Mg and O from short-lived, massive stars. To reach solar N/Mg ratios

the star-formation time-scales must at least be longer than the life-time of N contributing stars. However the main production sources of N are believed to be intermediate mass stars with life-times less than 0.4 Gyr (see Section 5.1.2). This obviously requires very short star formation time-scales for the argument above to hold. If instead low mass stars with longer life-times contribute significantly to the production of N, more extended star formation time-scales would be allowed without solar N/Mg ratios to be reached. Such indications have been reported by Thuan, Pilyugin & Zinchenko (2010) from emission lines of SDSS star-forming galaxies, who find that significant amounts of N are produced in 1.5-2$M_{\odot}$ stars with lifetimes of 2-3 Gyr.

In the low velocity dispersion regime (of our sample) we find [N/Fe]<0.0 (see lower left panel of Fig. 5.10). This would require N to be produced over longer time-scales than Fe and could constrain the upper formation time-scale limit for the low mass systems, if the production sites of N were well constrained. Considering the stellar mass range suggested by Thuan, Pilyugin & Zinchenko (2010) for N contribution, an upper limit of $\sim$2.5 Gyr (life-time of a 1.5 $M_{\odot}$ stars, Castellani et al., 1992; Bertelli et al., 2008) may be implied for the galaxies in our sample with 1.8< σ <2.0 that have [N/Fe]<0.0. Future models with better constrained N yields are needed to quantify this to a higher degree.

However, besides the under-abundance of N the slopes of the N/Fe-σ, N/Mg-σ and N/O-σ relationships suggest that the abundance ratios are higher in more massive galaxies. Following the discussion above longer formation time-scales would be required for such systems compared to the lower mass galaxies. This is obviously in contradiction to the shorter formation time-scales of more massive systems implied by the better constrained, in terms of the sources of Mg production, Mg/Fe ratios. Hence in the scenario discussed above the N/E ratio does not hold as formation time-scale indicator for the most massive systems

Instead the Mg/Fe ratio would set an upper limit on the formation time-scales of the most massive systems and N/Fe provides an additional upper limit on lower mass galaxies. On the other hand if N is mainly produced in stars with masses above 4$M_{\odot}$, the delayed enrichment of Fe from SNIa will result in a correlation with velocity dispersion also for [N/Fe] (see discussion in Section 5.4.3). Still this correlation is stronger than for [O/Fe], [Mg/Fe] and [C/Fe]. In either case, the higher N/E ratios in the more massive systems still need to be explained. Independent of the lower stellar mass limit for significant N contribution, at least four different scenarios can steepen the N/Fe-σ, N/O-σ and N/Mg-σ trends

i) **Metallicity dependent secondary N production.** As mentioned secondary production of N will cause a strong increase in N abundances with increasing metallicity. With the higher velocity dispersion galaxies being overall more metal-rich the steep

[N/Fe]-σ trends could intuitively be explained by the secondary production of N in intermediate mass stars. The metallicity range covered is relatively small, however, and it seems contrived if metallicity effects in secondary N production can explain the steep [N/Fe]-σ relationship alone.

ii) **Primordial gas inflow.** The ratios between secondary and primary elements are useful indicators of primordial gas accretion, while the ratios between two primary elements are unaffected by such events (Köppen & Edmunds, 1999; Henry et al., 2000). Hence N/Mg and N/O ratios are tracers of primordial gas inflow (e.g. Henry et al., 2000) that results in lower N abundances compared to Mg and O. Fig. 5.13 shows the [N/O]-σ relationship. An under-abundance of N of $\sim$0.2 dex is accompanied by a significant slope. This trend could be caused by a stronger dilution of the ISM in low mass galaxies. If the high velocity dispersion galaxies experienced very intensive gas accretion over time-scales shorter than the star formation time-scale, high N abundances are achieved since dilution of the ISM does not take place over the entire star formation history. If low velocity dispersion galaxies instead experience gas accretion along with star formation the ISM instead gets diluted with primordial gas over the entire star formation history and the N abundances become lower. This scenario fits with the results of Dekel & Birnboim (2006) who show that the shutdown of gas supply from cold streams is dependent on halo mass, such that it continues over longer time-scales in less massive halos. Such a scenario can steepen the slope of the [N/O,Mg]-σ relationships and consequently [N/Fe]-σ, but also for this case it is not clear if it can produce the observed trends alone. Tracing gas inflow in the X-ray combined with SFRs for high redshift galaxies with varying masses may provide evidence for whether this scenario actually occurs.

iii) **Stellar cluster star formation fraction.** Another intriguing scenario is an increasing fraction of globular clusters (GCs) with increasing velocity dispersion that can be partly responsible for the steep trends found between [N/Fe] and velocity dispersion. In Thomas et al. (2011a) we find galactic GCs with very strong enhancements of [N/Fe]. This is in agreement with high resolution spectroscopy of individual globular clusters stars (Thomas et al., 2011a, and references therein). A higher fraction of GCs in more massive early-type galaxies would result in stronger [N/Fe] for higher velocity dispersions. Such a scenario gets support from the work of Peng et al. (2008) who find a higher specific frequency of GC systems in more massive and luminous early-type galaxies compared to intermediate mass systems. Resolving individual stars with future extremely large telescopes may provide evidence to whether a larger fraction of stars in more massive early-type galaxies show the typical abundance patterns of GCs and if the fractions of such stars are large enough to account for the observed [N/Fe] trends.

iv) **Varying IMF.** IMF variations have been considered throughout the literature to explain variations of element ratios in early-type galaxies, especially the trend between

[Mg/Fe] and velocity dispersion (e.g. Thomas et al., 1999b; Trager et al., 2000b; Maraston et al., 2003; Matteucci, 1994; Sánchez-Blázquez et al., 2006a; Smith et al., 2009). However, the variations considered also affect absorption line indices (Sánchez-Blázquez et al., 2006a) and galaxy scaling relations (Renzini & Ciotti, 1993; Maraston et al., 2003, and references therein) in negative ways questioning the plausibility of IMF dependencies on galaxy mass. Since intermediate mass stars are believed to be the dominant sources of N, IMF variations with galaxy mass dependent weights in the (approximate) stellar mass range $5M_{\odot}<M<8M_{\odot}$ (particularly high N yields, van den Hoek & Groenewegen, 1997) are needed to vary the N abundances. IMF variations with emphasis on such a specific mass range have not been observed and are unlikely to occur. Also, this would affect C abundances as well and hence the more or less constant C/Mg ratios (over the velocity dispersion range covered) does not speak in favour such IMF variations.

The first three mechanisms (i-iii) could work together to cause the observed trends with velocity dispersion. To theoretically evaluate if the scenarios discussed above are plausible simulations of chemical evolution are needed taking these mechanisms into account. However, in Pipino et al. (2010) (P10) up-to-date models of chemical evolution fail at reproducing observed [N/Fe]-mass trends of early-type galaxies. P10 adopt the models of Pipino & Matteucci (2004) (PM04) that reproduce the observed pattern of increasing Mg/Fe ratios with increasing stellar mass in early-type galaxies, by assuming star formation histories compatible with the down-sizing scenario and Mg contributed by SN II. The models also reproduce the observed abundances of Ca by adopting yields where contributions to this element come from both SN II and SN Ia.

Implementing different recipes of stellar yields P10 compare modified versions of the PM04 models to the observed element abundance ratios of Graves et al. (2007). The modified versions mainly differ in the prescription of stellar mass-loss and rotation, which impacts on the abundances of C and N. Stellar rotation causes a mixing of elements in different stellar layers and mass-loss the ejection of newly synthesised element into the ISM. With the new prescriptions P10 are able to match the observed [C/Fe]-σ trend, both in zero-point and slope. The results indicate that there must be a substantial contribution to the production of C from massive stars and metallicity dependent yields possible due to metallicity dependent mass-loss rates. For [N/Fe] they instead find a very large scatter between the different models such that the observed steep trend of the [N/Fe]-σ relationship can not be simultaneously matched with the overall high [N/Fe] ratios. Also, to reach these high abundance ratios they must adopt a prescription that is not physically justified.

In Appendix A stellar population parameters derived for the Padova model version (see Section 3.2.1) are compared to the analogous presented here for the Cassisi model version. A very good agreement is found for all parameters except [N/Fe]. For this

element ratio the Padova model version is typically higher by ∼0.15 dex, while an even steeper trend with velocity dispersion is found. However, this systematic uncertainty can not account for the discrepancy found between observations and models by P10.

5.5 Conclusions

We present light-averaged ages, metallicities and element abundance ratios for 3802 SDSS early-type galaxies drawn from the MOSES catalogue (Schawinski et al., 2007) with visual morphology classifications. The parameters are derived using the method presented in Chapter 4 which is base on the stellar population models of absorption line indices presented in Chapter 3.

We study the relationships between the stellar population parameters and galaxy stellar velocity dispersion. In agreement with the literature stellar population age and total metallicity correlate with velocity dispersion. [Fe/H] instead does not show such a correlation over the entire parameter range covered, but for a fixed age a steep trend is found for the [Fe/H]-σ relation. This trend is shallower than the analogous for [Z/H] due to suppressed Fe enrichment in more massive galaxies because of time-scale dependent contribution from SN Ia

Similar trends are found for [O/Fe], [Mg/Fe] and [C/Fe], i.e. strong correlations with velocity dispersion in agreement with the literature. The first two are expected to be similar, since both O and Mg belong to the group of α-elements produced in massive stars through SN II. This is also in favour of the down-sizing scenario of early-type galaxies that set an upper limit on the star formation time-scales and where more massive systems experience shorter time-scales (e.g. Thomas et al., 2010).

The C/Mg ratios are close to solar values, which instead sets a lower limit for the formation time-scales of early-type galaxies. Stars with masses down to ∼3 $M_{\odot}$ contribute significantly to the production of C. To reach solar C/Mg ratios formation time-scales need to be long enough for such stars to eject C into the ISM. The inferred lower formation time-scale limit is then ∼0.4 Gyr, which is the life-time of a 3 $M_{\odot}$ star.

The [N/Fe] ratios are overall lower by ∼0.2 dex compared to [O/Fe] and [Mg/Fe] and the trend with velocity dispersion is very steep, i.e. more massive galaxies have significantly higher [N/Fe] ratios. The observed [N/Fe]-σ trends are difficult to interpret due to uncertainties in the origin of N. The zero-point and slope of this relationship can not be simultaneously matched by up-to-date models of chemical evolution (Pipino et al., 2010). Either the theoretical stellar yields have to be increased by a significant factor or other prescriptions have to be incorporated into the models that affect the N yields. Such prescriptions could be: 1. N yields with a stronger dependence on metallicity, since more

massive early-type galaxies are more metal-rich. 2. A dependence on galaxy mass for the ratio between the time-scale of star formation and the time-scale of primordial gas inflow, which affects the N/O, N/Mg and N/Fe ratios due to the secondary nature of N.

We do not find any dependence on environmental density for the element ratios studied. This is in contradiction to previous studies that have reported environmental dependencies for C and N abundances. Hence different formation scenarios for field and cluster early-type galaxies can not be inferred from the element ratios studied in this work.

The [Ca/Fe] ratios do not correlate significantly with velocity dispersion and are close to solar values over the entire velocity dispersion range covered. Although tentative, due to large errors, Ti shows a behaviour similar to Ca. This indicates an atomic number dependent contribution from SN Ia to the production of α-elements, i.e. the yields from SN Ia are higher for heavier α-elements. This is now universally found since similar patterns have been found in the stellar populations of the Milky Way (see Section 4) and puts strong constraints on supernova nucleosynthesis.

Chapter 6

SN Ia host galaxy properties from SDSS-II spectroscopy

In this chapter we analyse the relationships for SN Ia properties with the host galaxy stellar population parameters age and metallicity, element abundance ratios, stellar velocity dispersion and stellar mass. A sub-sample of 84 host galaxies from the Sloan Digital Sky Survey-II (SDSS-II) SN Survey with available host galaxy spectra is used. The sub-sample is selected depending on the quality of the host galaxy spectra and accuracy of the derived SNIa parameters. The method presented in the Chapter 4 is used to derive stellar population ages and metallicities and element abundance ratios. We find a larger fraction of SN Ia events and higher SALT2 stretch factor values (i.e. more luminous and slower declining SN Ia) in galaxies classified as star forming compared to galaxies without detected emission lines. A strong anti-correlation between SALT2 stretch factor and luminosity-weighted age is found. Hence stellar population age seems to be the dominant driver of SN Ia luminosity. As a result of this trend we also find an anti-correlation between galaxy mass and velocity dispersion with SALT2 stretch factor, while only weak anti-correlations are found for metallicity and the element abundance ratios.

Previous studies report dependencies on the host galaxy properties mass and metallicity for the SN Ia peak luminosities even after light-curve corrections. This is worrying as it may affect the derived cosmology, since host galaxy properties evolve with redshift. In this work we find no significant trends between Hubble residual (scatter in the redshift-distance relation) and the stellar population parameters, element abundance ratios or stellar velocity dispersion. The stellar masses are derived from photometry and confirms the lack of Hubble residual dependencies found for stellar velocity dispersion. The contradiction with the literature is found to depend on the models and technique used for deriving the masses. The lack of Hubble residual dependencies indicates that the

currently derived cosmology from SN Ia peak luminosities is robust. Although, higher quality spectroscopy will be needed to confirm this.

6.1 Background

The standardised explosions of SN Ia are useful for constraining cosmology. The bright peak luminosities can probe vast cosmological distances and connect redshift space to luminosity distance. This led to the discovery of an accelerating expansion of the universe (Riess et al., 1998; Perlmutter et al., 1999).

Ideally all SNIa explosions should have the same peak luminosity, but this is not the case. The observed SNIa span a range in peak luminosities accompanied by varying decline rates (Phillips, 1993), i.e. the peak luminosity decreases with increasing decline rate and also the colours become redder. This can be corrected for such that a stretch factor is applied to the light-curve to find a standardised peak luminosity, i.e. the shape of the light-curve (decline rate) and the peak luminosity are simultaneously changed until the standardised light-curve is matched. Several light-curve fitting tools are available (Jha et al., 2007; Guy et al., 2007; Conley et al., 2008; Kessler et al., 2009), where the shape of the light-curve and the colour are corrected to match the standardised peak luminosity. The light-curve shape correction is known as stretch-factor.

Correcting the light-curves increase the precision of the derived luminosity distances and consequently the scatter in the redshift-distance relation (Hubble residuals). Reducing the Hubble residuals in turn increase the precision of the derived cosmological parameters. Even after light-curve corrections the Hubble residuals are non-negligible. Understanding systematic uncertainties in the derived SN Ia light-curve parameters is key to improve supernovae cosmology.

Several authors report dependencies on host galaxy mass and metallicity for the Hubble residuals (Gallagher et al., 2008; Howell et al., 2009; Neill et al., 2009; Kelly et al., 2010; Lampeitl et al., 2010; Sullivan et al., 2010). This is alarming for large redshift surveys used for constraining cosmology, since stellar population parameters change with redshift. Thus the derived cosmological parameters may be biased towards stellar populations at certain cosmological epochs.

The accepted idea governing SN Ia is thermonuclear explosion of a carbon-oxygen WD that reach the Chandrasekhar limit (Whelan & Iben, 1973; Hillebrandt & Niemeyer, 2000). This can happen through two different channels, either the single-degenerate (SD) scenario where mass is accreted from an evolved main-sequence binary companion or the double-degenerate (DD) case of merging of two WD's (e.g Woosley & Weaver, 1986; Branch et al., 1995; Branch, 2001; Hoflich, Khokhlov & Wheeler, 1995; Greggio,

2005; Yungelson & Livio, 2000). This indicates that different SN Ia populations may be present, but it has been shown that a DD system is likely to lead to accretion-induced collapse rather than a thermonuclear explosion (Saio & Nomoto, 1998).

The delay time, the time between progenitor formation and explosion, in the DD scenario is determined by the life-time of the WD progenitors and the orbit of the two binary stars. The delay-time of a SD system is instead dependent on the main-sequence lifetime of the companion star. In this case the mass of the companion star determines the delay time. A wide range of delay times have been observationally suggested, ranging from <1 Gyr (Barris & Tonry, 2006) to > 2 Gyr (Gal-Yam & Maoz, 2004; Strolger et al., 2004, 2005). Considering several different progenitor systems theoretical models find the rate of SN Ia explosions (SNR) to peak at delay times below or close to 1 Gyr (Yungelson & Livio, 2000; Greggio, 2005; Ruiter et al., 2010). The SNR of most progenitor systems then smoothly decline and becomes 10-100 times lower at delay times of $\sim$10 Gyr. Comparing observed delay times to theoretical predictions can constrain possible progenitor systems.

It is well established that the SNR is higher in star-forming late-type than in passive early-type galaxies (e.g. Oemler & Tinsley, 1979; van den Bergh, 1990; Mannucci et al., 2005; Sullivan et al., 2006). Several authors have found a dependence on host galaxy mass for the decline rate of SN Ia (Kelly et al., 2010; Lampeitl et al., 2010; Sullivan et al., 2010). Since galaxy mass in turn correlate with stellar population parameters and properties of the inter-stellar medium (Tremonti et al., 2004; Gallazzi et al., 2005; Thomas et al., 2010), mass may be a proxy for more fundamental correlations with such parameters as age, metallicity and element abundance ratios. The tight relation between SN Ia decline rate and peak brightness indicate a primary dependence on one of these parameters for luminosity.

The luminosity of SNe Ia arise from the radioactive decay of ^{56}Ni to ^{56}Co, that then decay to ^{56}Fe (Colgate & McKee, 1969; Arnett, 1982), such that the varying peak brightness depend on the ^{56}Ni mass. Timmes et al. (2003) show theoretically that metallicity effects, in the range 1/3-3 $Z_{\odot}$, can induce a 25% variation in the ^{56}Ni mass. Several authors have observationally found dependencies on age and/or metallicity for SN Ia decline rate (Hamuy et al., 2000; Gallagher et al., 2008; Howell et al., 2009; Neill et al., 2009). These studies indicate that stellar population age may be the main driver of SN Ia luminosity. However, either fairly small samples have been used (Hamuy et al., 2000; Gallagher et al., 2008) or metallicity has been indirectly measured (Howell et al., 2009; Neill et al., 2009). According to Umeda et al. (1999) the carbon mass fraction or consequently the C/O ratio is responsible for the luminosity variations and is determined by the metallicity and mass of the WD progenitor.

We study the stellar population parameters age and metallicity, element abundance ratios, stellar velocity dispersion and stellar mass for a statistically significant sample of host galaxies from the SDSS-II SN survey with available spectroscopy and photometry. We use the method presented in Chapter 4, which is based on our up-to-date stellar population models of absorption line indices from Chapter 3, to derive ages and metallicities together with the element abundance ratios [C/Fe], [O/Fe], [N/Fe], [Mg/Fe], [Ca/Fe] and [Ti/Fe]. The stellar velocity dispersions are derived from spectroscopy, while the stellar masses are derived from photometry.

SN Ia light-curve properties and stellar masses are derived by Mathew Smith and Janine Pforr, respectively, while stellar population parameters, element ratios and emission line diagnostics are derived by the main author.

The chapter is organised as follows. The data sample used is described in Section 6.2 and the relationships between SN Ia properties and host galaxy parameters are presented in Section 6.3. We discuss the results in Section 6.4 and concluding remarks are given in Section 6.5.

6.2 Data sample

The sample is drawn from the SDSS-II Supernova Survey (Frieman et al., 2008; Sako et al., 2008; Holtzman et al., 2008) and consists of confirmed SNIa with available SDSS host galaxy spectra (York et al., 2000). The SDSS-II SN Survey was performed during the period 2005-2007 to image transient objects in the SDSS Stripe 82 region. Thousands of potential SN candidates were observed and ∼500 were confirmed as being SN Ia by spectroscopy. SDSS spectra are available for 277 out of these. The derived SN Ia properties, host galaxy parameters and final sample are described in the following sections.

6.2.1 SNIa properties

A number of light-curve methods exist in the literature and several authors have confirmed that the results are robust against using the different available algorithms (Kelly et al., 2010; Lampeitl et al., 2010; Sullivan et al., 2010). SALT2 (Spectral Adaptive Light-curve Template 2, Guy et al., 2007) is adopted in this work, which is one of the most common light-curve fitting techniques. The output of SALT2 are B-Band apparent brightness (mB), stretch factor (x_1) and colour (c) term. The SALT2 parameters used are consistent with the analogous from Lampeitl et al. (2010). The distance modulus (μ_{SN}) is then calculated as

$$\mu_{SN} = (mB - M) + \alpha x_1 - \beta c \tag{6.1}$$

where M is the standardised absolute SN Ia magnitude for x_1 = c = 0, α describes the overall stretch law for the sample, and β is the colour law for the whole sample. These parameters are determined by minimising the scatter in the luminosity distance-redshift relation or the Hubble residuals (HR)

$$HR = \mu_{SN}(M, \alpha, \beta) - \mu_{cosmo}(z, H_0, \Omega_m, \Omega_\Lambda) \tag{6.2}$$

where μ_{cosmo} is the distance modulus determined by the adopted/derived cosmology, H_0 is the Hubble constant, Ω_M is the energy density of matter and Ω_Λ is the cosmological constant. We aim at detecting systematic trends in the derived Hubble residuals and therefore adopt a priori fixed cosmology with H_0=65 km s^{-1} Mpc^{-1}, Ω_m=0.3 and Ω_Λ=0.7. The resulting light-curve parameters are M=-30.11, α=0.12 and β=2.86.

Hence for a negative Hubble residual the cosmology puts the SN Ia further away than the peak luminosity, i.e. $\mu_{cosmo} > \mu_{SN}$. This also means that the SN Ia peak luminosity has not been fully corrected and it is too bright to match the cosmology.

6.2.2 Host galaxy properties

The aim of this work is to analyse the host galaxy properties of SNIa from a spectroscopic point of view, particularly using absorption line indices. For this purpose we need clean absorption spectra of the host galaxies, free from contaminating emission line fill in. The 25 Lick indices (see Section 2.1.2) are measured on the clean absorption spectra. We then use the method detailed in Chapter 4 to derive the stellar population parameters age, total metallicity and element abundance ratios.

Kinematics and Lick indices

We utilise the code GANDALF (Sarzi et al., 2006) to obtain clean absorption spectra, which is based on on the penalised pixel-fitting method of Cappellari & Emsellem (2004). A brief description of the code is given here, while the reader is referred to Sarzi et al. (2006) and Cappellari & Emsellem (2004) for a detailed description. GANDALF simulanteously fits stellar templates and emission line gaussians to galaxy spectra. The result is a separation of emission and absorption spectra. As stellar templates we adopt the single stellar population SEDs of Maraston & Strömbäck (2011). Besides the clean absorption spectra useful output of GANDALF for this work are stellar and gas kinematics, E(B-V) dust reddening and emission line fluxes/EW's.

We measure the Lick indices (see Section 2.1.2) on the clean absorption spectra, free from contaminating emission line fill in, using the latest definitions of Trager et al. (1998). The resolution of the spectra are downgraded to the Lick/IDS resolution

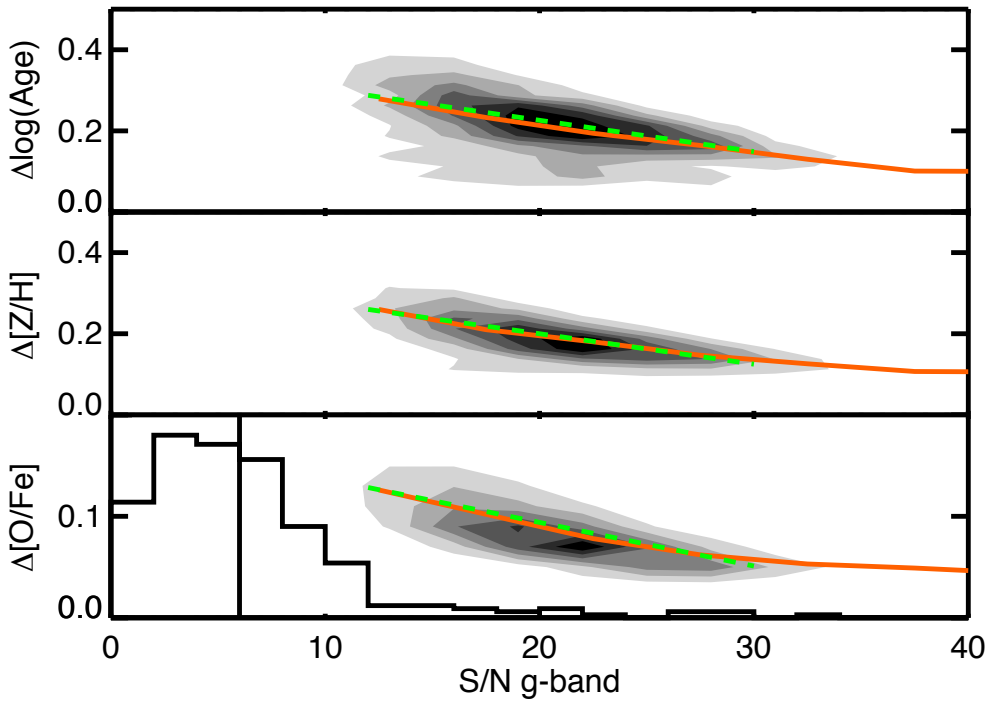

Figure 6.1: Remake of Fig. 5.2 for the relationship between error in stellar population parameters and quality of galaxy spectra, in terms of S/N in the g-band. Contour represent the 3802 SDSS early-type galaxies from the MOSES sample studied in Chapter 5 for error in age (upper panel), total metallicity (middle panel) and [O/Fe] (lower panel). The orange lines connect the mean errors in bins of g-band S/N. The distribution of the full sample of SNIa host galaxies (277 objects) is presented by the black histogram, scaled with 0.18/60. Black vertical line represents the cut at S/N=6.0.

(Worthey & Ottaviani, 1997) prior to measuring the indices. The index measurements are then corrected for velocity dispersion broadening. For this purpose we use the velocity dispersions output by GANDALF together with the best fit stellar templates. The Lick indices are measured on the best fit stellar templates broadened to the Lick/IDS resolution, both before and after further broadening with respect to the velocity dispersion measurements. The difference between these two measurements gives the correction factor which we apply to the Lick indices measured on the galaxy spectra. Using the error vectors provided with each SDSS spectra we estimate Lick index errors through Monte Carlo simulations.

6.2.3 Sample cuts

Fig. 6.1 is a remake of Fig. 5.2, showing errors (contours) in the stellar population parameters age (upper panel), total metallicity (middle panel) and [O/Fe] (lower panel) as a function of the median signal-to-noise (S/N) per pixel in the g-band from Chapter 5.

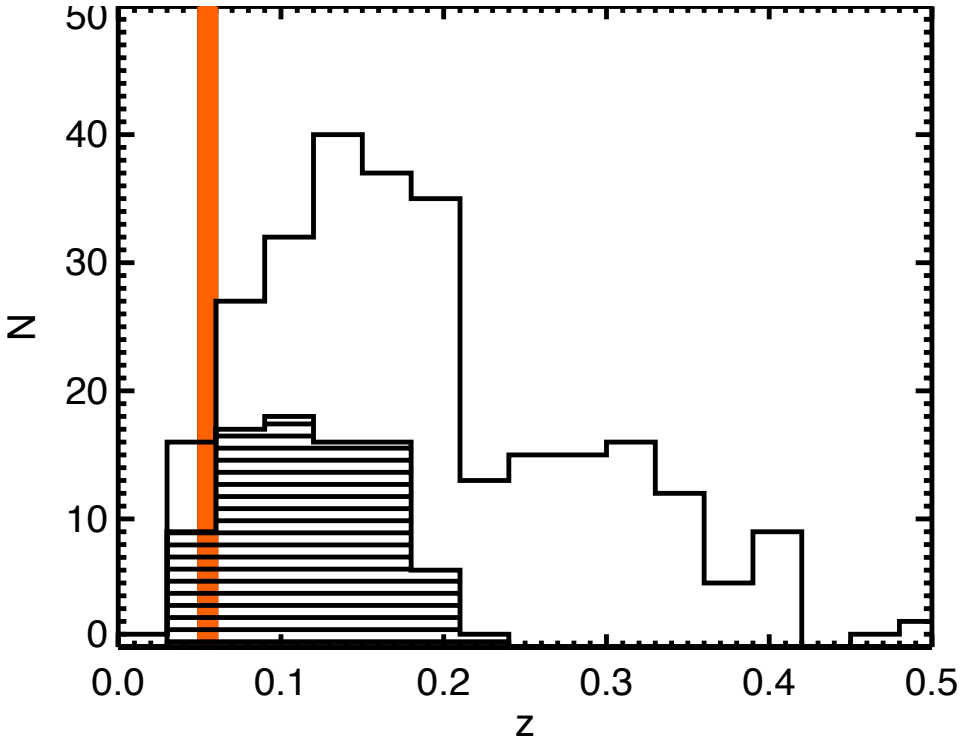

Figure 6.2: Distribution in redshift for the full sample of SNIa (open histogram) and the final sample (dash-filled histogram). The orange area represents the redshift range covered by the early-type galaxy sample used in Fig. 6.1 to show the relationship between stellar population parameter errors and quality of corresponding luminosity-weighted galaxy spectra.

The quality, in terms of S/N in the g-band, of the host galaxy spectra is illustrated by the black histogram in the lower panel of Fig. 6.1.

The distribution in redshift-space for the full SNIa sample is shown in Fig. 6.2 (open histogram) together with the redshift-range covered by the MOSES sub-sample (orange area). Only a small fraction of the SNIa sample falls in and below the redshift-range of the MOSES sub-sample. Thus the majority of the SNIa host galaxies have a lower S/N than the MOSES sub-sample (see Fig. 6.1). To avoid including data with too large uncertainties in the derived stellar population parameters we cut the sample to only include host galaxies with S/N>6 in the g-band (vertical black line in lower panel of Fig. 6.1). This cut reduces the sample to 122 objects.

We cut the sample further to exclude the lowest quality SN Ia observations, in order to avoid further contamination of low quality data. SN Ia with stretch factor errors greater than 1.0 dex and colour errors greater than 0.1 dex are therefore removed. Following Lampeitl et al. (2010) we keep SN Ia's with SALT2 parameters inside the ranges -4.5<x_1 <2.0 and -0.3<colour<0.6. Outside these ranges Lampeitl et al. (2010) found the derived parameters to be unreliable.

Moreover, it is possible that parameter gradients and local deviations from the integrated parameters will affect the results. Hence we discard SN Ia that are separated by more than 0.15' from the host galaxy, which is three times the SDSS aperture (0.05'). We also find 1 spectra showing quasar features and 2 objects with telluric contaminated Mgb absorption features, which are discarded. These cuts leaves a final sample of 84 objects. The redshift distribution of this sub-sample is shown by the dash-filled histogram in Fig. 6.2. The final sample cover redshifts up to $\sim$0.2.

6.3 Results

Relationships between host galaxy parameters age, metallicity, element ratios, velocity dispersion and stellar mass with SN Ia properties stretch factor and Hubble residual are presented in this section. We do not find any significant trends between the host galaxy parameters and SALT2 colour hence such relations are not further discussed.

6.3.1 Emission line diagnostics

Emission line diagnostics are measured on the emission line spectra separated from the galaxy absorption spectra (see Section 6.2.2). We use the emission line equivalent widths (EWs) and A/N ratios to classify each galaxy as emission line free, star-forming (SF) or hosting an AGN. Following Baldwin, Phillips & Terlevich (1981) (BPT) the ratios [OIII](λ5007)/Hβ and [NII](λ6584)/Hα separate SF and AGN activity. The A/N for [OIII](λ5007), [NII](λ6584) and Hα sets the limit for emission line detection. Due to low S/N of the galaxy spectra (see Section 6.2.3) we allow an A/N limit of 1.5, compared to 3.0 used in Kauffmann et al. (2003b); Schawinski et al. (2007). Hence the galaxies are classified as emission line free if they don't have an A/N$>$1.5 for [OIII](λ5007), [NII](λ6584) and Hα. With this limit we find 25 out of the 84 galaxies in the final sample (see Section 6.2.3) to be emission line free, i.e. 30 % of the SN Ia in our sample occur in emission line free galaxies.

Fig. 6.3 shows the location of the emission line detected galaxies in the BPT-diagram. The solid curved line is the theoretical SF limit from Kewley et al. (2001) and the dashed curved line is the empirical separation of AGN and purely SF galaxies from Kauffmann et al. (2003b). Objects that fall between these lines are transition objects, hosting both SF and AGN activity. For this work we are interested in detecting SF activity and consequently label everything below the Kewley et al. (2001) line as SF (blue points). The fraction of SF galaxies is 41 out of 84 ($\sim$50 %) and 18 galaxies are AGN ($\sim$20 %, green points). The separation of LINER (Low-Ionization Nuclear Emission-line Region) and Seyfert AGN's from Schawinski et al. (2007) is also indicated by the solid straight line.

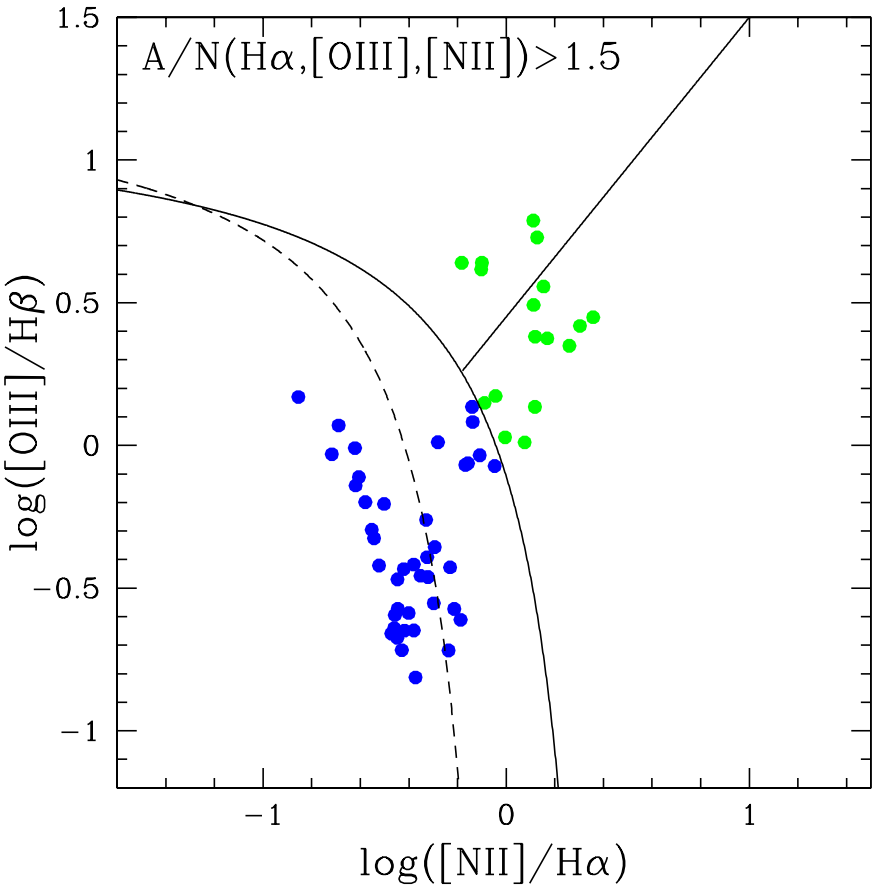

Figure 6.3: BPT-diagram for the 59 galaxies with detected emission lines, i.e. A/N>1.5 for Hα, [OIII](λ5007) and [NII](λ6584). The solid curved line is the theoretical SF limit from Kewley et al. (2001) (Ke01) and the dashed curved line is the empirical separation of AGN and purely SF galaxies from Kauffmann et al. (2003b) (Ka03). Objects that fall between these lines are transition objects, hosting both SF and AGN activity. The separation of LINER and Seyfert AGN's from Schawinski et al. (2007) (S07) is indicated by the solid straight line.

12 out of 17 AGN labeled galaxies are LINERs and consequently 6 are Seyfert AGN's. The colour coding (blue=SF, green=AGN) is kept throughout this chapter, adding a red colour for emission line free objects.

6.3.2 Velocity dispersion and stellar mass

Velocity dispersion can be used as a proxy for the mass of the systems when it comes to elliptical galaxies (Bender et al., 1992; Cappellari et al., 2006). This sample is however not selected by morphology, such that any type of galaxy may be included. Thus velocity dispersion may not be a valid proxy for galaxy mass in this case. On the other hand the SDSS aperture is fairly small (3", see Section 6.2.3), such that for late-type disk galaxies included in the sample a large fraction of the light will come from the bulge. Hence we use the velocity dispersion measurements derived in this work as proxies for mass. This

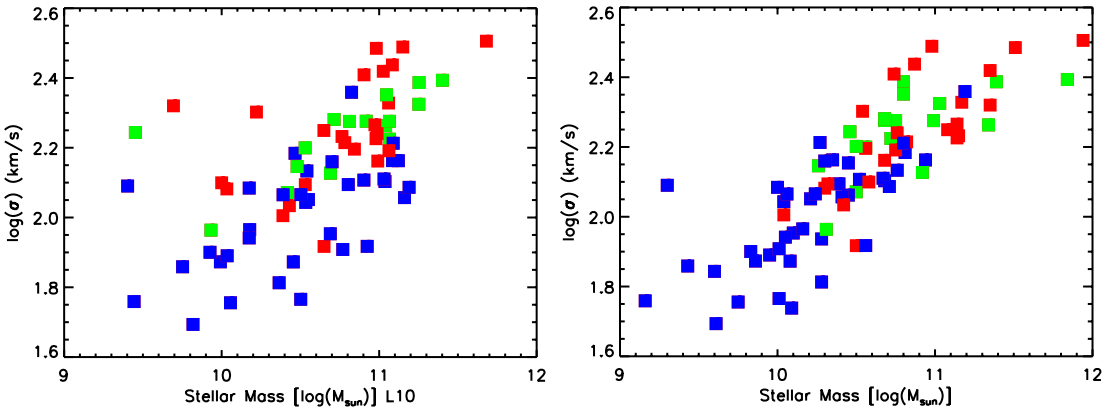

Figure 6.4: Comparison between stellar velocity dispersion and stellar mass, for masses from Lampeitl et al. (2010) (L10, left hand panel) and masses derived in this work (right hand panel). Data points are colour labelled according to their emission line classifications from Section 6.3.1, i.e. blue points are star forming galaxies, green points are galaxies that host AGN activity and red points are galaxies without detected emission lines.

is justified by a strong correlation found between our velocity dispersion measurements and stellar mass estimates (see Fig. 6.4 and text below).

In Fig. 6.4 we compare the velocity dispersion measurements output by Gandalf (see Section 6.2.2) to the stellar masses from Lampeitl et al. (2010) (L10, left hand panel). From their work we find mass estimates for 81 out of 84 objects of the final sample. The data points are labeled according to their emission line classifications from Section 6.3.1. We have also re-derived the stellar masses through spectro-photometric SED-fitting using the technique of Pforr et al. based on M05 models. The major differences from the mass derivation of L10 are different models that take into account the TP-AGB phase of stellar evolution and that reddening is not included in the fitting. The comparison between stellar velocity dispersion and the new mass estimates is also included in Fig. 6.4 (right hand panel).

M05 showed that TP-AGB stars are very luminous in stellar populations with ages between $\sim$0.2 and 2 Gyr. Hence the derived stellar masses will be overestimated in this age regime when SSP models without TP-AGB treatment are used. This can also be seen in the left hand panel of Fig. 6.4 where a number of young galaxies (blue points) have high L10 stellar masses ($\sim 10^{11} M_{\odot}$) compared to velocity dispersion. Pforr et al. further showed that stellar masses are best recovered when reddening is not considered in the fitting. If reddening is instead included, as in the L10 case, the masses tend to be underestimated. This can also be seen in Fig. 6.4 where a number of old galaxies (red points) have lower L10 stellar masses compared to the masses derived in this work. To summarize, the best agreement with stellar velocity dispersion is found when the most accurate description for deriving stellar masses is used. Hence, the correlation between

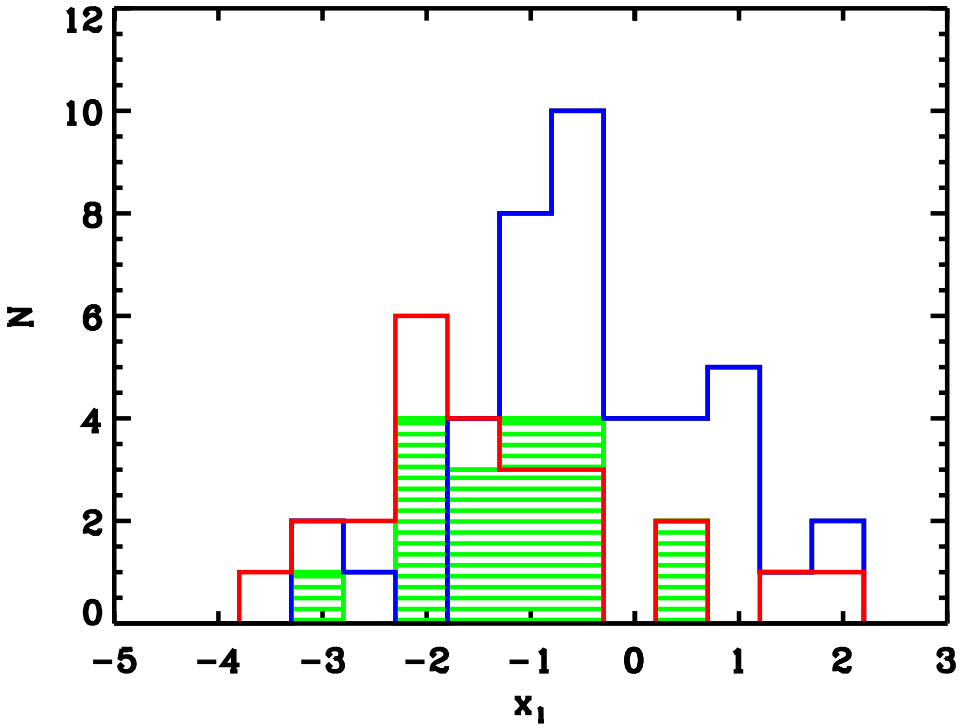

Figure 6.5: Distribution of the stretch factor x_1 for the different emission classifications (see Section 6.3.1). Blue histogram represents SF, green AGN and red emission line free galaxies.

the new masses and velocity dispersion is stronger and has less scatter than for the L10 masses. Also, the connection with the emission line classifications makes more sense for the new masses compared to L10, i.e. more massive galaxies tend to be passive (emission line free, red points) while less massive galaxies are typically star-forming (blue points). The new masses are therefore used throughout the rest of this chapter.

Even though velocity dispersion is a proxy for dynamical mass rather than stellar mass, a strong correlation indicating higher velocity dispersions for higher stellar masses is found. Thus we consider the velocity dispersion measurements good proxies for mass.

6.3.3 Stretch factor

Final sample

Fig. 6.5 shows the distribution in stretch factor x_1 for SF (blue histrogram), AGN (green histogram) and emission line free galaxies (red histogram), classified according to their emission line strengths (see Section 6.3.1). It is clear that SN Ia observed in emission line free galaxies have the lowest x_1 values hence the shortest decline rates and SF galaxies contain the brightest SN Ia's. SN Ia observed in galaxies with AGN activity seem to have x_1 values falling in between those with SF and emission line free host stellar populations.

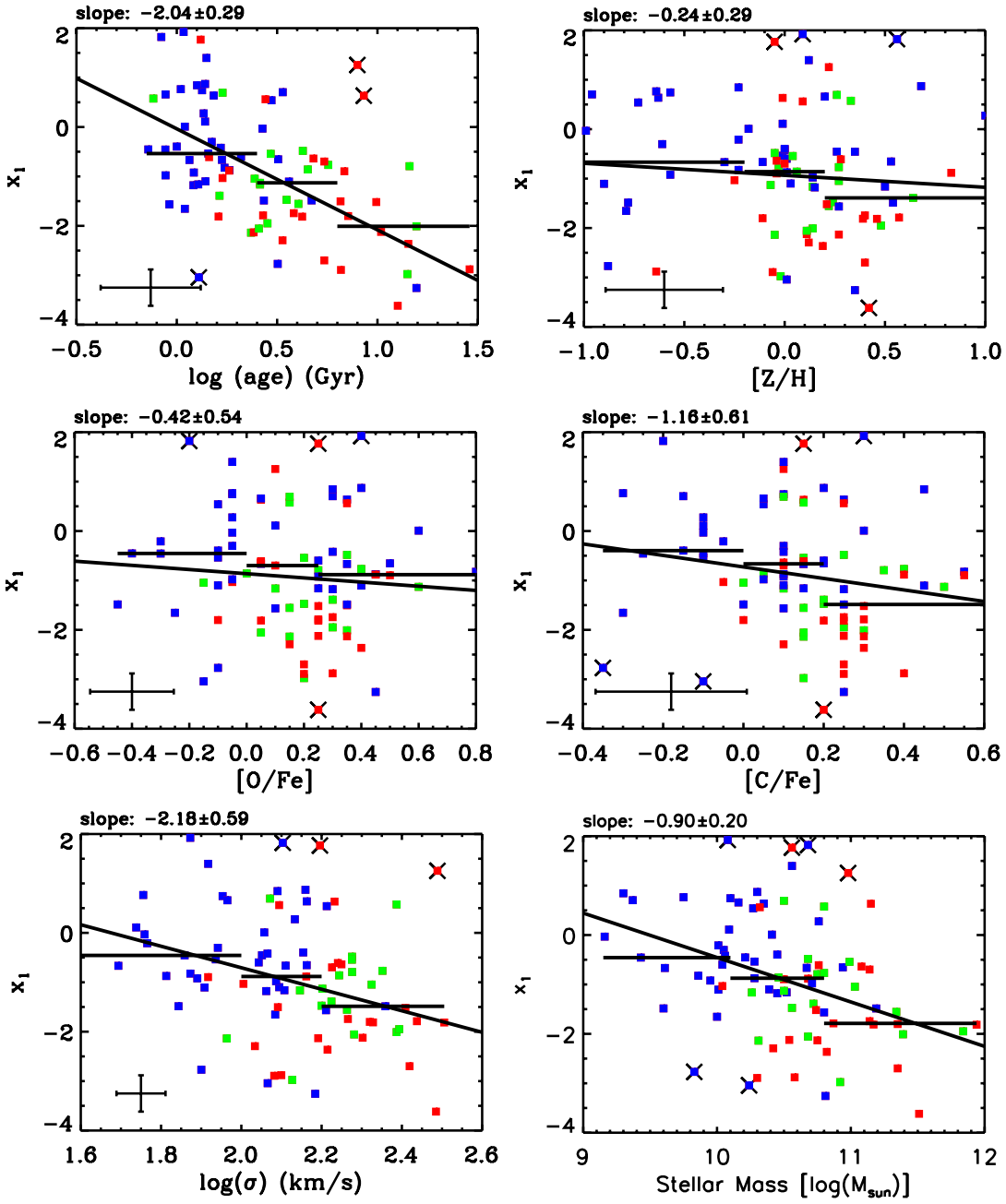

Figure 6.6: Relationship with host galaxy age (upper left panel), Z/H (upper middle panel), velocity dispersion (upper right panel), O/Fe (lower left panel), C/Fe (lower middle panel) and stellar mass (lower right panel) for the SALT2 stretch factor x_1. The data points are coloured according to the emission line classification of the host galaxies from Section 6.3.1, i.e. blue=SF, green=AGN and red=emission line free. Solid lines are one time sigma-clipped (2σ level) least-square fits and over-plotted crosses are removed data points. The slopes of the fits are given at the top of the panels. Horizontal lines are median x_1-values in bins of the x-axis parameters with lengths indicating the width of the bins. Error bars in the lower left corners are average 1σ errors.

Relationships between host galaxy age, Z/H, O/Fe and C/Fe, velocity dispersion and stellar mass with SALT2 stretch factor x_1 are presented in Fig. 6.6. The data points are colour coded according to Fig. 6.5. Solid lines are least-square fits that have been sigma-clipped one time at a 2σ level. The slope of the fits are given at the top of the panels and sigma-clipped data points are indicated by over-plotted crosses. Horizontal lines are median values in bins of the x-axis parameters, where the length of the lines indicate the width of the bins. Mean 1σ errors are shown by the error bars in the lower left corners.

Clear anti-correlations between stretch factor and stellar population age, galaxy velocity dispersion and stellar mass are found. Hence higher stretch factors, i.e. brighter SN Ia's, are found in younger and lower-mass galaxies. We find the slopes of the least-square fits to be different from zero at a 7σ, 4.5σ and 3.7σ level for the x_1-log(age), x_1-mass and x_1-$\log(\sigma)$ relationships, respectively. The stretch-factor also anti-correlates with Z/H, O/Fe and C/Fe, but these relations are significantly weaker than for age, mass and velocity dispersion. The slopes of the least-square fits are shallower and differ from zero at less than a 1σ level for both Z/H and O/Fe and at a 1.9σ level for C/Fe. To summarise, the stretch factor depends mostly on the age of the host galaxy stellar populations. This age dependence is well in line with the correlation with star formation fraction discussed above.

We find no significant correlations for x_1 with the stellar population parameters N/Fe, Mg/Fe, Ca/Fe and Ti/Fe that add valuable information to the analysis. N/Fe, Ca/Fe and Ti/Fe require higher S/N than the other parameters and Mg/Fe reflect O/Fe. Hence we do not further discuss these abundance ratios.

Stacked spectra

Due to the low S/N of the individual spectra used in the previous section, in the following we perform consistency checks by using stacked spectra with relatively high S/N. We stack the spectra of the final sample in bins of x_1. The spectra are first de-redshifted using the SDSS spectroscopic redshifts and linearly interpolated to the same wavelength binning. We then normalise to the median flux in the rest-frame wavelength range 5000-5500 Å. The stacking is finally performed by taking the median flux value in each wavelength pixel (Lee et al., 2010). Using the median value is a safeguard against unreal data, telluric contamination, features of individual spectra and does not bias against the very highest S/N spectra. Following Lee et al. (2010) we estimate the error in each pixel of the median stacked spectra with

$$(S/N)_s = \sqrt{\sum (S/N)_i^2} \tag{6.3}$$

where $(S/N)_s$ is the S/N of the stacked spectrum and $(S/N)_i$ is the S/N of the individual spectra.

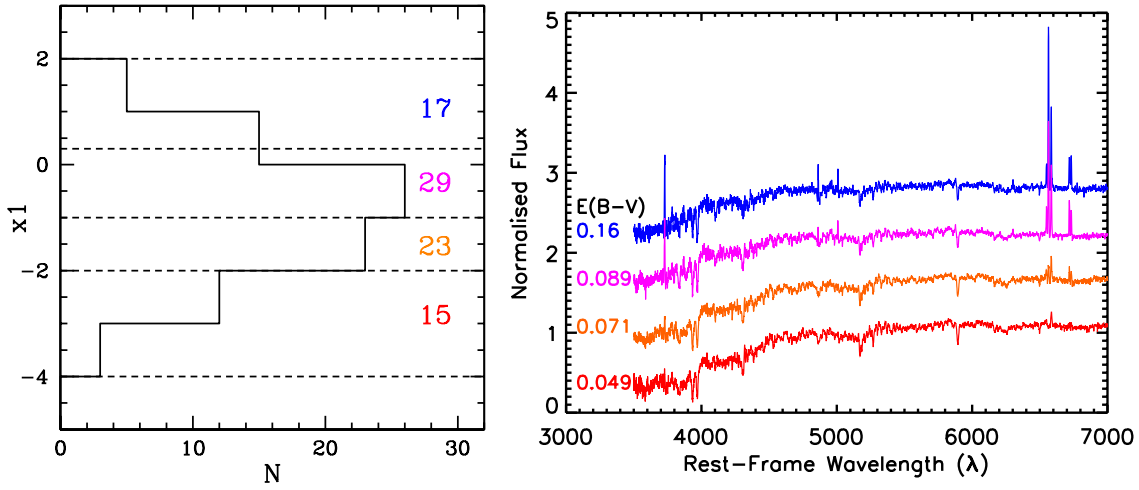

Figure 6.7: Left hand panel: binning in x_1 for stacking of spectra, where the limits of the bins are indicated by the horizontal dashed lines. Coloured labels state the number of objects within each individual bin. The histogram is distribution of x_1. Right hand panel: resulting stacked spectra at rest-frame wavelength and for normalised flux, coloured according to the bin labels of the left hand panel. The labels, with corresponding colours, state the E(B-V) value for each stacked spectrum.

The x_1 range covered by the final sample (see Section 6.2.3) is divided into four bins, chosen to include a fair number of data points in each bin. The left hand panel of Fig. 6.7 shows the widths of the bins separated by the dashed horizontal lines, together with the corresponding number of objects in each bin. The histogram is the x_1 distribution for the final sample. The procedures applied to the individual spectra to compute the stellar population parameters are then applied to the stacked spectra.

The right hand panel of Fig. 6.7 shows the stacked spectra for each bin, following the colour coding of the left hand panel. The output E(B-V) values from GANDALF (see Section 6.2.2) for each stacked spectrum are given by the labels with corresponding colours. The stacked spectra show very distinct features and emission lines that clearly change as a function of stretch factor. The largest stretch factors are found in host galaxies with the most pronounced star formation activity and with it the highest dust extinction. The host galaxies of faint supernovae with small stretch factors, instead, are emission line and dust free, and show strong absorption features in their spectra.

Analogue to Fig. 6.6, Fig. 6.8 shows the relationships between stretch factor and stellar population properties and galaxy velocity dispersion for the stacked spectra. The data points in each panel are coloured according to Fig. 6.7 and the vertical bars indicate the size of the bins. The x_1 values are the average within each bin. 1σ error bars are shown for each data point in the x-direction. The 1σ errors are very similar for log(age), [Z/H], [O/Fe] and [C/Fe], i.e. smaller than 0.1 dex. The least-square fits to the final sample from Section 6.3.3 are included for comparison (dashed lines). The x-range covered in each

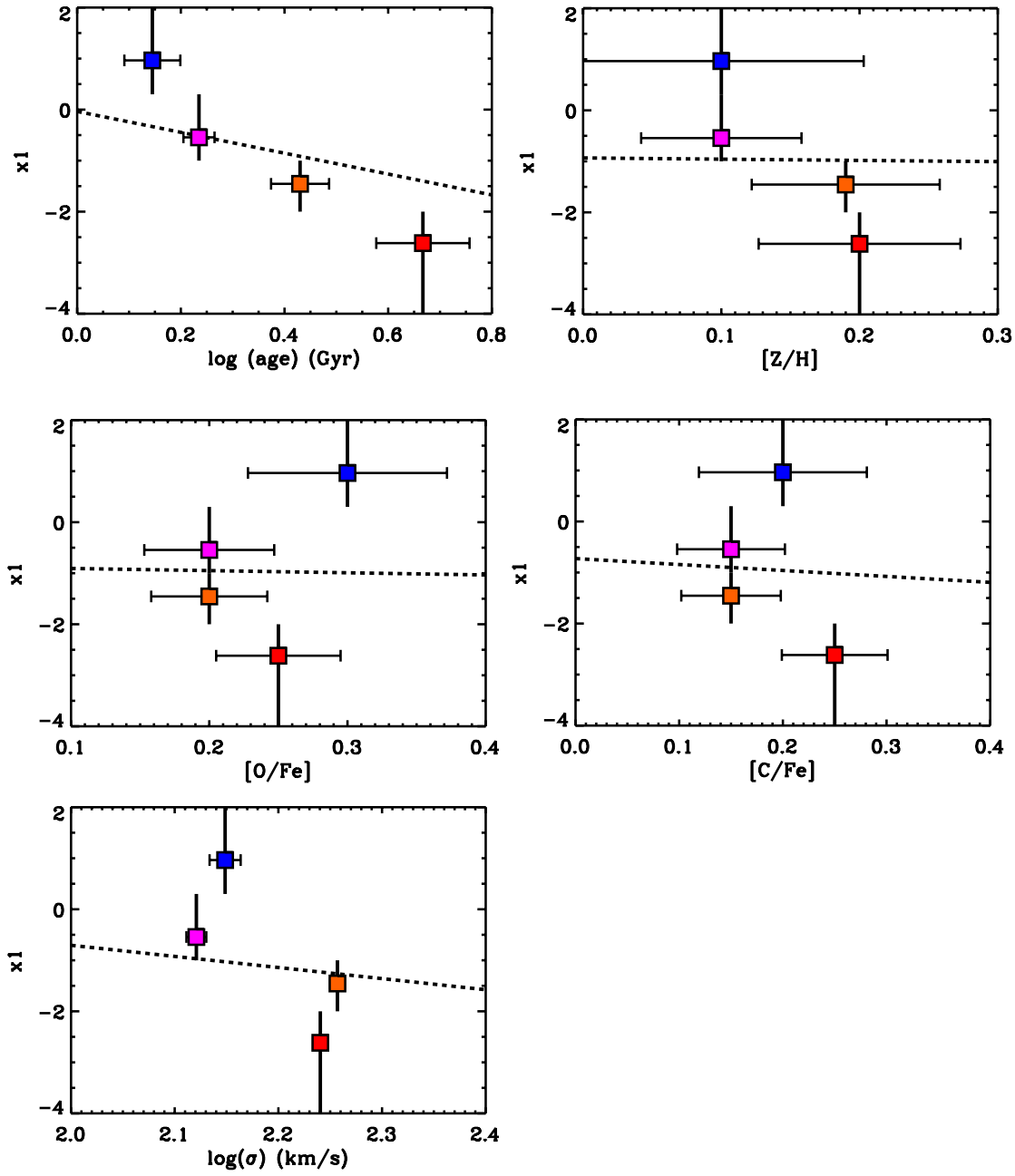

Figure 6.8: Relationship with host galaxy age (upper left panel), Z/H (upper right panel), O/Fe (middle left panel), C/Fe (middle right panel) and velocity dispersion (lower left panel) for SALT2 x_1 for the stacked spectra. The data points are coloured according to the colours of the binned spectra in Fig. 6.7. 1σ errors for the x-axis parameters are indicated by the horizontal error bars. The bin widths are shown by the vertical bars. The x_1 value for each data point is the average x_1 value in the corresponding bin. Dashed lines are the least-square fits for the corresponding relationships of the individual spectra from Fig. 6.6.

panel has been truncated compared to Fig. 6.6 to better resemble the parameter range covered by the data of the stacked spectra.

Lower x_1 values show higher velocity dispersions, older ages and higher total metallicities, in agreement with the case of the individual spectra (see Section 6.3.3). However, only for age we see this trend clearly for all data points adjacent in x_1 space and significantly beyond the 1σ error level. For total metallicity the trend with x_1 is diminished by the error bar overlap, which is due to the short range covered by this parameter ($\sim$0.1 dex). A short parameter range is also found for [O/Fe] ($\sim$0.1 dex) and [C/Fe] ($\sim$0.1 dex), resulting in a significant error bar overlap. We see no clear trends for these parameters. Hence the result of the individual spectra from Section 6.3.3 is reproduced for the stacked spectra, i.e. x_1 show the strongest dependence on stellar population age.

6.3.4 Hubble residual

Several authors have studied relationships between Hubble residual and the stellar population parameters age and metallicity. Gallagher et al. (2008) find metallicity to be the source of systematic Hubble residual variations, while Howell et al. (2009) instead report that metallicity is not responsible for such variations. Neill et al. (2009) find a relation between age and Hubble residual. For the sample studied in this work we do not find significant trends between either of the stellar population parameters age, metallicity or element ratios with Hubble residual.

Several authors have also reported Hubble residual dependencies on host galaxy mass (Kelly et al., 2010; Lampeitl et al., 2010; Sullivan et al., 2010). Fig. 6.9 shows Hubble residual as a function of stellar population age (upper left panel), [Z/H] (upper right panel), [O/Fe] (middle left panel), [C/Fe] (middle right panel), velocity dispersion (lower left panel) and stellar mass (lower right panel) for the final sample. The same colour coding and symbols as in Fig. 6.6 are used. We do not find significant trends for either of the parameters studies ($<2\sigma$ level for all parameters) with Hubble residual. Hence we need to investigate whether the lack of Hubble residual dependencies for the sample studied in this work are real or due to selection effects.

The final sample was selected to include the highest quality of the spectroscopic data available. Since the masses are derived using photometry, however, we can study this parameter for the full sample (277 objects, see Section 6.2). No significant Hubble residual-mass trend is found neither for this larger sample. In fact the slope of the Hubble residual-mass relation is lower for the full sample (-0.03) than the final sample (-0.05) and different from zero at a $<1\sigma$ level.

Looking at the L10 masses (see Section 6.3.2) we instead find stronger trends with Hubble residual for both the final and the full the sample compared to the masses derived

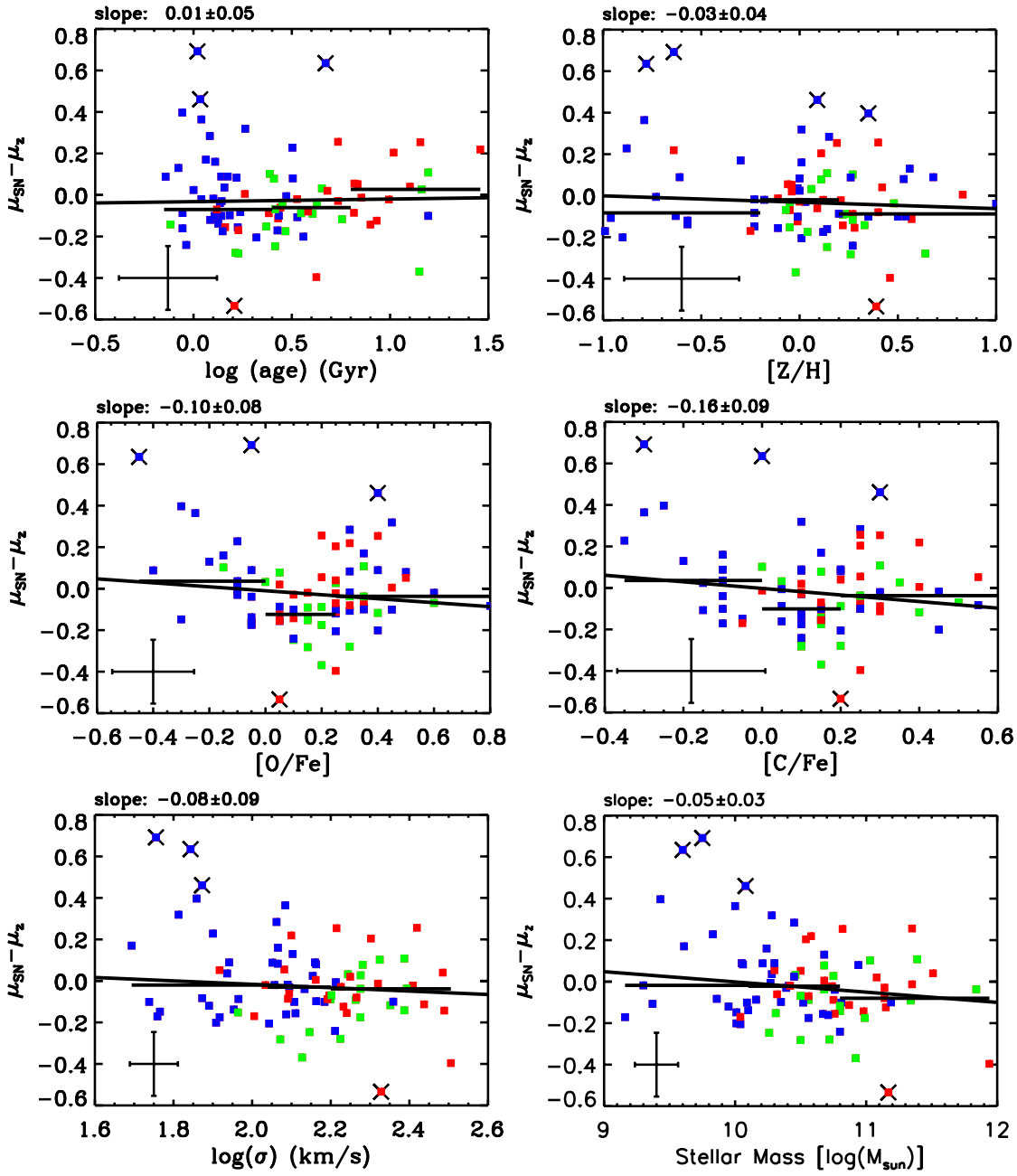

Figure 6.9: Relationship between stellar population age (upper left panel), [Z/H] (upper right panel), [O/Fe] (middle left panel), [C/Fe] (middle right panel), velocity dispersion (lower left panel) and stellar mass (lower right panel) with Hubble residual. The data points are coloured according to the emission line classification of the host galaxies from Section 6.3.1, i.e. blue=SF, green=AGN and red=emission line free. Solid lines are one time sigma-clipped (2σ level) least-square fits and over-plotted crosses are removed data points. The slopes and corresponding errors are given at the top of the panels. Horizontal lines are median Hubble residuals in bins of the x-axis parameters with lengths according to the width of the bins. Error bars the in lower left corner are average 1σ errors.

in this work. In agreement with L10 and the literature negative Hubble residuals are found in massive galaxies and positive Hubble residual are found in low mass galaxies when studying the L10 masses. The slope of the Hubble residual-L10 mass relations are different from zero at a 2.2σ level and has a value of -0.08 for the final sample and at a 3.1σ level with a value of -0.09 for the full sample, compared to the analogous from L10 of -0.069. Hence we reproduce the result of Lampeitl et al. (2010) and the final sample does not seem to be biased by selection effects.

To summarise, velocity dispersion and the stellar masses derived in this work (see Section 6.3.2) are in agreement such that they do not correlate with Hubble residual. Also, no clear Hubble residual dependencies are found for the stellar population parameters age, metallicity and element ratios. Still, the very weak mass dependencies found show the same pattern as L10 and the literature. Thus the lack of Hubble residual dependencies need to be confirmed with a larger, spectroscopically higher quality data set.

6.4 Discussion

We derive host galaxy stellar population parameters for SN Ia from the SDSS-II Supernova survey. The stellar population parameters are derived from absorption line indices through comparison with stellar population model predictions (see Section 6.2.2). Due to the low S/N of the host galaxy spectra we focus on the highest quality objects, considering both the SN Ia observations and host galaxies, which results in a final sample of 84 objects (see Section 6.2.3). For the first time for a statistically significant sample we consider the full range of stellar population parameters, including stellar kinematics and velocity dispersion, luminosity weighted age, metallicity and element abundance ratios. This allow us to pin down the main driver of SN Ia light-curve and luminosity variations.

We do not find any dependencies on the host galaxy parameters for SALT2 colour, in agreement with the literature. Host galaxy dependencies for SALT2 stretch factor and Hubble residuals are discussed in the following sections.

6.4.1 Comparison with the literature

In agreement with Oemler & Tinsley (1979), van den Bergh (1990), Mannucci et al. (2005) and Sullivan et al. (2006) we find a higher fraction of SN Ia events in SF compared to passive (i.e. emission line free) galaxies. The SF galaxies do also show slower decline rates, i.e more luminous SN Ia, compared to the emission line free galaxies, a pattern first noticed by Sullivan et al. (2006) and further confirmed by Howell et al. (2009), Neill et al. (2009) and Lampeitl et al. (2010). For the first time we establish an

anti-correlation between host galaxy velocity dispersion and stretch factor. A similar relationship is found for the derived masses, suggesting faster decline rates in more massive galaxies, in agreement with Kelly et al. (2010), Lampeitl et al. (2010) and Sullivan et al. (2010).

We find a clear anti-correlation between decline rate and luminosity-weighted age, more prominent than found for velocity dispersion, while metallicity and element abundance ratios only show weak dependencies. This is true for both individual objects and stacked host galaxy spectra. The x_1-age relationship shows a smooth transition over the age range covered. Hamuy et al. (2000) and Gallagher et al. (2008) study absorption line indices allowing for distinction between age and metallicity effects. The former prefer metallicity over age as the main driver of SN Ia luminosity, using only 5 objects as pointed out by the authors. Gallagher et al. (2008) instead study 29 SN Ia with host galaxies and instead find age to be the dominant stellar population parameter affecting SN Ia luminosity. However, with a fairly small sample they can not determine whether the luminosity-age relation is smooth or showing two distinct populations. Two recent studies, Howell et al. (2009) and Neill et al. (2009), have derived host galaxy parameters from photometry. Both authors favour age over metallicity as the SN Ia luminosity dependent factor, but determine the latter only indirectly by using derived masses and the mass-metallicity relationship from Tremonti et al. (2004). In a study parallel with this work Gupta et al. also find faster decline rates for older stellar populations using photometry, but do not include metallicity or element abundance ratios in their study. To conclude, this analysis strengthens the emerging trend in the literature that host galaxy age is the main driver of SN Ia light-curve shape and luminosity, such that more luminous SN Ia events occur in younger stellar populations.

6.4.2 Hubble residual

The discrepancies between the masses derived in this work and the L10 masses are due to different SSP models and SED-fitting techniques used (see Section 6.3.2). The L10 masses tend to be overestimated for star-forming galaxies and underestimated for emission-line free galaxies. This seems to mimick a Hubble residual dependency on galaxy mass. If instead the most accurate description for deriving stellar masses is used, which also shows the best correlation with velocity dispersion, the dependence on stellar mass for the Hubble residuals vanishes.

Hence, contrary to the literature we do not find any correlation with stellar mass or metallicity for the Hubble residuals. The appearance of such correlations are alarming for the derived cosmology. It basically means that studying different samples of SN Ia can result in different cosmologies. Since stellar population parameters evolve with

redshift the z-range covered can severely bias the derived cosmological parameters. The lack of Hubble residual dependencies on host galaxy parameters found here imply that the light-curve corrections are good enough to standardise the SN Ia peak luminosities. Most importantly, it indicates the that the derived SN Ia cosmology in the literature is robust.

6.4.3 Progenitor systems

Considering several different progenitor systems theoretical models of SN Ia explosions find the SN Ia rates (SNRs) peaking at delay times below or close to 1 Gyr (Yungelson & Livio, 2000; Greggio, 2005; Ruiter et al., 2010). The SNRs then smoothly decline and becomes 10-100 times lower at delay times of $\sim$10 Gyr. Thus theory implies that the delay times of SN Ia span the range from instantaneous explosions to explosions delayed by a Hubble time. Using the host galaxy stellar population ages as delay time proxies observations support theory as we find a wide range of luminosity-weighted ages from below 1 Gyr to $>$10 Gyr. Similarly Gupta et al. find SN Ia events in stellar populations with mass-weighted ages $>$10 Gyr and down to $\sim$2 Gyrs, while Howell et al. (2009) and Neill et al. (2009) present luminosity-weighted ages from $\sim$100 Myr up to $>$10 Gyr. All these studies agree with theory such that a higher fraction of SN Ia events are found in young SF galaxies compared to old emission line free galaxies. Considering the strong anti-correlation between stretch factor and stellar population age there is a clear connection such that those SN Ia with the shortest delay times, hence most massive progenitors, are the brightest and vice versa. This anti-correlation shows a smooth behaviour, indicating a single progenitor system present. If both the SD and DD systems were present it is likely that a less smooth stretch factor-age anti-correlation would be seen.

Yungelson & Livio (2000) show that the SNR for a DD system peaks at delay times of $\sim$100 Myr, while the analogous for a SD system is $\sim$1 Gyr. Thus the lower age limit of the stellar populations hosting SN Ia could be used to constrain possible progenitor systems. However, it may be far fetched to consider the integrated light of a galaxy a good proxy for SN Ia delay times, considering the range of different stellar populations possibly presents. An alternative could be to use observations confined to the vicinity of the SN Ia. However, it is likely that a mixing of stellar populations occur over a long time span. The probability to find the ”true” parent stellar population for a SN Ia progenitor should increase for an observed younger stellar population. It may therefore be possible to constrain the lower delay time limit using the stellar populations of the vicinity of the SN Ia. This can then in turn constrain possible progenitor systems when comparing to theoretical SN Ia models.

Theoretical models of SN Ia explosions can match the varying observed light-curves by altering the produced ^{56}N masses (e.g. Kasen et al., 2009). Higher ^{56}N masses result in brighter peak luminosities. However, mainly metallicity variations have been considered in the modelled progenitors and have been found to induce a variation in the produced ^{56}N (e.g. Timmes et al., 2003). Observations, including the analysis in this work, indicate that the light-curves instead show the strongest dependency on stellar age, in turn dependent on stellar initial mass, of the progenitors. However, it is not clear how e.g. a varying mass of the companion star in the SD scenario would affect the ^{56}N production during the explosion event.

6.5 Conclusions

We compare SN Ia properties to host galaxy stellar population parameters for a sample drawn from the SDSS-II Supernova survey. 84 objects are used in the analysis, selected on the quality of both the host galaxy spectra and SN Ia properties. Using spectral fitting and absorption line indices, we can consider the full range of stellar population parameters for the first time for a statistically significant sample. This allow us to pin down the main driver of SN Ia light-curve and luminosity variations. The derived stellar population parameters include emission line diagnostics, stellar kinematics, luminosity weighted age, metallicity and element abundance ratios.

We confirm previous results of having higher SALT2 stretch factor values and a larger fraction of SN Ia in SF compared to passive (i.e. emission line free) galaxies. The well known anti-correlation between decline rate and luminosity implies that more luminous SN Ia reside in SF galaxies. We also reproduce previous results of having lower stretch factor values in more massive galaxies. The above mentioned relationships are considered effects of more fundamental relationships between SN Ia properties and stellar population parameters. Age and metallicity have been likely parameters considered to drive the explosion of SN Ia, where recent results speak in favour of the former. We strengthen such results and show that SN Ia stretch factors strongly depend on age rather than metallicity or abundance ratios. Thus SN Ia have a slower decline rate and are more luminous in younger stellar populations. To ensure that the quality of the host galaxies are not affecting by the selected sample, we also stack the spectra. This confirmed the above discussed results and assured age being the main driver of SN Ia peak luminosity. The strong dependence on age indicates that progenitor mass is the true driver of SN Ia peak luminosity.

Reports in the literature of host galaxy dependencies on stellar mass and metallicity for the Hubble residuals are worrying. This indicates that the derived cosmological

parameters could be biased towards the observed samples. In this study we find no significant trends for any of the host galaxy properties studied, including metallicity, stellar velocity dispersion and stellar mass. This implies that the derived cosmological parameters are robust.

Chapter 7

Conclusions and outlook

Stars light up galaxies that are the major building blocks of the Universe. Throughout this thesis we have covered the analysis of stars and stellar populations to gain knowledge on the formation of galaxies and the evolution of the Universe. Understanding massive early-type galaxies is key to understand mass assembly and the formation and evolution of galaxies in the Universe.

The spectra of stellar populations carry a wealth of information regarding galaxy formation and evolution. Absorption lines are particularly useful as they are tracers of galaxy formation epoch and time-scale. Models of stellar populations are important tools for the analysis of galaxies. The accuracy of such models are crucial for the accuracy of the derived results. The first step in my thesis was therefore to improve upon current single stellar population models based on absorption line indices. Calibration of the models with galactic globular cluster is crucial, since these are known to be close to single stellar populations. We have then applied the models to the analysis of early-type galaxies and SN Ia host galaxies.

7.1 Empirical calibrations of stellar libraries

Stellar population models of absorption line indices rely on empirical calibrations of the indices with stellar parameters based on stellar libraries. The empirical calibrations most frequently used in the literature are based on the non flux calibrated Lick/IDS stellar library, requiring Lick index offsets between observations and models. To overcome this we attempted to derive universal Lick offsets using three flux-calibrated libraries in the literature (Chapter 2), namely *MILES*, *ELODIE* and *STELIB*. However, we found inconsistencies between the three libraries hampering the derivation of a universal offset. For

this reason we decided to focus on *MILES* to derive new empirical calibrations (Chapter 2), which is the the most comprehensive library of the three in terms of stellar parameter coverage and it has been carefully flux calibrated. Our measurements of the 25 Lick indices on *MILES* show a significant improvement in terms of typical errors compared to the Lick/IDS library.

The Lick indices are sensitive to T_{eff}, $\log g$, [Fe/H] and element abundance ratios. However, *MILES* (and every other available stellar library) are based on the stars in the solar neighbourhood that show a narrow range in element ratios as a function of metallicity. Hence the stellar library only allows for the calibration on the stellar parameters T_{eff}, $\log g$ and [Fe/H]. To account for the complex behaviour of the Lick indices on these parameters we have derived polynomial fitting functions in various regions of T_{eff}, $\log g$, [Fe/H] parameter space. The final fitting functions show an overall good agreement with fitting functions in the literature.

7.2 Stellar population model of absorption line indices

The empirical calibrations of the *MILES* stellar library have been used to produce state of the art stellar population models of absorption line indices (Chapter 3). The models are applicable to flux calibrated spectra without Lick index calibrations, since the *MILES* stellar spectra have been carefully flux-calibrated. The models are an updated version of the Thomas et al. (2003a) and Thomas et al. (2004) (TMB/K) models, which allow element abundance variations through the Lick index response functions of Korn et al. (2005). These models mainly include abundance variations of the α- and Fe-like elements. We have extended this to produce models with abundance variations of a large range of elements to which the Lick indices are sensitive, including C, N, O, Mg, Ca, Ti, Fe and Cr. Similarly to the TMB/K models we account for the element ratio bias of the Milky Way.

We have derived random errors for the model predictions based on uncertainties in the calibration functions and the underlying stellar parameter estimates. These errors are in general very small and only blow up at the edges of the parameters space covered by the *MILES* stellar library. We calibrate the base models, i.e. varying ages, metallicities and [α/Fe] ratios, with Lick indices derived from integrated spectroscopy of galactic globular clusters with independent parameter measurements from resolved photometry and spectroscopy of individual cluster stars. Those indices that are only sensitive to the base parameters are in general very well calibrated, while indices sensitive to individual element abundance variations show offsets to the globular cluster data.

7.3 Element abundance ratios of globular clusters

Based on the new stellar population models we have developed a method for deriving the stellar population parameters age, metallicity and a wide range of element abundance ratios (Chapter 4), including [O/Fe] (inferred from [α/Fe]), [C/Fe], [N/Fe], [Mg/Fe], [Ca/Fe] and for the first time for unresolved stellar populations [Ti/Fe]. In subsequent steps we use in turn particular sets of Lick indices that are sensitive to the element the abundance of which we want to determine. Since several indices are sensitive to the variation of more than one element abundance we iteratively derive the set of element ratios until convergence is found.

The method is applied to the sample of galactic globular clusters and we find that the model fits to a number of indices improve considerably when the individual element ratios are considered. The metallicities and ages we derive agree well with the literature and the latter are all consistent with the age of the universe within the measurement errors. For some objects we tend to slightly underestimate the metallicity and overestimate the age, in line with the age-metallicity degeneracy. We also find good agreement with independent measurements of the element ratios from high-resolution spectroscopy of individual cluster stars. The Lick index sensitivities to element abundance variations become very weak below an iron abundance of [Fe/H]$\sim$-1 dex. Thus the derivation of individual element abundance ratios is not reliable in this regime. The [α/Fe] ratio is on the other hand robust at all metallicities. The discussion of individual element ratios focuses therefore on globular clusters with [Fe/H]$>$-1 dex.

The elements O and Mg follow the same general enhancement with almost identical distributions of [O/Fe] and [Mg/Fe]. We find slightly lower [C/Fe] and very high [N/Fe] ratios, instead. Hence N is significantly enhanced and C slightly depressed in globular clusters with respect to the other light elements. This chemical anomaly commonly attributed to self-enrichment is well known in globular clusters from individual stellar spectroscopy, and it is the first time that this pattern is derived also from the integrated light. [Ca/Fe] and [Ti/Fe] are typically suppressed by $\sim$0.2 dex compared to [Mg/Fe] and [O/Fe]. This indicates that the nucleosynthesis of α-elements from SN Ia is dependent on atomic number, i.e. SN Ia contributes more to the enrichment of the heavy α-elements Ca and Ti compared to lighter elements such as Mg.

7.4 Chemical enrichment histories of SDSS early-type galaxies

The method developed for deriving element abundance ratios is applied to ∼4000 SDSS early-type galaxies (Chapter 5). We confirm previous findings of increasing ages and total metallicities with stellar velocity dispersion. [Fe/H] shows a flat behaviour with velocity dispersion over the entire parameter range covered, but for fixed age we find a steep trend for the [Fe/H]-σ relation. This trend is weaker than the analogous for total metallicity (which also shows steeper trends at fixed age) owing to the lower Fe contribution from SN Ia for more massive early-type galaxies. The element abundance ratios [O/Fe], [Mg/Fe] and [C/Fe] all show similar values and strongly correlate with velocity dispersion. Hence C/Mg and C/O are close to solar values over the velocity dispersion range covered. These trends constrain the lower limit on the time-scales of star formation and star-burst components in early-type galaxies, since the full C enrichment must be reached. We find this limit to be ∼0.4 Gyr inferred from the lifetime of a $3M_{\odot}$ star, which is the lowest stellar mass that contribute significantly to the production of C.

[N/Fe] is found to be lower by ∼0.2 dex compared to the other element ratios and to show a stronger correlation with velocity dispersion. We discuss three possible mechanisms that can contribute to the steep [N/Fe]-σ relationship. 1. N yields with a strong dependence on metallicity. 2. A dependence on galaxy mass for the ratio between the time-scale of star formation and the time-scale of primordial gas inflow. 3. Star formation fraction in globular clusters that is dependent on galaxy mass. These mechanisms can work together to produce higher [N/Fe] ratios in more massive galaxies. We do not find any environmental dependencies for the abundances of C and N, contrary to the previous reports in the literature.

We find that [Ca/Fe] ratio are close to solar values over the velocity dispersion range covered and that [Ca/Fe] does not correlate with stellar velocity dispersion. Tentative, due to large scatter, the results for [Ti/Fe] indicate that Ti follows the trends of Ca. Hence similar to the globular cluster case we find that Ca and Ti scale with Fe rather than the lighter α elements O and Mg. This implies that the significant contribution from SN Ia to the enrichment of heavy α-elements is universally found and puts strong constraints on supernova nucleosynthesis and models of galactic chemical evolution.

7.5 SN Ia host galaxies

SN Ia are useful standard candles with peak luminosities that can probe vast distances. This can be used to connect luminosity distance to redshift space to constrain cosmolog-

ical parameters. There are indications in the literature that the SN Ia peak luminosities after light-curve corrections are dependent on host galaxy properties and the parameters of their stellar populations. This is worrying as it may affect the derived cosmological parameters, since host galaxy properties evolve with redshift.

We have derived stellar population parameters, element abundance ratios, emission line diagnostics, stellar velocity dispersions and stellar masses for SN Ia host galaxies from the SDSS-II SN survey (Chapter 6). Due to low quality of the host galaxy observations a sub-sample of 84 galaxies have been selected depending on the S/N of the host galaxy spectra and accuracy of the SALT2 fitted SN Ia parameters.

We find a larger fraction of SN Ia and higher SALT2 stretch factor values (i.e. more luminous and slower declining SN Ia) in star formation classified galaxies compared to galaxies without detected emission lines. A strong anti-correlation between SALT2 stretch factor and luminosity-weighted age is found. Hence age seems to be the dominant driver of SN Ia peak luminosity. As a result of this dependence the SALT2 stretch factor values also show a significant dependence on stellar velocity dispersion and mass, while only weak dependencies are found for metallicity and the element ratios. We confirm this behaviour by stacking host galaxy spectra in bins of SALT2 stretch factor. Due to a strong relationship between SN Ia decline rate and peak luminosity the anti-correlation between SALT2 stretch factor and stellar population age indicates that progenitor mass is the true driver of SN Ia peak luminosity. We do not find any significant dependencies on the host galaxies for the SALT2 colour term.

Most importantly, after light-curve corrections we do not find any significant dependencies on host galaxy properties and stellar population parameters for the resulting scatter in the luminosity-distance relationship, contrary to reports in the literature. This indicates that the currently derived cosmology from SN Ia peak luminosities is robust and not biased towards the stellar populations at certain cosmological epochs.

7.6 Outlook

We have developed a powerful method for studying stellar populations. It is desirable to apply this method to new and future data sets and instruments to better constrain galaxy evolution. Some of these data sets and instruments are listed and discussed below.

Galaxy Zoo. Galaxy Zoo is built on SDSS by having hundreds of thousands of public users visually classify the morphology of hundreds of thousands of galaxies. This gives the opportunity to study the stellar population parameters and element ratios as a function of galaxy morphology. The Galaxy Zoo sample provides great number statistics

to compare different morphological galaxy populations in detail. Specifically interesting categories available within this sample are red spirals and blue early-type galaxies.

BOSS. The latest incarnation of the SDSS collaboration (SDSS-III) performs observations of 1.5 million massive galaxies up to z$\sim$0.7 wihtin the Baryonic Acoustic Oscillation Survey (BOSS). The intention of BOSS is to map the spatial distribution of luminous red galaxies (LRGs) and quasars to detect the characteristic scale imprinted by baryon acoustic oscillations in the early universe. The large number of LRGs observed over a wide redshift range provides an excellent opportunity to study the redshift evolution of massive galaxies.

IFU spectroscopy. The use of IFU spectroscopy provides high spatial resolution. This allows for the detailed analysis of dynamical structure and gradients of stellar population parameters and element abundance ratios. The stellar population gradients are useful for identifying merger and accretion histories. To date no gradients of element ratios besides α/Fe have been studied and relatively small galaxy samples have been studied with IFU spectroscopy (e.g. SAURON, ATLAS3D). CALIFA (Calar Alto Legacy Integral Field spectroscopy Area survey) is currently ongoing with the aim to spatially resolve $\sim$600 nearby galaxies. A possible successor to the SDSS legacy is MaNGA (Mapping Nearby Galaxies at the Apache point observatory, proposal submitted at date and observing start planned to 2014) which has the intention to perform IFU spectroscopy of $\sim$10,000 nearby galaxies.

A key obstacle of current studies of host galaxy dependencies for SN Ia properties, including the work presented here, is the restriction to the integrated light of the host galaxies. Significantly better accuracy can be obtained, if host galaxy properties are studied closer to the explosion site of the supernova within the galaxy. The spatially resolved spectroscopy of MaNGA will make this possible. We will be in the position to study the exact ages and element abundances of the progenitor stars of the supernovae. Key here is the 10k sample size of MaNGA as supernovae are relatively rare events.

KMOS. The use of infrared spectra allow studies of rest-frame optical wavelengths of high redshift galaxies. For this purpose several instruments are or will be available. FMOS (Fibre Multi Object Spectrograph) is operational on the Subaru telescope and can measure the infrared spectra from 400 objects simultaneously. KMOS (K-band Multi Object Spectrometer) is a near infrared multi-object IFU spectrograph for the VLT (Very Large Telescope) which is planned to be operational in late 2011. One aim of KMOS is to investigate the physical processes which drive galaxy formation and evolution over the

redshift range $1<z<10$.

Hence, the future holds many exciting data sets. In an even longer perspective the instalment of future extremely large telescopes will open up a whole new dimension of possibilities to study the stellar populations of high redshift galaxies.

References

Allanson S., Hudson M., Smith R., Lucey J., 2009, ApJ, 702, 1275

Annibali F., Bressan A., Rampazzo R., Zeilinger W. W., Danese L., 2007, A&A, 463, 455

Arnett W., 1982, ApJ, 253, 785

Asplund M., Grevesse N., Sauval A. J., Scott P., 2009, ARA&A, 47, 481

Bacon R., et al., 2001, MNRAS, 326, 23

Baldry I., Glazebrook K., Brinkmann J., Ivezić, Ź., Lupton R., Nichol R., Szalay A., 2004, ApJ, 600, 681

Baldwin J., Phillips M., Terlevich R., 1981, PASP, 93, 5 (BPT)

Balogh M., Baldry I., Nichol R., Miller C., Bower R., Glazebrook K., 2004, ApJ, 615L, 101

Bamford S., et al., 2009,MNRAS, 393, 1324

Barnes J., Hernquist L.,1996, ApJ, 471, 115

Barris B., Tonry J., 2006, ApJ, 637, 427

Baum W., 1959, PASP, 71, 106

Bower R., Lucey J., Ellis R., 1992, MNRAS, 254, 601

Beifiori A., Maraston C., Thomas D., Johansson J., 2011, A&A, 531, 109

Bell E., et al., 2004, ApJ, 608, 752

Bender R., Burstein D., Faber S., 1992, ApJ, 399, 462

Bender R., Saglia R., Ziegler Bodo., Belloni P., Greggio L., Hopp U., Bruzual G., 1998, ApJ, 493, 529

Bensby T., Feltzing S., Lundström I., 2004, A&A, 415, 155

Bensby T. et al., 2010, A&A, 512, 41

Bernardi M., Nichol R. C., Sheth R. K., Miller C. J., Brinkmann J., 2006, AJ, 131, 1288

Bertelli G., Girardi L., Marigo P., Nasi E., 2008, A&A, 484, 815.

Bertelli G., Nasi E., Girardi L., Marigo P., 2009, A&A, 508, 355

Bono G., Caputo F., Cassisi S., Castellani V., Marconi M., 1997, ApJ, 489, 822

Borges A. C., Idiart T. P., de freitas Pacheco J. A., Thévenin F., 1995, AJ, 110, 2408

Bosma A., 1981, AJ, 86, 1825

Branch D., Livio M., Yungelson L., Boffi F., Baron E., 1995, PASP, 107, 1019

Branch D., 2001, PASP, 113, 169

Brodie J. P., Strader J., Denicoló G., Beasley M. A., Cenarro A. J., Larsen S. S., Kuntschner H., Forbes D. A., 2005, AJ, 129, 2643

Bruzual G., Charlot S., 2003, MNRAS, 344, 1000

Burstein D., Faber S. M., Gaskell C. M., Krumm N., 1984, ApJ, 287, 586

Buzzoni A., Gariboldi G., Mantegazza L., 1992, AJ, 103, 1814

Buzzoni A., Mantegazza L., Gariboldi G., 1994, AJ, 107, 513

Cappellari M., Emsellem E., 2004, PASP, 116, 138

Cappellari M., 2006, MNRAS, 366, 1126

Carney B. W., 1996, PASP, 108, 900

Carretta E., Gratton R. G., Lucatello S., Bragaglia A., Bonifacio P., 2005, A&A, 433, 597

Carson D,. Nichol R., 2010, MNRAS, 408, 213

Cassisi S., Castellani M., Castellani V., 1997, A&A, 317, 10 (Cassisi)

Castellani V., Chieffi A., Straniero O., 1992, ApJS, 78, 517

Cenarro A. J., Gorgas J., Cardiel N., Vazdekis A., Peletier R. F., 2002, MNRAS, 329, 863

Cenarro A. J., Gorgas J., Vazdekis A., Cardiel N., Peletier R. F., 2003, mnras, 339, L12

Cenarro A. J., Peletier R. F., Sánchez-Blázquez P. et al., 2007, MNRAS, 374, 664

Cervantes J. L., Vazdekis A., 2009, MNRAS, 392, 691

Cescutti G., Matteucci F., McWilliam A., Chiappini C., 2009, A&A, 505, 605

Chen Y.-M., Wild V., Kauffmann G., Blaizot J., Davis M., Noeske K., Wang J.-M., Willmer C., 2009, MNRAS, 393, 406

Chiappini C., Matteucci F., Gratton R. G., 1997, ApJ, 477, 765

Chou R., Bridge C., Abraham R., 2011, AJ, 141, 87

Cimatti A., Daddi E., Renzini A., 2006, A&A, 453, L29

Clemens M. S., Bressan A., Nikolic B., Alexander P., Annibali F., Rampazzo R., 2006, MNRAS, 370, 702

Clemens M., Bressan A., Nikolic B., Rampazzo R., 2009, MNRAS, 392, 35

Coelho P., Bruzual G., Charlot S., Weiss A., Barbuy B., Ferguson J. W., 2007, MNRAS, 382, 498

Cohen J.G., 1983, ApJ, 270, 654

Colgate S., McKee C., 1969, ApJ, 157, 623

Conley A. et al., 2008, ApJ, 681, 482

Cowie L., Songaila A., Hu E., Cohen J., 1996, AJ, 112, 839

Cox T., Jonsson P., Primack J., Somerville R., 2006, MNRAS, 373, 1013

Davies R., 1981, MNRAS, 194, 879

Davies R., Illingworth G., 1983, ApJ, 266, 516

Davies R., et al., 2001, ApJ, 548, 33

Davies R. L., Sadler E. M., Peletier R. F., 1993, MNRAS, 262, 650

De Angeli F., Piotto G., Cassisi S., Busso G., Recio-Blanco A., Salaris M., Aparicio A., Rosenberg A., 2005, AJ, 130, 116

Dekel A., Birnboim Y., 2006, MNRAS, 368, 2

De Lucia G., Blaizot J., MNRAS, 375, 2

de Vaucouleurs G., 1959, HDP, 53, 275

Djorgovski S., Davis M., 1987, ApJ, 313, 59

Dotter A., Chaboyer B., Ferguson J. W., Lee H., Worthey G., Jevremović D., Baron E., 2007, ApJ, 666, 403

Dressler A., 1980, ApJ, 236, 351

Dressler A., Lynden-Bell D., Burstein D., Davies R., Faber S., Terlevich R., Wegner G., 1987, ApJ, 313, 42

Dressler A., Oemler A. Jr., Couch W., Smail I., Ellis R., Barger A., Butcher H., Poggianti B., Sharples R., 1997, ApJ, 490, 577

Edvardsson B., Andersen J., Gustafsson B., Lambert D. L., Nissen P. E., Tomkin J., 1993, A&A, 275, 101

Faber S. M., Friel E. D., Burstein D., Gaskell C. M., 1985, ApJS, 57, 711

Faber S., 2007, ApJ, 665, 265

Feltzing S., Primas F., Johnson R., 2009, A&A, 493, 913

Forbes D. A., Beasley M. A., Brodie J. P., Kissler-Patig M.,2001, ApJ, 563, 143

Frieman J., et al. 2008, AJ, 135, 338

Fuhrmann K., 1998, A&A, 338, 161

Fukugita M., Hogan C., Peebles P.,1998, ApJ, 503, 518

Gallagher J., Garnavich P., Caldwell N., Kirshner R., Jha S., Li W., Ganeshalingam M., Filippenko A., 2008, ApJ, 685, 752

Gallazzi A., Charlot S., Brinchmann J., White S., Tremonti C., 2005, MNRAS, 362, 41

Gallazzi A., Charlot S., Brinchmann J., White S., 2006, MNRAS, 370, 1106

Gal-Yam A., Maoz D., 2004, MNRAS, 347, 942

Giallongo E., Salimbeni S., Menci N., Zamorani G., Fontana A., Dickinson M., Cristiani S., Pozzetti L., 2005, ApJ, 622, 116

Giovanelli R., Haynes M., Chincarini G., 1986, ApJ, 300, 77

Girardi L., Bressan A., Bertelli G., Chiosi C., 2000, A&AS, 141, 371

González J., 1993, PhD thesis, Univ. California, Santa Cruz

Gorgas, J., Faber S. M., Burstein D., Gonzalez J. J., Courteau S., Prosser C., 1993, ApJS, 86, 153

Gorgas J., Cardiel N., Pedraz S., González J. J., 1999 A&AS, 139, 29

Graham A., Erwin P., Trujillo I., Asensio Ramos A., 2003, AJ, 125, 2951

Granato G., De Zotti G., Silva L., Bressan A., Danese L., 2004, ApJ, 600, 580

Graves G. J., Schiavon R. P., 2008, ApJS, 177, 446

Graves G., Faber S., Schiavon R., Yan R., 2007, ApJ, 671, 243

Greggio L., Renzini A., 1983, A&A, 118, 217

Greggio L., 1997, MNRAS, 285, 151

Greggio L., 2005, A&A, 441, 1055

Grevesse N., Noels A., Sauval A., 1996, ASPC, 99, 117

Gupta R., 2011 (submitted)

Guy J. et al., 2007, A&A, 466, 11

Hamuy M., Trager S., Pinto P., Phillips M., Schommer R., Ivanov V., Suntzeff N., 2000, AJ, 120, 1479

Harris W. E., 1996, AJ, 112, 1487

Henry R. B. C., & Worthey G., 1999, PASP, 111, 919

Henry R., Edmunds M., Köppen J., 2000, ApJ, 541, 660

Hillebrandt W., Niemeyer J., 2000, ARA&A, 38, 191

Hirschi R, 2007, A&A, 461, 571

Hoflich P., Khokhlov A., Wheeler J., 1995, ApJ, 444, 831

Hogg D., et al., 2003, ApJ, 585L, 5

Holtzman, 2008, AJ, 136, 2306

Hopkins P., Hernquist L., Cox T., Di Matteo T., Robertson B., Springel V., 2006, ApJS, 163, 1

Houdashelt M. L., Trager S. C., Worthey G., 2005, Highlights Astron., 13, 585

Howell D., et al., 2009, ApJ, 691, 661

Hubble E., 1936, Realm of the Nebulae. Yale University Press, New Haven

Iben I., Jr., Truran J., 1978, ApJ, 220, 980

Illingworth G., 1977, ApJ, 218, L43

Izotov Y., Thuan T., 1999, ApJ, 511, 639

Jha S, Riess A., Kirshner R., 2007, ApJ, 659, 122

Jimenez R., Bernardi M., Haiman Z., Panter B., Heavens A., 2007, ApJ, 669, 947

Johansson J., Thomas D., Maraston C., 2010, MNRAS, 406, 165

Johansson J., Thomas D., Maraston C., 2012a, MNRAS, 421, 1908

Johansson J., Thomas D., Nichol R., Maraston C., Pforr J., Smith M., Lampeitl H., 2012b, in prep.

Jones L. A., 1999, Ph.D. thesis, Univ. North carolina

Karim A., Schinnerer E., Martinez-Sansigre A., et al., 2011ApJ, 730, 61

Kasen D., Röpke F., Woosley S., 2009, Nature, 460, 869

Kauffmann G., 1996, MNRAS, 281, 487

Kauffmann G., White S. D. M., Guiderdoni B., 1993, MNRAS, 264, 201

Kauffmann G., et al., 2003a, MNRAS, 341, 33

Kauffmann G., et al., 2003b, MNRAS, 346, 1055

Kelly P., Hicken M., Burke D., Mandel K., Kirshner R., 2010, ApJ, 715, 743

Kelson D., Illingworth G., Franx M., van Dokkum P., 2006, ApJ, 653, 159

Kessler R. et al., 2009, PASP, 121, 1028

Kewley L., Dopita M., Sutherland R., Heisler C., Trevena J., 2001, ApJ, 556, 121

Kissler-Patig M., Brodie J. P., Schroder L. L., Forbes D. A., Grillmair C. J., Huchra J. P., 1998, AJ, 115, 105

Kodama T., 2004, MNRAS, 350, 1005

Komatsu E. et al., 2011, ApJS, in press (arXiv:1001.4538)

Kormendy J., Fisher D., Cornell M., Bender R., 2009, ApJS, 182, 216

Korn A. J., Maraston C., Thomas D., 2005, A&A, 438, 685

Kuntschner H., 2000, MNRAS, 315, 184

Kuntschner H., 2001, Ap&SS, 276, 885

Kuntschner H., Davies R. L., 1998, MNRAS, 295, 29

Kuntschner H., Ziegler B.L., Sharples R. M., Worthey G., Fricke K. J., 2002, A&A, 395, 761

Kuntschner H. et al., 2006, MNRAS, 369, 497

Kuntschner H. et al., 2010, MNRAS, 408, 97

Köppen J., Edmunds M., 1999, MNRAS. 306, 317

Lampeitl H., 2010, ApJ, 722, 566

Le Borgne J. F., Bruzual G., Pelló R. et al., 2003, A&A, 402, 433

Lee H., Worthey G., Dotter A., 2009a, AJ, 138, 1442

Lee H. et al., 2009b, ApJ, 694, 902

Lee J., Hwang H., Lee M., Lee J., Matsuhara H., 2010, ApJ, 719, 1946

Leitherer C., Schaerer D., Goldader J. D. et al., 1999, ApJS, 123, 3

Lin H., Yee H., Carlberg R., Morris S., Sawicki M., Patton D., Wirth, G., Shepherd C., 1999, ApJ, 518, 533

MacArthur L. A., 2005, ApJ, 623, 795

Maeder A., 1992A&A, 264, 105

Mannucci F., Della Valle M., Panagia N., Cappellaro E., Cresci G., Maiolino R., Petrosian A., Turatto M., 2005, A&A, 433, 807

Maraston C., 1998, MNRAS, 300, 872

Maraston C., 2005, MNRAS, 362, 799

Maraston C., Thomas D., 2000, ApJ, 541, 126

Maraston C., Strömbäck G., 2011, submitted to MNRAS

Maraston C., Greggio L., Renzini A., Ortolani S., Saglia R. P., Puzia T. H., Kissler-Patig M., 2003, A&A, 400, 823

Maraston C., Nieves Colmenárez L., Bender R., Thomas D., 2009, A&A, 493, 425

Marín-Franch A., et al., 2009, ApJ, 694, 1498

Masters K., et al., 2010, MNRAS, 405, 783

Matteucci F., 1986, MNRAS, 221, 911

Matteucci F., Greggio L., 1986, A&A, 154, 279

Matteucci F., Francois P., 1989, MNRAS, 239, 885

Matteucci F., 1994, A&A, 288, 57

Matteucci F., Romano D., Molaro P., 1999, A&A, 341, 458

McWilliam A., 1997, ARA&A, 35, 503

Mendel J. T., Proctor R. N., Forbes D. A., 2007, MNRAS, 379, 1618

Meynet G., Maeder A., 2002, A&A, 390, 561

Michielsen D., De Rijcke S., Dejonghe H., Zeilinger W. W., Hau G. K. T., 2003, ApJ, 597, L21

Mihos J., Hernquist L., 1994, ApJ, 431, L9

Milone A., Barbuy B., Schiavon R., 2000, AJ, 120, 131

Milone A., Sansom A. E., Sánchez-Blázquez P., submitted, in Bruzual G. R., Charlot S., eds, Proc. IAU Symp. 262, Stellar Populations - Planning for the Next Decade.

Murray N., Quataert E., Thompson T., 2005, ApJ, 618, 569

Neill J., et al., 2009, ApJ, 707, 1449

Nelan J. E., Smith R. J., Hudson M. J., Wegner G. A., Lucey J. R., Moore S. A. W., Quinney S. J., Suntzelt N. B., 2005, ApJ, 632, 137

Nomoto K., Thielemann F.-K., Yokoi K., 1984, ApJ, 286, 644

Norris J., Freeman K. C., Da Costa G. S., 1984, ApJ, 277, 615

O'Connell R., 1976, ApJ, 206, 370

Oemler A. Jr., Tinsley B., 1979, AJ, 84, 985

Ortolani S., Renzini A., Gilmozzi R., Marconi G., Barbuy B., Bica E., Rich R. M., 1995, Nature, 377, 701

Pagel B., Tautvaisiene G., 1995, MNRAS, 276, 505

Panter B., Jimenez R., Heavens A. F., Charlot S, 2007, MNRAS, 378, 1550

Peng E., Jordán A., Côté P., et al., 2008, ApJ, 681, 197

Perlmutter S., Aldering G., Goldhaber G., et al., 1999, ApJ, 517, 565

Persic M., Salucci P., Stel F., 1996, MNRAS, 283, 1102

Peterson R., 1976, ApJ, 210, L123

Pforr J., Maraston C., Tonini C., MNRAS, submitted

Phillips M., 1993, ApJ, 413, 105

Pinto P., Eastman R., 2000, ApJ, 530, 744

Pipino A., Matteucci F., 2004, MNRAS, 347, 968 (PM04)

Pipino A., Chiappini C., Graves G., Matteucci F., 2009, MNRAS, 396, 1151 (P10)

Poole V., Worthey G., Lee H., Serven J., 2010, AJ, 139, 809

Postman M., Geller M., 1984, ApJ, 281, 95

Pozzetti L., Bolzonella M., Zucca E. et al., 2010, 523, 13

Price J., Phillips S., Huxor A., Smith R., Lucey J., 2011, MNRAS, 411, 2558

Pritzl B. J., Venn K. A., Irwin M., 2005, AJ, 130, 2140

Proctor R. N., Forbes D. A., Hau G. K. T., Beasley M. A., De Silva G. M., Contreras R., Terlevich A. I., 2004, MNRAS, 349, 1381

Prugniel, Ph., Soubiran C., 2001, A&A, 369, 1048

Puzia T. H., Saglia R. P., Kissler-Patig M., Maraston C., Greggio L., Renzini A., & Ortolani S., 2002, A&A, 395, 45

Puzia T. H., Kissler-Patig M., Thomas D., Maraston C., Saglia R. P., Bender R., Goudfrooij P., Hempel M., 2005, A&A, 439, 997

Reimers D., 1975, Mém. R. Soc. Liége, 8, 369

Renzini A., 1998, AJ, 115, 2459

Renzini A., Voli M., 1981, A&A, 94, 175

Renzini A., Ciotti L., 1993, ApJ, 416, 49

Riess A., et al., 1998, AJ, 116, 1009

Rodríguez-Merino L. H., Chavez M., Bertone E., Buzzoni A., 2005, ApJ, 626, 411

Rose J. A., Bower R. G., Caldwell N., Ellis R. S., Sharples R. M., Teague P., 1994, AJ, 108, 2054

Rubin V., Ford W. Jr., Thonnard N., 1980, ApJ, 238, 471

Ruiter A., Belczynski K., Sim S., Hillebrandt W., Fryer C., Fink M., Kromer M., 2010, arXiv1011.1407

Saglia R. P., Maraston C., Thomas D., Bender R., Colless M., 2002, ApJ, 579, L13

Saio H., Nomoto K., 1998, ApJ, 500, 388

Sako M., 2008, AJ, 135, 348

Salaris M., Cassisi S., 1996, A&A, 305, 858

Salaris M., Chieffi A., Straniero O. 1993, ApJ, 414, 580

Sandage A., 1961, The Hubble Atlas. Carnegie Inst., Washington

Sandage A., Visvanathan N., 1978a, ApJ, 223, 707

Sandage A., Visvanathan N., 1978b, ApJ, 225, 742

Sanders D., Mirabel I., 1996, ARA&A, 34, 749

Sánchez-Blázquez P., Gorgas J., Cardiel N., Cenarro J., González J., 2003, ApJ, 590, 91

Sánchez-Blázquez P., Gorgas J., Cardiel N., González J., 2006a, A&A, 457, 787

Sánchez-Blázquez P., Peletier R. F., Jiménez-Vicente J. et al., 2006b, MNRAS, 371, 703

Sánchez-Blázquez P., Jablonka P., Noll S. et al., 2009, A&A, 499, 47

Sarzi M., et al., 2006, MNRAS, 366, 1151

Schawinski K., Thomas D., Sarzi M., Maraston C., Kaviraj S., Joo S.-J., Yi S.K., Silk J., 2007, MNRAS, 382, 1415

Schechter P., Gunn, J., 1979, ApJ, 229, 472

Schiavon R. P., 2007, ApJS, 171, 146

Schiavon R. P., Faber S. M., Rose J. A., Castilho B. V., 2002, ApJ, 580, 873

Schiavon R. P., Rose J. A., Courteau S., MacArthur L. A., 2005, ApJS, 160, 163

Serra P., Trager S., 2007, MNRAS, 374, 769

Serven J., Worthey G., Briley M. M., 2005, ApJ, 627, 754

Smith R. J., Lucey J. R., Hudson M. J., Bridges T. J., 2009, MNRAS, 398, 119

Springel V., White S., Jenkins A. et al., 2005a, Nature, 435, 629

Springel V., Di Matteo T., Hernquist L., 2005b, ApJ, 620, L79

Strateva I., et al., 2001, AJ, 122, 1861

Strolger, L.-G., et al., 2004, ApJ, 613, 200

Strolger, L.-G., et al., 2005, ApJ, 635, 1370

Sullivan M., et al., 2006, ApJ, 648, 868

Sullivan M., et al., 2010, MNRAS, 406, 782

Surma P., Bender R.,1995, A&A, 298, 405

Sweigart A., Greggio L., Renzini A., 1989, ApJS, 69, 911

Tantalo R., Chiosi C., Bressan A., 1998, A&A, 333, 419

Thielemann F.-K., Nomoto K., Hashimoto M., 1996, ApJ, 460, 408

Thomas D., 1999a, MNRAS, 306, 655

Thomas D., Davies R. L., 2006, MNRAS, 366, 510

Thomas D., Maraston C., 2003, A&A, 401, 429

Thomas D., Greggio L., Bender R., 1998, MNRAS, 296, 119

Thomas D., Greggio L., Bender R., 1999b, MNRAS, 302, 537

Thomas D., Maraston C., Bender R., 2003a, MNRAS, 339, 897

Thomas D., Maraston C., Bender R., 2003b, MNRAS, 343, 279

Thomas D., Maraston C., Korn A., 2004, MNRAS, 351, 19

Thomas D., Maraston C., Bender R., Mendes de Oliveira C., 2005, ApJ, 621, 673

Thomas D., Maraston C., Schawinski K., Sarzi M., Silk J., 2010, MNRAS, 404, 1775 (T10)

Thomas D., Johansson J., Maraston C., 2011a, MNRAS, 412, 2199 (Paper II)

Thomas D., Maraston C., Johansson J., 2011b, MNRAS, 412, 2183 (Paper I)

Thuan T., Pilyugin L., and Zinchenko I., 2010, ApJ, 712,1029

Timmes F., Brown E., Truran J., 2003, ApJ, 590, 83

Tolstoy E., Hill V., Tosi M., 2009, ARA&A, 47, 371

Tojeiro R., Heavens A. F., Jimenez R., Panter B., 2007, MNRAS, 381, 1252

Toomre A., Toomre J., 1972, ApJ, 178, 623

Trager S. C., Worthey G., Faber S. M., Burstein D., Gonzalez J. J., 1998, ApJS, 116, 1

Trager S., Faber S., Worthey G., González J., 2000a, AJ, 119, 1645

Trager S., Faber S., Worthey G., González J., 2000b, AJ, 120, 165

Tremonti C., 2004, ApJ, 613, 898

Tripicco M. J., Bell R. A., 1995, AJ, 110, 3035

Trujillo I., Erwin P., Asensio Ramos A., Graham A., 2004, AJ, 127, 1917

Tsujimoto T., Nomoto K., Yoshii Y., Hashimoto M., Yanagida S., Thielemann F., 1995, MNRAS, 277, 945

Umeda H., Nomoto K., Kobayashi C., Hachisu I., Kato M., 1999, ApJ, 522, 43

van den Bergh S., 1990, PASP, 102, 1318

van den Hoek L., Groenewegen M., 1997, A&AS, 123, 305

Vazdekis A., 1999, ApJ, 513, 224

Vazdekis A., Casuso E., Peletier R. F., Beckman J. E., 1996, ApJS, 106, 307

Vazdekis A., Peletier R. F., Beckman J. E., Casuso E., 1997, ApJS, 111, 203

Vazdekis A., Salaris M., Arimoto N., Rose J. A., 2001, ApJ, 549, 274

Vazdekis A., Sánchez-Blázquez P., Falcón-Barroso J., Cenarro A., Beasley M., Cardiel N., Gorgas J., Peletier R., 2010, MNRAS, 404, 1639

Ventura P., Caloi V., D'Antona F., Ferguson J., Milone A., Piotto G. P., 2009, MNRAS, 399, 934

Visvanathan N., Sandage A., 1977, ApJ, 216, 214

Walcher C. J., Coelho P., Gallazzi A., Charlot S., 2009, MNRAS, 398, L44

Weiss A., Salaris M., Ferguson J. W., Alexander D. R., 2006, A&A, submitted (astro-ph/0605666)

Weiner, B., et al., 2005, ApJ, 620, 595

Whelan J., Iben I. Jr., 1973, ApJ, 186, 1007

White S. D. M., Rees M. J., 1978, MNRAS, 183, 341

Willmer C., et al., 2006, ApJ, 647, 853

Woosley S., Weaver T., 1986, ARA&A, 24, 205

Woosley S. E., Weaver T. A., 1995, ApJS, 101, 181

Worthey G., 1994, ApJS, 95, 107

Worthey G., 1998, PASP, 110, 888

Worthey G., Ottaviani D. L., 1997, ApJS, 111, 377

Worthey G., Faber S. M., Gonzalez J. J., 1992, ApJ, 398, 69

Worthey G, Faber S. M., Gonzalez J. J., Burstein D., 1994, ApJS, 94, 687

York D. G., Adelman J., Anderson J. E. Jr. et al., 2000, AJ, 120, 1579

Yungelson L., Livio M., 2000, ApJ, 528, 108

Ziegler B. L., Thomas D., Bo?hm A., Bender R., Fritz A., Maraston C., 2005, A&A, 433, 519

Zinn R., West M. J., 1984, ApJS, 55, 45

Appendix A

Element abundance ratios from the Padova model version

We have derived stellar population parameters for both model versions presented in Chapter 3, that are partly based on different stellar evolutionary tracks (see Section 3.2.1). The results for the Cassisi version are presented in Section 5.3. Fig. A.1 shows the derived results using the Padova version, for the full sample (grey contours) and red sequence population (red contours and least-squared fitted lines). The results derived using the Cassisi version for the red sequence population are shown for comparison (orange lines). The slope and intercept of the least-square fit to the red sequence population derived for Padova version are given in the toplabels.

We find the two model versions to give in general very consistent results. The Padova model version reproduce the main features found for the Cassisi model version in Section 5.3, i.e. a red sequence and a rejuvenated population. The base Padova model version only contain ages down to 2.8 Gyr (log(age)=0.45). These have been extrapolated to include younger ages. However, at such young ages the models change drastically for several indices and an extrapolation of the models may not provide fully representable models for the ages in question. This produce uncertainties in the derived results for ages younger than log(age)$\sim$0.4. Details in the results for the rejuvenated population can therefore not be trusted, while the fraction of rejuvenated galaxies should be reliable. Hence, we do not show contours for the rejuvenated population derived for the Padova version, but the fraction of rejuvenated galaxies is indicated below the separation line in the upper left panel of Fig. A.1 showing the result for the derived ages.

The trends with velocity dispersion for the two model versions are almost identical except for the [N/Fe] case. For this abundance ratio we find a clear difference between

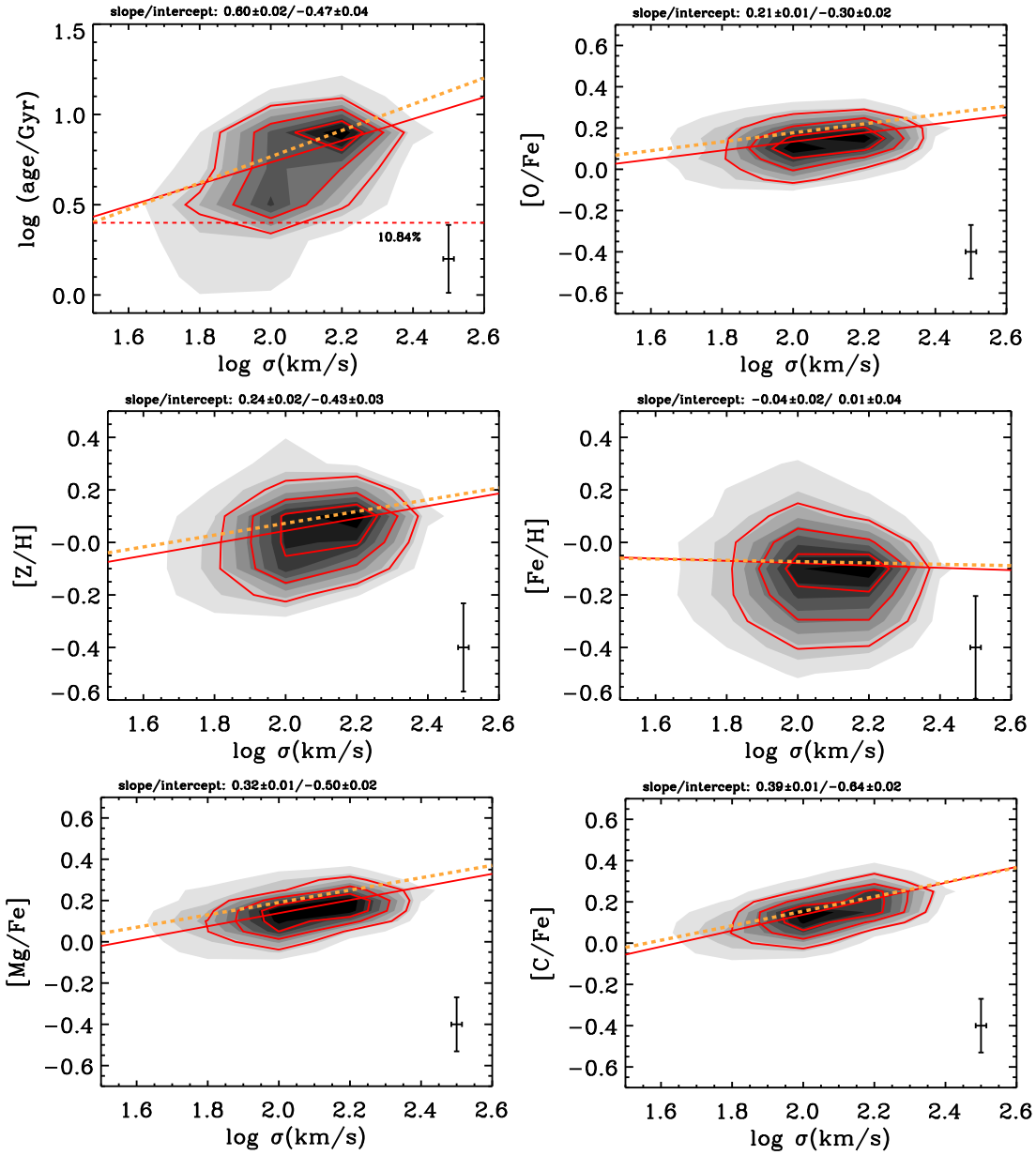

Figure A.1: Comparison between the Padova and Cassisi model results for the 3802 early-type galaxies studied in Chapter 5. Grey contours show the full sample for the Padova model, red contours are the red sequence sample for the Padova model and the red solid lines are least-square fits to the latter. Orange dashed lines are the red sequence least-square fits for the Cassisi model version, presented in Chapter 5.

the two model versions. This difference appears in both slope and intercept for the least-square fits, such that [N/Fe] show a stronger increase with σ for the Padova version and overall weaker abundance ratios for the Cassisi version.

In Chapter 3 we find CN_1 and CN_2 to be two of the indices that show the biggest differences between the Cassisi and Padova model versions. Since these are two of the most N sensitive indices they are responsible for the derived differences in [N/Fe]. CN_1

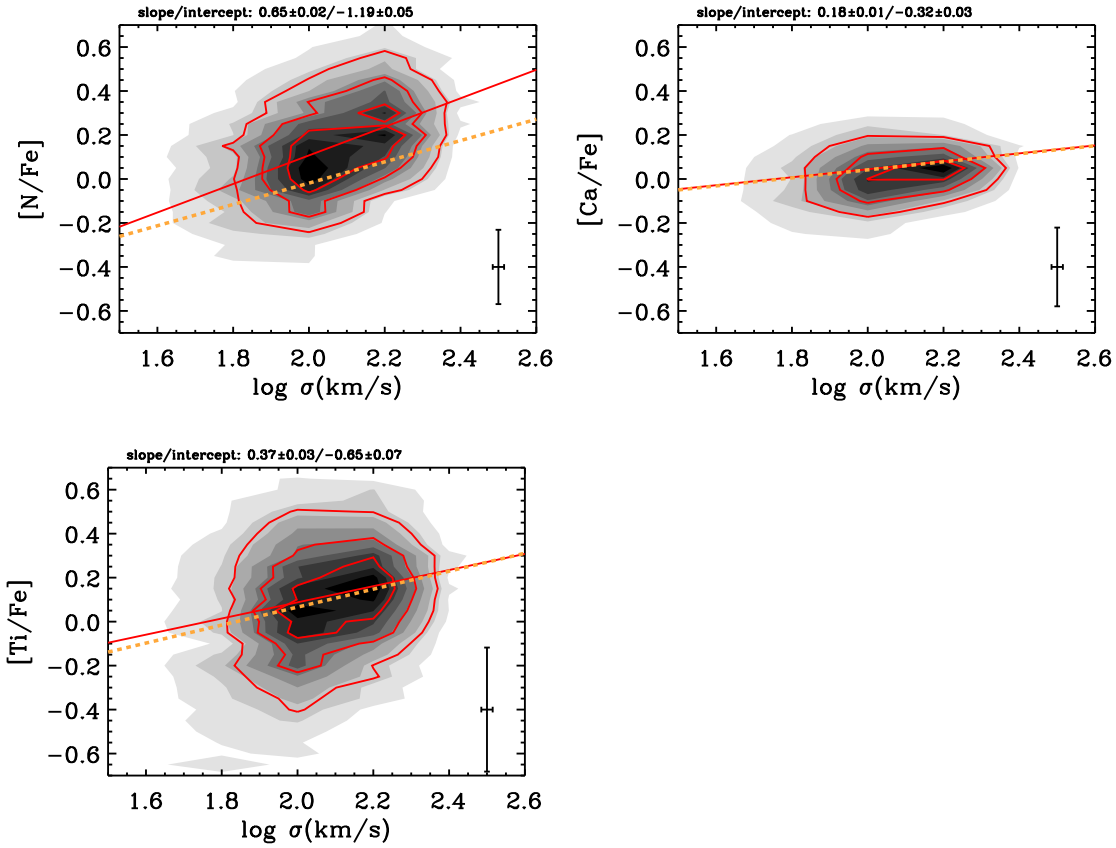

Figure A.1: Continued.

and CN_2 are also sensitive to C, but other indices (e.g. $C_2$4668) that show stronger signals to variations in this element do not show significant differences between the two model versions. The derived [C/Fe] are therefore not affected by the model differences found for CN_1 and CN_2. We investigate the source of the difference in the modelled CN-indices in terms of stellar evolutionary phases. Fig. A.2 shows the cumulative difference in the modelled CN_1 index between the two model versions for an age of 10 Gyr and solar metallicity. Starting at the MS we compare the two model versions and add the contribution from more advanced stellar evolutionary phases to find the phases that are responsible for the model differences. The post-MS evolutionary phases considered are the turn-off (TO), the SGB, the RGB, the HB and the AGB, where the HB and AGB are combined. Fig. A.2 shows that the early evolutionary phases MS, TO and SGB result in minor differences between the two model versions. The late evolutionary phases, namely the RGB and HB+AGB instead appears to be the major sources of the differences found for the derived [N/Fe]. These post-MS phases are affected by the different treatment of overshooting and mixing-length for the Cassisi and Padova evolutionary tracks (see Maraston (2005) and references therein for more details).

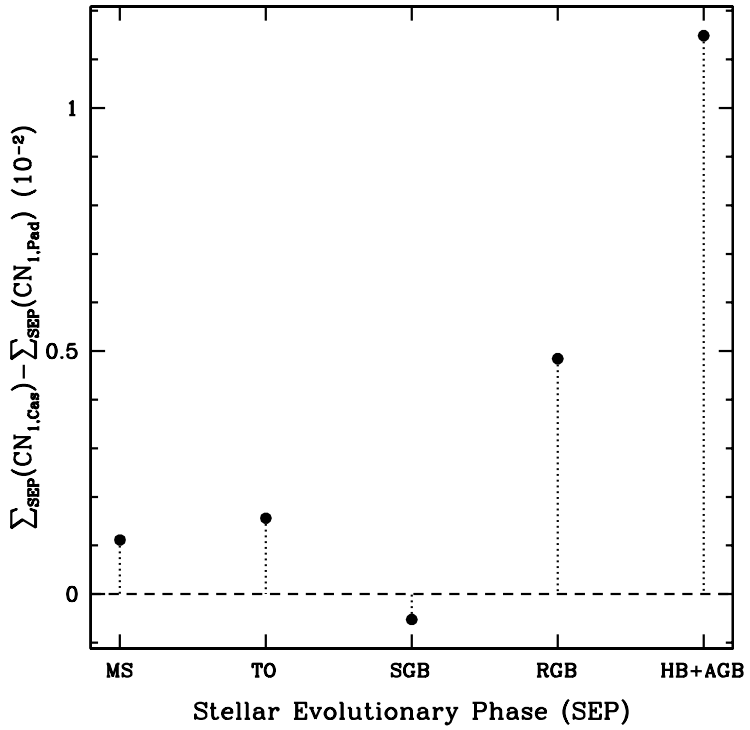

Figure A.2: Cumulative CN_1 index strength along the different stellar evolutionary phases MS, TO, SGB, RGB and HB+AGB.

In summary, we find the adopted post-MS stellar evolutionary recipes to affect the derived N abundances. This induces a systematic uncertainty in the derived [N/Fe] ratios, while the other element abundance ratios seem insensitive to uncertainties in stellar evolution theory touched by the Cassisi and Padova stellar evolutionary tracks. Still, the results derived with the two different model versions are consistent with having a strong dependence of [N/Fe] with σ and an under-abundance of N at low σ compared to O, Mg and C.

Appendix B

Environmental dependencies

T10 found no environmental dependencies for the red sequence population ($\log$(age)$>$0.4, see Section 5.3.4) for log(age), [Z/H] and [α/Fe] (represented by [O/Fe] in this work), while the fraction of rejuvenated galaxies increase in environments of lower galaxy density. These results are reproduced in this work and environmental dependencies for the individual element abundance ratios are investigated here. The derived environmental densities are described in T10 and we follow their limits of defining low and high density environments. Fig. B.1 compares different environmental densities for the results of the red sequence population derived with the Cassisi model version. We find consistent results for the Padova model version. Contours of the results and the corresponding least-square fits for low and high density environments are shown with blue and green colors, respectively. The full sample is shown for comparison as grey-shaded contours. The orange line represents the least-square fit to the full red sequence population, i.e. all environmental densities.

Fig. B.1 shows close to identical behaviours for the different environmental densities of [Mg/Fe], [C/Fe] and [Ca/Fe]. For [N/Fe] and [Ti/Fe] we find a weak spread in slope between the different environments. This is probably an artefact of the larger scatter in the derived abundance ratios found for [N/Fe] and [Ti/Fe]. The latter shows the largest scatter (see Section 5.3) and is also the abundance ratio that shows the largest difference in slope. In summary, we find no significant environmental dependencies for the abundance ratios considered in this work.

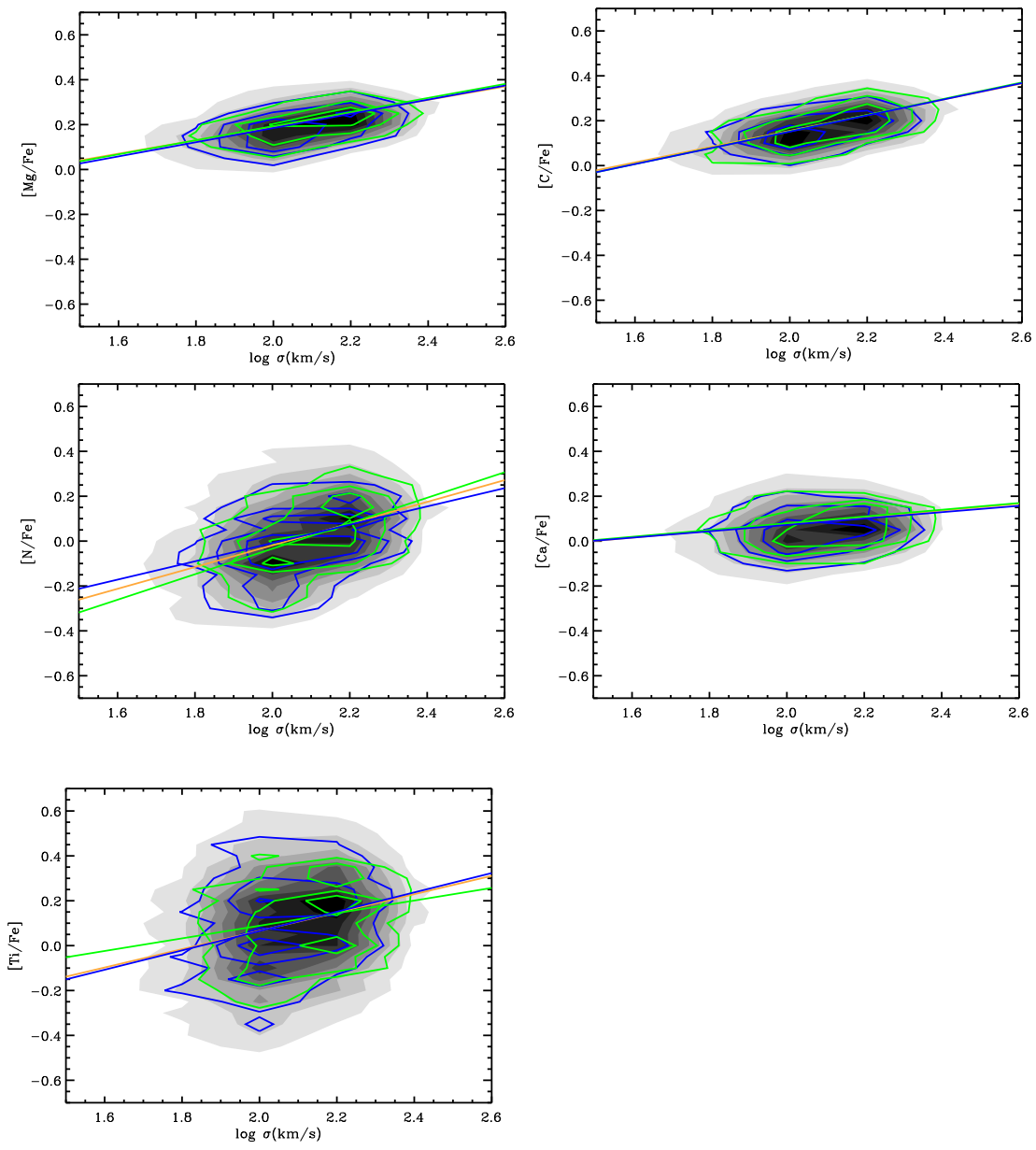

Figure B.1: Environmental dependencies for the element ratios for the Cassisi model version. Contours of the results and the corresponding least-square fits for low and high density environments are shown with blue and green colors, respectively. The full sample is shown for comparison as grey-shaded contours. The orange line represents the least-square fit to the full red sequence population, i.e. all environmental densities.